JAERI-M
93-184

IDEAL MAGNETOHYDRODYNAMIC STABILITIES IN JT-60 AND DIII-D TOKAMAK PLASMAS

October 1993

Takahisa OZEKI

日本原子力研究所
Japan Atomic Energy Research Institute

JAERI-Mレポートは，日本原子力研究所が不定期に公刊している研究報告書です。
入手の問合わせは，日本原子力研究所技術情報部情報資料課（〒319-11茨城県那珂郡東海村）あて，お申しこしください。なお，このほかに財団法人原子力弘済会資料センター（〒319-11 茨城県那珂郡東海村日本原子力研究所内）で複写による実費頒布をおこなっております。

JAERI-M reports are issued irregularly.
Inquiries about availability of the reports should be addressed to Information Division Department of Technical Information, Japan Atomic Energy Research Institute, Tokai-mura, Naka-gun, Ibaraki-ken 319-11, Japan.

編集兼発行　日本原子力研究所
印　　刷　いばらき印刷㈱

JAERI-M 93-184

Ideal Magnetohydrodynamic Stabilities in JT-60 and DIII-D Tokamak Plasmas

Takahisa OZEKI

Department of Fusion Plasma Research
Naka Fusion Research Establishment
Japan Atomic Energy Research Institute
Naka-machi, Naka-gun, Ibaraki-ken

(Received August 31, 1993)

Magnetohydrodynamic (MHD) instabilities of plasmas with a good (enhanced) energy confinement, obtained in the H-mode or after pellet injection in JT-60 and DIII-D tokamaks, are investigated. In enhanced-confinement plasmas, many kinds of MHD instabilities occurred and they inhibit further improvement. In the present thesis, therefore, the mechanism of MHD stability is investigated by computational analysis, and ways to further improve the confinement by suppression of MHD instabilities are discussed.

(1) The divertor configuration is produced by an axisymmetric divertor coil located outside the plasma. Since the divertor coil with the current flowing in the same direction as the plasma current attracts the plasma ring, positional stability becomes a problem. Results of the analysis show that even in the divertor configuration a wide window is obtained for positional stability because of the stabilizing effect of the poloidal field coils used for shaping the plasma cross-section. Another feature of the divertor configuration is the large magnetic shear near the X-point. This shear strongly reduces the growth rate of the external kink mode and enlarges the stability window.

(2) The MHD activities near the plasma surface called edge-localized modes (ELMs) occur during the H-mode plasma. The ELMs degrade the particle and energy confinement at the plasma edge and inhibit any increase in the plasma density. Theoretical analysis of experimental data indicates that giant ELMs in DIII-D are triggered by the ideal ballooning mode, and

can be suppressed when the plasma is in the connection region between the first and the second stable region for the ballooning mode by changing the plasma shape. It is also shown that plasmas with a large safety factor and a small global shear near the plasma surface can access the second stability regime through the connection region. Plasmas with a low aspect ratio and a positive triangularity can also facilitate access to the second stability regime.

(3) Centrally peaked pressure profiles obtained by pellet injection in JT-60 have maximum values of the central β (ratio of plasma pressure to magnetic pressure), β_{p1}, limited by MHD activities. The analysis of the ideal MHD stability along with the experimental observations show that the limitation of β_{p1} is caused by the n=1 internal kink mode. With the aim of obtaining larger β_{p1}, the nature of the internal kink mode stability was numerically investigated. High toroidal field can produce peaked pressure profiles, and these profiles can increase the critical β_{p1} of the internal kink mode. Though the critical β_{p1} decreases with an increase in the elongation, it can improve with triangularity.

Keywords: MHD, Stability, JT-60, DIII-D, Tokamak, Position, Kink, Ballooning, Divertor, H-mode, Pellet

JAERI-M 93-184

ＪＴ－６０及びＤⅢ－Ｄトカマクプラズマにおける理想磁気流体安定性

日本原子力研究所那珂研究所炉心プラズマ研究部
小関　隆久

（1993年８月31日受理）

本研究では，ＪＴ－６０トカマクとＤⅢ－Ｄトカマクにおける，Ｈモードやペレット入射によって，エネルギ閉じ込めが改善されたプラズマの磁気流体（ＭＨＤ）不安定性を解析する。閉じ込め改善されたプラズマでは様々なＭＨＤ不安定性が生じ，閉じ込め向上を制限している。そこで，数値解析や実験結果の解析からこれらの不安定性の機構を解明し，ＭＨＤモードを安定化することにより，閉じ込め性能を向上させる方法を検討する。

(1) ダイバータ配位は，プラズマの外側に位置する軸対称コイルによって作られる。このダイバータ・コイルはプラズマ電流と同方向に電流を流すため，プラズマリングを引付ける力が働き，軸対称モードの安定性が問題となる。解析結果，プラズマ断面形状を決めるポロイダル・コイルによる安定化効果の働きで，ダイバータ配位であっても広い安定窓があることが明らかにされた。もう一つのダイバータ配位の特徴は，磁場のＸ点（ヌル点）によって生じるプラズマ表面付近の大きな磁気シャーである。この強いシャーは外部キンクモードの成長率を大きく下げ，安定領域を拡げる強い安定化効果があることが示された。

(2) Ｈモード中ではＥＬＭと呼ばれるプラズマ周辺でのＭＨＤ現象が生じる。ＥＬＭは，プラズマ周辺の粒子及びエネルギ閉じ込めを悪化させ，密度の上昇を防げる。ＤⅢ－Ｄの実験結果の理論的解析から巨大ＥＬＭは，理想バルーニングモードの不安定化によって発生するが，プラズマの形状を変えることにより，プラズマをバルーニングモードの第二安定領域に導き，ＥＬＭを抑制できることが示された。さらにまた，数値解析により第二安定領域へ導くためには，プラズマ形状の他に，安全係数ｑを大きくするかシャーｓを下げることであることが明らかにされた。低アスペクト比で正の三角度を持ったプラズマもまた第二安定領域へアクセスしやすい。

(3) ＪＴ－６０において水素ペレット入射実験においては，中心ピークした圧力分布が形成されたが，中心の圧力限界β（プラズマ圧力と磁気圧の比），β_{P1}，はＭＨＤ不安定性により制限された。実験結果の理論的解析から，β_{P1}は，内部キンクモードの不安定化によって生じること

那珂研究所：〒311－01　茨城県那珂郡那珂町大字向山801－1

が示された。また，より高いβ_{P1}を得るために，ピークした圧力分布を持つプラズマの内部キンクモードの安定性について解析した。その結果，トロイダル磁場の高い方が圧力勾配を高くでき，高い圧力勾配すなわち強くピークした分布を持つプラズマの方が，内部キンクモードの安定限界を高くできることが示された。このβ_{P1}は楕円度と共に下がるが，三角度により改善できる。

Contents

目　　次

Chapter 1

Introduction

1.1 Introduction

Controlled thermonuclear fusion is considered to be the ultimate energy source for the human being. In order to obtain nuclear fusion, it is necessary to create and sustain a plasma with high thermal energy. Presently, fusion research concentrates on the problems of heating and stably confining such a plasma. Large-scale magnetohydrodynamic (MHD) instabilities have been a major obstacle in the way of progress toward nuclear fusion. The purpose of this thesis is to understand the properties of ideal MHD stability with the aim of obtaining high performance plasmas approaching nuclear fusion.

1.2 Nuclear Fusion

A possible alternative power reactor is a system in which usable energy results from the fusion of light nuclides such as deuterium, tritium, helium-3 and lithium. Deuterium exists abundantly in nature, so that it could supply enough energy. The fusion process itself does not leave long-lived radioactive products, and the problem of radio-active-waste disposal is much less serious than for fission reactors. However, this immense reserve of nuclear energy is still in the stage of basic research, where its scientific feasibility must still be proven.

Table 1.1 Fusion reactions of primary interest

Reaction		Thermonuclear Energy Release	Threshold Energy
D + T	→ ^{4}He(3.52MeV) + n(14.06MeV)	17.6MeV	4KeV
D + D	→ T(1.01MeV) + p(3.02MeV)	4.0MeV	35KeV
	→ ^{3}He(0.82MeV) + n(2.45MeV)	3.3MeV	35KeV
D + ^{3}He	→ ^{4}He(3.62MeV) + p(14.67MeV)	18.3MeV	30KeV

Nuclear reactions of interest for fusion reactors are shown in Table 1.1. This table also gives the amount of thermonuclear energy produced by a fusion event. A large amount of the binding energy can be released when the light nuclides are fused. The D-T reaction has the smallest threshold energy of those reactions and the amount of energy released is large. The D-T reaction, therefore, is the most plausible for a fusion reactor in the present stage.

The cross sections for these fusion reactions are appreciable only for incident energies above 5keV. However, accelerated beams of deuterons bombarding a target will not demonstrate fusion, because most of the deuterons will lose their energy by scattering before undergoing a fusion reaction. Thus, it is necessary to create a plasma in which the thermal energies are in the 10-keV range. In a plasma with a very high temperature, the ions have velocities large enough to overcome their mutual Coulomb repulsion, so that fusion can take place.

The energy released in the nuclear reaction must be larger than that necessary to maintain the hot plasma. Lawson has derived the condition, called the "Lawson condition", for the energy balance in a fusion reactor [1]. It is expressed in terms of the parameters $n\tau_E$ and T, where n (m^{-3}) is the plasma number density, T (keV) is the plasma temperature, and τ_E (sec) is the energy confinement time, which is the amount of energy balance, i.e. the ratio of the containing plasma energy to the input power into

the plasma. At reactor conditions $n\tau_E \geq f(T)$, where typically $f(T) \approx 3 \times 10^{20} m^{-3} s$ at the optimized temperature $T \approx$15 keV.

1.3 The Tokamak Device

In order to satisfy the Lawson condition, a variety of fusion devices has been developed. The tokamak is presently the most advanced machine and has been the most successful one [2,3]. The main components of an experimental tokamak are illustrated in Fig. 1.1. It is essentially a transformer in which the primary coil drives a current through an axisymmetric toroidal plasma in a strong magnetic field. The plasma is produced inside a toroidal vacuum vessel, which must be sufficiently resistive so that the induced toroidal electric field drives current in the plasma volume rather than in the vessel itself. Plasma currents are usually in the range 0.5-3MA in present-day experiments. A set of massive toroidal field coils generates the principal toroidal magnetic field (B_t), typically in the range 1-5Tesla. The strong toroidal magnetic field is necessary to suppress the major MHD instabilities. The poloidal magnetic field (B_p) of the plasma current adds to the toroidal field to give a resultant helical field.

An iron core may be added to improve the coupling between the primary coils and the plasma. In recent large tokamaks, however, an iron core has not been employed because of the following disadvantages: first, the volt-second requirement of the discharge may be so large that the iron core saturates, thus generating asymmetric stray magnetic fields. Secondly, the magnetic attraction of the core tends to destabilize the positioning of the plasma column.

The vacuum inside the tokamak chamber before the discharge is typically about 10^{-8}Torr. In typical tokamak operation, the chamber is filled with a short pulse of hydrogen/deuterium gas, called gas-puff, and then toroidal current is driven by an initial voltage. As the plasma current builds up, ohmic heating raises the electron temperature, so that the resistive voltage falls to the $\sim 1V$ range. Once this stage is

reached, the primary coil and the other poloidal field coils maintain the plasma current and the plasma position.

To further increase the plasma temperature, various kinds of heating systems have been considered. Neutral beam heating (NB) [4] is one of the most useful methods. A high-current ion beam (typically in the 50-100keV, 1-20MW range) is produced by an ion source and is converted to a neutral-atom beam by charge exchange in a gas cell. The neutral atoms then pass freely through the magnetic field structure of the tokamak, until they become reionized by electron or ion impact, or charge exchange within the tokamak plasma. The injected particles are then trapped as energetic ions in the tokamak magnetic field and slow down gradually by collisions with the bulk-plasma electrons and ions, thus heating the plasma.

During the last two decades, there has been continuous progress in the tokamak concept. At the present time, reactor-relevant physics issues are under investigation both in theory and in experiments.

1.4 MHD Stabilities in Tokamaks

MHD instabilities have imposed severe limitations on the amount of plasma current and plasma pressure ($= nT$) in a magnetically confined plasma. Ideal MHD is the simplest single-fluid model for determining the macroscopic equilibrium and stability properties of plasmas. From the early days of fusion research, the study of ideal MHD stability has been promoted. This work is summarized in Refs. [5] and [6]. There is a general consensus that any configuration meriting consideration for a fusion reactor must satisfy the equilibrium and stability limits set by ideal MHD. If not, catastrophic termination of the plasma on a very short time scale (compare to experimental times) is the usual consequence. The main MHD instabilities in tokamaks are described below.

The basic stability problems in tokamaks are axisymmetric modes. In a torus, as shown in Fig. 1.2, a vertically applied external field (B_z) is required in order to prevent an expansion of the toroidal ring of plasma in the major radial direction. If the vertical field is not properly designed, however, the plasma, particularly if it is elongated vertically, also has a tendency to drift upward or downward. A simple model illustrating the basic nature of the stability of axisymmetric modes was first investigated by Osovets [7] and later analyzed further by Yoshikawa[8]. It involves the simple index n_z,

$$n_z = -\frac{R}{B_z}\frac{\partial B_z}{\partial R}, \tag{1. 1}$$

which characterizes the bending of the vertical field lines. Here, R is the horizontal coordinate. From this model a stability window is obtained, existing between the vertically unstable region ($n_z < 0$) and the horizontally unstable region ($n_z > 1.5$).

A significant MHD instability in tokamaks is driven by the plasma current flowing parallel to the magnetic field. It causes the plasma to twist and kink, as shown in Fig. 1.3, and so it is called the kink mode. It is stabilized in certain types of current profiles and by the appropriate choice of safety factor. Here, the safety factor, q, is

defined as the number of times a magnetic field line winds the long way around the toroid divided by the number of times it winds the short way around,

$$q \equiv \frac{\text{winding number long away}}{\text{winding number short away}} = \frac{r}{R}\frac{B_t}{B_p} , \qquad (1.2)$$

where r is the minor radius of the torus. Stability of the kink mode depends on the relationship between the helicity of the perturbation and the helicity of the field lines, i.e. the safety factor. The stability region as a function of the safety factor and the current profile has been obtained by Wesson for a simple circular cross-section plasma[9].

When the plasma pressure is increased, a new class of instabilities are predicted to exist in tokamaks. They cause the plasma to "bulge out" where both the pressure gradient and curvature are strongest and point in roughly the same direction. Hence, as shown in Fig. 1.4, they are typically strongest at the outer side of a torus at the flux surface with the highest pressure gradient. This instability, called the ballooning mode, imposes a limit on the pressure gradients or total pressure in the whole plasma region. The ballooning mode has been investigated by a number of authors. A complete theory has been given by Connor et al.[10]. The general stability diagram of the ballooning mode has been obtained by Green and Chance[11].

1.5 Enhanced Confinement Plasmas in Tokamaks

It has been clarified from recent experiments that a improved confinement of plasmas is required in order to reach the Lawson condition. When a strong heating is used to obtain a high temperature, tokamak discharges usually show a deterioration of plasma confinement (L-mode) due to anomalous transport processes. In an L-mode discharge, the energy confinement time (τ_E) falls with input heating power P_{IN} as $\tau_E \propto P_{IN}^{-0.5}$, which is called L-mode scaling, first elucidated by Goldston [12,13]. However, enhanced confinement may be obtained in the divertor configuration (H-mode) or with pellet injections.

H-mode: A regime with good (enhanced) energy and particle confinement, called H-mode, has been found in tokamaks [14-16]. The H-mode is obtained usually in the divertor configuration when the input power, for example NB heating, increases above a certain threshold value causing a transition from the L-mode. Figure 1.5 shows a schematic drawing of a divertor configuration compared with a limiter configuration. In the limiter configuration, the plasma surface is defined by some material limiters, whereas in the divertor configuration, the plasma boundary is defined by a magnetically limited surface, separated from the wall of the vacuum chamber. The separation of the plasma from the wall is an essential point in obtaining a transition to H-mode. Consequently, the temperature and the density just inside the plasma surface increase due to the improved transport characteristics near the plasma surface, and τ_E is improved by a factor of about 2 above the L-mode value.

Pellet injection: From the early stages of fusion research, the improvement of particle and energy confinement by central fuelling has been expected, in contrast with the improvement near the plasma surface in an H-mode plasma. Injection of solid hydrogen pellets to the plasma center is an useful method for the central fuelling [17]. (This is done as an alternative to fuelling the plasma by gas-puffing.) The pellet injector accelerates the pellets up to $1 - 2km/s$, for example, by the high pressure gas, and

throws the pellets to the plasma center. Ablation of the pellet near the plasma center results in a peaked density profile. The enhanced central values of density and τ_E, can bring the plasma closer to satisfying the Lawson criterion.

1.6 Purpose of This Thesis

In this thesis, MHD stabilities of enhanced confinement plasmas in JT-60 and DIII-D tokamaks are considered. JT-60 tokamak (JAERI Tokamak-60) [20] in Japan is one of the three large tokamaks in the world, the other two being TFTR (Tokamak Fusion Test Reactor) in the United States [18], and JET (Joint European Torus) of the European Community [19]. In JT-60 tokamak, enhanced confinement plasmas were obtained in the central plasma region by means of pellet injection. DIII-D tokamak is smaller than the three large tokamaks and has a non-circular cross section plasma in a divertor configuration. In DIII-D, enhanced confinement was observed in H-mode plasmas.

These enhanced confinement plasmas in JT-60 and DIII-D encounter the following obstacles of MHD stability: (1) In the divertor configuration, the divertor coil with the current flowing in the same direction as the plasma current attracts the toroidal ring of plasma, which may destabilize the axisymmetric mode. On the other hand, the stagnation point (or X-point) of the poloidal field, produced near the divertor coil, makes a significantly large value of the magnetic shear S $(= (r/q)(dq/dr))$, which has a stabilizing effect near the plasma surface. Therefore, it is important to investigate these MHD characteristics for making a stable plasma in the divertor configuration. (2) During H-mode discharges, an MHD instability near the plasma surface, called Edge Localized Mode (ELM), is observed and results in a degradation of the energy confinement. It is important to investigate the ELM for the purpose of sustaining the good confinement. (3) As the peakedness of the plasma pressure profile increases by pellet injection, the limitation of the pressure due to MHD instability is observed. It is

necessary to clarify the cause of this limitation and to understand methods for improving the peak pressure. Despite the concentration of effort in the the MHD stability as described in the previous section, there are still uncertainties in the properties of MHD stability in an actual tokamak plasma, especially in enhanced confinement plasmas. The purpose of this thesis is, by computational analyses, to clarify the properties of MHD stability and to find a method to obtain more attractive plasmas for a fusion reactor.

The work of this thesis is focused on the following subjects. (1) Investigation of the properties of ideal MHD stability of plasmas in the divertor configuration. (2) Investigation of the cause of MHD instability near the plasma surface (ELM) in H-mode plasmas in DIII-D and the suppression of this MHD activity. (3) Investigation of the correlation of MHD instability with the limitation of the centrally peaked pressure produced by the pellet injection in JT-60, and understanding the further improvement of the limitation of the peaked pressure profile.

This thesis is organized as follows. In Chapter 2, the ideal MHD equations and the energy principle are derived in order to determine whether a given plasma is stable or unstable, and basic MHD stability properties in a tokamak are described. In Chapter 3, the JT-60 and DIII-D tokamaks are described, and MHD instabilities encountered in these devices are explained. The numerical codes used for the analysis of the MHD stability are also explained. In Chapter 4, the effects of the divertor configuration on the axisymmetric modes and kink modes are discussed. In Chapter 5, a comparison of MHD activity near the plasma surface with expected ballooning mode behaviour is discussed for DIII-D H-mode plasmas. In Chapter 6, the effect of kink modes and ballooning modes in pellet-fuelled plasmas in JT-60 are discussed. Finally, in Chapter 7, the main results and prospects for future tokamaks are summarized as concluding remarks.

References

[1] J.D. Lawson: Proc. Phys. Soc. B**70** (1957) 6.

[2] L.A. Artsimovich: Nucl. Fusion **12** (1972) 215.

[3] H.P. Furth: Fusion (ed. by E.Teller) Vol.1, Academic Press, New York, 123.

[4] D.L. Jassby: Nucl. Fusion **17** (1977) 309.

[5] J.A. Wesson: Nucl. Fusion **18** (1978) 87.

[6] J.P. Freidberg: Rev. Mod. Phys. **54** (1982) 80.

[7] S.M. Osovets: in Plasma Physics and the Problems of Controlled Thermonuclear Reactions (Pergamon, Oxford), Vol.2,322.

[8] S. Yoshikawa: Phys. Fluids **7** (1964) 278.

[9] J.A. Wesson, A. Sykes: in Plasma Physics and Controlled Nuclear Fusion Research 1974 (IAEA,Vienna), Vol.II (1975) 529.

[10] J.W. Connor, R.J. Hastie, J.B. Taylor: Proc. Roy. Soc. **A365** (1979) 1.

[11] J.M. Greene, M.S. Chance: Nucl. Fusion **21** (1981) 453.

[12] R.J. Goldston: Plasma Phys. Controll. Fusion **26** (1984) 87.

[13] S.M. Kaye, R.J. Goldston: Nucl. Fusion **25** (1985) 65.

[14] F. Wagner, et al.: Phys. Rev. Lett. **49** (1982) 1408.

[15] F. Wagner, et al.: in Plasma Physics and Controlled Nuclear Fusion Research 1982 (Proc. 9th Int. Conf. Baltimore, 1982) Vol.I IAEA, Vienna (1983) 43.

[16] K.H. Burrell, et al.: in Controlled Fusion and Plasma Physics (Proc. 11th Europ. Conf. Oxford, 1983) Vol.1 (1983) 11.

[17] M. Kaufmann: Plasma Phys. Controll. Fusion **28** (1986) 1341.

[18] K.M. Young et al.: Plasma Phys. Controll. Fusion **26** (1984) 11.

[19] P.H. Rebut et al.: Plasma Phys. Controll. Fusion **26** (1984) 1.

[20] JT-60 Team: Plasma Phys. Controll. Fusion **28** (1986) 165.

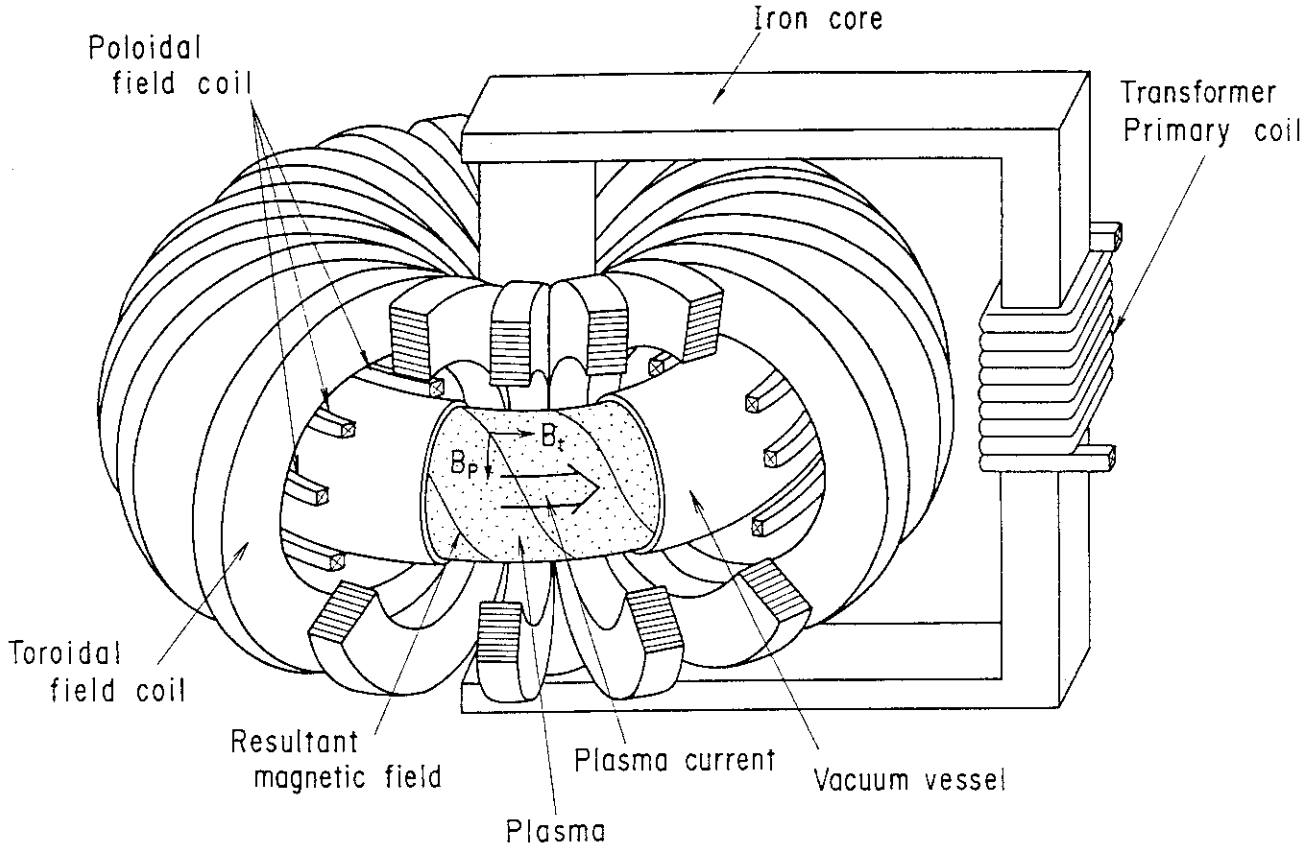

Fig. 1.1 Schematic of a tokamak with iron-core transformer. The plasma is produced inside a toroidal vacuum vessel. The plasma current is induced by the transformer action of the primary coil. The vertical field required for equilibrium is produced by poloidal field coils. The strong toroidal field (B_t) is produced by toroidal field coils and the poloidal field (B_p) is produced by the plasma current.

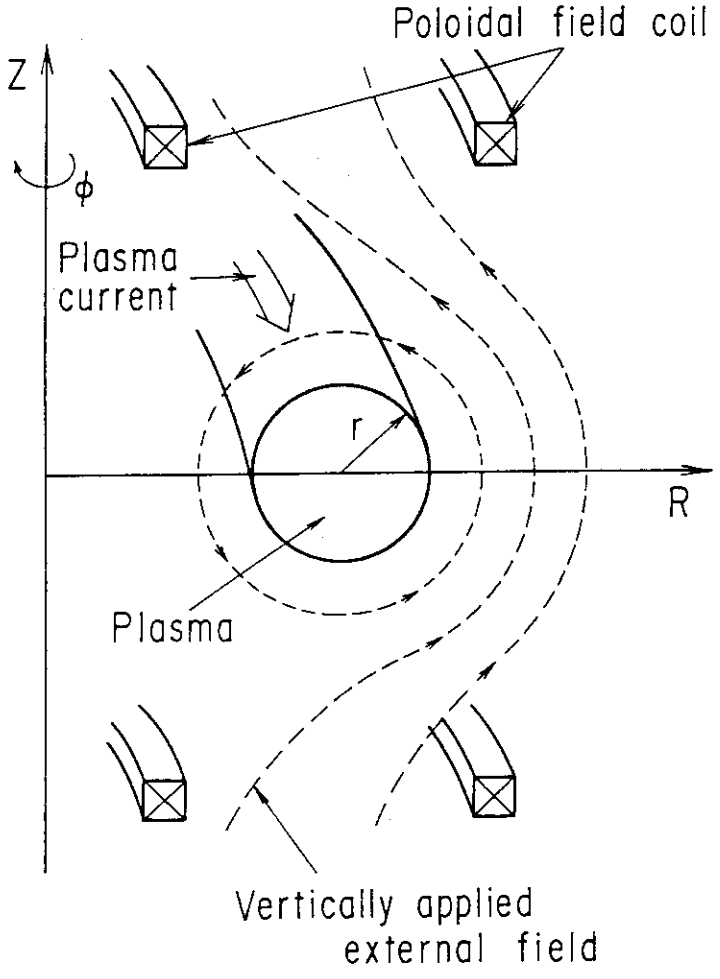

Fig. 1.2 The poloidal magnetic field from toroidal plasma current contributes to the outward radial force. An externally applied vertical magnetic field from the poloidal field coils provides an inward force.

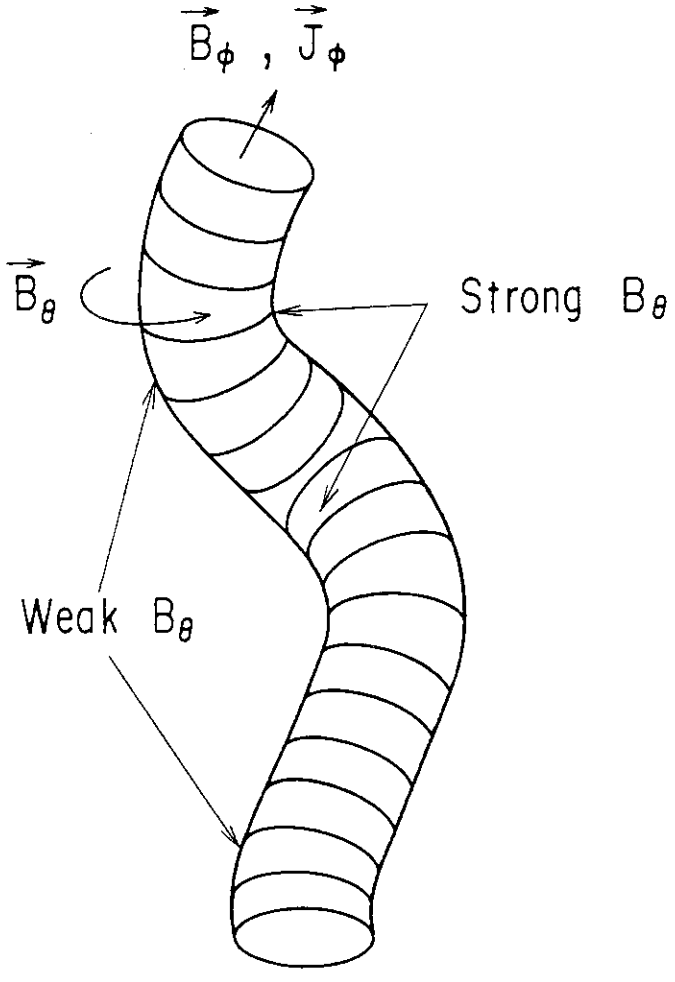

Fig. 1.3 Physical mechanism of the kink instability. B_θ is stronger on the inside than on the outside of the bend, which produces a net force that further kinks the plasma column.

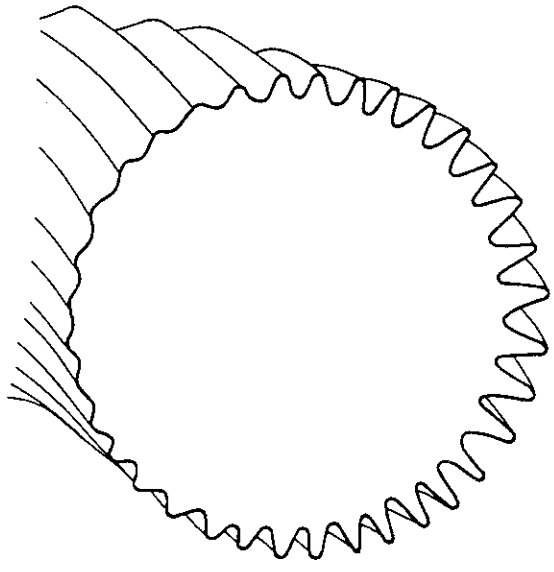

Fig. 1.4 The ballooning instability in a tokamak. The perturbation is larger on the outer (major radial) side of the torus than on the inner side.

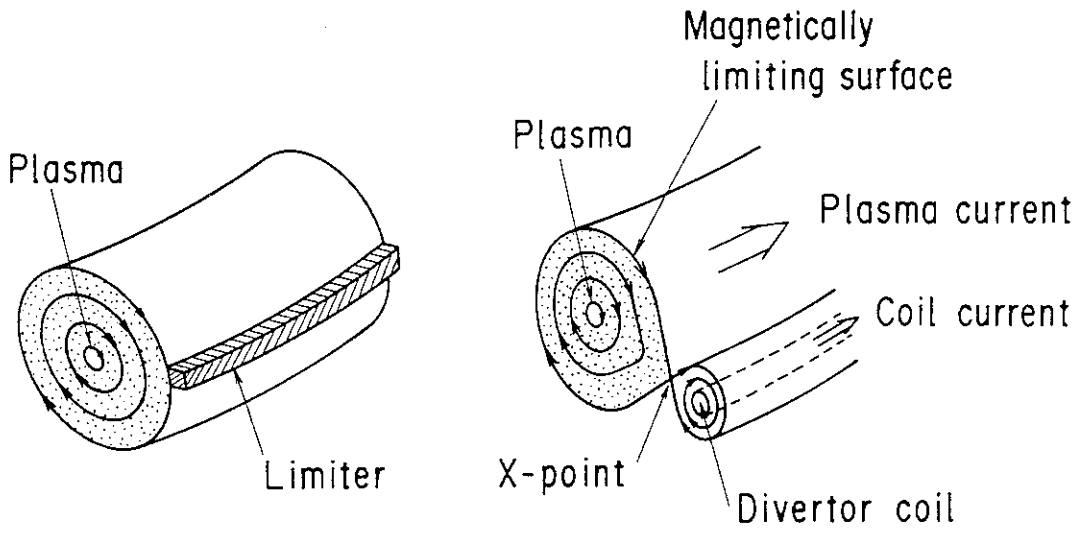

Fig. 1.5 Schematic of limiter and divertor configurations. (a) In the limiter configuration, the plasma surface is defined by a material structure, called a limiter. (b) In the divertor configuration, the plasma surface is limited by a magnetic structure produced by a divertor coil in which the current flows in the same direction as the plasma current.

Chapter 2

Ideal MHD Stabilities

2.1 Introduction

This chapter describes the ideal magnetohydrodynamics (MHD) model and stabilities in the tokamak. MHD equations describe a "fluid model" of a plasma in a magnetic field because the plasma behaves as a fluid under reasonable conditions expected in controlled thermonuclear fusion. The MHD model is a set of simple equations which can be applied to a wide range of fusion plasmas. The assumptions of the MHD model and the introduction of the ideal MHD equations are presented in Section 2.2. In a tokamak plasma, MHD instabilities may be driven by the plasma current or by the plasma pressure. These instabilities sometimes break the magnetic flux, or enhance the diffusion and degrade the energy confinement. Therefore, MHD stabilities are important research subjects in the area of controlled thermonuclear fusion. In order to study the MHD instability, at first, a steady state plasma called equilibrium is necessary, in which the pressure gradient force just balances the Lorentz magnetic forces. The equilibrium in a tokamak is described in Section 2.3. If the plasma is perturbed from this equilibrium state, the resulting perturbed forces either restore the plasma to its original equilibrium (stable) or cause a further enhancement of the initial disturbance (unstable). To analyze this condition, linear stability theory using the energy principle in a tokamak is a useful method. The linear stability theory is described in Section 2.4. A review of typical MHD stabilities in a tokamak, including the positional stability, kink stability and ballooning stability, is briefly presented in Section 2.5.

2.2 Ideal MHD Equations

The ideal MHD model is one of the simplest models for describing the phenomena of a perfect conducting plasma in a magnetic field. The ideal MHD model is derived from the full set of Maxwell's equations coupled with a kinetic model of the plasma, described by a Boltzmann equation for each species[1]. To derive the ideal MHD equations, assumptions are implied in the MHD model: (1) high collisionality, (2) characteristic dimensions much larger than an ion gyro radius, (3) small electric resistivity. In the assumption of (1), the full pressure tensor $\overleftrightarrow{P}$ reduces to a simple scalar isotropic pressure p, because many collisions take place on a time scale short compared to those of interest, (namely, $L/V_T \gg \tau_{ii}$, where L is the spatial scale, V_T is the ion thermal velocity ($= (2T_i/m_i)^{1/2}$), and τ_{ii} is the ion-ion collision time.) The assumption of (2) represents that valid scale lengths are long compared to the characteristic length of the lowest plasma frequency, which is the ion gyro radius ($L \gg r_{Li}$, where r_{Li} is the ion gyro radius). This model implies that $L \gg \lambda_D$ because $r_{Li} > \lambda_D$, where λ_D is the Debye length. The use of this condition represents that the electrons and ions respond together (charge neutrality). In the area of the assumption of (3), the resistive diffusion time τ_D $(= \mu_0 L^2/\eta = R_M L/V_T)$ is long compared to the characteristic time (L/V_T) since $R_M = V_T L \mu_0/\eta \gg 1$, where R_M is magnetic Reynolds number, η is resistivity. The use of this assumption represents the plasma is frozen to the magnetic field lines.

The ideal MHD equations are

$$\rho(\frac{\partial}{\partial t} + \mathbf{V}\cdot\nabla)\mathbf{V} = -\nabla p + \mathbf{J}\times\mathbf{B}, \tag{2. 1}$$

$$\frac{\partial \rho}{\partial t} + \nabla(\rho\mathbf{V}) = 0, \tag{2. 2}$$

$$(\frac{\partial}{\partial t} + \mathbf{V}\cdot\nabla)(p\rho^{-\Gamma}) = 0, \tag{2. 3}$$

$$\mathbf{E} + \mathbf{V}\times\mathbf{B} = 0, \tag{2. 4}$$

$$\nabla\times\mathbf{E} = -\frac{\partial \mathbf{B}}{\partial t}, \tag{2. 5}$$

$$\nabla \times \mathbf{B} = \mu_0 \mathbf{J}. \tag{2. 6}$$

The state of the system at any point in space and time is given by the variables $\mathbf{V}$, $\mathbf{B}$, p, and ρ, where $\mathbf{V}$ is the macroscopic fluid velocity, $\mathbf{B}$ is the magnetic field, p is the thermal pressure, and ρ is the mass density. The electric field $\mathbf{E}$ and the current density $\mathbf{J}$ are treated as auxiliary quantities.

The first MHD equation of Eq. (2. 1) represents the acceleration of the fluid in response to local forces. The pressure gradient term on the right in Eq. (2. 1) may be thought as the force resulting from a difference in thermal pressure on opposite sides of an infinitesimal element of fluid. The $\mathbf{J} \times \mathbf{B}$ forces comes from the sum of Lorentz magnetic forces $Z_i e \mathbf{V}_i \times \mathbf{B}$ on the individual charged particles that make up the plasma ($Z_i e$ is the charge and $\mathbf{V}_i$ is the velocity of each particle).

The plasma motion alters the pressure and mass density through the thermodynamic equations of Eqs. (2. 2) and (2. 3). These equations can be re-written as follows

$$\frac{\partial}{\partial t}\rho = -\mathbf{V} \cdot \nabla \rho - \rho \nabla \cdot \mathbf{V}, \tag{2. 2'}$$

$$\frac{\partial}{\partial t}p = -\mathbf{V} \cdot \nabla p - \Gamma p \nabla \cdot \mathbf{V}. \tag{2. 3'}$$

The $\mathbf{V} \cdot \nabla p$ and $\mathbf{V} \cdot \nabla \rho$ terms on the right side of these equations represent the effect of convection. If these terms stood alone, the pressure and density of each fluid element would never change, but they would simply be carried along with the fluid. The $\Gamma p \nabla \cdot \mathbf{V}$ and $\rho \nabla \cdot \mathbf{V}$ terms in these equations represent the effect of compression and expansion. As a result of these terms, the pressure and density change as the fluid elements change size in response to changes in pressure. The constant $\Gamma = 5/3$ represents the ratio of specific heats for an ideal gas with three degree of freedom.

Equation (2. 4) is Ohm's law, which implies that in a reference frame moving with plasma the electric field is zero; that is the plasma is a perfect conductor. It is the perfect conductivity assumption of Ohm's law that gives rise to the name "Ideal MHD".

Remaining relation, Eqs. (2. 5) and (2. 6), indicate that in ideal MHD the electromagnetic behaviour is governed by the low-frequency Maxwell's equations. The motion of the plasma alters the magnetic field through Ohm's law Eq. (2. 4) and Faraday's law Eq. (2. 5), while the magnetic acts on the motion of the plasma through the equation of motion Eq. (2. 1). In Eq. (2. 6), the displacement current $\epsilon\partial\mathbf{E}/\partial t$ is neglected. This magnetostatic approximation is valid whenever the Alfvén velocity $v_A \equiv B/\sqrt{\mu_0\rho}$ is much smaller than the speed of light. μ_0 is the magnetic permeability in a vacuum, which is equal to $4\pi \times 10^{-7}$ henrys/meter.

2.3 MHD Equilibrium in Tokamak

In the MHD theory of magnetically confined plasma, an equilibrium means the complete balance of forces. Since an instability is the tendency to move away from equilibrium, it is important to start to consider a property of equilibrium.

2.3.1 Tokamak equilibrium

The MHD equilibrium are obtained from the equation of motion Eq. (2. 1) neglecting the inertia term, and Maxwell's equations.

$$\nabla p = \mathbf{J} \times \mathbf{B} \tag{2. 7}$$

$$\nabla \times \mathbf{B} = \mu_0 \mathbf{J}, \tag{2. 8}$$

$$\nabla \cdot \mathbf{B} = 0. \tag{2. 9}$$

These equations apply to the plasma in steady state ($\partial/\partial t = 0$) with no flow ($\mathbf{V} = 0$). These are most commonly used assumption for the equilibrium state in magnetically confined plasmas, such as a tokamak.

The tokamak is a configuration with a toroidal geometry, as shown in Fig. 2.1, in which the hot plasma is confined by the poloidal field of a current circulating in it and a strong toroidal magnetic field parallel to the current[2]. The resulting magnetic field has ideally a simply helical structure. Here, most of the field lines continue indefinitely, ergodically covering a set of simply nested toroidal surfaces. Any surface that is covered by a magnetic field line is called a magnetic surface. Simply nested magnetic surfaces, one within the other, surround a field line called the magnetic axis. Properties of the MHD equilibrium can be clarified from these Eq. (2. 7)-(2. 9). Equation (2. 7) obviously states that $\mathbf{J}$ and $\mathbf{B}$ are each perpendicular to ∇p ($\mathbf{B} \cdot \nabla p = \mathbf{J} \cdot \nabla p = 0$) and ∇p is everywhere normal to the surface $p = const.$ $\mathbf{J}$ and $\mathbf{B}$, therefore, must lie on the surfaces

of constant p. In the tokamak, there is a smooth radial pressure gradient so that the surfaces of constant pressure are nested tori.

Substitution of Eq. (2.8) to Eq. (2.7) leads to a pressure balance in terms of the pressure and magnetic field.

$$\nabla p = \frac{1}{\mu_0}\left\{(\mathbf{B}\cdot\nabla)\,\mathbf{B} - \nabla\left(\frac{B^2}{2}\right)\right\}. \tag{2.10}$$

When the system is axially symmetric and the curvature of the toroidal magnetic field line is neglected, Eq. (2.10) reduces to

$$\frac{\partial}{\partial r}\left(p + \frac{B_t^2}{2\mu_0} + \frac{B_p^2}{2\mu_0}\right) = -\frac{B_p^2}{r\mu_0}\ , \tag{2.11}$$

where B_t and B_p are the toroidal and poloidal field, respectively. The pressure balance at the plasma surface can be obtain by integrating by parts.

$$\left[p + \frac{B_t^2}{2\mu_0} + \frac{B_p^2}{2\mu_0}\right]_{r=a} = \frac{1}{\pi a^2}\int_0^a \left(p + \frac{B_t^2}{2\mu_0}\right) 2\pi r\,dr,$$

i.e.,

$$\bar{p} + \frac{\bar{B}_i^2}{2\mu_0} = \frac{B_p^2}{2\mu_0} + \frac{B_e^2}{2\mu_0}\ , \tag{2.12}$$

where B_i and B_e are the toroidal field inside and outside the plasma, respectively. The volume average $\bar{X}$ of a variable X is defined by a integral of a whole plasma volume,

$$\bar{X} \equiv \int_{Volume} X\,dV \Big/ \int_{Volume} dV. \tag{2.13}$$

Thus the radial force due to the plasma pressure is principally balanced by the poloidal field (B_p). The toroidal field contributes to the pressure balance only in the region within the plasma, where the volume average, $\bar{B}_i^2$, differs from the average over the plasma surface, B_e^2.

If the ratio of the averaged plasma pressure to the pressure of poloidal magnetic field is defined as,

$$\beta_p \equiv \frac{\bar{p}}{\dfrac{B_p^2}{2\mu_0}}, \tag{2.14}$$

the following relation is derived from Eq. (2.12) and Eq. (2.14)

$$\beta_p = 1 + \frac{B_e^2 - \bar{B}_i^2}{B_p^2}. \tag{2.15}$$

In the low β_p plasma ($\beta_p < 1$), the plasma exhibits a paramagnetic phenomena, in which the field inside the plasma increases due to the Larmor gyration of particles moving along the field line ($B_e^2 < \bar{B}_i^2$). In the high β_p plasma ($\beta_p > 1$), the perpendicular current $\mathbf{J}_\perp$ (to be described in Eq. (2.36)), which is produced by the pressure gradient, decreases the field inside the plasma ($B_e^2 > \bar{B}_i^2$). The plasma β is a important parameter that measures the efficiency of plasma confinement by the magnetic field and affects to the MHD stability.

By carrying out appropriate integral over the flux surfaces or the plasma volume, one can define a number of quantities that are of importance to the MHD stability. The poloidal magnetic flux Ψ

$$\Psi = \int_{S_p} \mathbf{B} d\mathbf{S}_p = 2\pi\psi, \tag{2.16}$$

where S_p is a plane extending from the minor (magnetic) axis out to the isobaric surface and encircling the major axis (see Fig. 2.1). Since $\mathbf{J}$ and $\mathbf{B}$ lie on the constant p contours, it follows that each of the quantities

$$\Phi = \int_{S_\phi} \mathbf{B} d\mathbf{S}_\phi, \tag{2.17}$$

$$I_\phi \ (= I_p \ ) \ = \int_{S_\phi} \mathbf{J} d\mathbf{S}_\phi, \tag{2.18}$$

$$I_\chi = \int_{S_p} \mathbf{J} d\mathbf{S}_p, \tag{2.19}$$

where S_ϕ is a cross sectional area bounded by the flux surface ψ=const. Φ is the toroidal flux, I_ϕ ($= I_p$) is the total toroidal current which is usually called the plasma current, and I_χ is the total poloidal current, respectively. These quantities, i.e., p, ψ, I, are function of a magnetic surface ψ only. These quantities are called surface quantities.

There are other surface quantities which often play an important role in the MHD equilibrium and stability. The first parameter is the amount of twist (helicity) of the magnetic field line, called safety factor, which varies for each flux surface and this can be defined by the ratio of toroidal to poloidal fluxes through the differential volume between adjacent flux surfaces ψ and $\psi + d\psi$

$$q(\psi) = \frac{d\Phi}{d\Psi} = \frac{1}{2\pi}\frac{d\Phi}{d\psi} = \frac{F}{2\pi}\oint \frac{d\ell_\chi}{R^2 B_p}. \tag{2.20}$$

where F is a flux function RB_t. $\oint d\ell_\chi$ is the line integral in the flux surface and normal to the toroidal direction. The function q is an important parameter in the MHD stability. The second quantity, called shear, is the amount of the change in pitch angle of a magnetic field line from one flux surface to the next is the shear. It plays an important role in stabilizing MHD instability. The shear is a surface quantity defined on each flux surface as follows:

$$S(\psi) = \frac{2V(\psi)}{q(\psi)}\frac{dq(\psi)}{dV(\psi)} \tag{2.21}$$

$V(\psi)$ is the plasma volume enclosed the flux surface of ψ.

2.3.2 Flux coordinates

The tokamak plasma is a toroidally nested structure and is axially symmetric for the torus center. To analyze this toroidal plasma, it is convenient to use the cylindrical coordinates (R, Z, ϕ), in which the Z-axis is the major axis of the torus, or the flux coordinates (ψ, χ, ϕ) system[3], as shown in Fig. 2.2.

The following guide to curvilinear coordinates by the tensor notation provides some of the relations needed to handle flux coordinates. The curvilinear coordinates will be labeled (u^1, u^2, u^3). Then

$$\mathbf{e}^i \equiv \nabla u^i$$

are called covariant basis vectors

$$\mathbf{e}_1 \equiv \sqrt{g}\ \nabla u^2 \times \nabla u^3$$

and its permutations are called contravariant basis vectors

$$\sqrt{g}^{-1} \equiv \nabla u^1 \cdot \nabla u^2 \times \nabla u^3 (\equiv J^{-1})$$

is the reciprocal of Jacobian J, which is related to the differential volume element in Cartesian coordinates by

$$dxdydz = \sqrt{g}\ du^1 du^2 du^3$$

Any vector may be expressed in terms of contravariant components a^i,

$$\mathbf{a} = a^i \mathbf{e}_i, \qquad a^i = \mathbf{a} \cdot \mathbf{e}^i,$$

or covariant components a_i, $\mathbf{a} = a_i \mathbf{e}^i$, $a_i \equiv \mathbf{a} \cdot \mathbf{e}_i$. The summation convention is implied on repeated indices. The metric tensors $g_{ij} \equiv \mathbf{e}_i \cdot \mathbf{e}_j$ and $g^{ij} \equiv \mathbf{e}^i \cdot \mathbf{e}^j$ are used to convert between covariant and contravariant components

$$a^i = g^{ij} a_j, \qquad a_i = g_{ij} a^j.$$

Note that

$$\mathbf{e_i} \cdot \mathbf{e^j} = \delta_{ij} = 1 \qquad \text{for} \quad i = j$$

$$= 0 \qquad \text{for} \quad i \neq j$$

and

$$g = |G| = |\det g_{ij}|$$

We now specialize to a flux coordinate system (ψ, χ, ϕ) in which ψ is the poloidal flux function, χ corresponds to an angle the short way around, and ϕ corresponds to angle the long way around the toroid (Fig. 2.2). The toroidal flux surfaces are assumed to be simply nested. It is usually assumed that χ and ϕ increase by 2π around the toroid in their respective directions. Since magnetic field lines lie in the flux surfaces ($\mathbf{B} \cdot \nabla\psi = 0$), the magnetic field can be written

$$\mathbf{B} = \sqrt{g}B^{\chi}\nabla\phi \times \nabla\psi + \sqrt{g}B^{\phi}\nabla\psi \times \nabla\chi, \tag{2.22}$$

where B^{χ}, B^{ϕ} are the contravariant component of $\mathbf{B}$. From the divergence free of $\mathbf{B}$,

$$\nabla \cdot \mathbf{B} = \frac{1}{\sqrt{g}}\left[\frac{\partial}{\partial\chi}\left(\sqrt{g}B^{\chi}\right) + \frac{\partial}{\partial\phi}\left(\sqrt{g}B^{\phi}\right)\right] = 0, \tag{2.23}$$

it follows that the magnetic field may be written in terms of a stream function ν

$$\sqrt{g}B^{\chi} = -\frac{\partial\nu}{\partial\phi}, \qquad \sqrt{g}B^{\phi} = \frac{\partial\nu}{\partial\chi}, \tag{2.24}$$

The differentiation of toroidal and poloidal magnetic fluxes with respect to ψ are

$$\begin{aligned}\frac{d\Phi}{d\psi} &= \frac{d}{d\psi}\int_{S_\phi} \mathbf{B}d\mathbf{S}_\phi \\ &= \frac{d}{d\psi}\int_0^{\psi}\int_0^{2\pi} B^{\phi}\sqrt{g}d\psi d\chi \\ &= 2\pi\sqrt{g}B^{\phi},\end{aligned} \tag{2.25}$$

and

$$\frac{d\Psi}{d\psi} = \frac{d}{d\psi}\int_{S_p} \mathbf{B}d\mathbf{S}_p$$
$$= \frac{d}{d\psi}\int_0^{\psi}\int_0^{2\pi} B^{\chi}\sqrt{g}d\psi d\phi$$
$$= 2\pi\sqrt{g}B^{\chi}, \tag{2.26}$$

respectively. Here, we use $\mathbf{B}d\mathbf{S}_i = \mathbf{B}\cdot\mathbf{e}^i\sqrt{g}d\psi d\chi = B^i\sqrt{g}d\psi d\chi$ (where $i = \phi$ and χ).

Since the magnetic field is single-valued, $\nu(\psi,\chi,\phi)$ must be the sum of terms that are linear or periodic in χ and ϕ.

$$\nu = \chi(\Phi'/2\pi) - \phi(\Psi'/2\pi) + \lambda(\psi,\chi,\phi) \tag{2.27}$$

where λ is a periodic function in χ and ϕ. The prime denotes differentiation with respect to ψ. It is always possible to eliminate the last term in Eq. (2.27) by a change of variables (e.g. $\chi_{new} = \chi_{old} + \lambda/\Phi'$, $\phi_{new} = \phi_{old}$). It follows that

$$\nu_{new} = \chi_{new}(\Phi'(\psi)/2\pi) - \phi_{new}(\Psi'(\psi)/2\pi) \tag{2.28}$$

and

$$\mathbf{B} = (\Phi'(\psi)/2\pi)\nabla\psi\times\nabla\chi + (\Psi'(\psi)/2\pi)\nabla\phi\times\nabla\psi. \tag{2.29}$$

If any flux surface is cut open and laid out with the angles χ and ϕ forming a Cartesian grid, it can be seen that the magnetic field points everywhere in the same direction, so that the field lines appear straight. Here we employ $\Psi/2\pi$ as a radial coordinate ψ, thus $\Psi' = 2\pi\psi' = 2\pi$. It is clear from this picture that q-value is just the ratio of the contravariant component of B

$$q = B^{\phi}/B^{\chi} = \Phi'/\Psi' = \Phi'/2\pi, \tag{2.30}$$

as described before Eq. (2.20). Thus substituting Eq. (2.30) to Eq. (2.29), we can express the well known expression for $\mathbf{B}$ in an axisymmetric torus.

$$\begin{aligned}\mathbf{B} &= q\nabla\psi \times \nabla\chi + \nabla\phi \times \nabla\psi \\ &= F(\psi)\nabla\phi + \nabla\phi \times \nabla\psi. \end{aligned} \tag{2.31}$$

where, $F(\psi) = RB_t$ is a flux function, and $|\nabla\phi| = R^{-1}$. Here, the first term is called the toroidal field $\mathbf{B}_t$, and the second term is the poloidal field $\mathbf{B}_p$. These fields are tangent to the ϕ and χ coordinate lines, but this coordinate system is not orthogonal. Here, the Jacobian for the system is

$$\sqrt{g}(\equiv J) = \frac{qR^2}{F}. \tag{2.32}$$

This coordinate system is used in the linear ideal MHD stability code, which will described in detail in Section 3.4.2.

2.3.3 Grad-Shafranov equation

Let us use the cylindrical coordinates (R, Z, ϕ), as shown in Fig. 2.2, and denote the magnetic surface by ψ and the poloidal angle by χ. The unit vectors to ψ, χ, ϕ directions are

$$\hat{n}_\psi = \frac{\nabla\psi}{|\nabla\psi|} = \frac{\nabla\psi}{RB_p}, \tag{2.33}$$

$$\hat{n}_\chi = \frac{\nabla\phi \times \nabla\psi}{|\nabla\phi \times \nabla\psi|} = \frac{\nabla\phi \times \nabla\psi}{B_p}, \tag{2.34}$$

$$\hat{n}_\phi = \frac{\nabla\phi}{|\nabla\phi|} = R\nabla\phi. \tag{2.35}$$

The plasma current can be divided into two components of the perpendicular and parallel to the magnetic field line. The perpendicular current, derived from Eqs. (2. 7) and (2.31), can be expressed as

$$\mathbf{J}_\perp = \frac{\mathbf{B} \times \nabla p}{B^2} = \frac{p'}{B^2}\Big[F(\nabla\phi \times \nabla\psi) - (RB_p)^2\nabla\phi\Big]. \tag{2.36}$$

We conclude immediately that the perpendicular current lies in the flux surface, because $\nabla\psi \cdot \mathbf{J}_\perp = 0$. The parallel current $\mathbf{J}_\parallel = J_\parallel \hat{\mathbf{n}}_\parallel = J_\parallel(\mathbf{B}/B)$ is obtained from the following equation, using the relation of $\mathbf{J} = \mathbf{J}_\perp + \mathbf{J}_\parallel$ and Eq. (2.36) in $\nabla \cdot \mathbf{J} = 0$.

$$B_p \frac{\partial}{\partial \ell_\chi}\left(\frac{J_\parallel}{B} + p'\frac{F}{B^2}\right) = 0. \tag{2.37}$$

Here ℓ_χ is the distance along the χ direction. We evaluate this constant quantity in brackets by taking the flux surface average of this constant, after multiplying through by B^2, to obtain an expression for the current parallel to the magnetic axis

$$\mathbf{J}_\parallel = \left[-\frac{p'F}{B}\left(1 - \frac{B^2}{< B^2 >}\right) + \frac{B < J_\parallel B >}{< B^2 >}\right]\hat{n}_\parallel, \tag{2.38}$$

where the flux surface average $< X >$ of a variable X is defined as

$$< X >= \oint_\psi \frac{X}{B_p} d\ell_\chi \Big/ \oint_\psi \frac{d\ell_\chi}{B_p}. \tag{2.39}$$

This parallel current plays a important role for the MHD instability.

We can construct the toroidal and poloidal currents in the flux surface from Eqs. (2.36) and (2.38)

$$J_\phi \equiv \hat{n}_\phi \cdot \mathbf{J}_\perp + \hat{n}_\phi \cdot \mathbf{J}_\parallel = -R\left(1 - \frac{B_\phi^2}{< B^2 >}\right) p' + \frac{B_\phi < J_\parallel B >}{< B^2 >}, \tag{2.40}$$

and

$$J_\chi \equiv \hat{n}_\chi \cdot \mathbf{J}_\perp + \hat{n}_\chi \cdot \mathbf{J}_\parallel = \frac{B_p F p'}{< B^2 >} + \frac{B_p < J_\parallel B >}{< B^2 >}. \tag{2.41}$$

These currents must be consistent with Ampere's law. The toroidal and poloidal components of Eq. (2. 8) are

$$\mu_0 J_\phi = R\nabla \cdot R^{-2}\nabla\psi = \frac{1}{R}\left(\frac{\partial^2\psi}{\partial R^2} - \frac{1}{R}\frac{\partial\psi}{\partial R} + \frac{\partial^2\psi}{\partial Z^2}\right) \quad (\equiv \frac{1}{R}\Delta^*\psi), \tag{2.42}$$

and

$$\mu_0 J_\chi = -B_p F', \tag{2.43}$$

where Δ^* is called Grad-Shafranov operator. Equating Eqs. (2.40) and (2.42) leads to the equilibrium equation, called Grad-Shafranov equation[4,5],

$$\left(\frac{\partial^2\psi}{\partial R^2} - \frac{1}{R}\frac{\partial\psi}{\partial R} + \frac{\partial^2\psi}{\partial Z^2}\right) = \mu_0 R J_\phi, \tag{2.44}$$

$$J_\phi = -R\frac{dp}{d\psi} - \frac{1}{\mu_0 R}F\frac{dF}{d\psi}. \tag{2.45}$$

Once p' and F are known, the flux surface topology ψ (R,Z,ϕ) in a cylindrical coordinate system can be found by solving Grad - Shafranov equation. Here, $F(\psi)$ can be determined by solving the following relation, which is obtained by Eq. (2.41) and (2.43),

$$F' = -\mu_0\left(\frac{Fp'}{< B^2 >} + \frac{< J_\parallel B >}{< B^2 >}\right). \tag{2.46}$$

2.3.4 The force balance for the toroidal equilibrium

The basic problem in all toroidal configuration is to compensate the force of outward expansion, because the loop plasma tend to expand to the major radius direction due to the plasma pressure, the hoop force and the tension of toroidal magnetic field. A way to balance the outward force is that the vertical fields generated ($\mathbf{B}_v$) by the external coils sustain the equilibrium by an inward compensating $\mathbf{J} \times \mathbf{B}_v$ force (see Fig. 2.3). The required vertical field for the equilibrium can be derived as follows. Here we consider the limit of $\epsilon \equiv a/R \ll 1$, where the plasma is assumed as a thin current-carrying loop of wire. The ϵ is called as the inverse aspect-ratio, R is the major radius and a is the minor radius of the plasma.

First, the hoop force by which the current ring of a plasma tends to expand is given by

$$F_h = \frac{\partial}{\partial R}\frac{L_p I_p^2}{2}\bigg|_{Ip=const.} \tag{2.47}$$

where L_p is the self-inductance of the current ring and I_p is the total plasma current:

$$L_p = \mu_0 R\left(ln\frac{8R}{a} + \frac{\ell_i}{2} - 2\right). \tag{2.48}$$

and ℓ_i is the internal self-inductance per unit length:

$$\ell_i \equiv \left(\frac{\langle B_p(r)^2\rangle}{B_p(a)^2}\right) = \frac{2}{a^2 B_p^2}\int_0^a B_p^2(r) r dr. \tag{2.49}$$

Accordingly, the hoop force is

$$F_h = \frac{\mu_0 I_p^2}{2}\left(ln\frac{8R}{a} + \frac{\ell_i}{2} - 1\right). \tag{2.50}$$

The next outward force F_p is exerted by the plasma pressure. If the plasma expand to outward ($= \delta R$) by the plasma pressure, the plasma volume increases by δV and the work due to the plasma pressure is given as follows,

$$F_p \delta R = \bar{p}\delta V = \bar{p} 2\pi\delta(R\pi a^2) \tag{2.51}$$

Thus the outward forces is

$$F_p = 2\pi^2 a^2 \bar{p}. \tag{2.52}$$

The third radial force is caused by the toroidal field. The inward force F_{b1} due to the tension of the toroidal field inside the plasma is

$$F_{b1} = -\frac{\bar{B}_i^2}{2\mu_0} 2\pi^2 a^2, \tag{2.53}$$

and outward force F_{b2} by the pressure due to the external magnetic field $B_{\phi e}$ is

$$F_{b2} = \frac{B_e^2}{2\mu_0} 2\pi^2 a^2. \tag{2.54}$$

where B_i, B_e are toroidal fields inside and outside the plasma, respectively. To compensate the outward force due to the toroidal plasma, the force F_J produced by the vertical field B_v is

$$F_J = -2\pi R I_p B_v. \tag{2.55}$$

Consequently, the equation of the radial force balance is given by

$$F_h + F_p + F_b + F_J = 0, \tag{2.56}$$

thus,

$$\frac{\mu_0 I_p^2}{2}\left(ln\frac{8R}{a} + \frac{\ell_i}{2} - 1\right) + 2\pi^2 a^2 \left(\bar{p} + \frac{B_e^2}{2\mu_0} - \frac{\bar{B}_i^2}{2\mu_0}\right) - 2\pi R I_p B_v = 0, \tag{2.57}$$

and, substituting Eq. (2.14)-(2.15), the amount of B_v necessary is[6,7]

$$B_v = \frac{\mu_0 I_p}{4\pi R}\left(ln\frac{8R}{a} + \frac{\ell_i}{2} + \beta_p - \frac{3}{2}\right). \tag{2.58}$$

2.4 Energy Principle

The MHD stability problems of plasmas can be studied by analyzing infinitesimal perturbations from the equilibrium state. We commence to introduce the linearization of the perturbation from the equilibrium. The linearized MHD equations are described in Section 2.4.1. To determine whether the plasma are linearly stable or unstable, there are two ways of doing this. The first is to solve the equation of motion. If the solved frequencies has $Im(\omega) > 0$, then $exp(-i\omega t) \sim exp[Im(\omega)t]$ will grow with time, and system is unstable. The second is to consider the potential energy of a system, and to ask whether that energy increase or decrease under a perturbation. If the energy increases, the perturbation will not grow. If the energy decreases, the perturbation can happen and have left over to go into kinetic energy of expansion; this is the mark of instability. The second method, called the energy principle, is employed in the present work, and described in Section 2.4.2.

2.4.1 Linearization of MHD equations

The first-order linearized equations of Eqs. (2. 1)-(2. 5) for $\mathbf{V}_0 = 0$ are

$$\rho_0 \frac{\partial \mathbf{V}}{\partial t} + \nabla p_1 = \mathbf{J}_0 \times \mathbf{B}_1 + \mathbf{J}_1 \times \mathbf{B}_0, \tag{2.59}$$

$$\frac{\partial \rho_1}{\partial t} + \nabla(\rho_0 \mathbf{V}) = 0, \tag{2.60}$$

$$\frac{\partial}{\partial t} p_1 + \mathbf{V} \cdot \nabla p_0 + \Gamma p_0 \nabla \cdot \mathbf{V} = 0, \tag{2.61}$$

$$\frac{\partial \mathbf{B}_1}{\partial t} = \nabla \times (\mathbf{V} \times \mathbf{B}_0), \tag{2.62}$$

where the values of ρ, p, $\mathbf{J}$, and $\mathbf{B}$ in the equilibrium state are denoted by the subscript "0", and the first-order perturbed quantities are denoted by the subscript "1" ($\mathbf{V} = \mathbf{V}_1$

). If a displacement of the plasma from the equilibrium position $\mathbf{r}_0$ is denoted by $\xi(\mathbf{r}_0, t)$, it follows that

$$\xi(\mathbf{r}_0, t) = \mathbf{r} - \mathbf{r}_0,$$
$$\mathbf{V} = \frac{d\xi}{dt} \approx \frac{\partial \xi}{\partial t}.$$

Equation (2.62) is reduced to

$$\frac{\partial \mathbf{B}_1}{\partial t} = \nabla \times (\frac{\partial \xi}{\partial t} \times \mathbf{B}_0),$$

and

$$\mathbf{B}_1 = \nabla \times (\xi \times \mathbf{B}_0). \tag{2.63}$$

From $\mu_0 \mathbf{J} = \nabla \times \mathbf{B}$, it follows that

$$\mu_0 \mathbf{J}_1 = \nabla \times \mathbf{B}_1. \tag{2.64}$$

Equations (2.60) and (2.61) yield

$$\rho_1 = -\nabla(\rho_0 \xi), \tag{2.65}$$

$$p_1 = -\xi \cdot \nabla p_0 - \Gamma p_0 \nabla \cdot \xi. \tag{2.66}$$

The substitution of these equations into Eq. (2.59) gives

$$\rho_0 \frac{\partial^2 \xi}{\partial t^2} = -\nabla p_1 + \frac{1}{\mu_0} \mathbf{j}_0 \times \mathbf{B}_1 + \frac{1}{\mu_0} (\nabla \times \mathbf{B}_1) \times \mathbf{B}_0, \tag{2.67a}$$

$$= \nabla(\xi \cdot \nabla p_0 + \Gamma p_0 \nabla \xi) + \frac{1}{\mu_0} (\nabla \times \mathbf{B}_0) \times \mathbf{B}_1 + \frac{1}{\mu_0} (\nabla \times \mathbf{B}_1) \times \mathbf{B}_0. \tag{2.67b}$$

This is the linearized equation of motion in terms of ξ.

2.4.2 Energy principle

When we introduce a potential energy associated with the displacement ξ using the linearized equations, the energy principle can apply to the stability problem[8]. The equation of motion has the form

$$\rho\frac{\partial^2\xi}{\partial t^2} = \mathbf{F}(\xi). \tag{2.68}$$

The total perturbed energy is constant in time

$$\frac{\partial}{\partial t}\Big[\delta T + \delta W\Big] = 0 \tag{2.69}$$

where δT and δW are the change of the kinetic energy and the potential energy due to the perturbation of the displacement ξ, respectively. Here,

$$\frac{\partial}{\partial t}\delta T = \frac{\partial}{\partial t}\frac{1}{2}\int \rho(\frac{\partial\xi}{\partial t})^2 dV = \int \rho\frac{\partial\xi}{\partial t}\cdot\frac{\partial^2\xi}{\partial t^2}dV. \tag{2.70}$$

The system is said to be self-adjoint if we can integrate by parts to demonstrate the identity

$$\int \eta\cdot\mathbf{F}(\xi)dV = \int \xi\cdot\mathbf{F}(\eta)dV \tag{2.71}$$

for any choice of η and ξ subject to the boundary condition, described later in Eq. (2.77) and Eq. (2.78). Using this property of self-adjointness, it follows from Eq. (2.70) the change of the potential energy

$$\delta W = -\frac{1}{2}\int \xi\cdot\mathbf{F}(\xi)dV. \tag{2.72}$$

From the constancy of the perturbed energy, it follows that any perturbation that decreases the potential energy ($\delta W < 0$) produces a corresponding increase in the kinetic energy which indicates that the system is linearly unstable. Alternatively, if

$$\delta W > 0$$

for all possible displacements, the system is stable.

Taking the scalar product of ξ with Eq. (2.67) and integrating over the volume of the system leads to

$$\delta W \equiv \frac{1}{2}\int \left[\xi\cdot\nabla p_1 + \frac{1}{\mu_0}(\xi\times\mathbf{B}_0)\cdot(\nabla\times\mathbf{B}_1) - \xi\cdot\mathbf{j}_0\times\mathbf{B}_1\right] dV. \tag{2.73}$$

The first term of the RHS of Eq. (2.73) can be integrated by parts using Gauss' theorem

$$\int_V \xi\cdot\nabla p_1 dV = \int_S \xi_n p_1 dS + \int_V \{(\xi\cdot\nabla)p_0 + \Gamma p_0(\nabla\cdot\xi)\}(\nabla\cdot\xi)dV, \tag{2.74}$$

where ξ_n is the outward component of the displacement on the plasma surface. The second term on the RHS of Eq. (2.73) can be transformed by a similar procedure

$$\frac{1}{\mu_0}\int(\xi\times\mathbf{B_0})\cdot(\nabla\times\mathbf{B_1})dV = \frac{1}{\mu_0}\int\xi_n(\mathbf{B_1}\cdot\mathbf{B_0})dS + \frac{1}{\mu_0}\int\left\{\nabla\times(\xi\times\mathbf{B_0})\right\}^2 dV, \tag{2.75}$$

where we have required that the normal component of the equilibrium field $(\mathbf{B}_0\cdot\mathbf{n})$ vanish on the exterior surface of the plasma.

Now we must consider the boundary conditions that are relevant to a plasma that is surrounded by a vacuum region and then a conducting wall. In the vacuum region, the perturbed field can be represented in term of a vector potential, $\mathbf{A}_1$:

$$\mathbf{B}_{1v} = \nabla\times\mathbf{A}_1. \tag{2.76}$$

where the subscript v refers to the vacuum region. The tangential component of the electric field must be continuous across the plasma-vacuum interface. From Eq. (2.76) and Faraday's law, a requirement can be written

$$\mathbf{n}\times\mathbf{A}_1 = \xi_n\mathbf{B}_{0e} \tag{2.77}$$

at the plasma-vacuum interface, where B_{0e} is the field just outside the plasma boundary. At a perfectly conducting wall, the tangential electric field must vanish, so that the requirement can be written after using Eq. (2.76) in Faraday's law as

$$\mathbf{n}\times\mathbf{A}_1 = 0 \tag{2.78}$$

at the vacuum-wall interface. The linearized pressure balance across the perturbed interface is

$$p_1 + \left(\frac{\mathbf{B}_0 \cdot \mathbf{B}_1}{\mu_0}\right) + \xi_n \mathbf{n} \cdot \nabla \left(p_0 + \frac{B_{0i}^2}{2\mu_0}\right) = \left(\frac{\mathbf{B}_{0v} \cdot \mathbf{B}_{1v}}{\mu_0}\right) + \xi_n \mathbf{n} \cdot \nabla \left(\frac{B_{0e}^2}{2\mu_0}\right), \quad (2.79)$$

where B_{0i} is the field just inside the plasma boundary. This equation can be multiplied by ξ_n and integrated over the plasma-vacuum interface, and the integral can be converted to a volume integral over the vacuum region. Using the boundary condition of Eqs. (2.77) and (2.78), the surface integral of Eq. (2.75) may be reduced to

$$\frac{1}{\mu_0}\int \xi_n \mathbf{B}_0 \cdot \mathbf{B}_1 dS = -\int \xi_n p_1 dS - \int \xi_n^2 \mathbf{n} \cdot \left(p_0 + \frac{B_{0i}^2}{2\mu_0} - \frac{B_{0e}^2}{2\mu_0}\right) dS + \frac{1}{\mu_0}\int_{Ve} (\nabla \times \mathbf{A}_1) \cdot (\nabla \times \mathbf{A}_1) dV, \quad (2.80)$$

where the volume integral is over the vacuum region. From these equations of Eq. (2.74), (2.75) and (2.80), the energy integral of Eq. (2.73) is reduced to the following equation,

$$\begin{aligned}\delta W = \frac{1}{2}\int_{V_i} &\frac{1}{\mu_0}(\nabla \times (\xi \times \mathbf{B}_0))^2 + \Gamma p_0 (\nabla \cdot \xi)^2 + (\nabla \cdot \xi)(\xi \cdot \nabla p_0) \\ &- \frac{1}{\mu_0}(\xi \times (\nabla \times \mathbf{B}_0)) \cdot (\nabla \times (\xi \times \mathbf{B}_0)) dV \\ + \frac{1}{2}\int_S \xi_n^2 &\frac{\partial}{\partial n}\left(\frac{B_{0e}^2}{2\mu_0} - \frac{B_{0i}^2}{2\mu_0} - p_0\right) dS \\ + \frac{1}{2}\int_{V_e} &\frac{\mathbf{B}_1^2}{2\mu_0} dV. \end{aligned} \quad (2.81)$$

The potential energy δW is divided into three terms: the first term is the contributions of the plasma internal region V_i ($= \delta W_p$) the second term is the boundary region S ($= \delta W_S$), and the last term is the external vacuum region V_e ($= \delta W_V$).

δW_V is the perturbation of the magnetic energy in the vacuum region, and δW_S is a surface contribution due to the surface current and the displacement at the plasma surface so that the δW_S vanishes unless the equilibrium has surface currents. δW_p is the perturbation of the fluid and magnetic energy in the plasma region. The most intuitive

form of δW_p has been given by Furth et al.[9]. Following terms of δW_p of Eq. (2.81) are separated into components

$$(\nabla \times (\xi \times \mathbf{B}_0))^2 = |\mathbf{B}_1|^2 = |\mathbf{B}_{1\perp}|^2 + |\mathbf{B}_{1\parallel}|^2 \tag{2.82}$$

$$\begin{aligned} -\frac{1}{\mu_0}(\xi \times (\nabla \times \mathbf{B}_0))(\nabla \times (\xi \times \mathbf{B}_0)) &= -\xi \cdot \mathbf{J} \times \mathbf{B}_1 \\ &= -(\xi_\perp + \xi_\parallel) \cdot \mathbf{J} \times \mathbf{B}_1 \\ &= -J_\parallel (\xi_\perp \times \mathbf{e}_b) \cdot \mathbf{B}_{1\perp} - B_{1\parallel}(\xi_\perp \cdot \mathbf{J}_\perp \times \mathbf{e}_b) - \xi_\parallel \cdot \mathbf{J} \times \mathbf{B}_1 \end{aligned} \tag{2.83}$$

$$(\xi \cdot \nabla p_0)(\nabla \cdot \xi) = (\xi \cdot \nabla p_0)(\nabla \cdot \xi_\parallel) + (\xi \cdot \nabla p_0)(\nabla \cdot \xi_\perp) \tag{2.84}$$

where $\mathbf{J}_\perp$ and $\mathbf{B}_{1\parallel}$ can be written as

$$\mathbf{J}_\perp = \frac{\mathbf{B_0} \times \nabla p_0}{B^2}, \tag{2.85}$$

$$\begin{aligned} B_{1\parallel} &= \mathbf{e}_b \cdot \nabla \times (\xi_\perp \times \mathbf{B}_0) \\ &= \mathbf{e}_b \cdot (\mathbf{B}_0 \cdot \nabla \xi_\perp - \xi_\perp \cdot \nabla \mathbf{B}_0 - \mathbf{B}_0 \nabla \cdot \xi_\perp) \\ &= -B_0(\nabla \cdot \xi_\perp + 2\xi \cdot \kappa) + \frac{\mu_0}{B_0}\xi \cdot \nabla p_0 \end{aligned} \tag{2.86}$$

Here, $\mathbf{e}_b$ ($= \mathbf{B}_0/B_0$) is the unit vector along the field line, and κ ($= \mathbf{e}_b \cdot \nabla \mathbf{e}_b$) is the curvature vector of the magnetic field lines. If equations (2.85) and (2.86) is substituted into Eq. (2.83) and (2.84),

$$\begin{aligned} &Eq.(2.83) + Eq.(2.84) \\ &= -J_\parallel (\xi_\perp \times \mathbf{e}_b) \cdot \mathbf{B}_{1\perp} - B_{1\parallel}(\xi_\perp \cdot \frac{\mathbf{B}_0 \times \nabla p_0}{B_0^2} \times \mathbf{e}_b) - \xi_\parallel \cdot \mathbf{J} \times \mathbf{B}_1 \\ &\quad + (\xi \cdot \nabla p_0)(\nabla \cdot \xi_\parallel) + (\xi \cdot \nabla p_0)\left\{ \frac{\mu_0}{B_0^2}\xi \cdot \nabla p - 2\xi \cdot \kappa - \frac{B_{1\parallel}}{B_0} \right\} \\ &= -J_\parallel (\xi_\perp \times \mathbf{e}_b) \cdot \mathbf{B}_{1\perp} - \frac{B_{1\parallel}}{B_0}(\xi_\perp \cdot \nabla p_0) + \frac{\xi_\parallel}{B_0}(\nabla p_0 \cdot \mathbf{B}_1) \\ &\quad + (\xi \cdot \nabla p_0)(\nabla \cdot \xi_\parallel) + \mu_0 \frac{(\xi \cdot \nabla p_0)^2}{B_0^2} - 2(\xi \cdot \nabla p_0)(\xi \cdot \kappa) - \frac{B_{1\parallel}}{B_0}(\xi \cdot \nabla p_0) \end{aligned}$$

$$= \mu_0 \frac{(\xi \cdot \nabla p_0)^2}{B_0^2} - 2\frac{B_{1_\parallel}}{B_0}(\xi \cdot \nabla p_0) - \frac{\mathbf{J}_0 \cdot \mathbf{B}_0}{B_0^2}(\xi \times \mathbf{B}_0)\mathbf{B}_1$$

$$- 2(\xi \cdot \nabla p_0)(\xi \cdot \kappa) + (\xi \cdot \nabla p_0)(\nabla \cdot \xi_\parallel) + \frac{\xi_\parallel}{B_0}(\nabla p_0 \cdot \mathbf{B}_1) \qquad (2.87).$$

The last two terms of Eq. (2.87) can be reduced to

$$\frac{\xi_\parallel}{B_0}(\nabla p_0 \cdot \mathbf{B}_1) + (\xi \cdot \nabla p_0)(\nabla \cdot \xi_\parallel) = \nabla \cdot (\xi_\parallel (\xi \cdot \nabla p_0)\mathbf{B}_0). \qquad (2.88)$$

Volume integral of Eq. (2.88) can be transform to the surface integral, so that this term can vanish because $\xi_\parallel \cdot \mathbf{n} = 0$. Equations (2.82) and (2.87) are then substituted back into Eq. (2.81).

$$\delta W_p = \frac{1}{2}\int dV \left\{ \frac{1}{\mu_0}|\mathbf{B}_{1_\perp}|^2 + \mu_0 \left| \frac{1}{\mu_0}\mathbf{B}_{1_\parallel} - \frac{\mathbf{B}_0}{B_0^2}\xi \cdot \nabla p_0 \right|^2 + \Gamma p_0 |\nabla \cdot \xi|^2 \right.$$

$$\left. - \frac{\mathbf{J}_0 \cdot \mathbf{B}_0}{B_0^2}(\xi \times \mathbf{B}_0) \cdot \mathbf{B}_1 - 2(\xi \cdot \nabla p_0)(\xi \cdot \kappa) \right\}. \qquad (2.89)$$

The $|\mathbf{B}_{1_\perp}|^2$ term represents the energy required to bend magnetic field lines. It is the dominant potential energy contribution to the shear Alfvén wave, which is the hydromagnetic wave along $\mathbf{B}_0$ and mainly produces the stabilization. The second term corresponds to the energy necessary to compress the magnetic field and describes the major potential energy contribution to the compressional Alfvén wave, which is the hydromagnetic wave perpendicular to $\mathbf{B}_0$ with the compressibility. The $\Gamma p_0 |\nabla \cdot \xi|^2$ term represents the energy required to compress the plasma. It is the main source of potential energy for the sound wave. Each of the contributions just described is stabilizing. The remaining two terms can be positive or negative and thus can drive instabilities. The first of these is proportional to $\mathbf{j}_0 \cdot \mathbf{B}_0 \sim J_\parallel$, while the second is proportional to $\nabla p_0 \sim \mathbf{J}_\perp \times \mathbf{B}_0$. Thus, either parallel or perpendicular currents represent potential sources of instability. The former type is sometimes referred to as current-driven modes and the latter as pressure-driven modes. The current driven term induces the kink modes and the pressure driven term induce the ballooning modes. These instabilities are described in the next Section 2.5.

The stability condition is $\delta W > 0$ for all possible ξ. The frequency or growth rate of a perturbation can be obtained from the energy integral. Since the linearized equation of motion, Eq. (2.68), has constant coefficient in time, they can be written as an eigenvalue equation,

$$\xi = \xi(\mathbf{r})\mathrm{e}^{-i\omega t}$$

and the equation of motion is

$$-\omega^2 \rho_0 \xi = \mathbf{F}. \tag{2.90}$$

The solution of the eigenvalue problem is the same as the solution based on the calculus of variations,

$$\omega^2 (= -\gamma^2) = \frac{2\delta W}{\int \rho_0 \xi^2 dV}. \tag{2.91}$$

where γ^2 is the growth rate of instability. In the MHD analysis of an ideal plasma with zero resistivity, the perturbation either increases or decreases monotonically, or else the perturbed plasma oscillates with constant amplitude.

2.5 Ideal MHD Stability in Tokamak

In this section, the important three instabilities induced in tokamak are described. While the current-free and infinite homogeneous plasma is stable, system with current flowing either parallel or perpendicular to the magnetic field can drive instabilities. These are referred to as current-driven mode or pressure-driven modes, respectively. A number of instabilities induced by the current and pressure in the tokamak, are classified according to their poloidal and toroidal mode number. The poloidal mode is the periodicity of the perturbation in the poloidal plane, as shown in Fig. 2.4. The toroidal mode shows the periodicity of the perturbation around the toroid, and represents the degree of a twist of the perturbation. The most basic problem is the positional instability (or $n = 0$ axisymmetric mode). This mode is the stability of the plasma equilibrium to vertical (Z-direction) or horizontal (R-direction) axisymmetric displacement. The stability boundary of the $n = 0$ mode is described in Section 2.5.1. Current-driven modes, called kink modes, have low n toroidal mode numbers (~ 1) and occur when the parallel current gradient and/or the total parallel current is too large. Kink modes are described in Section 2.5.2. The least stable pressure-driven modes, called ballooning modes, have large toroidal mode number and occur when the average or local curvature of the magnetic field lines is convex to the outside of torus. Ballooning modes are described in Section 2.5.3.

2.5.1 Positional stability (n=0 axisymmetric mode)

The toroidal instability to be firstly considered is the positional stability[10,11]. This perturbation corresponds to an n=0 axisymmetric mode which is the instability of the plasma equilibrium shifting to vertical direction (Z-direction), or expanding the horizontal direction (R-direction). It is important to stabilize these modes since they represent a macroscopic motion of the plasma towards the wall of the discharge chamber.

To sustain the plasma equilibrium, the externally applied vertical field B_v is required, as described in Section 2.3.5. In the assumption of $\epsilon(\equiv a/R) \ll 1$, the outward force F_O due to the toroidal plasma is

$$F_O = F_h + F_p + F_b = \frac{\mu_0 I_p^2}{2}\left(\ell n\frac{8R}{a} + \Lambda - \frac{1}{2}\right), \tag{2.92}$$

where

$$\Lambda = \frac{\ell_i}{2} + \beta_p - 1. \tag{2.93}$$

If the externally applied vertical field is uniform in space, the equilibrium is neutral with regard to changes of plasma position, namely no restoring force against Z-direction. When the lines of the vertical field are curved, namely the radial component B_R of the external field is produced, as shown in Fig. 2.5, the plasma position is stable with regard to up and down (Z-direction) motion. The Z component F_z of the magnetic force applied to a plasma current ring is

$$F_z = 2\pi R I_p B_R. \tag{2.94}$$

in the cylindrical coordinate system, shown in Fig. 2.2. From the relation $\partial B_R/\partial Z - \partial B_Z/\partial R = 0$ because $\nabla \times \mathbf{B} = 0$ on the externally applied field,

$$\frac{\partial F_z}{\partial Z} = 2\pi R I_p \frac{\partial B_R}{\partial Z} = -2\pi I_p B_Z\left(-\frac{R}{B_Z}\frac{\partial B_Z}{\partial R}\right). \tag{2.95}$$

The stability condition is $\partial F_z/\partial Z < 0$, so that

$$n_z \equiv -\frac{R}{B_Z}\frac{\partial B_Z}{\partial R} > 0. \tag{2.96}$$

where n_z is called the field decay index. Thus, the curvature of vertical field is the appropriate one for the stability as a requirement upon the field index $n_z > 0$.

The horizontal component F_R of the magnetic force is given by Eq. (2.92)

$$\begin{aligned} F_R &= F_O - 2\pi R I_p B_Z \\ &= \frac{\mu_0 I_p^2}{2}\left(\ell n\frac{8R}{a} + \Lambda - \frac{1}{2}\right) - 2\pi R I_p B_Z \end{aligned} \tag{2.97}.$$

The amount of B_Z is the vertical component of the externally applied field. When the plasma is ideally conductive, the magnetic flux through the plasma ring Ψ ($\equiv= L_pI_p - 2\pi\int_0^R B_Z R'dR'$) is conserved, namely,

$$\frac{\partial}{\partial R}L_pI_p - 2\pi RB_Z = 0. \tag{2.98}$$

Here the self-inductance is $L_p = \mu_0 R(ln(8R/a) + \ell_i/2 - 2)$. In the equilibrium state under the assumption $ln(8R/a) \gg 1$ and $\beta_p \sim \ell_i \sim 1$, Eq. (2.97) is

$$F_R = \frac{1}{2}\mu_0 \ell n\left(\frac{8R}{a}\right) I_p^2 - 2\pi RI_pB_Z = 0. \tag{2.99}$$

The stability condition is

$$\frac{\partial F_R}{\partial R} = \frac{1}{2R}\mu_0 I_p^2 + \left\{\mu_0 ln\left(\frac{8R}{a}\right) I_p - 2\pi RB_Z\right\}\left(\frac{\partial I_p}{\partial R}\right) - 2\pi I_pB_Z(1-n_z) < 0. \tag{2.100}$$

Using Eqs. (2.98)-(2.99), the stability condition for horizontal movement is simplified,

$$\frac{\partial F_R}{\partial R} = -2\pi I_pB_Z\left(\frac{3}{2} - n_z\right) < 0. \tag{2.101}$$

Hence we can express the condition for the stability of the equilibrium against axisymmetric, or rigid-body, displacements in terms of the decay index[11,7]:

$$0 < n_z < \frac{3}{2} \tag{2.102}$$

Plasmas with a stagnation point of the poloidal field line is recommended to the fusion reactor, because the good confinement and the impurity controll are obtained in the recent tokamak experiments. In the plasma with a stagnation point, however, the n_z is not spatially uniform in the poloidal cross section, and changes extremely from $-\infty$ to $+\infty$. Therefore, the more detailed analysis is necessary for these plasma. In Chapter 4, we discuss the positional stability of plasmas with the stagnation point.

2.5.2 Kink stability

A current driven mode is one in which the dominant driving source of instability is proportional to the $\mathbf{J}_0 \cdot \mathbf{B}_0$ term in Eq.(2.89). These modes are driven by the parallel currents and can exist even in a zero-pressure force-free plasma. Current-driven instabilities are often knows as "kink" modes. In general the significantly large perturbations in kink modes are the low m and n modes (~ 1). Current-driven modes can have the form of either internal or external perturbations depending upon the location of the resonance surface, where the pitch of the field (i.e., the safety factor) coincides with the pitch of the perturbation. As such, these modes are usually subdivided into two categories: internal kinks and external kinks.

The external kink mode[12], whose resonance surface is outside the plasma, has larger growth rate than the internal kink mode in a tokamak. A plasma column can be unstable with respect to the corkscrew, or kink, type of perturbations seen in Fig. 1.3. The mechanism is that B_θ is stronger on the inside than on the outside of bend, which produces a net force that further kinks the plasma column. The tension in the toroidal field lines resists the kinking, so that if the toroidal field is sufficiently strong relative to the poloidal field, the kink instability can be suppressed. Kink instabilities thus place an upper limit on the plasma current for a given toroidal field, which is called by Kruskal-Shafranov limit [13,14]. For a tokamak, this limit can be characterized in term of safety factor of Eq. (2.20) ($q > 1$).

Much of the basic insight concerning external kinks has been summarized by Wesson[15]. Here we describe basic characteristics by the following model. The plasma is a high aspect ratio tokamak ($\epsilon = a/R \ll 1$, where R is the major radius and a is the minor radius), i.e., approximately same as the cylindrical plasma, and is surrounded by a perfect conductor with a minor radius of b. The nonlocal, helical perturbations of the type seen in Fig. 1.3 can be represented in a high aspect-ratio tokamak by

$$\xi = \xi(r,\theta,\phi)e^{-i\omega t} = \xi(r)e^{i(m\theta - n\phi)}e^{-i\omega t}, \tag{2.103}$$

where θ and ϕ are the poloidal and toroidal angles, respectively. The potential energy for displacements, δW, described in Eq. (2.81) with radial displacement of Eq. (2.103) can be written

$$\delta W = \frac{\pi}{2\mu_0}\int_0^b \left\{ f\left(\frac{d\xi}{dr}\right)^2 + g\xi^2 \right\} dr \tag{2.104}$$

$$f = \frac{r(mB_\theta - krB_\phi)^2}{m^2 + k^2r^2} \tag{2.105}$$

$$g = \frac{1}{r}\frac{r(mB_\theta + krB_\phi)^2}{m^2 + k^2r^2} + \frac{1}{r}(mB_\theta - krB_\phi)^2 - \frac{2B_\phi}{r}\frac{d}{dr}(rB_\theta) + \frac{d}{dr}\left(\frac{m^2B_\theta^2 - k^2r^2B_\phi^2}{m^2 + k^2r^2}\right) \tag{2.106a}$$

$$= \frac{2\mu_0 k^2r^2}{m^2 + k^2r^2}\frac{dp_0}{dr} + \frac{1}{r}(mB_\theta - krB_\phi)^2\frac{k^2r^2 + m^2 - 1}{m^2 + k^2r^2} + \frac{2k^2r}{(m^2 + k^2r^2)^2}(k^2r^2B_\phi^2 - m^2B_\theta^2) \tag{2.106b}$$

where $k = n/R$. The potential energy δW is divided into three terms which are

$$\delta W_p = \frac{\pi}{2\mu_0}\int_0^a \left\{ f\left(\frac{d\xi}{dr}\right)^2 + g\xi^2 \right\} dr \tag{2.107}$$

$$\delta W_S = \frac{\pi}{2\mu_0}\frac{(mB_a - kaB_\phi)^2 - 2mB_a(mB_a - kaB_\phi)}{m^2 + k^2a^2}\xi_a^2 \tag{2.108}$$

$$\delta W_V = \frac{\pi}{2\mu_0}\int_a^b \left\{ \frac{1}{m^2 + k^2r^2}\left(\frac{d\eta}{dr}\right)^2 + \frac{\eta^2}{r^2} \right\} r\,dr \tag{2.109}$$

where ξ_a and B_a are the displacement ξ and the poloidal field B_θ at the plasma surface ($r = a$). Here η

$$\eta = \left(\frac{mB_a a}{r} - krB_\phi\right)\xi.$$

The minimization of δW_p and δW_V are obtained by the Euler equations,

$$\frac{d}{dr}\left(f\frac{d\xi}{dr}\right) - g\xi = 0 \qquad (r \le a), \tag{2.110}$$

$$\frac{d}{dr}\left(\frac{r}{m^2 + k^2r^2}\frac{d\eta}{dr}\right) - \frac{\eta}{r} = 0 \qquad (r \ge a), \tag{2.111}$$

using the boundary condition $\xi(b) = 0$. The minimum potential energy of δW for the assumption of $\epsilon \ll 1$ (or $kr \ll m$),

$$\delta W = \frac{\pi B_\phi^2}{\mu_0 R_0}\left[\int_0^a \left\{\left(r\frac{d\xi}{dr}\right)^2 + (m^2-1)\xi^2\right\}\left(\frac{n}{m}-\frac{1}{q}\right)^2 rdr\right.$$

$$\left. + \left\{\frac{2}{q_a}\left(\frac{n}{m}-\frac{1}{q_a}\right) + (1+m\lambda)\left(\frac{n}{m}-\frac{1}{q_a}\right)^2\right\} a^2\xi_a^2\right] \tag{2.112}$$

where

$$\lambda \equiv \frac{1+(a/b)^{2m}}{1-(a/b)^{2m}}, \tag{2.113}$$

and $q = rB_\phi/RB_\theta$.

Only the second term in Eq. (2.112) can contribute a negative term to δW. Therefore, the external kink mode may occur if there is a vacuum region between the plasma and the wall ($\xi_a \neq 0$). Any kink mode (n, m) is stable ($\delta W > 0$) if $q(a) > m/n$. Since $n \geq 1$ for kink modes ($n = 0$ mode is the axisymmetric mode), $q(a) > m/n$ is a sufficient condition for the stability against mode m. The second point to notice is that, if the wall is on the plasma surface, so that $b = a$ and $\xi_a = 0$, then $\delta W \geq 0$ and the system is stable. From calculations considering the plasma current distribution (or q distribution) as a function of the minor radius, for example, in the parabolic current profile, the unstable region increasingly localizes and the growth rate decreases as m increases.

The internal kink modes[16] are modes with a resonant surface within the plasma. For the internal modes ξ_a may usually be put to zero, so that, as previously described in the large aspect-ratio and circular cross-section model given in Eq. (2.112), δW is

$$\delta W = \frac{\pi B_\phi^2}{\mu_0 R_0}\int_0^a \left(r\frac{d\xi}{dr}\right)^2\left(1-\frac{1}{q}\right)^2 rdr$$

for the $m = 1/n = 1$ mode. This mode is stable. Here the ordering $p/B_\phi^2 \sim k^2r^2 \ll 1$ are used, i.e., the first term of RHS in Eq. (2.106b) is neglected. It is therefore necessary to consider the higher order to determine the stability of the internal mode. Assuming

that, as in the typical tokamak case, q increase with r, then, if q has a value of unity within the plasma, δW of Eq. (2.104) is minimized to zero by the function ξ, that is

$$\xi = \begin{cases} \xi_0 = const. & 0 < r < r_s - \delta \quad (\delta \to 0) \\ \xi_0 \dfrac{r_s - r}{\delta} & r_s - \delta < r < r_s \quad (\delta \to 0) \\ 0 & r_s < r < a \end{cases} \tag{2.114}$$

where r_s is the resonance surface given by $r_s = RB_\theta/B_\phi$. The potential energy is then given from Eq. (2.107)

$$\delta W = \frac{\pi}{2\mu_0}\xi_0^2 \int_0^{r_s} g dr \tag{2.115}$$

When $q_{r\to 0}$ is decreased, the $q = 1$ resonant surface first appears at $r = 0$ and then δW is given by

$$\delta W = \pi \xi_0^2 \int_0^{r_s \to 0} \frac{r^2}{R^2}\frac{dp}{dr} dr \tag{2.116}$$

so that, for the usual case with $dp/dr < 0$, the stability boundary is crossed with a $q = 1$ resonant surface appeared at the axis. Hence the stability criterion is

$$q_0 > 1 \tag{2.117}$$

for the $m = 1/n = 1$ internal kink mode.

In the case of m=1 mode, the perturbations are concentrated between the $q = 1/n$ surface and the magnetic axis. The growth rate will be a factor ϵ^2 small rather than external mode, where $\epsilon = a/R$ [15]. In the low m modes ($m > 1$), the perturbations are concentrated around the appropriate resonance surface, $q(= m/n)$. The modes must be restricted to regions where the value of $(1 - nq/m)^2$ is small. The larger the value of m, the more the mode is localized around the resonance surface.

The high shear is in general favorable for stability of kink modes. In the divertor configuration, the poloidal field B_p vanishes at the X-point so that the safety factor q and the shear s increase logarithmically. In Chapter 4, we discuss the shear stabilization near the plasma surface on the external kink modes. Around the plasma axis, where the shear is relatively low, the internal kink modes are induced especially in plasmas with the high pressure. We discuss the relation of the internal kink modes with the limitation of energy confinement in Chapter 6.

2.5.3 Ballooning stability (infinite n mode)

The low n modes due to the pressure driven term ($\sim \nabla p$) in the energy principle is induced with the current driven term ($\sim J_{\parallel}$), so that this mode is classified to one of kink modes, called internal modes or kink-ballooning modes, in which a large number of poloidal modes are excited in the whole plasma region[17]. These modes can be analyzed by the energy principle considering the toroidal configuration. The high n modes due to ∇p, called Ballooning mode[18,19], are only destabilized by the pressure driven term in the energy principle, where the current driven mode can be negligible. Ballooning mode is the most unstable pressure driven instability, which has the long parallel wavelength and very short perpendicular wave length to the magnetic field ($\kappa_{\perp} a \gg 1$). This mode allows the plasma displacement to "balloon" in the region of unfavorable curvature, where the magnetic field line is convex to the outside of the torus. This mode is important, because this determines one set of criteria which limits the maximum achievable value of β, and also they degrade the energy confinement at the flux surface with the high pressure gradient even in the low β plasma. In this section, we describe the high n ballooning modes in a toroidal configuration.

The ballooning mode formalism has been derived by Connor et al.[20,21] completely from the equation of δW, Eq. (2.81). By using an individual Fourier mode $\xi = \xi(\psi, \chi) exp(in\phi)$, δW can be expressed in the flux coordinates as follows

$$\delta W = \frac{1}{2} \int \left\{ \frac{B^2}{R^2 B_p^2} \left| k_{\parallel} X \right|^2 + \frac{R^2}{J^2} \left| \frac{\partial U}{\partial \chi} - F \frac{\partial}{\partial \psi} \left(\frac{JX}{R^2} \right) \right|^2 \right.$$

$$\left. + B_p^2 \left| inU + \frac{\partial X}{\partial \psi} + \frac{J_{\phi}}{RB_p^2} X \right|^2 - 2K \left| X \right|^2 \right\} J d\psi d\chi d\phi. \tag{2.118}$$

The metric of this coordinate is $ds^2 = (d\psi / RB_p)^2 + (JB_p d\chi)^2 + (Rd\phi)^2$ where the volume element $d\tau = J d\psi d\chi d\phi$. In this expression $X = RB_p \xi_{\psi}$ and $U = \xi_{\phi} / R -$

$(F/R^2B_p)\xi_\chi$ are proportional to the two components of $\xi_\perp$, J represents the Jacobian of the transformation, $k_\parallel$ represents the derivative along the field line

$$ik_\parallel = \frac{1}{JB}\left(\frac{\partial}{\partial\chi} + in\nu\right), \quad \nu(\psi,\xi) = FJ/R^2, \tag{2.119}$$

and the quantity K is given by

$$K = \frac{FF'}{R^2}\frac{\partial}{\partial\psi}(lnR) - \frac{J_\phi}{R}\frac{\partial}{\partial\psi}(lnJB_p), \tag{2.120}$$

$$J_\phi = Rp' + \frac{FF'}{R} = -\frac{R}{J}\frac{\partial}{\partial\psi}(JB_p^2) \tag{2.121}$$

Note that ν $(= B^\phi/B^\chi)$ is the local safety factor ($\oint \nu d\chi = 2\pi q(\psi)$) and the plasma compressibility term $\Gamma p(\nabla\cdot\xi)^2$ has been eliminated by a proper choice of $Z(=\xi_\chi/B_p)$.

Consider now the limit $n \to \infty$. Equation (2.118) implies that unless the parallel gradients remains of the order of unity ($k_\parallel \sim O(1)$), δW will be large and positive because of the line bending terms; that is, instabilities can only occur for the perturbations which are nearly constant along a field line. Similarly, unless there is rapid variation perpendicular to the field (i.e., the perpendicular gradients of the perturbation are order n, $\partial X/\partial\psi \sim inU$), there is a large stabilizing contribution from the magnetic compression terms. Using these properties, the second and third terms in Eq. (2.118) is minimized with respect to U.

Carrying out this procedure yields an expression for the leading-order δW of the $1/n$ expansion which is a function only of X and which is valid for ballooning modes:

$$\delta W = \pi\int\left\{\frac{B^2}{R^2B_p^2}|k_\parallel X|^2 + R^2B_p^2|\frac{1}{n}\frac{\partial}{\partial\psi}k_\parallel X|^2 \right.$$
$$\left. -2p'\left(\frac{\kappa_n}{RB_p}|X|^2 - i\frac{RB_p\kappa_s}{B}\frac{X}{n}\frac{\partial X}{\partial\psi}\right)\right\} Jd\psi d\chi. \tag{2.122}$$

Here, κ_n and κ_s are the normal and geodesic components of the curvature, $\mathbf{k} = -\mathbf{B}\times[\mathbf{B}\times\nabla(p+B/2)]B^{-4}$, respectively,

$$\kappa_n = \frac{\mathbf{k}\cdot\nabla\psi}{|\nabla\psi|} = \frac{RB_p}{B^2}\frac{\partial}{\partial\psi}\left(p+\frac{B^2}{2}\right), \tag{2.123}$$

$$\kappa_s = \frac{\mathbf{k}\cdot\mathbf{B}\times\nabla\psi}{|\mathbf{B}\times\nabla\psi|} = \frac{F}{JRB_pB^3}\frac{\partial}{\partial\chi}\left(\frac{B^2}{2}\right), \tag{2.124}$$

Equation (2.122) indicates that the ballooning mode is only destabilized by the pressure gradient. The current-driven term is negligible in the limit $n \to \infty$.

The Euler equation, obtained by minimizing Eq. (2.122) over all function $X(\psi, \chi)$ which are periodic in χ, is

$$Bk_{\parallel}\left[\frac{B}{R^2B_p^2}\left\{1-\left(\frac{R^2B_p^2}{nB}\right)^2\frac{\partial^2}{\partial\psi^2}\right\}k_{\parallel}X\right]-2\frac{dp}{d\psi}\left(\frac{\kappa_n X}{RB_p}-\frac{i\kappa_s RB_p}{Bn}\frac{\partial X}{\partial\psi}\right)=0. \tag{2.125}$$

If the periodicity in χ with high frequency is relaxed by Fourier analysis, the Eq. (2.125) can be solved easily. Here the following transformation is introduced,

$$X(\psi,\chi)=\sum_m exp\left(\frac{-2\pi im\chi}{\oint d\chi}\right)\int_{-\infty}^{+\infty}exp\left(\frac{2\pi imy}{\oint d\chi}\right)\hat{X}(\psi,y)dy. \tag{2.126}$$

This converts the Euler equation Eq. (2.125) for X into an identical equation for $\hat{X}$ but with $\hat{X}$ in the infinite domain $-\infty < y < \infty$ and free of periodicity requirements. Because $\hat{X}$ is free of periodicity constraints it can be represented in the form

$$\hat{X}(\psi,y)=\hat{F}(\psi,y)exp\left(-in\int_{y_0}^{y}\nu dy\right), \tag{2.127}$$

in which all the rapid variation of $\hat{X}$ is contained in the exponential phase factor and the amplitude $\hat{F}(\psi, y)$ remains a more slowly varying function as $n \to \infty$. Here F satisfies the ordinary differential equation

$$\frac{1}{J}\frac{d}{dy}\left[\frac{1}{JR^2B_p^2}\left\{1+\left(\frac{R^2B_p^2}{B}\int_{y_0}^{y}\frac{\partial\nu}{\partial\psi}dy\right)^2\right\}\frac{d\hat{F}}{dy}\right]$$
$$+\frac{2}{RB_p}\frac{dp}{d\psi}\left(\kappa_n-\frac{(RB_p)^2}{B}\kappa_s\int_{y_0}^{y}\frac{\partial\nu}{\partial\psi}dy\right)\hat{F}=0, \tag{2.128}$$

in which ψ appears only as a parameter. Equation (2.128) can be solved separately on each flux surface ψ_0 once an equilibrium is specified. Here the boundary conditions require that $\hat{F}$ vanishes at sufficiently large y ($= \pm\infty$). The limit of the stable pressure gradient for the prescribed equilibrium can be obtained by computing the $dp/d\psi$ of Eq. (2.128) as the corresponding eigenvalue of a two-point boundary value problem. y_0

is a free constant. In principle, δW must be minimized over all y_0. It often turns out in practice that $y_0 = 0$ is the most unstable case.

Ballooning modes are pressure-driven instability localized in the region of unfavorable curvature on the outside of the torus ($\kappa_n < 0$). High shear is in general favorable to widen the stability boundary, which is called by the first stability region. These modes are important in that they ultimately set an upper limit on the maximum allowable β. The ballooning modes also have a second stability region where sufficiently large pressure gradients are stabilized for low shear. This unanticipated result is a consequence of a pressure-driven modulation of the local shear and represents an attractive prospect for the future tokamak. The property of the second stability is described in detail in Chapter 5 and the application for the analysis of the actual plasma is discussed.

2.6 Summary

In this chapter the feature of ideal MHD stability theory has been described. The ideal MHD equations are available in some assumptions; high collisionality ($L/V_T \gg \tau_{ii}$), characteristic dimensions much larger than an ion gyro radius ($L \gg r_{Li} > \lambda_D$), and perfect conductivity ($R_M = V_T L \mu_0/\eta \gg 1$). For the real plasmas encountered in the tokamak experiments, however, the ideal MHD model provides a very reliable description of the equilibria and the stability of magnetically confined fusion plasmas.

The starting point of ideal MHD analysis is to determine the MHD equilibrium which has a balance of forces. The Grad-Shafranov equation is introduced to obtain the MHD equilibrium of tokamak plasma, which provides the magnetic geometries. The surface quantities of the magnetic surface are derived, which are important to the MHD stability. By the linearization of the ideal MHD equations from the equilibrium, the energy principle is introduced, which is a powerful method to determine linear MHD stability.

The typical MHD instabilities in tokamak are described . The stability condition of the n=0 axisymmetric modes, which is necessary to sustain the equilibrium, is obtained by the decay index in the large aspect ratio approximation. From the energy principle of the ideal MHD, instabilities can be driven by currents flowing parallel to the field (current driven modes) or perpendicular to the field (pressure driven modes). On the actual plasma experiments, these two modes are observed as kink modes or ballooning modes. In the following chapters, the instabilities encountered in the real tokamak plasmas are discussed. Depending on the mode in question, the improvement of stability could be obtained by the modification of equilibrium features such as β, the safety factor, the shear, the aspect-ratio, or shapes of plasma cross-section.

References

[1] S.I. Braginskii: in Reviews of Plasma Physics, (Consultants Bureau, New York) Vol.1 (1965).

[2] L.A. Artsimovich: Nucl. Fusion **12**, (1972) 215.

[3] L.S. Solov'ev, V.D. Shafranov: in Reviews of Plasma Physics, (Consultants Bureau, New York) Vol.5 (1970).

[4] H. Grad, H.Rubin: in Proceeding of the Second United Nations International Conference on the Peaceful Uses of Atomic Energy (United Nations, Geneva), Vol.31 (1958) 190.

[5] V.D. Shafranov: Sov. Phys. -JETP **26** (1960) 682.

[6] J.M. Green, J.L. Johnson, K.E. Weimer: Phys. Fluids **14** (1971) 671.

[7] V.S. Mukhovatov, V.D. Shafranov: Nucl. Fusion **11**, (1971) 605.

[8] I.B. Bernstein, E.A. Frieman, M.D. Kruskal, R.M. Kulsrud: Proc. Roy. Soc. A**244**, (1958) 17.

[9] H.P. Furth, J. Killeen, M.N. Rosenbluth, B. Coppi: in Plasma Physics and Controlled Nuclear Fusion Research 1964 (IAEA,Vienna), Vol.I, (1965) 103.

[10] S.M. Osovets: in Plasma Physics and the problem of Controlled Thermonuclear Reactions (pergamon, Oxford) Vol.2 (1959) 322.

[11] S. Yoshikawa: Phys. Fluids **7** (1964) 278.

[12] V.D. Shafranov: Sov. Phys. -Tech. Phys. **15** (1970) 175.

[13] M.D. Kruskal, J.L. Johnson, M.B. Gottlieb, et al.: Phys. Fluids A**1**, (1954) 421.

[14] V.D. Shafranov: Sov. Phys. -JETP **6** (1958) 545.

[15] J.A. Wesson: Nucl. Fusion **18**, (1978) 87.

[16] M.N. Rosenbluth, R.Y. Dagazian, P.H. Rutherford Phys. Fluids **16**, (1973) 1894.

[17] A.M.M. Todd, M.S. Chance, J.M. Greene, et al.: Phys. Rev. Lett. **38**, (1977) 826.

[18] B. Coppi: Phys. Rev. Lett. **39**, (1977) 939.

[19] D. Dobrott, D.B. Nelson, J.M. Greene, et al.: Phys. Rev. Lett. **39**, (1977) 943.

[20] J.W. Connor, R.J. Hastie, J.B. Taylor: Phys. Rev. Lett. **40**, 396 (1978).

[21] J.W. Connor, R.J. Hastie, J.B. Taylor: Proc. Roy. Soc. A**365**, 1 (1979).

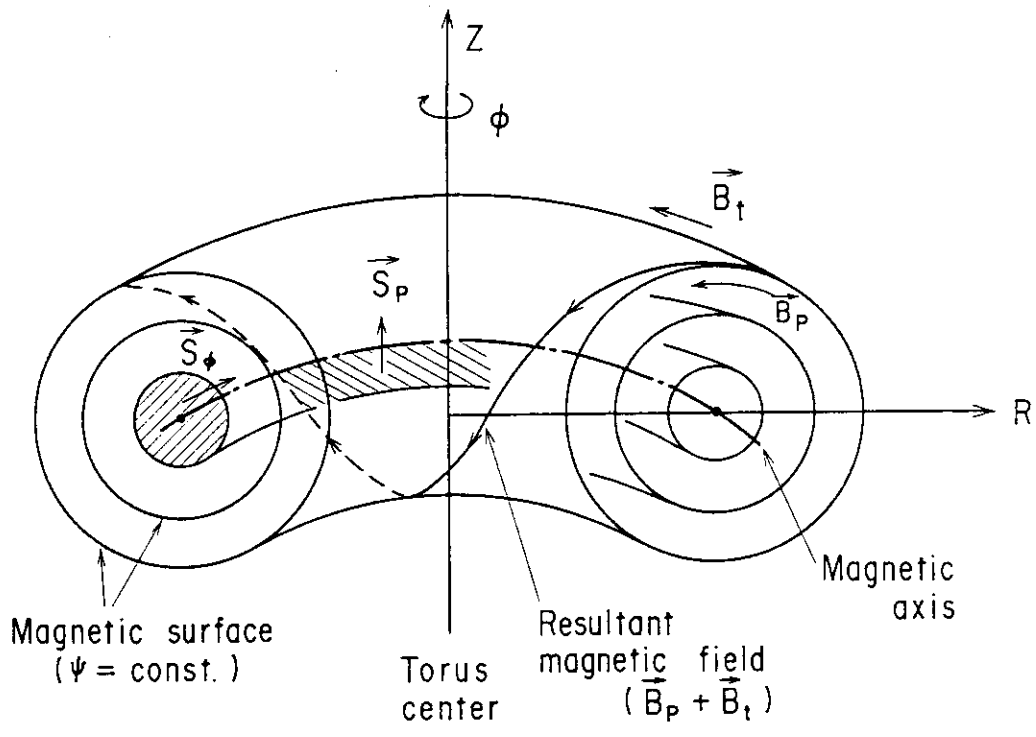

Fig. 2.1 Tokamak magnetic geometry. Nested magnetic flux surfaces and helical magnetic fields are produced by poloidal (B_p) and toroidal (B_t) magnetic fields.

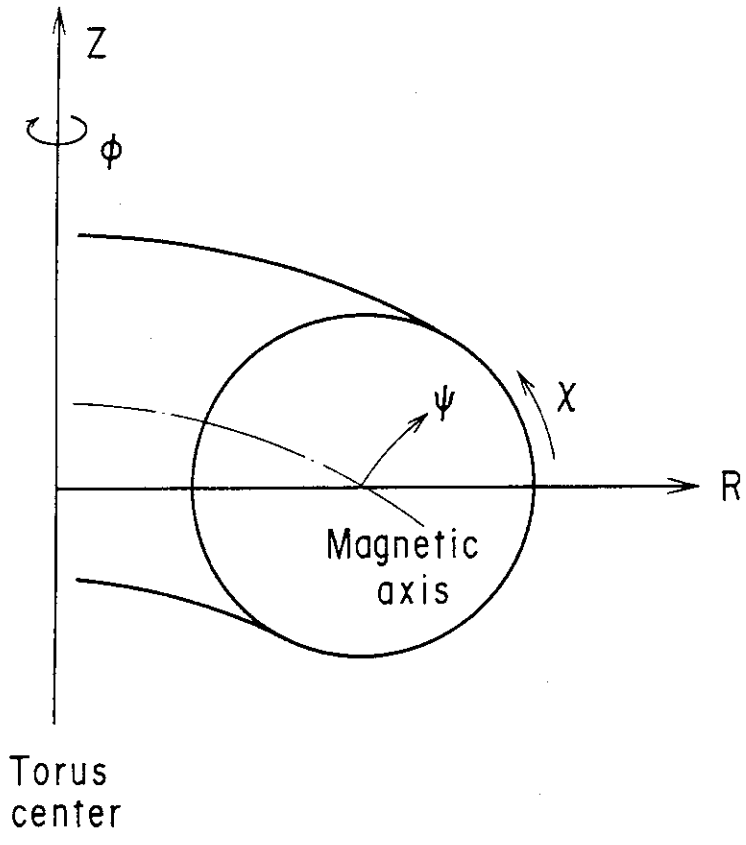

Fig. 2.2 Cylindrical (R, Z, ϕ) and flux (ψ, χ, ϕ) coordinate systems.

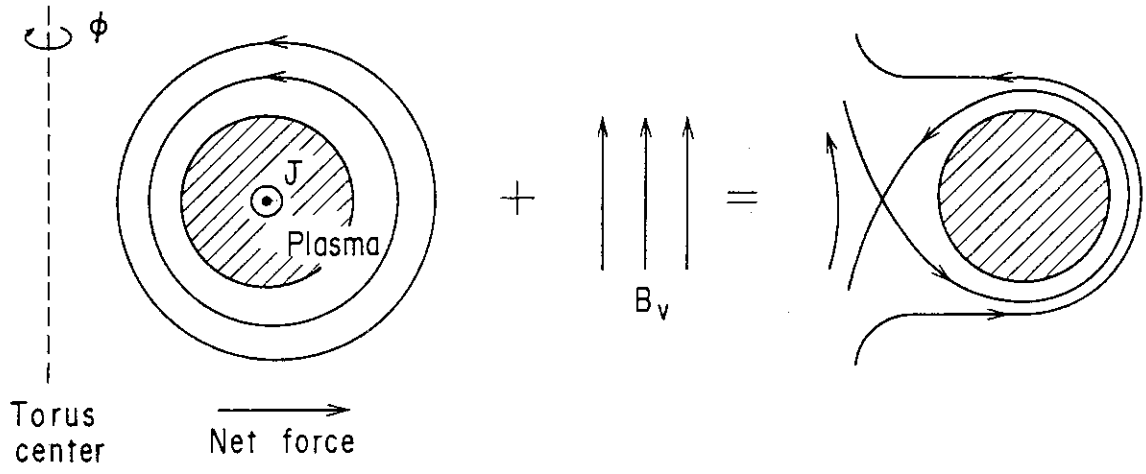

Fig. 2.3 Radial force balance in a tokamak. An externally applied vertical field provides an inward force.

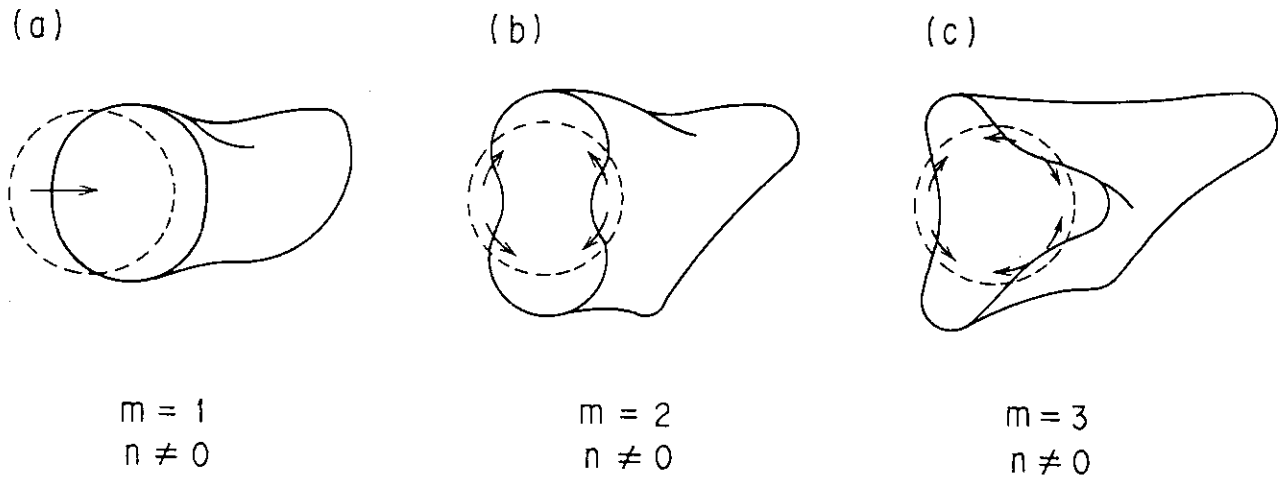

Fig. 2.4 Plasma deformations for the poloidal mode number m of 1, 2 and 3 with $n \neq 0$.

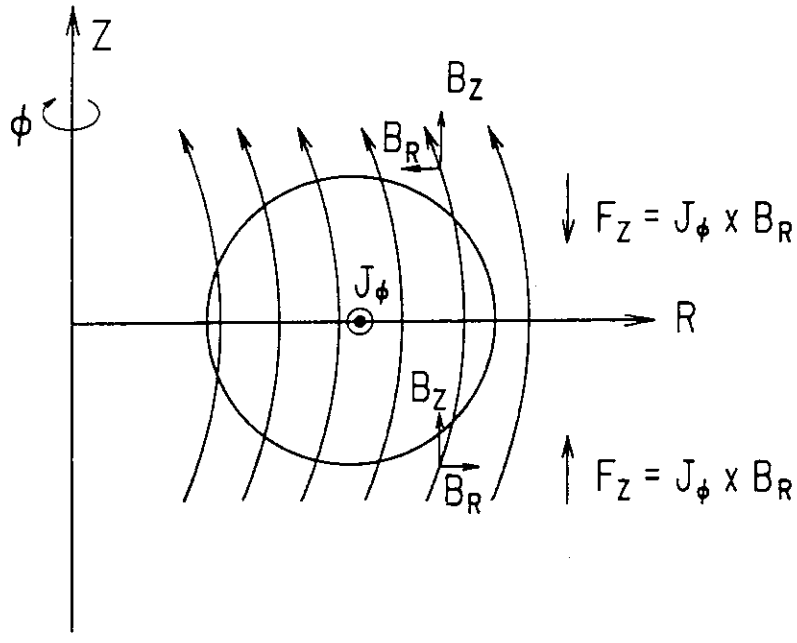

Fig. 2.5 Restoring force against vertical displacement by the curvature of an externally applied vertical field.

Chapter 3

JT-60 and DIII-D Tokamaks and Their MHD Stabilities

3.1 Introduction

The objectives are to solve practical MHD stability problems in real tokamaks, i.e., JT-60 and DIII-D, using the ideal MHD theory described in the previous chapter. As fusion devices become larger and more complicated, and as more detailed experiments are carried out, further quantitative analyses using a more realistic model and computational methods are required. In this chapter, in Section 3.2, we introduce the two tokamak devices, JT-60 and DIII-D. In Section 3.3, problems of MHD stability occurring in actual tokamak devices are presented. In Section 3.4, we describe the computer codes used in this thesis, i.e., the equilibrium code and stability codes, for the analysis of JT-60 and DIII-D plasmas.

3.2 Overview of JT-60 and DIII-D Tokamaks

3.2.1 JT-60 tokamak

JT-60 (Japan) is one of three large tokamaks with TFTR (United States) and JET (European Community). These large tokamaks are aiming at the scientific demonstration of the critical condition of fusion reactors. JT-60 has various features to study physical and technological aspects of reactor relevant plasmas. Its main objective is

to investigate a plasma confinement and heating in reactor relevant plasmas. JT-60 has a poloidal divertor for a impurity control and a confinement improvement, a long discharge duration of 10 seconds, and NB and RF heating for a high input power and a current drive. Figure 3.1 shows a schematic of JT-60, which has no iron-core (air-core), and is characterized by the divertor coil installed in the outside of torus. The cross section of the plasma is nearly circular. Major parameters of JT-60 are listed in Table 3.1. Detailed technological descriptions of JT-60 are provided in Refs.[1,2].

Table 3.1 Main parameter of JT-60

Parameter	Design capability
Major radius	3.0m
Minor radius	0.95m
Toroidal field at $R = 3m$	4.5T (4.8T achieved)
Number of toroidal field coil	18
Plasma current	
Limiter	2.7MA (3.2MA achieved)
Outside divertor	2.1MA (2.7MA achieved)
Lower divertor	2.2MA (2.0MA achieved)
Pulse length	10sec
Heating power (into torus)	
NBI	20MW (25MW achieved)
LHRF	15MW (11MW achieved)
ICRF	5MW (3.1MW achieved)
Pellet (velocity,size)	2.3km/s, 4mm × 4mm$^{\phi}$
Fuelled gas	Hydrogen

Figure 3.2 shows the poloidal coil system and typical examples of equilibrium with limiter and divertor configurations in JT-60. The divertor coil system consists of two types coils: the main divertor coils with current flowing in the same direction as the plasma current and sub-divertor coils with current flowing in the opposite direction. The total current of the sub-divertor coils is the same as that of the main divertor coils.

Therefore, equilibrium in the divertor configuration are similar to those in the limiter configuration, except near the X-point, as shown in Fig. 3.2.

Fuelling of hydrogen or deuterium gases is usually performed by a puff of gas. To search an improved confinement near the plasma center, a pneumatic pellet injector was installed in early 1988 [3]. This injector produces four ice pellets of hydrogen which are cylindrical shapes of 3mm (diameter) × 3mm (length) to 4mm (diameter) × 4mm (length). Maximally, four pellets can be injected by the high pressure gas with a velocity up to 2.3km/s[4]. Figure 3.3 shows the pellet injector in JT-60 tokamak. The small and the large pellets contain 0.7×10^{21} and 2.0×10^{21} atoms, respectively, corresponding to volume averaged electron densities, $< n_e >= 1.7 \times 10^{-19} m^{-3}$ and $< n_e >= 4.9 \times 10^{-19} m^{-3}$, in the JT-60 divertor configuration ($R = 3.0m$, $a = 0.7m$, $Volume = 40m^3$) [5]. The averaged fuelling efficiency of each pellet is about 70 to 80% of the particle inventory as determined by pellet dimensions, and the remaining particles are lost in the formation and acceleration phases. The pellets are injected at an angle of 47° with respect to the midplane.

The JT-60 tokamak has been operated in the limiter configuration and the two types of divertor configurations. Originally, it stared in April 1985 [6] with limiter (Fig. 3.2(a)) and divertor configuration where the X-point is located outside the torus (Fig. 3.2(b)). In 1988, an extra divertor coil was added under the bottom of the vacuum chamber so that operation in the lower X-point configuration became possible[7]. This thesis mainly deals with the ideal MHD characteristics in the limiter configuration and the divertor configuration with outer X-point in JT-60. In 1989, a maximum product of $n_e(0)\tau_E T_i(o)$ ($\sim 1.2 \times 10^{20} m^{-3} skeV$) has been achieved in hydrogen discharges with the combination of pellet injector and NB heating at the high plasma current ($I_p = 3.1MA$)[8].

3.2.2 DIII-D tokamak

DIII-D device, which was produced in General Atomics (United States), is a tokamak with parameters comparable to other three large tokamak [9]. DIII-D was designed to demonstrate the role of plasma shaping, which in turn relates to the achievement of enhanced energy confinement and high value of β. Figure 3.4 shows the schematic view of DIII-D. The configuration of DIII-D is characterized by its elongated, D-shaped vacuum vessel surrounded by 24 toroidal field coils. The air core poloidal field coil set is adopted for the drive of plasma currents. The compact design of DIII-D yields a low aspect ratio which contributes to a high level of performance. Here, parameters of plasma shape is defined in Fig. 3.5. Plasmas can be shaped the plasma into various configurations from circular to D-shaped cross section which is produced by a elongation and a positive triangularity, and from the limiter configuration to the divertor configuration.

A simplified divertor configuration can be established in the DIII-D device using the coils external to the vessel in order to shape the separatrix. Here the divertor configuration is specialized to having the X-point at the bottom of the chamber. Figure 3.6 shows the typical divertor configuration in DIII-D. The plasma has a large elongation and a moderate triangularity in order to obtain the high β, and also it has an enough gap between the X-point and the bottom wall to obtain the H-mode confinement, as introduced in Section 1.5.

The DIII-D device was converted from Doublet-III device[10] in 1985 to obtain a larger plasma volume and higher plasma current. The DIII-D has been operated since February 1986. Research in DIII-D has emphasized plasma shaping and high β operations. The DIII-D tokamak demonstrated these high β and enhanced confinement features of non-circular divertor geometry that would be adapted in the fusion reactor designs. Until 1990, significant results were obtained that are the achievement of high beta in the highly elongated plasma ($\beta_T = 10.7\%$, $\beta_p = 5.1$) and of high energy

confinement in the H-mode plasma ($\tau_E = 0.34s$ at P_{IN} of 2.8MW, $T_i(0) = 17keV$ not simultaneously)[11].

Table 3.2 Main parameter of DIII-D

Parameter	Design capability
Major radius	1.67m
Minor radius	0.67m
Aspect ratio	2.5
Toroidal field on axis	2.2T
Plasma current	5MA (3MA achieved)
Current flattop (divertor at 2MA)	5sec
Heating power	
NBI	20MW
ECH	1.8MW
ICRF	2MW
Fuelled gas	Deuterium/Hydrogen

3.3 Problems of MHD Stabilities in JT-60 and DIII-D Tokamaks

3.3.1 Effects of X-point on MHD stability

The divertor configuration, i.e., the X-point, has two kinds of the salient MHD feature. First is that the divertor coil current attracts the plasma ring, therefore the positional stability becomes problem. The positional stability of a tokamak is primarily related to the gradient of the externally applied magnetic field, and usually a decay index n_z ($= -(R/B_z)(\partial B_z/\partial R)$) are sufficient to identify the stability condition for this instability, as described in section 2.5.1. The stability condition is expressed as $0 < n_z < 1.5$ for a rigid model. When a tokamak has a divertor coil on the median plane ($Z = 0$ plane) as in the case of the JT-60 tokamak, the external magnetic field, i.e., the vertical field B_z, changes its sign near the X-point. Consequently, the n_z varies from plus infinity to minus infinity near the X-point, (Fig. 3.7(b)), while in the limiter configuration the variation of n_z is small in the plasma region (Fig. 3.7(a)). The widely used rigid model by n_z becomes useless for the identification of the stability condition of these system which has a local large variation of n_z.

Second important MHD property due to the X-point is the strong shear near the plasma surface. In the divertor configuration, the poloidal field B_p vanishes at the X-point on the separatrix magnetic surface. Thus, the safety factor q ($= aB_t/RB_p$) becomes large to infinity and the magnetic shear S ($= (V/q)(dq/dV)$) has logarithmic singularity on the separatrix magnetic surface. Figure 3.8 shows the typical shear profile against the minor radius. In the limiter configuration, the shear gradually increases from the plasma axis to the plasma surface. In the divertor configuration, however, the shear increases rapidly near the plasma surface. This shear is expected to stabilize the MHD stability, especially, the external kink mode which has a large displacement at the plasma surface.

Typical models used for analyses of the positional stability are (1) rigid model, (2) rigid displacement model, and (3) general linearized ideal MHD model. In the rigid

model a toroidal plasma is represented by a current carrying rigid conductor where the plasma deformation is neglected and the instability is analyzed electrodynamically. In the rigid displacement model, uniform plasma displacement over the whole plasma cross section is assumed and the variational principle is applied for this uniform displacement[12,13]. In the general MHD model no such assumption is introduced to the plasma displacement and the instability is analyzed by using a general linearized ideal MHD code such as ERATO [14]. Kumagai et al.[15] analyzed the positional instability for the Solov'ev equilibrium [16] on the basis of the above three models. They found that the stability conditions obtained for the rigid displacement model are rather stable than the general linearized model, especially when the non-circularity is large and/or the aspect ratio is small. It is, therefore, concluded that the general MHD model is indispensable to analyze the positional instability in a present-day large tokamak with highly shaped cross section, small aspect ratio and, especially, X-point.

The basic characteristics of kink modes are commonly studied in terms of the circular cross-section 'straight tokamak' model, in which toroidicity is neglected except for its role in stabilizing the $n = 1/m = 1$ internal kink, as described in Section 2.5.2. This model has been seemed as a quite satisfactory basis for the interpretation of most kink stability results. In such a system which has locally strong shear, however, it is necessary to examine kink modes by using the realized toroidal equilibrium and general MHD stability codes, such as ERATO. In Chapter 4, we discuss the effect of X-point on the positional stability and kink stability.

3.3.2 MHD activity of H-mode plasmas in DIII-D tokamak

In H-mode plasmas of various tokamaks, MHD instabilities near the plasma surface, called as edge-localized modes (ELMs), are observed. The ELMs are one of the major MHD instability to influence the energy confinement. Figure 3.9 shows the temporal events in a typical H-mode discharges with ELMs in DIII-D. ELMs are characterized in the spikes of H_α (Balmer α line radiated from a hydrogen atom), which corresponds to the pulsed particle flow from the plasma to the outside [17]. Within several msec after the transition from L-mode to H-mode at t = 1875msec, the averaged density and the stored energy continuously increases during the entire H-phase until the ELM occurs. The ELMs generally tend to degrade particle and energy confinement at the plasma edge and inhibit increases in the plasma density. Presence of steep-edge electron density and temperature gradients is general characteristics of the H-mode [18,19] and believed to be the result of a transport barrier at the edge [20]. In H-mode plasmas of DIII-D, extremely steep-edge density gradients and correspondingly high-edge pressure gradients are observed, which is produced by the accumulation of particle in the edge region. When the ELM happened, the particle in the edge is expelled to the outside of the plasma, and tens of mega-watts of power, which is about 10-20% of the stored energy, can be dumped to the outside of the plasma [21]. The change in the electron temperature due to the ELM is relatively small. Thus, the high edge-electron pressure gradient produced just before the ELM is dramatically reduced by the ELM. From the ideal MHD theory, the infinite-n ballooning mode is the most plausible candidate to this MHD activity.

Comparison of electron density and temperature profile during the occurrence of ELMs with the finite-n ballooning mode show that the experimental edge pressure gradient before a ELM is close to the theoretically predicted marginal stability limit for the ideal ballooning mode. These results are obtained over a large range of plasma currents in DIII-D (1 to 2MA). From spectroscopic observations, the ELMs originate in

the bad curvature regime for the infinite-n ballooning mode. Thus the ELMs in DIII-D are considered to be triggered by the MHD ballooning modes [17,22].

From the understanding of ELMs mechanism, that the ELMs are triggered by the ballooning mode, the suppression of ELMs could be expected by the stabilization of the ballooning mode. In Chapter 5, we discuss the suppression of ELMs and the stability regime of ballooning modes, and explore the condition to access the second stability regime.

3.3.3 MHD activity of pellet fuelled plasmas in JT-60

In JT-60, pellet injections in combination with neutral beam (NB) heating improved τ_E by 40% over the values found for gas fuelled discharges. The improved discharges are characterized by a pressure profile that is strongly peaked around the magnetic axis i.e., inside the $q = 1$ surface (q is the safety factor). The peakedness depends strongly on the penetration length of the pellets. If the good penetration of pellets is obtained, however, the limitation of enhanced confinement is observed. Figure 3.10 shows pressure profiles estimated with the soft X-ray (SX) intensity from the interior of plasma for various input power. Every pressure profile consists of a parabolic shaped bias portion (outside the $q = 1$ surface) and a central 'cap' portion (inside the $q = 1$ surface). This bias parts increases with the input power, but the cap's parts remain almost unchanged. This limitation relates to the MHD activity, that is an appearance of a large sawteeth and the saturation of the increase in the pressure gradients [23].

An important contribution to obtain a further improvement of the enhanced confinements could result from deeper understanding of the mechanism of MHD activity and of the limitation of the peakedness of the plasma pressure. In Chapter 6, we compare the experimental results with the results of the ideal MHD instability analysis, i.e.,

kink modes and ballooning modes, and discuss the feature of the MHD stability of the plasma with a centrally peaked pressure.

3.4 MHD Codes for Stability Analyses

To analyze the MHD stability in the practical plasma, numerical codes with high accuracy are required, dealing with an actual plasma, for example, the shape of the cross-section, the aspect-ratio, β, the X-point and so on. This section explains the numerical codes: equilibrium and stability codes used in this thesis.

3.4.1 Equilibrium code

A full toroidal equilibrium with free boundary is numerically solved in the cylindrical co-ordinates (R, Z, ϕ) for prescribed current and pressure profiles in the following way [24].

The Grad-Shafranov equation (Eq. (2.24-25)) includes two differentiation operators ∇ and $d/d\psi$ defined in the two different spaces. One of the method to solve this equation is the nonlinear eigenvalue problem in which the functional forms of pressure $p(\psi)$ and toroidal field function $F(\psi)$ are prescribed and the absolute value of them are determined from the eigenvalue of the system. The Grad-Shafranov equation can be rewritten as the nonlinear eigenvalue problem

$$\Delta^* \psi = \lambda f(\psi, R) \tag{3. 1}$$

where

$$f(\psi, R) \equiv \mu_0 R J_{\phi 0} = \mu_0 R J_\phi / \lambda. \tag{3. 2}$$

Δ^* is the Grad-Shafranov operator and J_ϕ is the toroidal current density. First, the above equation is solved with some appropriate numerical method and eigenvalue λ is obtained. In this calculation the variable range of ψ is fixed as $(-1,0)$ in the plasma and the following iteration scheme is adopted [24]:

(1) Prepare initial values, ψ^0, λ^0;

(2) Solve the following equation for ψ^{n+1},

$$\psi^{n+1} = \Delta^{*^{-1}} \lambda^n f(\psi^n, R), \tag{3. 3}$$

(3) Normalize the ψ values by the value at the magnetic axis and obtain $n+1th$ eigenvalue λ^{n+1},

$$\lambda^{n+1} = \frac{1}{\psi_{axis}^{n+1}} \lambda^n, \tag{3. 4}$$

(4) Repeat the above iteration procedure.

Equation (3.3) is solved on the basis of the finite differential method. Regular rectangular meshes with a five-points difference formula are employed for the finite difference discretization of an equilibrium solver. This equilibrium solver is based on the double cyclic reduction (DCR) method obtained by Buneman [25]. DCR method has a very efficient algorithm, but it requires a large memory size. When we consider a rectangular mesh with constant spacing in the R-direction and in the Z-direction, mesh numbers in the R- and Z-directions, N_R and N_Z respectively, must be a power of 2, i.e., $N_R = 2^k$ and $N_Z = 2^\ell$. In the present works, we use the fine mesh ($k \sim \ell = 7 - 9$) to obtain a high accuracy.

3.4.2 Linear ideal MHD stability code: ERATO-J

Ideal MHD stability against the low n modes is studied with the ERATO-J code, which solves the linearized ideal MHD equations in variational form using a finite hybrid element approach. The ERATO code was originally developed in CRPP (Switzerland) [14] and modified to ERATO-J in JAERI (Japan) [26,27].

This computer code treats the stability of a torus plasma described by the linearized ideal MHD equations (Eq. (2.64-65)). The plasma is considered to be in an equilibrium state. After perturbation of such an equilibrium, the evolution of the normal modes can be calculated by the energy principle.

ERATO-J code is written by using a flux coordinate system and the various metric quantities necessary for the stability analyses are given at the mesh points defined on the flux coordinates. In this study, therefore, at first we obtain the equilibrium solution given by the real space (R, Z, ϕ coordinates) data, described in the previous section. Next, the solution is mapped from the real space coordinates to the flux coordinates (ψ, χ, ϕ coordinates). Here, the angular coordinate χ is defined by a line integral on a contour of ψ as

$$\chi = \int \frac{dl_\chi}{JB_p} = \int \frac{F}{qR^2 B_p} dl_\chi, \tag{3. 5}$$

where magnetic field lines are straight in the χ, ϕ space and J is the Jacobian. Here we note that $\oint dl_\chi / JB_p = \oint \sqrt{g_{\chi\chi}} d\chi / JB_p = \oint d\chi = 2\pi$.

The variational form ($\delta L = \delta(T + W) = 0$ from Eq. (2.69)) of the 2D ideal MHD equations is treated by a finite hybrid element approach [28], which proves to be well suited to describe the features of the problem with sufficient accuracy. The eigenvalue problem $A\mathbf{x} = \omega^2 B\mathbf{x}$ is solved by an inverse vector iteration, where $\mathbf{x}$ is a displacement on each mesh, matrices A and B are a potential energy and a kinetic energy on each mesh, respectively.

A method called σ−scaling is useful for the parameter scanning in the stability calculation. By means of a scaling factor σ, it is possible to transform one equilibrium into another one. Calculating one numerical equilibrium makes it possible to perform a whole stability study in q as a parameter. The scaling of equilibrium quantities is given as follows:

$$\hat{\psi} = \sigma\psi, \qquad \hat{B}_p = \sigma B_p, \qquad \hat{J}_\phi = \sigma J_\phi, \qquad \hat{p} = \sigma^2 p,$$
$$\hat{F}\frac{d\hat{F}}{d\psi} = \sigma F \frac{dF}{d\psi}, \quad \hat{F}^2 = F_0^2 + \sigma^2(F^2 - F_0^2), \quad \hat{q}^2 = q^2 \frac{\hat{F}^2}{F^2\sigma^2}, \tag{3. 6}$$

where the quantities with hats are new quantities scaled by σ. The subscript with 0 represents values at the magnetic axis.

3.4.3 Ideal infinite-n ballooning mode code

To ascertain the pressure driven mode for the given equilibrium, the infinite-n ballooning stability is analyzed with three numerical codes, BETA[29], MBC[30] and CAMINO[31].

Ballooning stability analysis was carried out by solving the ordinary infinite-n ballooning equation (Eq. (2.126)) on each flux surface. This equation is numerically solved by the shooting method with the boundary condition that the radial displacement (at $y = \pm\infty$) =0. Flux function shape and the pressure current profiles in the exact toroidal geometry, which have been reconstructed by the equilibrium code, are used for stability analysis.

BETA code is written in the cylindrical coordinates, and the marginal pressure gradient is obtained for a particular equilibrium. In MBC and CAMINO codes, the equilibrium data are mapped into the flux coordinates. In MBC code, to find the optimized (or maximized) ballooning stability associated with a particular equilibrium, the pressure gradient $dp/d\psi$ on a given flux surface is varied until the growth rate $\gamma = 0$

in a flux conserving manner holding the safety factor q profile fixed. As $dp/d\psi$ is varied, the coefficients in the ideal infinite-n ballooning equation are updated analytically based on the method of equilibrium perturbation described in detail in Ref.[32]. After the variation of $dp/d\psi$, an obtainable maximum $dp/d\psi$ is the marginal pressure gradient on that flux surface. In addition to the $dp/d\psi$ variation, CAMINO code also includes the equilibrium perturbation on $dq/d\psi$. Thus, CAMINO code can make a stability diagram in the $dq/d\psi - dp/d\psi$ space on each flux surface. The results from these codes have been compared and found to be very consistent.

3.5 Summary

The problems of MHD stability encountered in two major tokamaks, JT-60 and DIII-D, were introduced, and the numerical codes for the analyses of the MHD stability used in this thesis were described.

In the divertor configuration of JT-60, the externally applied field produces the large n_z which is spatially localized near the X-point so that the axisymmetric mode may become unstable. The divertor configuration also produces the high shear near the separatrix magnetic surface. This high shear could suppress kink modes, especially, the external kink mode. Thus, the axisymmetric mode and the kink mode in the divertor configuration must be re-examined in the general ideal MHD model considering the plasma deformation. In the H-mode discharges of DIII-D, the ELMs were observed which degrade the energy confinement. The results of the stability analyses of the ballooning mode using the DIII-D experimental data show that the pressure gradient near the edge region approaches the ballooning limit, just before the occurrence of ELM. One of the solution to suppress the ELMs is to stabilize the ballooning modes. It is a crucial problem to find the stability region of the ballooning mode near the plasma surface. In JT-60 pellet fuelled experiments, improved discharges characterized by a peaked pressure profile inside the $q = 1$ surface were obtained. The limitation of peakedness, however, was observed when a large sawtooth recovered or when the pressure gradient reached a critical value. It is an important problem to clarify the mechanism of this limitation. These problems are discussed from the next chapter using the numerical codes.

The numerical codes used in this thesis are the equilibrium code, the linear ideal stability code (ERATO-J) and the infinite-n ballooning codes (BETA, MBC, CAMINO). The equilibrium code can calculate the high accuracy equilibria in a full toroidal geometry with a fine mesh ($N_R = 512$, $N_Z = 256$). By using this equilibrium data, the external and internal kink modes and the positional stability can be analyzed by the

ERATO-J code. The infinite-n ballooning mode is also calculated by BETA using this equilibrium, or by MBC and CAMINO using the equilibrium data which is produced in their own codes.

References

[1] JT-60 Team (presented by M.Yoshikawa): Plasma Phys. Controll. Fusion **28** (1986) 165.

[2] JT-60 Team (presented by S.Tamura): Plasma Phys. Controll. Fusion **28** (1986) 1377.

[3] K. Kawasaki, H. Hiratsuka, H. Takatsu, et al.: in Fusion Technology (Proc. 15th Symp. Utrecht, 1988) Pergamon Press, Oxford C06 (1989) 724.

[4] M. Onozuka, T. Shimomura, N. Tanaka, et al.: in Proc. Thirteenth Symposium on Fusion Eng. IEEE Vol.2 (1989) 1259.

[5] S. Tsuji, M. Akiba, T. Ando, et al.: in Plasma Physics and Controlled Nuclear Fusion Research 1988 (Proc. 12th Int. Conf, Nice, 1988) IAEA, Vienna, Vol.I (1989) 265.

[6] JT-60 Team: in Plasma Physics and Controlled Nuclear Fusion Research 1986 (Proc. 11th Int. Conf, Kyoto, 1986) IAEA, Vienna, Vol.I (1987) 11.

[7] JT-60 Team: in Plasma Physics and Controlled Nuclear Fusion Research 1988 (Proc. 12th Int. Conf, Nice, 1988) IAEA, Vienna, Vol.I (1989) 67.

[8] JT-60 Team: in Plasma Physics and Controlled Nuclear Fusion Research 1990 (Proc. 12th Int. Conf, Washington, 1990) (IAEA,Vienna), IAEA-CN-53/A-1-3.

[9] J.L. Luxon, L.G.Davis, GA Technologies Inc.: Fusion Technology **8** (1985) 441.

[10] Annual report fiscal 1982: Rep. GA-A17383, GA Technologies Inc., San Diego, CA (1982).

[11] J.L. Luxon, et al.: Plasma Phys. Controll. Fusion **32** (1990) 869.

[12] E. Rebhan: Nucl. Fusion **15** (1975) 277.

[13] H. Ninomiya, Y.Suzuki, A.Kameari: Jpn. J. Appl. Phys. **15** (1976) 2201.

[14] R. Gruber, F. Troyon, D. Berger, L.C. Bernard, S. Rousset, et al.: Comput. Phys. Commun. **21** (1981) 323.

[15] M. Kumagai, T. Tsunematsu, S. Tokuda, T.Takeda: Rep. JAERI-M 83-085, Japan Atomic Energy Research Institute Report, Ibaraki (1983).

[16] L.S. Solov'ev: Sov. Phys. JETP **26** (1968) 400.

[17] P. Gohil, M.Ali Mahdavi, L.L. Lao, K.H. Burrell, M.S. Chu, et al.: Phys. Rev. Lett. **61** (1988) 1603.

[18] S.M. Kaye et al.: J. Nucl. Mater. **121** (1984) 115.

[19] M. Keilhacker et al.: Plasma Phys. Controll. Fusion **26** (1984) 49.

[20] M. Keilhacker et al.: Plasma Phys. Controll. Fusion **28** (1986) 29.

[21] D. Hill et al.: Nucl. Fusion **28** (1988) 902.

[22] L.L. Lao, E.J. Strait, T.S. Taylor, M.S. Chu, T. Ozeki, et al.: Plasma Phys. Controll. Fusion **31** (1989) 509.

[23] Y. Kamada, R. Yoshino, M. Nagami, T.Ozeki, T.Hirayama, et al.: Nucl. Fusion **29** (1989) 1785.

[24] T. Takeda, S. Tokuda: J. Comput. Phys. **93** (1991) 1.

[25] O. Buneman: Rep. SUIPR-294, Stanford University, CA (1968).

[26] T. Tsunematsu. T. Takeda, T. Matsuura, G. Kurita, M. Azumi: Comput. Phys. Commun. **19** (1980) 179.

[27] S. Tokuda, T. Tsunematsu, M. Azumi, T. Takizuka, K. Naraoka, et al.: Rep. JAERI-M 9899, Japan Atomic Energy Research Institute Report, Ibaraki (1982).

[28] R. Gruber: J. Comput. Phys. **26** (1978) 379.

[29] M. Azumi, T. Takizuka, T. Tsunematsu, G. Kurita, S. Tokuda, et al,: in Plasma Physics (Proc. Int. Conf. Lausanne, 1984), Vol. 1, CEC, Brussels (1985) 375.

[30] R.W. Moore: Rep. GA-A16243, General Atomics, San Diego, CA (1981).

[31] M.S. Chance: in Theory of Fusion Plasmas (Proc. Workshop Varenna, 1987), Editrice Compositori, Bologna (1987) 87.

[32] J.M Greene, M.S. Chance: Nucl. Fusion **21** (1981) 453.

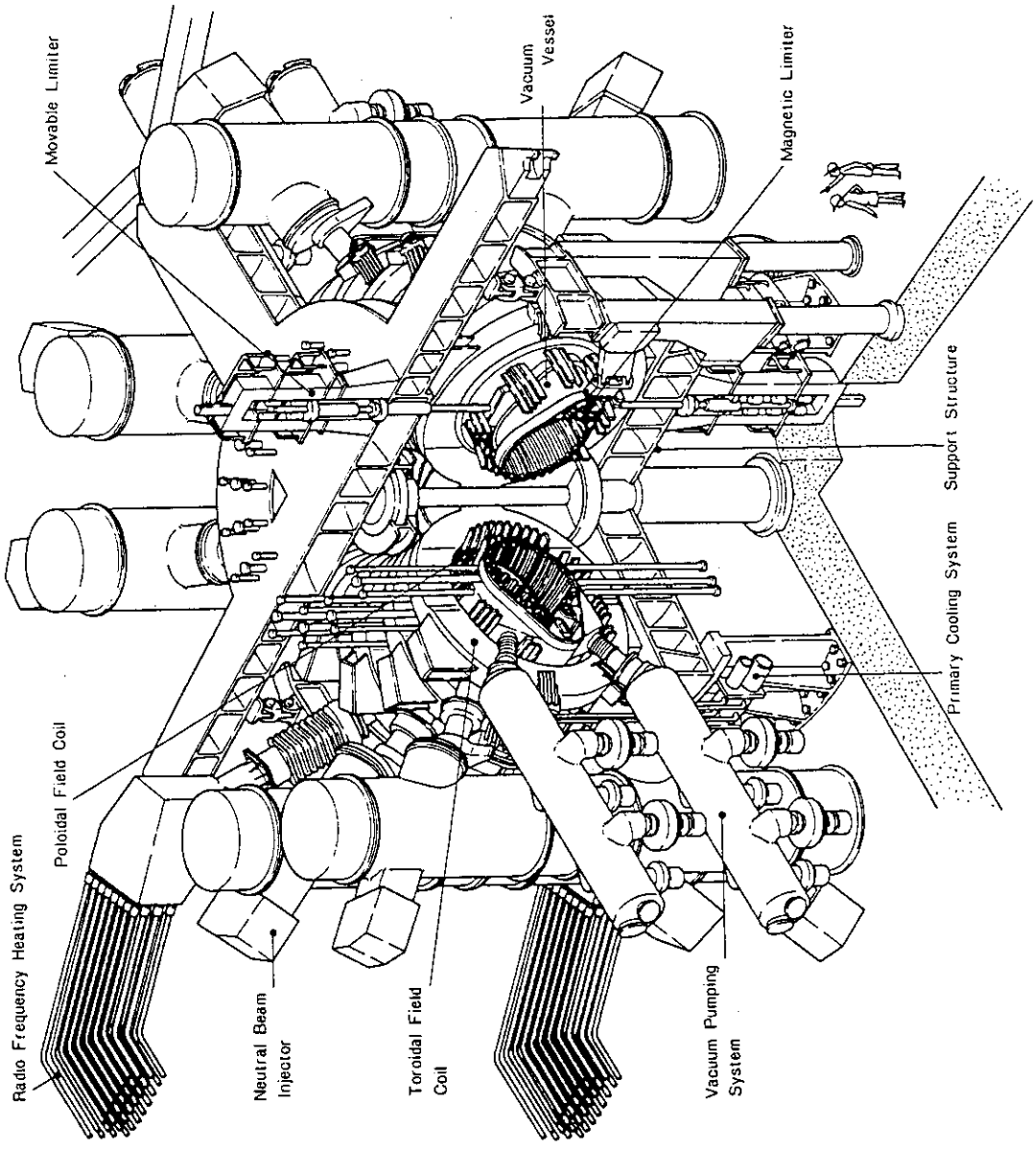

Fig. 3.1 Schematic of JT-60.

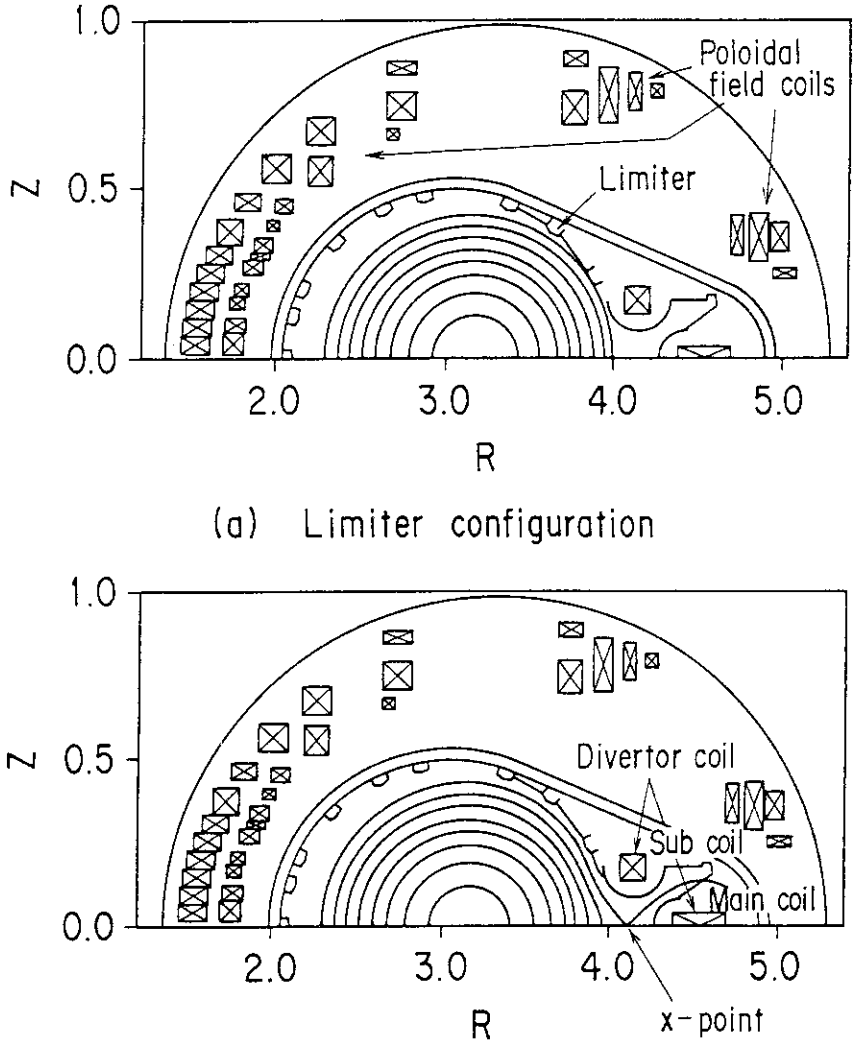

Fig. 3.2 Cross-section of typical limiter configurations and divertor configuration plasma in JT-60, with the poloidal coil system.

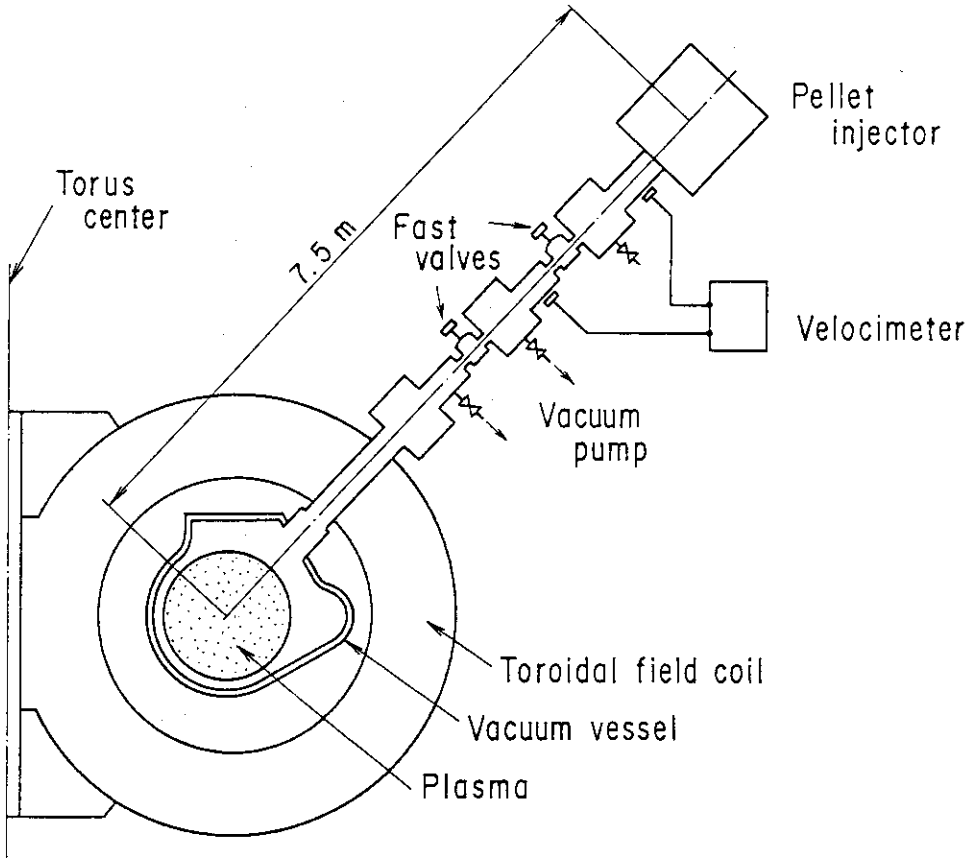

Fig. 3.3 Schematic of pellet injector installed on the JT-60 tokamak. Frozen hydrogen pellets are formed within the liquid-helium-cooled pellet injector and expelled by pressurized hydrogen gas at 10MPa.

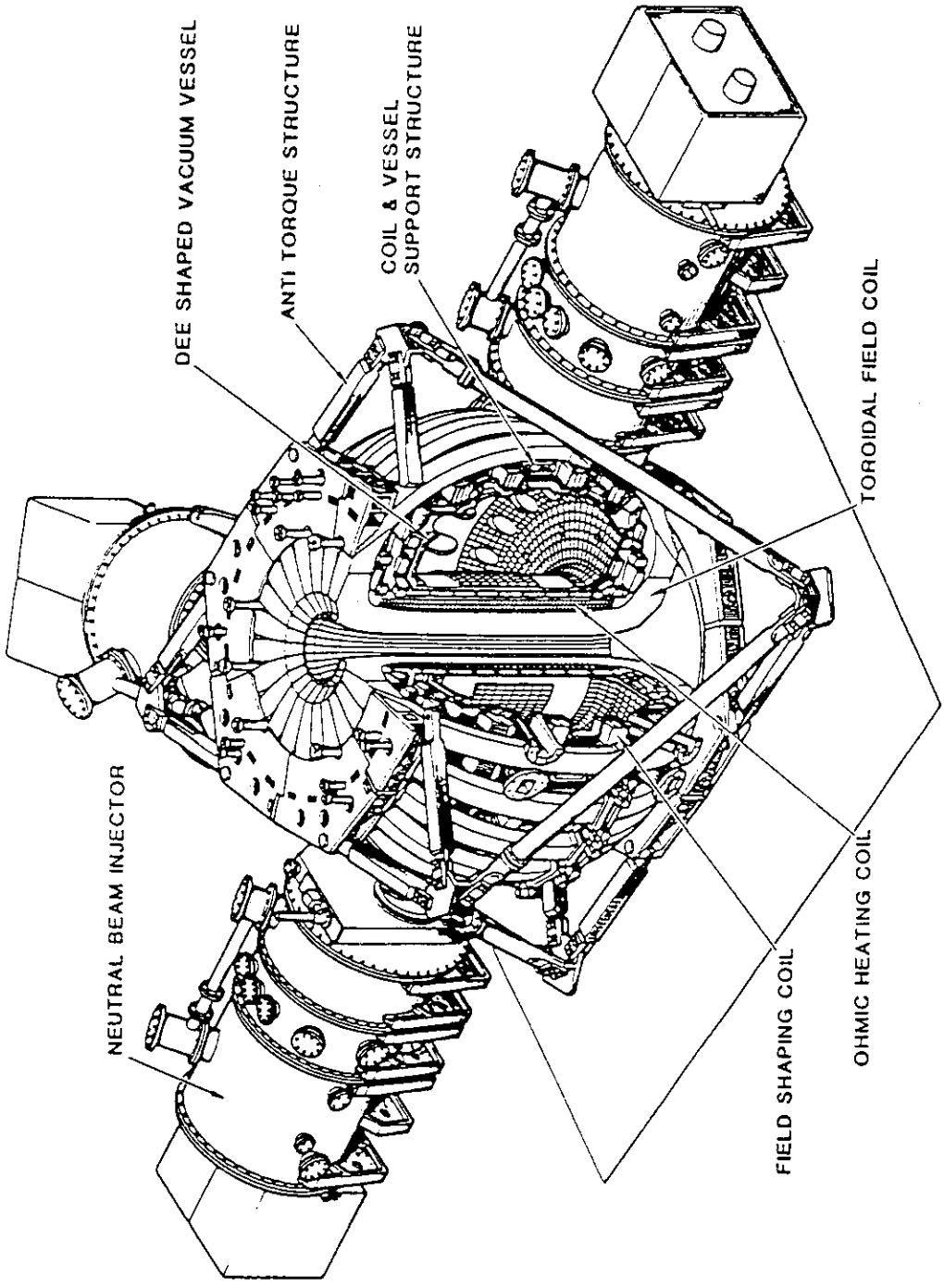

Fig. 3.4 Cutaway view of DIII-D.

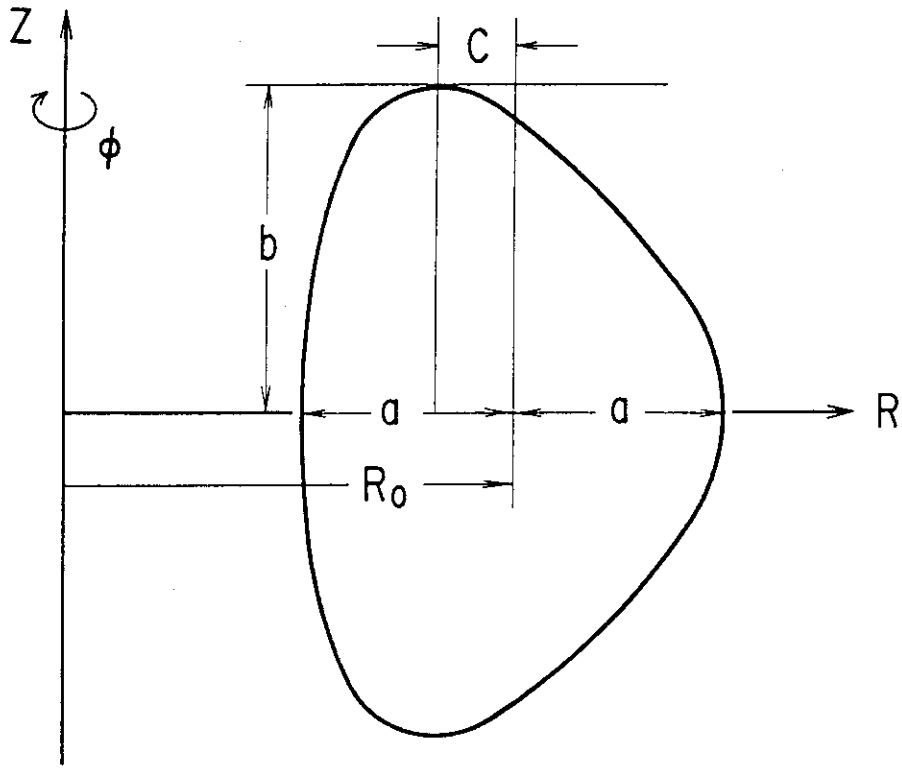

Fig. 3.5 Definition of plasma shape parameters: aspect ratio $A = R_0/a$, elongation $\kappa = b/a$, triangularity $\delta = c/a$.

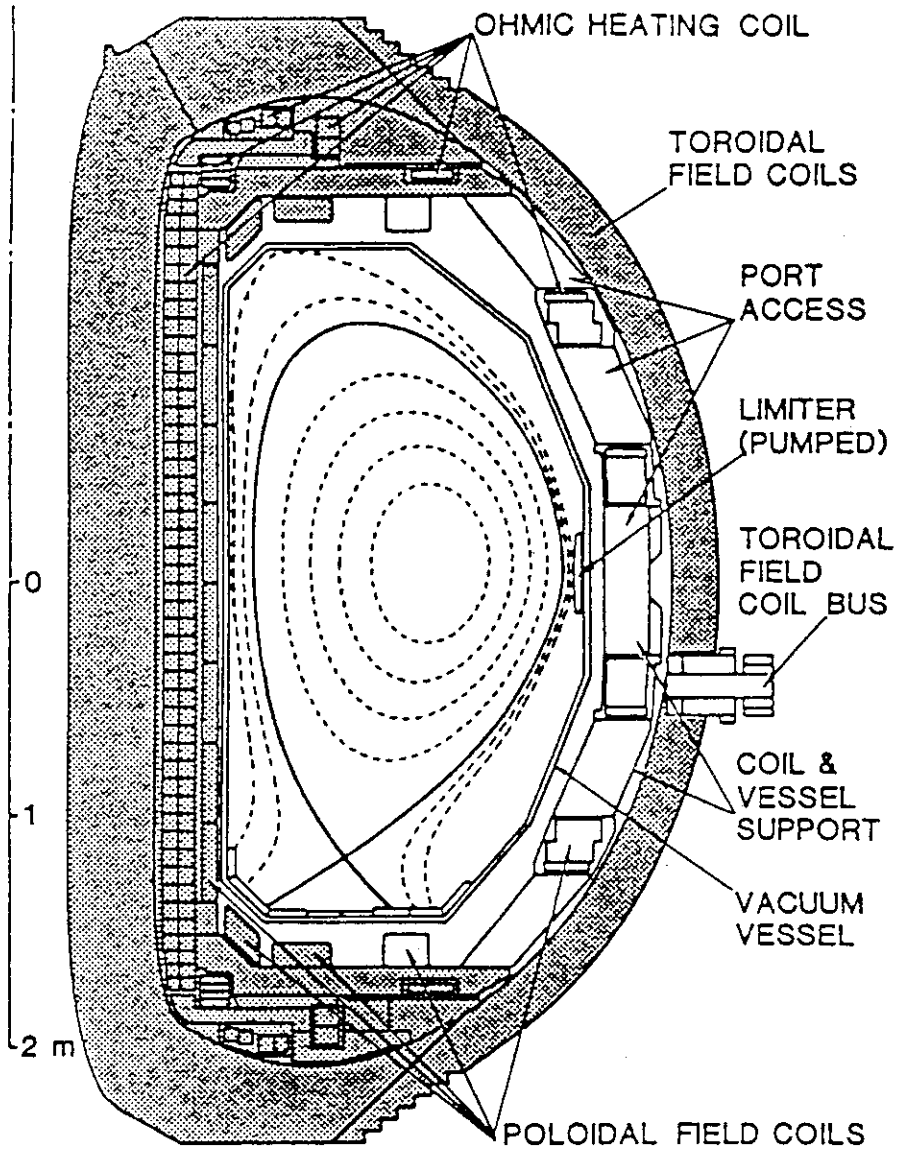

Fig. 3.6 Cross-section of DIII-D with elongated plasma of lower X-point.

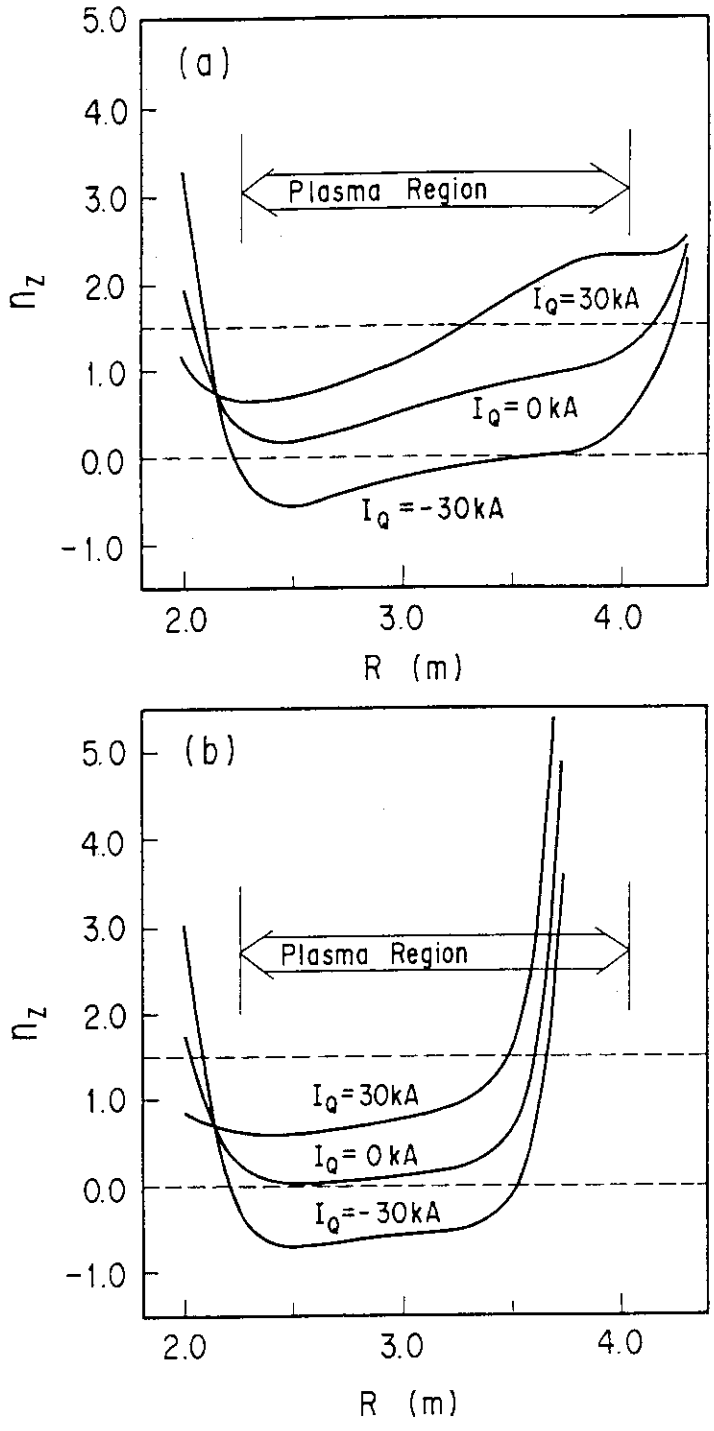

Fig. 3.7 Spatial variation of the decay index on the midplane (a) for the limiter and (b) the divertor configurations. I_Q is the current of the quadrupole field coil.

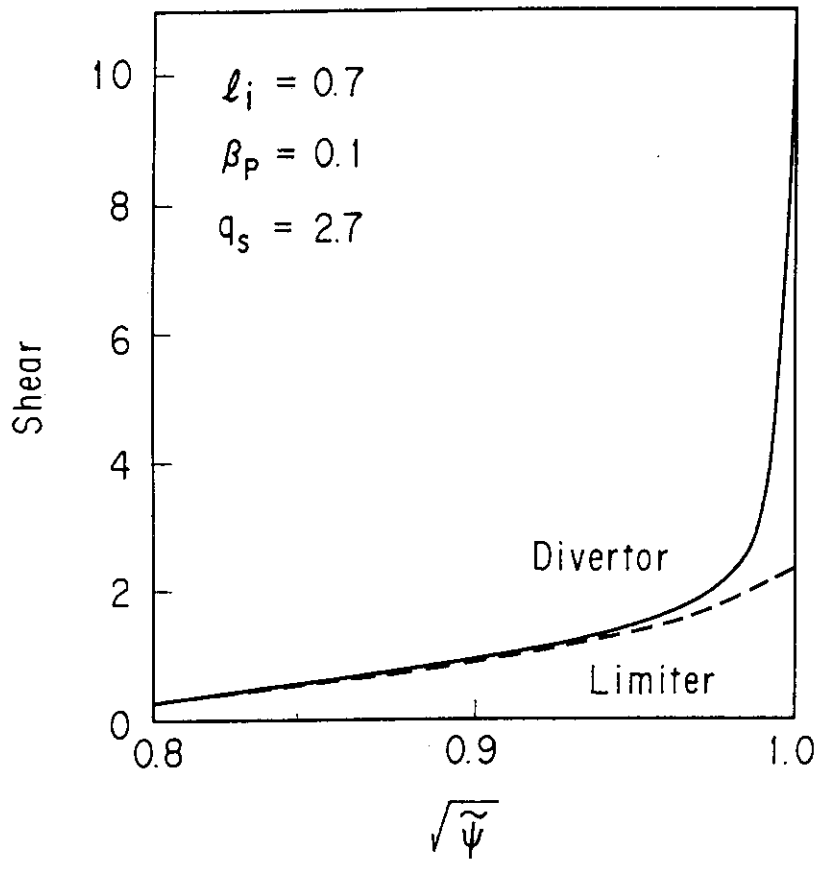

Fig. 3.8 Radial profiles of shear s in the limiter and divertor configuration for a flat current ($\ell_i = 0.7$), low beta ($\beta_p = 0.1$) and low q ($q_s = 2.7$) plasma.

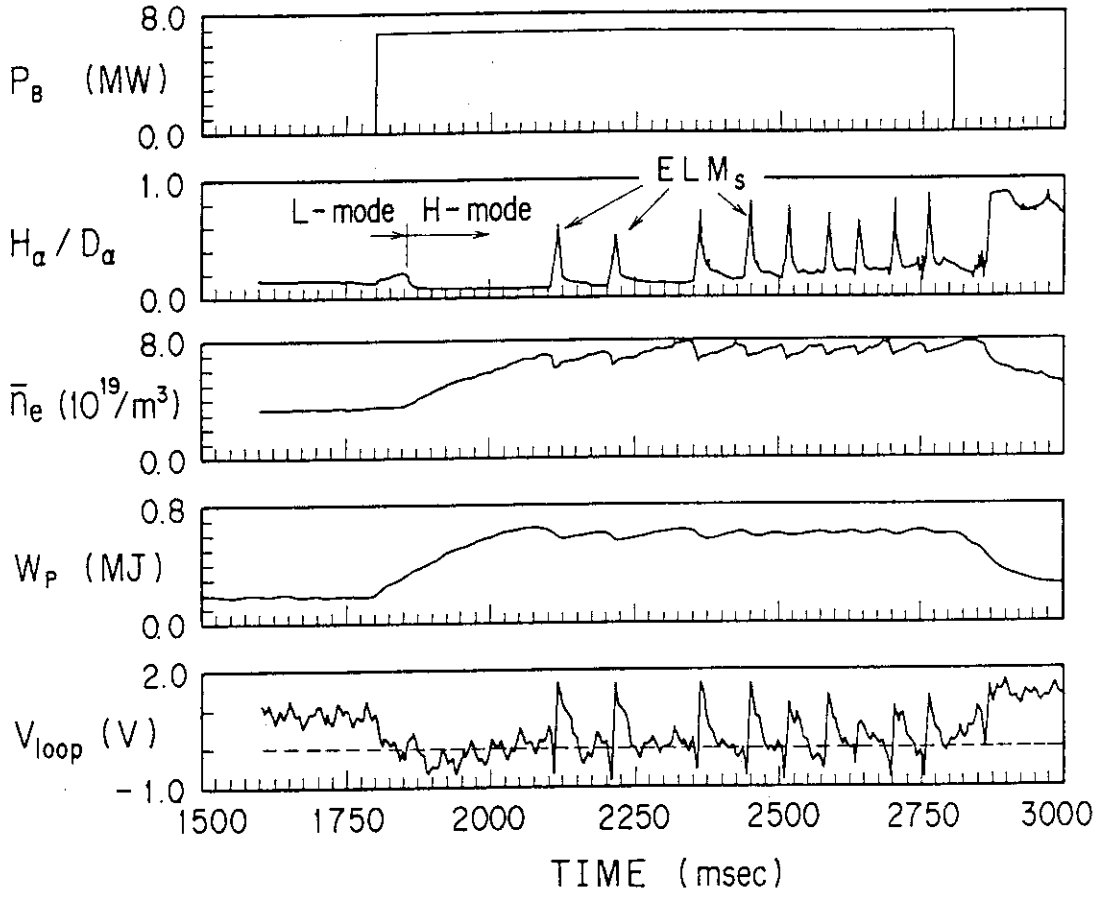

Fig. 3.9 Time histories from a typical H-mode discharge with ELMs for 1.25MA plasma current and 2.1T toroidal field. P_B is NB input power. H_α/D_α is Balmer α line of hydrogen or deuterium from the divertor region. $\bar{n}_e$ is line-averaged electron density. W_p is plasma stored energy. V_{loop} is loop voltage.[17]

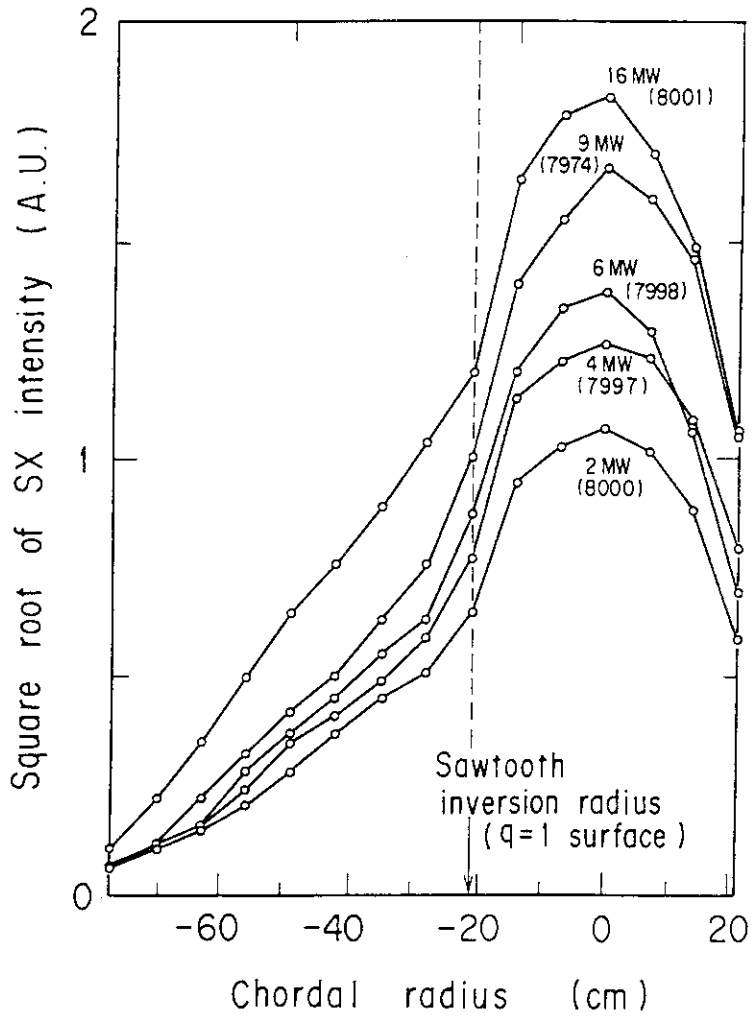

Fig. 3.10 Plasma pressure profiles estimated with the SX signals for the various input power in the series of 1.5MA lower X-point discharges. Chordal radius, which is a nearest distance from the plasma center to the chord of SX measurement, corresponds to the minor radius of the plasma.

Chapter 4

Effects of Divertor Configuration on the Stabilities of Axisymmetric Modes and Kink Modes

4.1 Introduction

Plasmas with a divertor configuration, as shown in Fig. 1.5(b), have been treated from the viewpoints of impurity control[1], remote cooling[2] and improvement of the energy confinement[3]. The divertor configuration has a stagnation point (or an X-point) of magnetic field lines at the plasma surface, and MHD stabilities are expected to have different characteristics from those in the limiter configuration, as described in Section 3.3.1. In this chapter, we numerically examine effects of the divertor configuration on stabilities of axisymmetric modes and external kink modes by using the equilibrium code and the ideal MHD stability code, ERATO-J, described in Section 3.4. We consider the equilibria of the limiter configuration and the divertor configuration which are produced by the JT-60 coil system. The effects of the poloidal location of the X-point and of the detailed structure of magnetic field lines near the X-point are also investigated by the artificially changing the location of the JT-60 magnetic coil.

One of the most dangerous MHD instabilities is the n=0 axisymmetric mode, introduced in Section 2.5.1. This instability is usually analysed with the decay-index, $n_z = -(R/B_z)(\partial B_z/\partial R)$, and the stability condition is obtained as $0 < n_z < 1.5$ in a conventional tokamak [4,5]. For the divertor configuration, the axisymmetric mode is more complicated because the X-point produces large variations of n_z in the plasma

region, as shown in Fig. 3.7. Ninomiya et al. analysed JT-60 divertor configuration using a rigid model and obtained a rather wide stability region of $n_z^{axis} < 2.3$, where the superscript 'axis' denotes the value at the magnetic axis [6]. The rigid model analysis, however, leads to more stable results than rigorous ideal MHD analyses which consider the distribution of the displacement [7,8]. The work by Bernard, et al.[8] using the general ideal MHD code: ERATO indicated that local displacement was enhanced by a strong curvature of the plasma surface due to the triangularity defined in Fig. 3.5. In the divertor configuration, displacement is also expected to be large because there is a strong curvature of the plasma surface near the X-point. Therefore we investigate the effects of X-points on the growth rate and the displacement pattern.

The effects of separatrices on the external kink modes were investigated by Lee[9], who found no significant differences in the stability properties of external kink modes between limiter and divertor configurations. The effect of shear was included in his work. However, the shear effect is sensitive to the numerical accuracy for the data near the separatrix surface. In the divertor configuration, the safety factor q and magnetic shear S have the logarithmic singularity on the separatrix magnetic surface. This large shear is expected to be effective especially in stabilizing external kink modes which exhibit a large displacement near the plasma surface. This shear stabilization in the divertor configuration may be also expected in a finite beta plasma, therefore it is of interest to investigate whether this shear stabilization is effective in finite beta plasmas.

This chapter is organized as follows. Section 4.2 describes procedures of computing equilibrium and MHD stability with high accuracy. Section 4.3 discusses divertor effects on the stability of the axisymmetric mode. Section 4.4 pertains to divertor effects on n=1 kink stability. In Section 4.5, the critical beta value of n=1 kink modes in the divertor configuration is analysed and compared with that in the limiter configuration. Finally, our conclusions are summarized in Section 4.6.

4.2 Computational Procedure

Axisymmetric equilibria with up-down symmetry are obtained by solving the Grad-Shafranov equation of Eqs. (2.44)-(2.45) in the cylindrical coordinates (R,Z,ϕ) by using the Buneman's DCR method [10] for prescribed parameters of plasma current profile, as described in Section 3.4.1. Since the accuracy of numerical solution is important especially in the divertor configuration, we employ the fine grid mesh with $N_R = 512$ in the R direction and $N_Z = 256$ in the Z direction, respectively, so that the ratio of grid size to the average minor radius of the plasma is about 5×10^{-3}. The convergence of the solution in the iteration procedure is checked by the strict condition of $\varepsilon < 10^{-6}$ where $\varepsilon = max|\psi_{ij}^n - \psi_{ij}^{n-1}|/max|\psi_{ij}^n|$, and ψ_{ij}^n is the poloidal flux at the i,j mesh in the n-th iteration step. As described in Section 2.3.3, the prescribed pressure and current profiles, i.e., $dp/d\psi$ and $F(dF/d\psi)$, are necessary in order to make a equilibrium. In this chapter, we employ the following form to define the toroidal current density J_ϕ,

$$J_\phi = -R\frac{dp}{d\psi} - \frac{1}{\mu_0 R}F\frac{dF}{d\psi}, \tag{4. 1}$$

$$\frac{dp}{d\psi} = \frac{j_0}{R_0}\beta_p\left(1-\tilde{\psi}^{j1}\right)^{j2}, \tag{4. 2}$$

$$F\frac{dF}{d\psi} = R_0^2\left(\frac{1}{\beta_p}-1\right)\mu_0\frac{dp}{d\psi}, \tag{4. 3}$$

where $\tilde{\psi} = (\psi - \psi_{axis})/(\psi_{surf} - \psi_{axis})$ is the normalized poloidal flux. ψ_{axis} and ψ_{surf} are the poloidal flux at the magnetic axis and at the plasma surface, respectively. R_0 is the major radius of a plasma center, j_0 is the toroidal current density at the magnetic axis and β_p is the poloidal beta. The parameters j_0, $j1$, $j2$ are adjusted in such a way that the safety factor q_0 at magnetic axis, the safety factor q_s at plasma surface and the normalized internal inductance ℓ_i have prescribed values; $\ell_i = < B_p^2 > / B_p^2(a)$, where $<$ $>$ denotes a volume average, $B_p(a) = \mu_0 I_p\sqrt{R_0/2V(a)}$, where I_p is the plasma current and $V(a)$ is the total plasma volume. In calculating the divertor configuration, we define the plasma surface by the magnetic surface, that is slightly inside the separatrix surface to avoid the singularity of the metric; otherwise Jacobian at the separatrix increases to

the infinity as clearly obtained from Eq. (2.32). Then the poloidal flux at the plasma surface ψ_{surf} is defined by

$$\psi_{surf} = \psi_{sep} - \delta \times |\psi_{sep} - \psi_{axis}| \tag{4. 4}$$

and ψ_{sep} is the poloidal flux at separatrix. In the following calculations, the parameter δ is adjusted to 0.001 and the effect of the value of δ on the results of calculation is discussed in Section 4.4. These free boundary equilibria are computed using the JT-60 coil configuration. For the study of the effect of the X-point location, we artificially change the location of the divertor coils.

Ideal MHD stabilities are studied with the ERATO-J code, described in Section 3.4.2. This two dimensional code computes the ideal-MHD spectrum by minimize the potential energy in the flux coordinates (ρ, χ), where $\rho = \sqrt{\tilde{\psi}}$ and the poloidal angle χ is selected as defined in Eq. (3. 5). When the displacement of the mode is localized at a region in the radial (ρ) direction, the larger number of radial mesh points are required to accurately express the eigenfunction. The mesh accumulation is a useful method, where the large number of mesh points are accumulated on the location of the large displacement fixing the total mesh number. We use the following function to determine the mesh points in the radial (ρ) direction:

$$\begin{aligned} \frac{dr}{d\rho} &= \frac{1}{1+c}\left\{1 + \frac{cf(\rho)}{\int_0^1 f(\rho)d\rho}\right\} \\ f(\rho) &= \frac{1}{\omega\left\{\left(\frac{\rho-\tilde{\rho}}{\omega}\right)^2 + 1\right\}} \end{aligned} \tag{4. 5}$$

where $\tilde{\rho}$ is the position of accumulation ($\tilde{\rho}$ = 1.0 at the plasma surface), ω is the width of the accumulation region, and c is the weight of the accumulation, respectively. The mesh points in the ρ direction are determined by the corresponding points in the r values that are the equi-distance points in $0 \leq r \leq 1$.

The effect of mesh accumulation on the stability calculation is shown in Fig.4.1 for the n=1 external kink modes in the divertor configuration. Figure 4.1(a) shows the dependence of the squared growth rate $\hat{\gamma}^2$ on the inverse of the squared mesh number N^{-2} for different degrees of mesh accumulation; $\hat{\gamma}$ is the growth rate normalized by the Alfvén velocity v_A and the major radius R_0 ($\hat{\gamma}^2 = \gamma^2/(v_A/R_0)^2$). The same mesh numbers are chosen in the ρ and χ directions ($N = N_\rho = N_\chi$). By increasing the mesh accumulation near the plasma surface, namely, increasing the value of c, the gradient of $\hat{\gamma}^2$ against N^{-2} becomes smaller with the same convergent value of $\hat{\gamma}^2$ at $N^2 = \infty$ and an offset linear dependence on N^{-2} is obtained for the parameters of $\tilde{\rho} = 1.0$, $w = 0.1$ and $c = 1.0$. Figure 4.1(b) compares the radial profiles of displacements near the plasma surface with the mesh number of $N = 60$ and 90. The two profiles are in good agreement with each other. Since the degree of the mesh accumulation is different for each mode and each configuration investigated, we have checked the offset linear dependence of $\hat{\gamma}^2$ on N^{-2} for all cases in this chapter.

4.3 Stability of Axisymmetric Modes

We commence to study the effect of the divertor configuration on the axisymmetric (or n=0) modes and to compare this effect with the effect of the limiter configuration. To simplify the problem, we analyse a nearly circular plasma without a effect of wall stabilization. The decay index n_z has large variation in the plasma with divertor configuration, so that we define the averaged decay-index $< n_z >$ over the cross section of the plasma by

$$< n_z >= -\frac{R^{axis}}{B_z^{axis}} \frac{\int J_\phi \frac{\partial B_z}{\partial R} dS}{\int J_\phi dS} \tag{4. 6}$$

where the integral is carried out in the entire cross section of the plasma.

First, we investigate the stability of the JT-60 plasma with poloidal beta β_p of 1.0 and internal inductance ℓ_i of 1.0. We generate the sequence of equilibria for the $< n_z >$ −scanning, and obtain the growth rates and the displacement vectors of unstable axisymmetric modes for each equilibrium using ERATO code. Figure 4.2 shows the dependence of the squared growth rate $\hat{\gamma}^2$ on $< n_z >$ in limiter and divertor configurations. Figure 4.3 represents typical examples of two dimensional profiles of displacement vectors. Axisymmetric modes are divided into two groups: vertical and horizontal modes. The vertical mode is unstable with low $< n_z >$ values. This mode has similar threshold values ($< n_z > \approx 0.0$) and similar growth rates in both configurations, as shown in Fig. 4.2. The displacement vectors in the divertor configuration (Fig. 4.3(b)), however, have profiles that are slightly different from those of the limiter configuration (Fig. 4.3(a)). In the limiter configuration, the plasma moves as a rigid body in the vertical direction (Fig.4.3(a)), as was shown in the previous work[8]. In the divertor configuration, the displacement is suppressed at the X-point and the plasma rotates around this point (Fig. 4.3(b)). On the other hand, there is much difference between the limiter configuration and the divertor configuration in the horizontal mode. The growth rate of the divertor configuration is reduced compared with that of the limiter

configuration and the threshold value of $< n_z >$ increases from 1.8 to 2.3, as shown in Fig. 4.2. The displacement of the horizontal mode in the limiter configuration is similar to a rigid-body movement (Fig. 4.3(c)); the displacement of the horizontal mode in the divertor configuration is localized near the plasma surface and the plasma flows into the X-point along the magnetic surface (Fig. 4.3(d)). It should be noted that, although the divertor coil is located in the outside of torus, where the divertor coil current could attract the plasma and might destabilize the horizontal mode, the stability window in the divertor configuration is wider than in the limiter configuration. These results are not sensitive to the variation of poloidal beta, internal inductance and safety factor.

The wide stability window in the divertor configuration is produced by the effect of sub divertor coil current, which flows in the direction opposite to the plasma current and the main divertor coil current. Figure 4.4 shows the effect of the sub divertor coil currents on the axisymmetric modes. The effect on the vertical mode is small. The threshold value of $< n_z >$ for the horizontal mode without sub-divertor coil currents is the same as in the limiter case. However, even without sub-divertor coils, the growth rates of these instabilities are reduced and the displacement is localized near the plasma surface, similar to Fig. 4.3(d). There is still a wide stability window because the attractive force due to the main divertor coil is reduced by the other poloidal field coils. The reason for this localization of the displacement is the location of the divertor coil close to the plasma surface.

Effect of the poloidal location of the X-point on the axisymmetric modes is evaluated by artificially changing the location of the magnetic coil of JT-60. Figure 4.5 shows the squared growth rate as a function of $< n_z >$ for three configurations: with an outside X-point, with an inner X-point and with top-bottom X-points. We obtain the differences of the threshold values for the horizontal mode and the growth rate for the vertical mode. For the horizontal mode, the configuration with an outer X-point has a wider stability window than the other two configurations. For the vertical mode, the plasma with top and bottom X-points has a smaller growth rate than that of the other

configurations. It is interesting to see that the vertical mode in the configuration with top and bottom X-points and the horizontal mode in the configuration with an outer X-point are more stable than that in the limiter configuration, as shown in Fig. 4.5. This stabilization is due to the repulsive force of the sub-divertor coil. Figure 4.6 shows the profiles of displacement vectors of the vertical mode for the three configurations of Fig. 4.5. In the configurations with an inside X-point and an outside X-point, the plasma moves like a rigid body. In the configuration with top and bottom X-points, the displacement vector is localized near the plasma surface. This localization is similar to that of the horizontal mode with the outside X-point, because the displacement is caused by the attractive force of the main divertor coil. Displacements toward the X-point are large near the plasma surface in all divertor configurations. Since the global growth rate of this mode is small, this localization of displacements is more acceptable. The finding is in contrast with the results of Bernard et al.[8] which described that the presence of the strong curvature or nearby X-points should be avoided.

4.4 Stability of n=1 Kink Modes

The n=1 external kink modes are more unstable than the higher-n modes when no conducting wall stabilization is assumed. For an investigation of kink mode instability in limiter and divertor configurations, we consider the stability of n=1 external kink modes for a free boundary plasma with a flat distribution of the current density ($\ell_i = 0.7$), a low poloidal beta ($\beta_p = 0.1$), and a circular poloidal shape. Figure 4.7 shows the dependence of the squared growth rate $\hat{\gamma}^2$ on the safety factor q_s at the plasma surface for the two configurations. The equilibrium is calculated for $q_s = 2.8$ and $q_0 = 1.9$, and the σ-scaling of Eq. (3.6) is used for the q_s scanning from 2.0 to 3.0. If we scale $\psi \rightarrow \sigma\psi$ and $p \rightarrow \sigma^2 p$, q scales approximately as q/σ and the shear is almost remained fixed. The stabilization of kink modes by the divertor configuration is clearly shown in this figure: the growth rate for the divertor configuration is much smaller than that for the limiter configuration and the stability window is wider. The projections of the displacement vector on a poloidal cross section are shown in Fig. 4.8 for the two configurations, with $q_s = 2.7$. A displacement with a poloidal mode number m=3 is dominant in both configurations, but the radial profiles are very different from each other. In the limiter configuration, the displacement increases gradually from the magnetic axis to the plasma surface, as in the cylindrical plasma [11]. In the divertor configuration, however, the displacement is localized near the plasma surface and the plasma moves along the magnetic surface. Compared with the displacement of the horizontal mode in the divertor configuration (see Fig. 4.3(d)), the displacement profile is more extended along the poloidal direction.

The magnetic shear is the key factor of the kink mode stability [11,12,13]. Figure 4.9 compares the radial profiles of the magnetic shear S and the absolute value of the displacement vector $|\xi|$ in the limiter and divertor configurations with $q_s = 2.7$. The shear of the divertor configuration is much larger than that of the limiter configuration, and the displacement vector in the divertor configuration is localized near the plasma surface.

As described in Section 4.2, the plasma surface is set slightly away from the separatrix magnetic surface by the small amount (δ). To investigate the role of the shear at the plasma surface, we calculate the dependence of the shear and the growth rate on the clearance δ between the plasma surface and the separatrix surface. Figure 4.10 is a plot of the shear at the plasma surface and the squared growth rate $\hat{\gamma}^2$ as a function of δ. Here, the safety factor at the plasma surface is fixed at $q_s = 2.7$. At $\delta > 0.1$, the shear is almost the same as in the limiter configuration, and so is the growth rate. As δ decreases, the shear increases inversely with δ and the growth rate decreases. Accordingly, it is clear that the stabilization in the divertor configuration is due to the shear near the plasma surface. For small values of δ (~ 0.001), the growth rate saturates. This is because the contribution of the stabilizing potential energy due to the shear is saturated, since the ratio of the plasma volume to the volume in the high shear region saturates as δ decreases to the quite small value.

Next, we study the effect of the poloidal location and the number of X-points on external kink modes. Figure 4.11 shows the dependence of $\hat{\gamma}^2$ on q_s in three different divertor configurations, where the plasma current profile is adjusted in such a way that the magnetic shear at the surface is the same for the given q_s values. The configurations with an inside X-point and with top and bottom X-points exhibit smaller growth rates and a wider stability window. This difference in stabilization comes from the difference in the radial profile of shear. The equilibrium calculations show the following points: (1) the high shear region in the peripheral plasma becomes wider as the location of the X-point shifts from the outer region of the torus to the inside of the torus. (2) The configuration with top-bottom X-points (double-null divertor) has a wider high shear region than in the configurations with a top X-point or a bottom X-point (single-null divertor). Therefore, a plasma with an inside X-point is more stabilized by the effect of the X-point location, and a plasma with top-bottom X-points is more stabilized by

both effects of the location and number of X-points. In the configuration without sub-divertor coil currents, the shear stabilization is also obtained since the shear profile is almost the same for the cases with and without sub-divertor coils.

We have also investigated the dependence of stability against the n=1 kink mode on the values of β_p, ℓ_i and q_s. Figure 4.12 is a stability diagram for limiter and divertor configurations in the $q_s - \ell_i$ space, with $\beta_p = 0.1$ and 0.5, where q_0 is fixed at 1.05 to avoid the m=1 internal kink mode (Section 2.5.2). The unstable condition is defined by $\hat{\gamma}^2 \geq 5 \times 10^{-5}$. The kink modes as indicated in the figure are unstable. The unstable region becomes smaller with increasing ℓ_i because of the decrease of the current driven term. In the divertor configuration the unstable region is slightly smaller than in the limiter configuration. This difference becomes small with increasing β_p because of the increase of the pressure driven term, as seen in Fig. 4.12(b).

With a higher beta value ($\beta_p = 1.0$), there is no difference in the stability windows between divertor and limiter configurations. With a flat current profile ($\ell_i = 0.8$), kink modes are always unstable for $q_s = 2.0 - 4.0$. This kink-ballooning mode is important when the beta values are high; this is discussed in Section 4.5.

4.5 Critical Beta against n=1 Kink Modes

We now investigate the divertor effect on the critical beta of the free boundary n=1 kink modes. The purpose of this study is to compare the effects of limiter and divertor configurations on finite beta, therefore, we do not optimize the pressure profile and plasma shape to obtain the critical beta. The pressure and current density profiles are assumed to be defined by the function of Eqs. (4.1)-(4.3). The circularly shaped plasmas are used.

Figure 4.13 shows the dependence of the growth rate γ on the toroidal beta value β_t for $q_s = 3.2$, $q_0 = 1.05$ and $\ell_i \approx 0.9$ in both configurations. For $q_s = 3.2$, the external kink modes are stable in low beta range, but they become unstable for beta values beyond $\beta_t \approx 1.2\%$. The growth rate in the divertor configuration is smaller than that in the limiter configuration and the critical beta is slightly improved (by 0.1%). It is useful to examine the displacement vector to see the effect of the divertor configuration. Figure 4.14 shows the results for the plasma with $\beta_t \approx 2.0\%$. In the limiter configuration (Fig. 4.14(a)), there is a large convective motion in the plasma, which is due to the ballooning nature of the unstable mode; this finding is similar to the results of Ref.[14]. In the divertor configuration, the displacement is localized near the plasma surface. The displacement on the inside of the plasma is larger than that in a low beta plasma (Fig. 4.14(b)).

In a high beta plasma, the destabilizing terms consist of pressure driven and current driven components of Eq. (2.89). These terms depend on the β value and the current profile (or the internal inductance). We have studied the dependences of the critical beta value β_c on the internal inductance ℓ_i for the divertor and limiter configurations with $q_s = 3.2$ and $q_0 = 1.05$, as shown in Fig. 4.15(a). Fig. 4.15(b) shows the dependence of the fraction of the current driven term (W_K) and the pressure driven term (W_B) on the internal inductance in the divertor configuration. A similar result is obtained for the limiter configuration. As seen in Fig. 4.15(a), the values of β_c is slightly higher in the

divertor configuration than the limiter configuration for all values of ℓ_i investigated. As the current profile shrinks (i.e., ℓ_i increases), β_c increases owing to the reduction of the current driven term. A further increase of ℓ_i raises the pressure driven term. When the pressure driven term dominates the current driven term, the critical beta value saturates. The saturation value of β_c is around 1.4%, which corresponds to the Troyon coefficient of $g = 2.6$, where Troyon coefficient is defined by $g = \beta_c(\%)/(I_p(MA)/a(m)B_t(T))$ [15]. A further increase of ℓ_i to more than 1.1 reduces β_c because the dominant pressure driven term increases according to the peaking of current profile.

4.6 Summary

We have numerically investigated the effects of the divertor configuration on axisymmetric modes and kink modes in a tokamak with nearly circular cross-section by using the ideal MHD stability code ERATO-J. Results are summarized as follows.

(a) Although a divertor configuration has a large variation of n_z over the plasma region, a wide stability window is obtained for axisymmetric modes because of the stabilizing effect of sub divertor coils. The threshold value of $< n_z >$ for the horizontal mode in the divertor configuration with an outside X-point is higher than the values in the limiter, and also higher than that in the divertor configurations with X-points on inner, top or bottom of the torus. In the unstable mode with displacement vectors moving toward the X-point, the perturbation is localized near the plasma surface and the growth rate is lower than that in the limiter configuration.

(b) The free boundary n=1 kink modes are stabilized by the large shear near the X-point. A reduction of the growth rate, a wider stability window and the localization of displacement are demonstrated in the divertor configuration. The shear stabilization effects are enhanced by moving the X-point location from the outside to the inside of torus and/or by increasing the number of X-point, because the enlargement of the high shear volume near the plasma surface enhances the stabilizing effect.

(c) The stabilizing effect is reduced with increasing the plasma pressure. However, the critical beta value is slightly improved (0.1%) in the divertor configuration. The critical beta value depends on the internal inductance. The maximum beta value is obtained for near-parabolic profiles ($\ell_i \approx 1.0$) in both the limiter configuration and the divertor configuration.

References

[1] DIVA Group: Nucl. Fusion **18** (1978) 1619.

[2] M. Shimada, et al.: Nucl. Fusion **22** (1982) 643.

[3] F. Wagner, et al.: Phys. Rev. Lett. **49** (1982) 1408.

[4] S.M. Osovets: Plasma physics and the Problem of Controlled Thermonuclear Reactions, Vol.2 (1958) 238.

[5] S. Yoshikawa: Phys.Fluids **7** (1964) 278.

[6] H. Ninomiya, Y. Suzuki, A. Kameari: Jpn. J. Appl. Phys. **15** (1976) 2201.

[7] M. Kumagai, T. Tsunematsu, S. Tokuda, T. Takeda: Positional Instability Analysis of Tokamak Plasma by ERATO, Jpn. At. Energy Res. Inst., JAERI-M 83-085 (1983)

[8] L.C. Bernard, D. Berger, R. Gruber, F. Troyon: Nucl.Fusion **18** (1978) 1331.

[9] J.K. Lee: Finite-beta Global MHD Stabilities for Circular and Highly-elongated Tokamaks with and without Poloidal Divertors, GA Technologies, GA-A18412 (1986)

[10] R.W. Hockney: in Methods in Computational Physics, Academic Press, New York, Vol.9 (1970) 135.

[11] J.A. Wesson: Nucl.Fusion **18** (1978) 87

[12] J.A. Wesson: in Controlled Fusion and Plasma Physics. (Proc.7th Europ.conf.) **2** (1975) 102.

[13] B.R. Suydam: Proc. 2nd United Nations Int. Conf. on Peaceful Use of Atomic Energy **31** Geneva (1958) 157.

[14] A.M.M. Todd, M.S. Chance, J.M. Greene, et al.: Phys. Rev. Lett. **38** (1977) 826.

[15] F. Troyon, R.Gruber: Phys. Lett. **110A** (1985) 29.

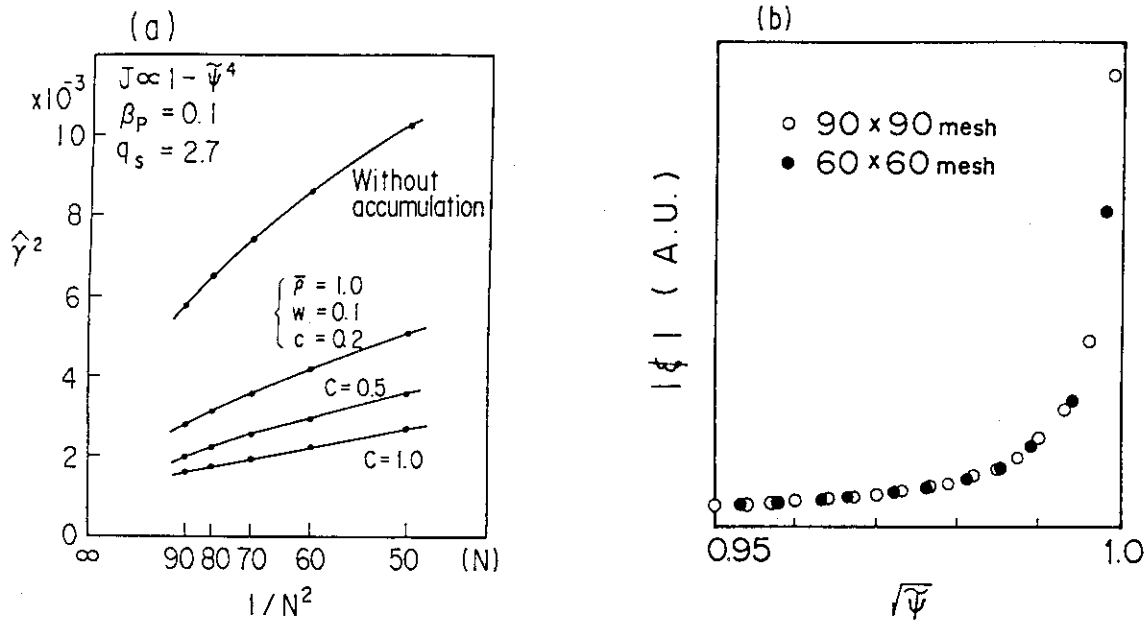

Fig. 4.1 Effect of mesh accumulation on the stability calculation by ERATO-J: (a) Squared growth rates $\hat{\gamma}^2$ as a function of the inverse of the squared mesh number N^{-2} for different accumulation values; ρ is the position of accumulation ($\tilde{\rho} = 1.0$ at the plasma surface), ω is the width and c is the weight. The value of c means the strength of the mesh accumulation on the point of $\tilde{\rho}$. (b) Radial profiles of the eigen function near the plasma surface for a 90×90 mesh (open circles) and a 60×60 mesh (closed circles), with mesh accumulation ($\tilde{\rho} = 1.0$, $\omega = 0.1$, $c = 1.0$).

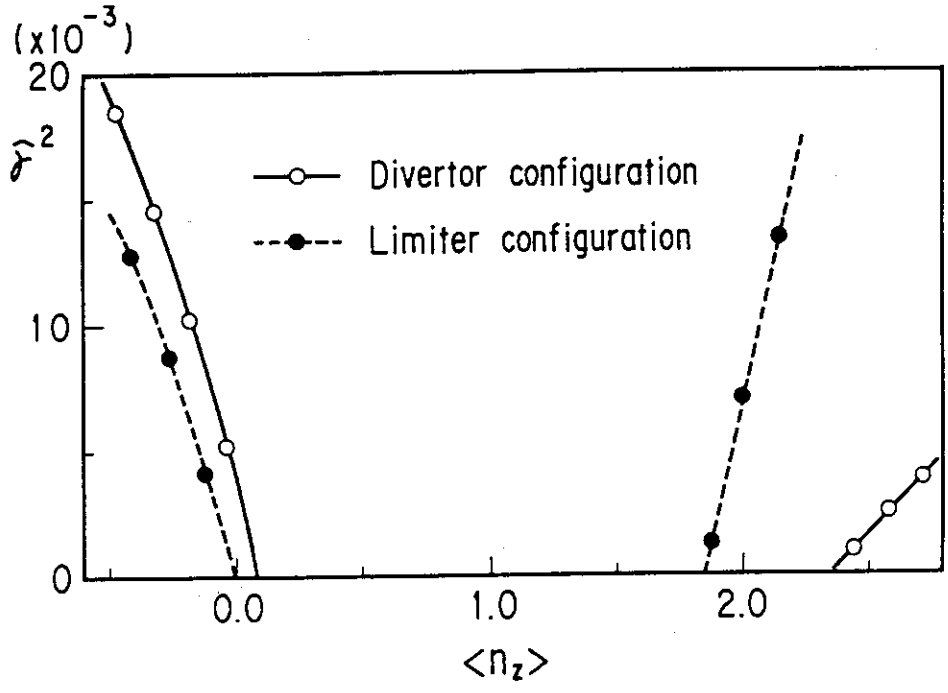

Fig. 4.2 Squared growth rates $\hat{\gamma}^2$ of axisymmetric modes in limiter (dashed line) and divertor configurations (solid line) with an outside X-point, as a function of the averaged n-index $< n_z >$ for a plasma with a parabolic current profile; $\ell_i = 1.0$ and $\beta_p = 1.0$.

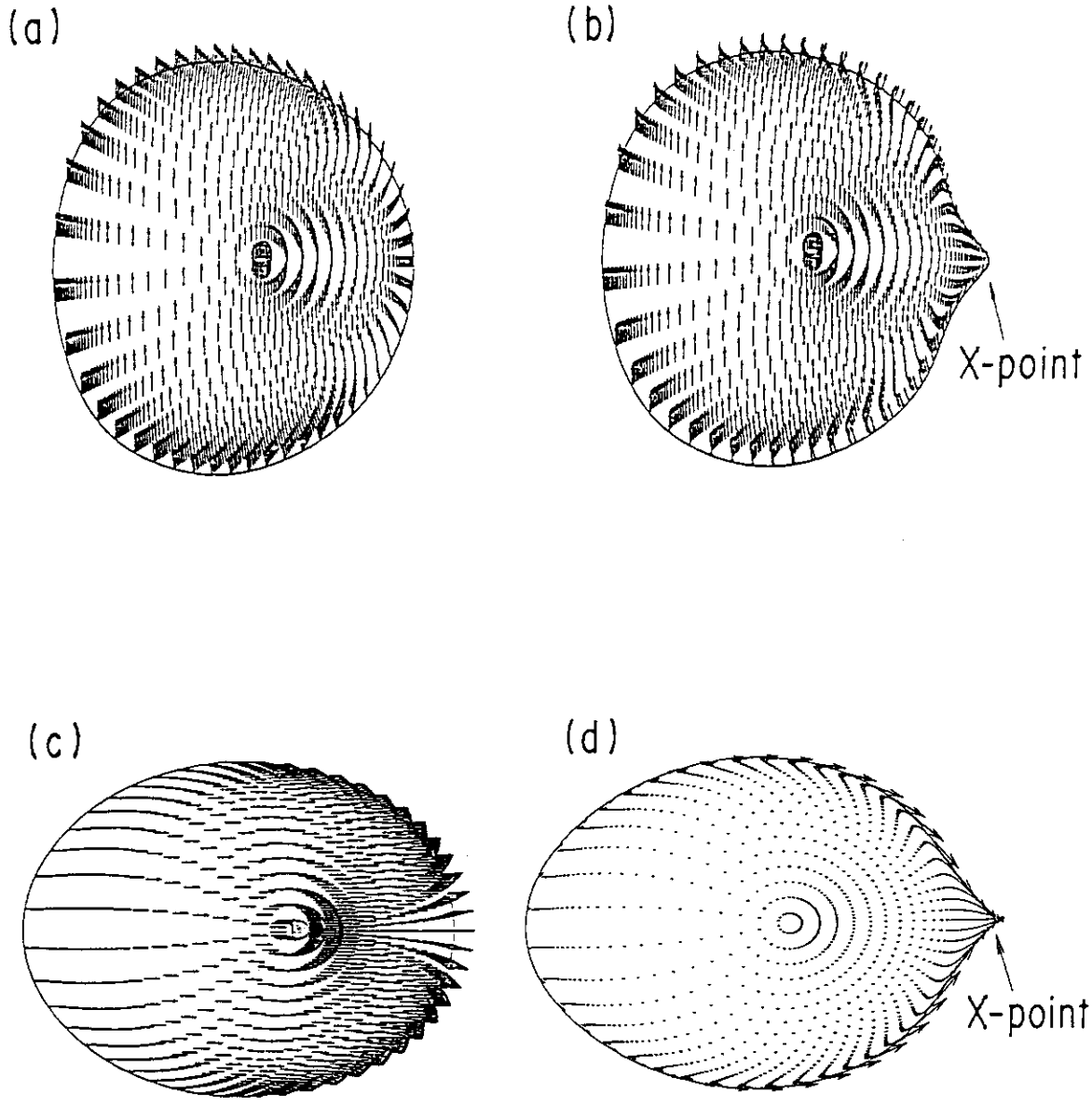

Fig. 4.3 Displacement vector in the poloidal plane for axisymmetric modes. The vertical mode behaves in the same way as in a rigid model in both the limiter configuration (a) and the divertor configuration (b) ($< n_z > \approx -0.25$). For the horizontal mode the displacement in the limiter configuration (c) is similar to that of the rigid model ($< n_z > = 2.0$) and the displacement in the divertor configuration (d) is localized near plasma surface ($< n_z > = 2.7$).

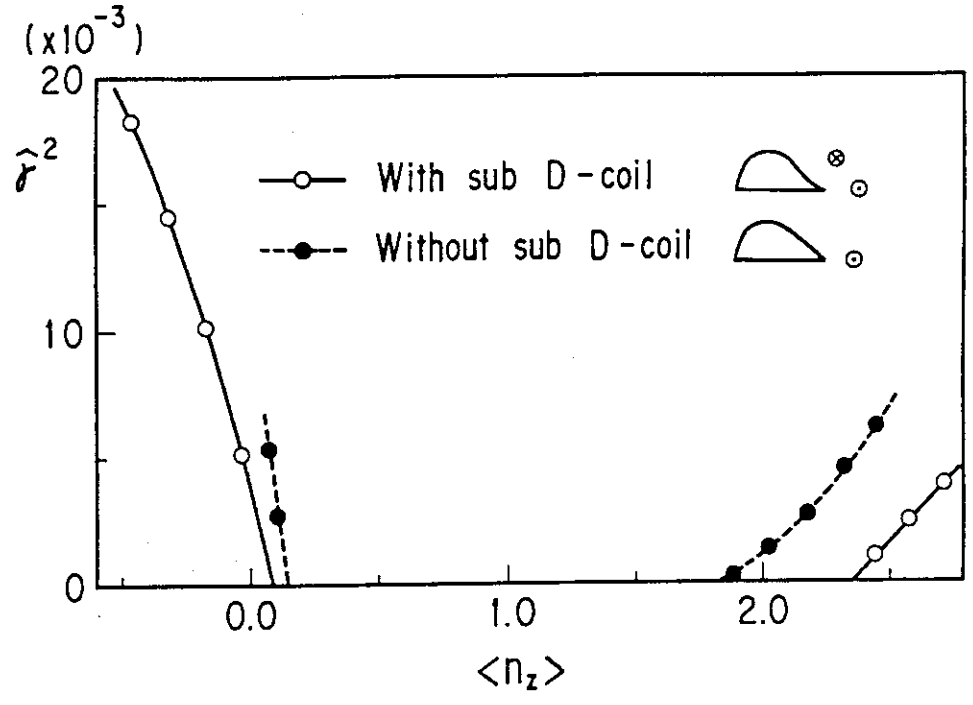

Fig. 4.4 Effect of the sub divertor coil current on axisymmetric modes. The squared growth rate $\hat{\gamma}^2$ is plotted as a function of $< n_z >$ for the divertor configurations with and without a sub divertor coil.

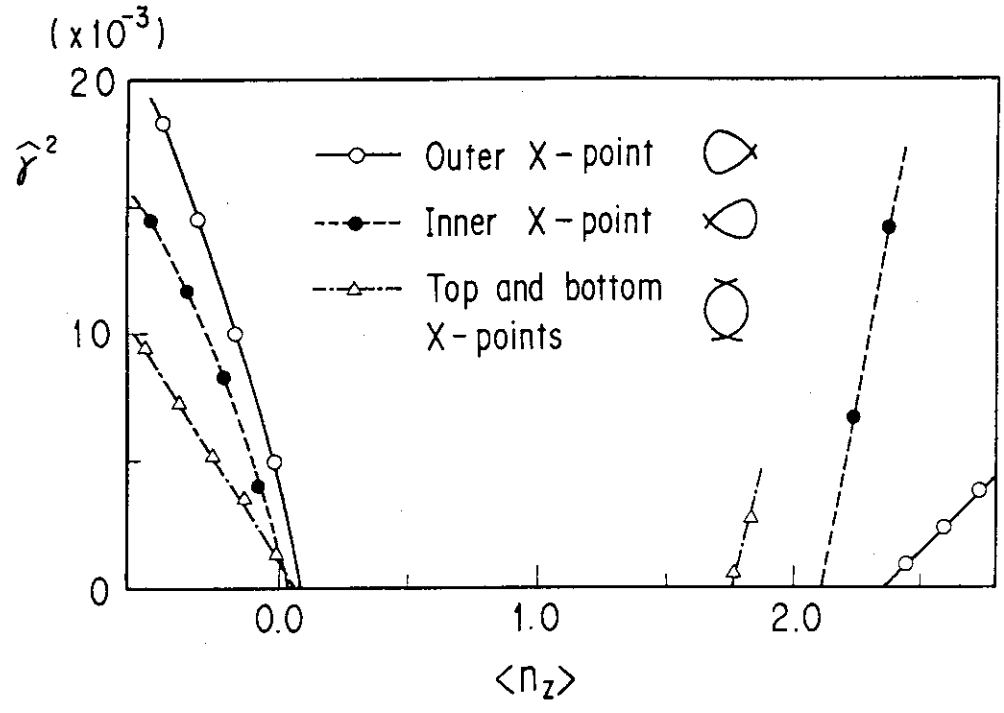

Fig. 4.5 Effect of the location of the X-point on axisymmetric modes. The squared growth rates $\hat{\gamma}^2$ is plotted as a function of $< n_z >$ for three divertor configurations: with an outside X-point, with an inside X-point and with top-bottom X-points.

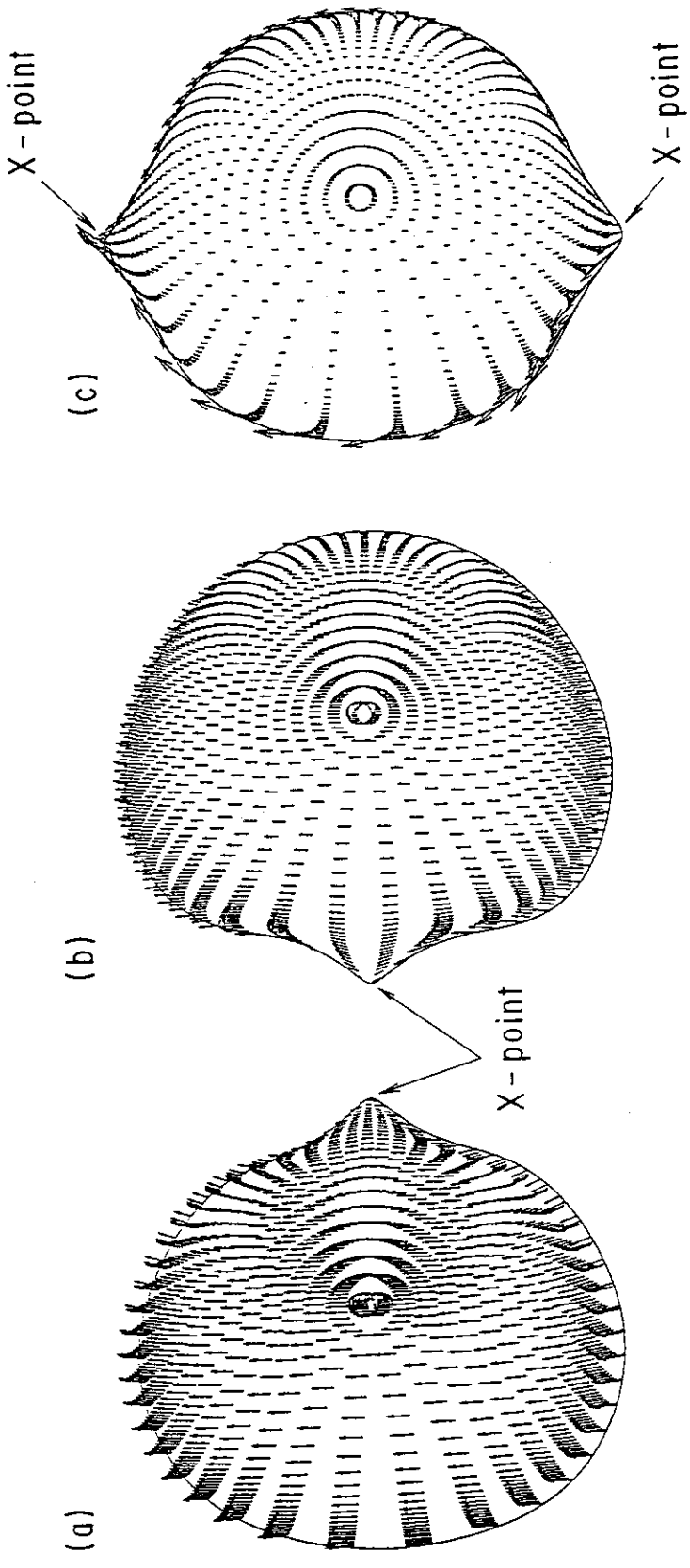

Fig. 4.6 Displacement vector of the vertical mode with (a) an outside X-point, (b) an inside X-point, and (c) top and bottom X-points, corresponding to Fig. 4.5 ($< n_z > \approx -0.25$). Localization of the displacement is observed only with the top-bottom X-points.

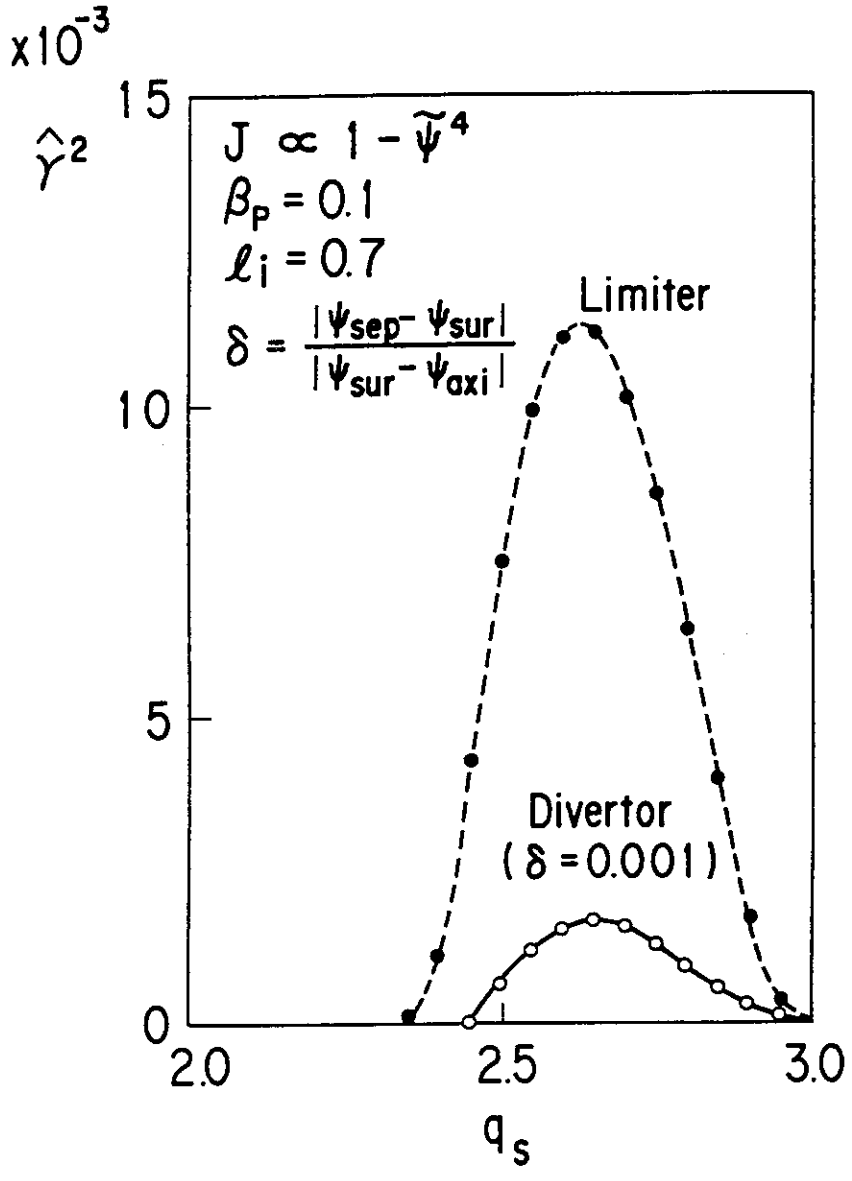

Fig. 4.7 Squared growth rate $\hat{\gamma}^2$ of external kink modes in limiter (dashed line) and divertor (solid line) configurations as a function of the safety factor at plasma surface q_s for a flat current ($\ell_i = 0.7$) and low beta ($\beta_p = 0.1$) plasma.

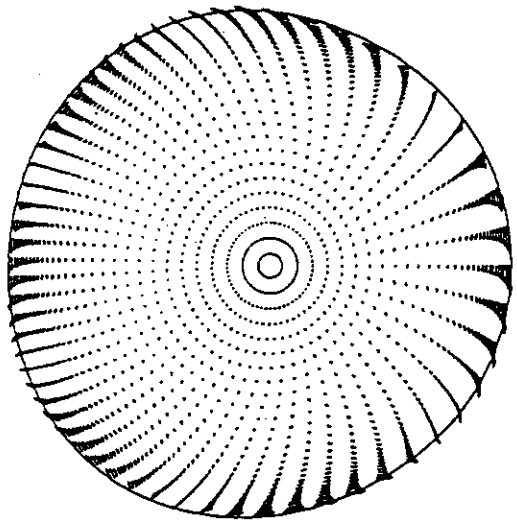

(a) LIMITER CONFIGURATION PLASMA

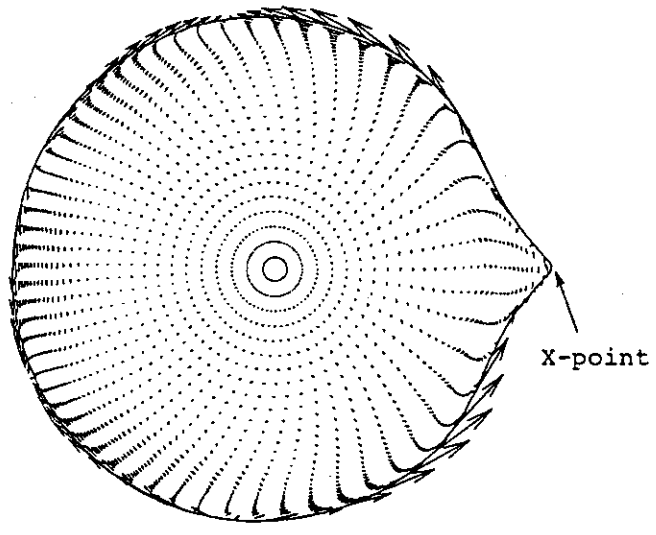

(b) DIVERTOR CONFIGURATION PLASMA

Fig. 4.8 Displacement vectors projected on the poloidal plane for (a) the limiter configuration and (b) the divertor configurations of Fig. 4.7, with $q_s = 2.7$ *and* $q_0 \approx 1.9$.

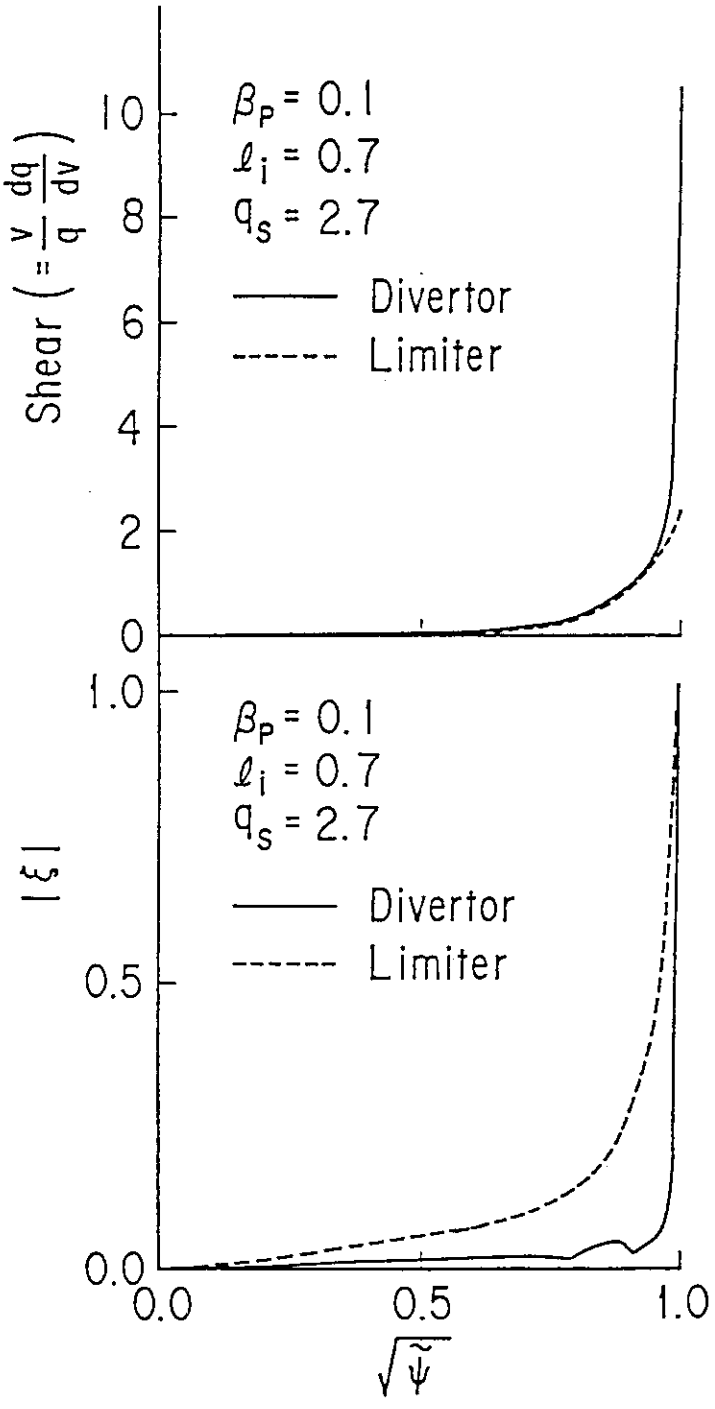

Fig. 4.9 Radial profiles of shear s and displacement $|\xi|$ for the limiter and divertor configurations of Fig. 4.8.

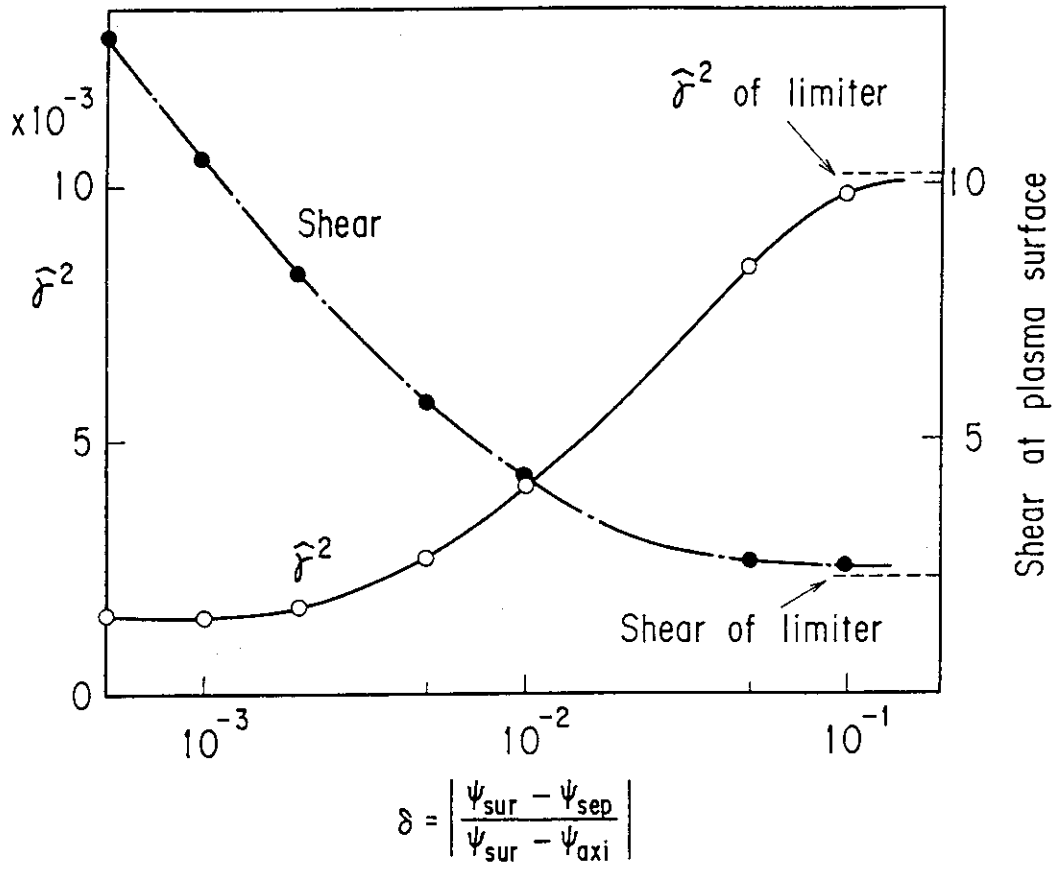

Fig. 4.10 Squared growth rate $\hat{\gamma}^2$ (open circles) and shear at the plasma surface (closed circles) as a function of δ. The broken line indicates the values of limiter configuration.

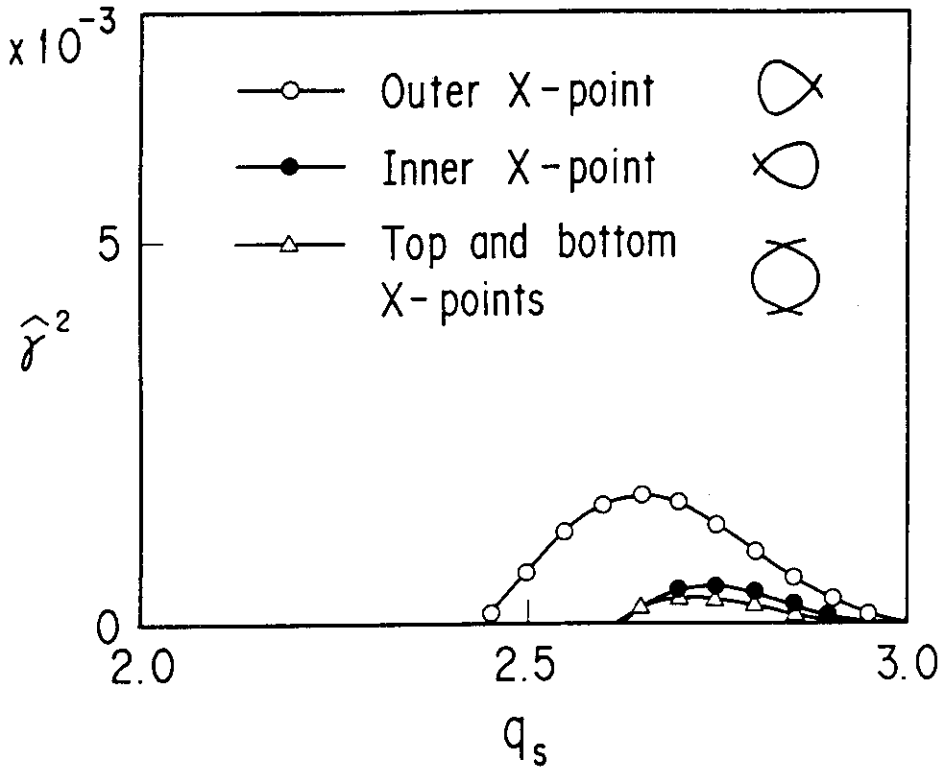

Fig. 4.11 Effect of the location of the X-point on external kink modes. The squared growth rate $\hat{\gamma}^2$ is plotted for three divertor configurations: with an outside X-point, an inside X-point and top-bottom X-points.

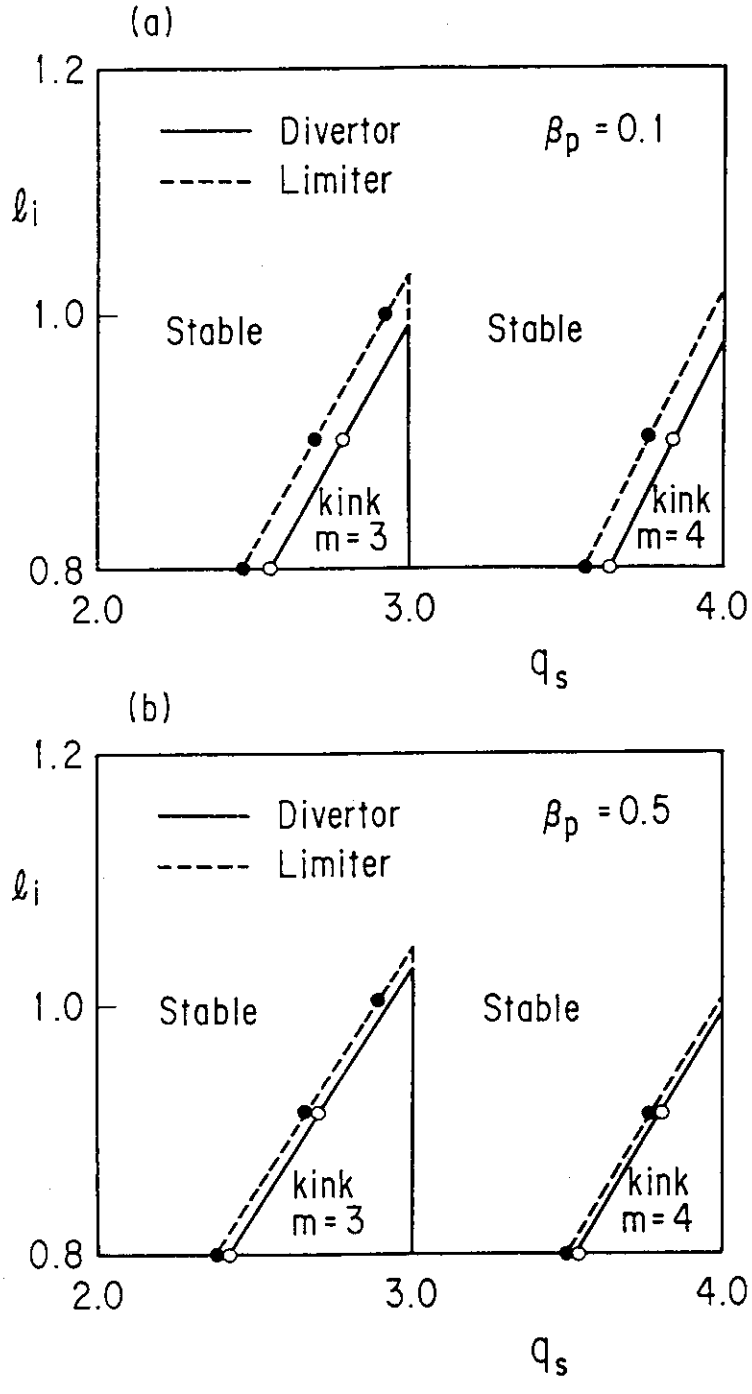

Fig. 4.12 Stability region in the $q_s - \ell_i$ space for m=3 and m=4 kink modes of limiter (dashed line) and divertor configurations (solid line) with a low beta, $\beta_p = 0.1$ (a) and $\beta_p = 0.5$ (b).

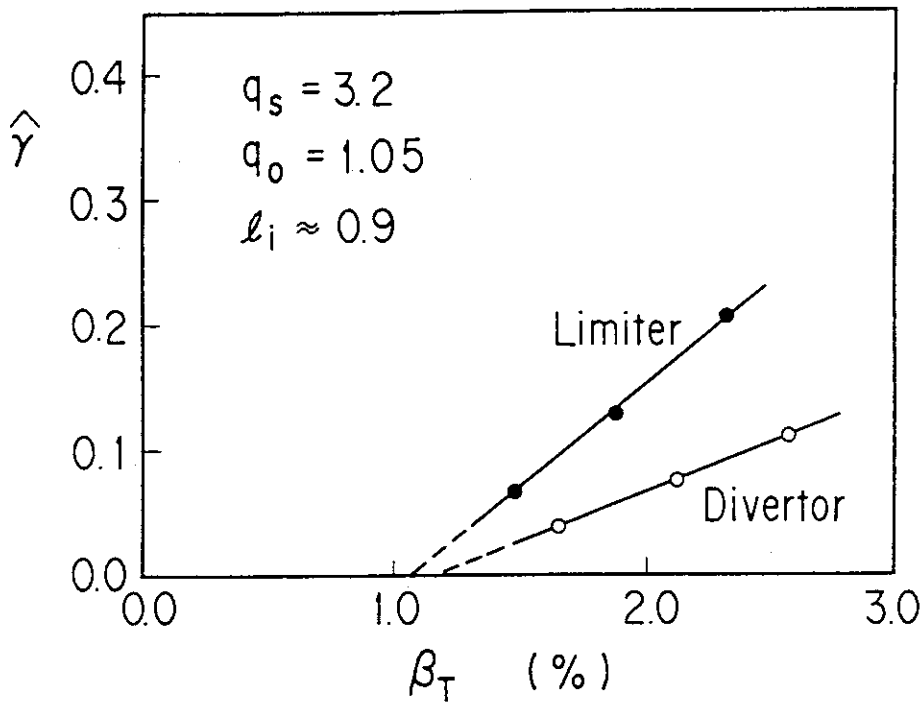

Fig. 4.13 Growth rate of kink modes in limiter and divertor configurations as a function of the toroidal beta for a plasma with $\ell_i = 0.9$ *and* $q_s = 3.2$.

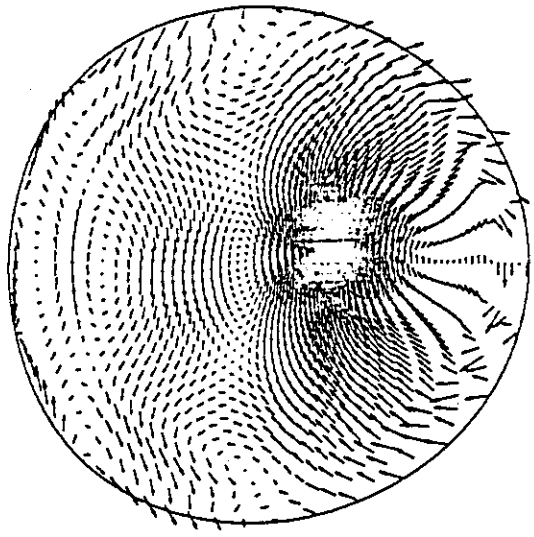

(a) LIMITER CONFIGURATION PLASMA

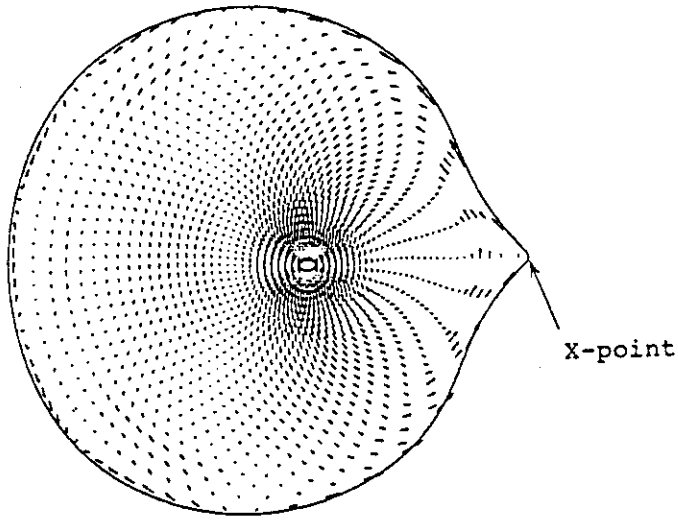

(b) DIVERTOR CONFIGURATION PLASMA

Fig. 4.14 Projection of the displacement vector on the poloidal plane for (a) the limiter configuration and (b) the divertor configuration of Fig. 4.13, with $\beta_t \approx 2.0\%$, $q_s = 3.2$ *and* $q_0 = 1.05$.

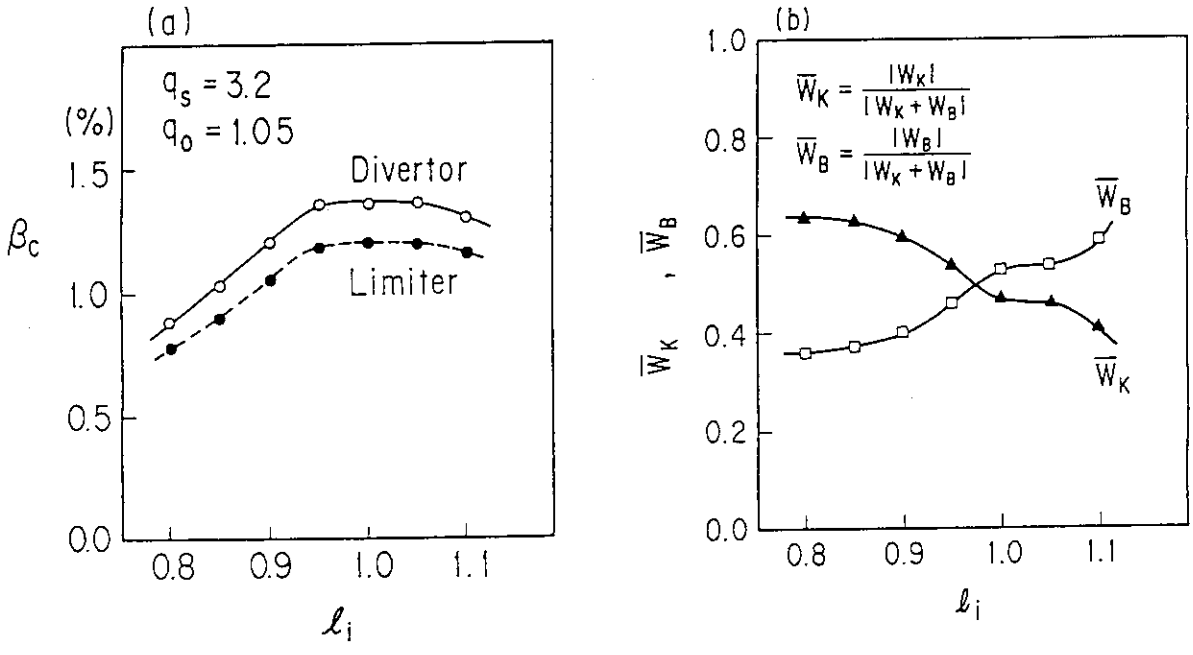

Fig. 4.15 Effect of the current profile on critical beta. (a) Critical beta as a function of the normalized internal inductance ℓ_i for limiter and divertor configurations with $q_s = 3.2$ and $q_0 = 1.05$. (b) Contribution of the current driven term $|W_K|$ and the pressure driven term $|W_B|$ to $|W_K + W_B|$ as a function of the internal inductance ℓ_i in the divertor configuration.

Chapter 5

Ballooning Stability near the Separatrix and ELMs in DIII-D

5.1 Introduction

An improved confinement during a phase of auxiliary heating, known as the H-mode[1,2], was observed in the divertor configuration, introduced in Section 1.5. In the H-mode experiments, the plasma edge region has been observed to sustain a large pressure gradient because of the improved edge confinement. The question naturally arises as to what, if there is any, is the limitation to the edge pressure gradient.

The infinite-n ballooning mode is the most unstable pressure-driven mode, as described in Section 2.5.3. Therefore, it is the most plausible candidate to explain the limit in the pressure gradient. The general stability diagram of the infinite-n ballooning mode in tokamaks with a positive shear $dq/d\psi \geq 0$ and a negative pressure gradient $dp/d\psi \leq 0$ has been given by Green and Chance [3], and it is represented schematically in Fig. 5.1. A characteristic of the stability of the ballooning mode in tokamaks is the existence of two stable regions (labelled (I) and (II) in Fig. 5.1). The remarkable point is that plasmas with sufficiently large values of the pressure gradient are stable in the second stable region ((II) in Fig. 5.1).

In DIII-D experiments in which H-modes were observed, the edge pressure gradient steadily increased until an edge MHD instability known as the edge localized mode (ELM) occurred. These ELMs degraded particle and energy confinement at the edge and

inhibited further increase in the plasma density. The pressure gradient limits observed in DIII-D experiments agreed with the theoretical limits given by the first stable region ((I) in Fig. 5.1) of the ballooning mode [4]. This lead to the hypothesis that giant ELMs in DIII-D are triggered by the ideal ballooning mode, and the edge plasma is always in the first stable region.

Bishop[5] has theoretically suggested that the edge pressure gradient in H-mode plasmas could be in the range where the plasma is in the second stable region ((II) in Fig. 5.1). This is more likely to occur when the plasma separatrix has an X-point pointing in the direction of increasing external magnetic field, i.e., the up-down X-point or the inner X-point. If the plasma is in the second stable region near the separatrix, it would be expected to have the higher limit of pressure gradient and to suppress the ELM.

In this chapter, first, we re-consider the suggestion of Bishop using the realistic DIII-D geometry. We demonstrate theoretically that the flux surfaces near the separatrix of DIII-D tokamak may be moved into the connection region ((C) in Fig. 5.1) between the first and second stability of the ideal ballooning modes by the plasma shaping, i.e., changing the elongation and the triangularity (defined in Fig.3.5). The edge flux surfaces are then predicted to have no limit to the sustainable pressure gradient. This prediction is compared with the experimentally observed disappearance of ELMs. Next, we obtain the accessible condition of the second stability near the plasma surface and clarify the possibility of suppressing the ELM and reaching high β plasma (β is the ratio of the volume averaged plasma pressure to the magnetic pressure). Here, we explore the wide parameter range in term of the aspect-ratio, the elongation, the triangularity, the safety factor and the shear.

In Section 5.2, the nature of the first and second stability of ballooning mode is described. In Section 5.3, the effect of plasma shaping on the edge ballooning stability

and the comparison with experiments in DIII-D is presented. In Section 5.4, the accessible condition for the the second stability is obtained. Finally, Section 5.5 is devoted to the conclusion.

5.2 First and Second Stability of Ballooning Modes

Since the infinite-n ballooning mode has the complicated and attractive characteristics, i.e., the first and second stability, this section summarizes briefly the ideal infinite-n ballooning theory and verifies the property of the ballooning mode.

5.2.1 First stability

At first, we re-consider the infinite-n ballooning equation, which determines the marginal pressure gradient of the ballooning mode. The ballooning equation can be written from Eq. (2.128) as follows,

$$\frac{1}{J}\frac{d}{dy}\left[\frac{1}{J}\frac{1}{|\nabla\psi|^2}\left\{1+\left(\frac{|\nabla\psi|^2}{B}I\right)^2\right\}\frac{d\hat{F}}{dy}\right]+\frac{2}{|\nabla\psi|}\frac{dp}{d\psi}\left(\kappa_n-\frac{|\nabla\psi|^2}{B}\kappa_s I\right)\hat{F}=0. \quad (5.\ 1)$$

where I is the integrated local shear ($=\int_{y_0}^{y}\frac{\partial\nu}{\partial\psi}dy$. Here, $\nu = B_t J/R$). $\hat{F}$ is the ballooning eigen function and κ_n and κ_s are the normal and geodesic components of the magnetic curvature, respectively. J is the Jacobian and y is the coordinate parallel to the magnetic field line. The flux function shape and the pressure and current profiles, which have been constructed by the equilibrium code, are used to determine the coefficients of Eq. (5. 1), i.e., I, $|\nabla\psi|$, B, κ_n and κ_s. The marginal pressure gradient, $dp/d\psi$, associated with a particular equilibrium, is obtained with the boundary condition that the radial displacement $\hat{F} = 0$ (at $y = \pm\infty$). The marginal pressure gradient is determined from two competitive terms. The first term in Eq. (5.1) contains the stabilizing effect of field line bending and shear. The second term contains the destabilizing effect that results from the combined effects of pressure gradient $dp/d\psi$ and magnetic curvature $\kappa_n - \frac{|\nabla\psi|^2}{B}\kappa_s I$.

The stability of the ballooning mode can be enhanced by the following effects. The first is the strengthening of the poloidal field on the outer side of the torus that results from the large outward shift of the magnetic surface characteristic of high-beta

equilibria or shaping of the poloidal cross section (the elongation and the triangularity). This shortens the distance along a magnetic field line within the region of unfavorable curvature. As shown by Eq. (5.1) the instability driving term associated with κ_n appears divided by $|\nabla\psi|$ ($= RB_p$). At the high beta plasma, $|\nabla\psi|$ is considerably enhanced in the region of unfavorable curvature ($\kappa_n < 0$), thus the instability drive of the normal curvature is depressed. The stabilizing term is also effectively enhanced by the increase in $(|\nabla\psi|^2 I/B)^2/|\nabla\psi|^2$ of the first term of Eq. (5.1). This is the so-called "shortening the connection length" stabilizing effect, i.e., shortening distance along a magnetic field line within the region of unfavorable curvature.

The second effect for the stability is the enhancement of the region of favorable magnetic curvature brought about by toroidal effects in configurations with small aspect ratio and large values of the safety factor q. This effect presents for all beta values. The normal component of the magnetic curvature κ_n acts as the destabilizing term in Eq. (5.1). The κ_n can be written as,

$$\kappa_n = -\frac{B_p^2}{rB^2} - \frac{\cos\chi}{R}\left(1 - \frac{r}{R}\cos\chi + \cdots\right). \tag{5. 2}$$

Here, χ is the poloidal angle and is taken to be zero at the outside of the torus. Keeping finite-aspect-ratio corrections to the first order for $\beta_p = O(1)$, we have

$$\kappa_n = -\frac{\cos\chi}{R_0} + \frac{r}{{R_0}^2}\left(\cos^2\chi - \frac{1}{q^2}\right). \tag{5. 3}$$

For sufficiently large q, the unfavorable contribution of the poloidal field is depressed and a net enhancement of the favorable region is obtained. Furthermore, by a toroidal modification of the curvature, a small aspect ratio (or a large r/R_0) makes the significant enhancement in the stability properties through κ_n.

5.2.2 Second stability

The existence of the second stability region was firstly demonstrated by Pogutse and Yurchenko [6]. Coppi et al. [7], using a sequence of flux conserving equilibria [8] with increasing pressure gradients, pointed out the possibility of reaching the second stable region ((II) in Fig.5.1) by raising the pressure gradient of the first region plasma ((I) in Fig.5.1) and passing through the unstable zone ((U) in Fig.5.1). The existence of the low shear connection region ((C) in Fig.5.1) between the first and second region was demonstrated numerically by Sugiyama and Mark [9].

A stable entrance into the second stability region can be explained as a combination of effects brought about by the high beta equilibrium that decrease the strength of the instability driving forces while enhancing the restoring force. The stabilizing effect of the high beta equilibrium can be explained by the local magnetic shear as follows.

The local magnetic shear, S_ν, plays an important role in ballooning stability theory, especially for the second stability. The dependence of Eq. (5.1) on S_ν occurs through the integrated local shear, I. We have

$$\begin{aligned} S_\nu &= -\frac{\mathbf{B}\times\nabla\psi}{|\nabla\psi|^2}\cdot\nabla\times\frac{\mathbf{B}\times\nabla\psi}{|\nabla\psi|^2} \\ &= -\mathbf{B}\cdot\nabla\left(\frac{\nabla\alpha\cdot\nabla\psi}{|\nabla\psi|^2}\right) = \mathbf{B}\cdot\nabla I \end{aligned} \tag{5. 4}$$

where $|\nabla\alpha|^2 = B^2/|\nabla\psi|^2 + |\nabla\psi|^2 I^2$. In low beta equilibria, the integrated local shear function I is positive in the bad curvature region, so that $\kappa_s I$ (> 0) in the second term of Eq. (5.1) acts as the destabilizing term. However, high-beta equilibria tend to decrease locally the value of the shear on the outside of the torus and this local shear can change sign so that, on the outer side, its sign is opposite to that of the average shear. In the case of $y_0 = 0$, the sign of $\kappa_s I$ becomes negative and it becomes the stabilizing term. To obtain the most unstable mode in such a high beta case, we may have to choose $y_0 \neq 0$, presumably in such a way that I is positive and a zero of I coincides with its local minimum. The minimum of I is by definition the point where

the local shear S_ν vanishes. By localizing the mode near the locus of vanishing local shear, we minimize the shear stabilization while obtaining a destabilizing contribution from the geodesic curvature $\kappa_s I$. However, if beta value is so high that the zero of the local shear has moved close to the region of favorable normal curvature ($\kappa_n > 0$), it may not be positive to construct an unstable mode. This is the second stability of the ballooning mode.

The reversal of the local shear is essential for the access to second stability, but other effects also facilitate to achieve a stable path from the first to the second stability regimes, i.e., the shortening of the connection length and the high q at the small aspect ratio. Especially, in a low aspect-ratio and high q tokamak plasma, geometric effects will decrease the local shear on the outside of the torus and thus facilitate to reverse the sign of the local shear.

5.3 Edge Ballooning Stability and ELM Behaviour in DIII-D

5.3.1 Introduction

In this section, first, we show that, by increasing the plasma elongation and triangularity in DIII-D divertor configuration when the edge safety factor is high, the edge plasma can be moved into the connection region between the first and second stable region of ideal ballooning modes. A sequence of experiments in DIII-D with controlled increase and decrease of the plasma elongation and triangularity showed that ELMs are suppressed when the plasma elongation is beyond 1.8, triangularity above 0.4, and when the normalized plasma edge shear (S_{95}/q^2) is less than 0.15. Here, S_{95} is $d\ell nq/d\ell n\tilde{\psi}$ at the flux surface of $\tilde{\psi} = 0.95$. Therefore, next, we compare the experimental results with the theoretical prediction. The correlation of the first and second stability with ELMs is discussed.

5.3.2. Effect of plasma shaping on edge ballooning stability in DIII-D

The purpose of the present section is to verify effects of plasma shaping for experimentally obtained equilibria in DIII-D. The equilibria used in the present section, as well as those in the next section for the comparison with experiments, are generated by utilizing the MHD equilibrium fitting code EFIT [10], with realistic DIII-D geometry, including the external coil locations.

The two unknown free functions, the plasma pressure $p(\psi)$ and the poloidal current $F(\psi)$, are obtained by parametrizing them linearly in terms of a number of parameters α_n and γ_n,

$$\frac{dp}{d\psi} = \sum_n \alpha_n \tilde{\psi}^n, \tag{5. 5}$$

$$F\frac{dF}{d\psi} = \sum_n \gamma_n \tilde{\psi}^n, \tag{5. 6}$$

where α_n and γ_n are chosen to fit the measured magnetic data in experiments. Here, $\tilde{\psi} = (\psi - \psi_{axis})/(\psi_{surf} - \psi_{axis})$ is the normalized poloidal flux. The safety factor on the magnetic axis q_0 was constrained to be 1.05, because of the observed sawtooth activity. (The sawtooth action at the center of the plasma is expected to regulate the q_0 value around 1.0 and, consequently, the ballooning stability property of the flux surfaces. However, varying the value of q_0 by ± 0.1 does not affect the edge plasma configuration to any noticeable extent.) The resulting edge q-profile and flux surfaces are then used in computing the marginally stable ballooning pressure gradient in the edge region.

To ascertain the ballooning stability predictions for these equilibria, the ballooning stability is analysed with two numerical codes, MBC [11] and CAMINO [12], wherein the equilibrium data are mapped into suitable flux co-ordinates, and the ideal infinite-n ballooning equation is solved on each flux surface. The full ballooning equation is solved in the exact toroidal geometry.

In these ballooning codes, since a flux coordinate system is used, the Jacobian $\sqrt{g}$ becomes infinite and the ballooning equation becomes singular at the X-point. This problem is avoided numerically by restricting the computational domain slightly away from the separatrix surface by setting $|\psi_{sep} - \psi_{bun}|/|\psi_{sep} - \psi_{axi}| < 0.001$, where ψ_{sep}, ψ_{bun} and ψ_{axi} are the poloidal flux at the separatrix, the plasma boundary and the magnetic axis.

To keep the calculation procedure of our previous work and to facilitate comparison with experimental measurements, we parameterize our results of computation in the same manner as Gohil et al. [4] and Lao et al. [13]. In Ref. [4], the measured pressure gradients near the separatrix before the giant ELMs are found to be close to the pressure gradient in the first ballooning stability limit. In Ref. [13], the normalized marginally stable ballooning pressure gradient $-(2\mu_0 R q^2 / B^2)(dp/dZ)$ near the separatrix is found to scale linearly with $\mu_B = S_{95}/{q_{95}}^2$ over a wide range $0.2 < \mu_B < 1.0$. Here, q_{95} is the safety factor and S_{95} is the global plasma shear $S = (dq/d\tilde{\psi})/q$ at

$(\psi - \psi_{axis}) = 0.95 \times (\psi_{sep} - \psi_{axis})$. Z is the vertical co-ordinate of the point on the flux surface, dp/dZ is related to $dp/d\psi$ through $dp/dZ = (dp/d\psi)(d\psi/dZ)$. This dependence is similar to the results for the circular tokamak [14], i.e. S is proportional to $\alpha = -(2\mu_0 Rq^2/B^2)(dp/dr))$ except in the low S region. This low shear region (or low μ_B region) is the region predicted by various authors to have no marginal pressure gradient and hence to provide a possibility for connection to the second stable region ((C) in Fig. 5.1).

In this study, therefore, we focus our attention on the ballooning stability near the separatrix for the plasma with low value of $\mu_B (< 0.15)$, lower than the values considered by the previous authors ($\mu_B > 0.2$) [4,13]. Except for plasma elongation and triangularity, these plasmas with low μ_B were further constrained to have otherwise identical DIII-D discharge parameters: major radius R = 1.69m, minor radius a = 0.65m, total plasma current I_p = 1MA, and toroidal field B_T = 2.1T.

Starting from an equilibrium with a moderate elongation, external shaping coil currents were programmed to change the plasma shape. The plasma shape is characterized by the elongation κ and the triangularity δ as shown in Fig. 3.5. For the DIII-D configuration with fixed total plasma current, μ_B is not a completely independent parameter. At high elongation, $\kappa \gtrsim 1.8$ and triangularity $\delta \gtrsim 0.4$, μ_B is observed to fall below 0.15. A typical single-null divertor equilibrium in this sequence is shown in Fig. 5.2. In this example $\kappa = 1.85$, $\delta = 0.5$, $q_{95} = 7.0$, $S_{95} = 5.8$, the equilibrium has a value of $\mu_B = 0.12$. Figure 5.3(a) shows the $q' - p'$ diagram (Shear−Pressure gradient diagram) at 95% of the enclosed poloidal flux for the case of moderate elongation, moderate triangularity, and low μ_B ($\kappa = 1.75$, $\delta = 0.25$ and $\mu_B = 0.14$). Figure 5.3(b) shows the $q' - p'$ diagram for the case of high elongation, high triangularity and low μ_B ($\kappa = 1.86$, $\delta = 0.5$ and $\mu_B = 0.12$). Here, $p' = dp/d\tilde{\psi}/\mu_0$, $q' = dq/d\tilde{\psi}$. These results were calculated from the CAMINO code [12]. In Fig. 5.3(a), the edge region is in the first stability regime, and it should not be possible to increase the pressure gradient beyond the first ballooning stable limit. In Fig. 5.3(b), the edge region is in the connection area between the first

and second ballooning stability region, and it might be possible to increase the pressure gradient beyond the nominal first ballooning stability limit given in Ref. [13]. Figure 5.4 shows the simulation results for various values of the elongation κ and triangularity δ, with parameters consistent with low μ_B ($0.11 < \mu_B < 0.16$). These results, which are calculated from the MBC code [11], are consistent with the results given in Fig. 5.3 obtained from the CAMINO code [12].

In the region where $\kappa \lesssim 1.8$ or $\delta \lesssim 0.4$, the edge region is in the first ballooning stability regime and the edge pressure gradient should be limited by the ideal ballooning stability. In the region where $\kappa \gtrsim 1.8$ or $\delta \gtrsim 0.4$, the edge region is in the connection area and no limit for the pressure gradient is found. We thus conclude that low μ_B or effectively low edge shear and high κ or effectively high q with large δ are essential for the edge region in DIII-D to be situated in the connection region (C). This is consistent with the analysis and model equilibrium predictions by the previous authors [5,6].

If giant ELMs are triggered by ballooning instabilities, the results of the present section suggest that in these DIII-D divertor configurations we should expect that giant ELMs are suppressed for plasmas with the high elongation ($\kappa \gtrsim 1.8$), high triangularity ($\delta \gtrsim 0.4$) and low μ_B ($I_p = 1\mathrm{MA}$, $B_T = 2.1\mathrm{T}$). In the next section, experimental results observed in DIII-D are compared with this prediction.

5.3.3. Comparison with experimental results in DIII-D

During DIII-D experiments, suppression of giant ELMs was observed when the plasma elongation was increased beyond 1.75 at low normalized shear μ_B ($= S_{95}/{q_{95}}^2$) during the H-mode phase ($I_p = 1.0MA$, $B_T = 2.1T$). These experiments were carried out for a fixed set of operating parameters (except for the plasma shaping parameters of elongation and triangularity) in a single-null divertor configuration, as given in Fig. 5.2. Figure 5.5 shows typical time traces of various plasma parameters for one of

these discharges, in which ELMs were suppressed. Up to a discharge time of 2.0 sec, the elongation κ was about 1.85, and giant ELMs were observed, which gave rise to large D_α/H_α spikes and caused rapid loss of density. At 2.0 sec, the elongation κ was increased to 1.9. These giant ELMs were suppressed, as evidenced by the disappearance of D_α/H_α spikes and the slight increase of density. Instead, grassy ELMs appeared. Nevertheless, the stored energy increased slightly, as indicated by the diamagnetic signal. At 2.5sec, as the elongation was reduced to 1.85, giant ELMs reappeared and the stored energy decreased. In this elongation scan, the plasma triangularity is programmed to increase together with the increase of the elongation, and X-point is pointed in the direction of increasing toroidal magnetic field. These observations indicate that plasma elongation and triangularity have a direct impact on the giant ELM behaviour in DIII-D.

To ascertain whether the change in the giant ELM behaviour was related to ballooning mode stability as described in the last section, we further reanalysed the ballooning stability for these elongation scan experiments using equilibria fitted to the experiments as discussed in Section 5.3.1. The resulting errors in plasma elongation and triangularity are limited to less than 3%, with q accurate to within 5% and $dp/d\psi$ accurate to within 10%. The analysis of the experimental data confirms the theoretical conjecture that the edge plasma enters the connection region between the first (I) and the second (II) ballooning stability regions. This is illustrated in Fig. 5.6, where the marginal ballooning stable pressure gradients and the measured pressure gradients near the separatrix at $\tilde{\psi} = 0.95$ for the discharges in this elongation scan are compared with each other. The marginally stable pressure gradients are computed using the ballooning stability code MBC[11] from the equilibria reconstructed using the magnetic data. The edge region quantities such as the plasma shape, q_{95} and $dq/d\tilde{\psi}$ are accurately determined by the external magnetic measurements [10]. The measured pressure gradients is obtained from Thomson scattering and interferometry data, and the ion pressure gradient that

we believe to be the same as the electron pressure. Generally, the results of measurements of edge T_i equal to those of T_e. Indeed, the electron-ion energy exchange is so large in these high density edge plasma that $T_e - T_i$ cannot be higher than 50eV.

In the low elongation ($\kappa < 1.82$) cases, giant ELMs are observed. The plasmas are predicted to be in the first ballooning stability regime. The measured pressure gradient is lower than, or up to, the marginally stable pressure gradient limits predicted by the ballooning mode code. The measured pressure gradients are slightly lower than the marginal values because these data are obtained between the giant ELMs and not just before the occurrence of ELMs. From previous measurements of the edge electron pressure on DIII-D [4], it has indeed been verified that the pressure gradient exceeds the ballooning mode limit just before the occurrence of the giant ELMs and reduces to a level below the ballooning mode limit by the action of the giant ELMs.

In the high elongation ($\kappa > 1.82$) case, giant ELMs disappear, and the plasma exhibits grassy ELM behaviour with reduced magnitude in edge pressure relaxation at a higher frequency. The corresponding diagram in triangularity and elongation space for this behaviour obtained from the experimental data is shown in Fig. 5.7. This is to be compared with Fig. 5.4 for the computationally predicted behaviour. The ballooning mode code indicates that no limit exists for the marginally stable pressure gradient when the pressure is increased in a flux conserving manner. Figure 5.8 shows the $q' - p'$ diagram at $\tilde{\psi} = 0.95$ for the high elongation ($\kappa = 1.92$) case, computed from the CAMINO code. The experimental data point, indicated by the symbol Δ, is clearly in the connection region. Since these conclusions are deduced from computationally reconstructed plasma equilibrium quantities, such as q and $dq/d\psi$, and experimentally measured quantities, such as electron temperature and density distributions, it is natural to study the effect of the uncertainties in the measurements on the conclusions. A spot check of the propagation of the error on the conclusions indicates that our conclusions would not change with a 10% change in the measured quantities. The stability criterion does not change within a 5% range of the flux surfaces. We thus conclude that as the

plasma elongation and triangularity increase, the plasma edge enters the connection region. Nevertheless, the edge pressure gradient does not increase. The grassy ELM behaviour, while allowing some edge pressure increase, may still retard the buildup of the edge pressure gradient. The grassy ELM behaviour may arise from somewhat different stability physics in the connection region.

5.3.4. Discussion and conclusion

In DIII-D single-null divertor configurations, depending on the elongation, triangularity and the normalized edge shear parameter $\mu_B = S_{95}/{q_{95}}^2$, the plasma edge can be situated in the first ballooning region (I) or the connection region (C) of the ideal MHD ballooning mode. The plasma edge is predicted to enter (C) for discharges with low μ_B (< 0.15) and high elongation κ ($\gtrsim 1.8$) with high triangularity δ ($\gtrsim 0.4$). In a sequence of DIII-D experiments, varying the plasma elongation and triangularity, giant ELMs, which are observed [4] regularly at lower elongation and triangularity, disappeared. These results indicate that the plasma with low S/q^2 is in the first stable region when the plasma elongation (and triangularity) is low, and in the connection region when the elongation (and triangularity) is high.

The theoretical prediction has been verified that the increase in the triangularity, the elongation and the safety factor makes it easier for the plasma edge to enter the region connecting the first and the second stable region of the ideal ballooning modes.

We also note that, in this sequence of experiments, the plasma elongation and triangularity are closely related through the programming of the shaping coil currents. As the plasma elongation increases, the triangularity increases and the safety factor at the plasma edge also increases because the total plasma current is kept fixed. Thus, the increase of the safety factor also acts for entering the connection region in addition to the shaping effect.

Experimentally, after suppression of giant ELMs by increasing the elongation and the triangularity, the grassy ELM was observed whereas the pressure gradient near the edge was not any higher than the value before giant ELM. This seems to be caused by the other factors. The nature of these fluctuations are left for a future study.

5.4 Access to Second Stability near the Separatrix

5.4.1 Introduction

In the previous section, the effect of shaping on the access to the second stable region was studied in DIII-D geometry. This section describes the accessible condition for second stability over a wide range of shaping, safety factor q and global shear S, and discusses the mechanism of the access to the second stable region near the plasma surface.

Studies about the second stability of the ballooning mode were carried out from a stand point of high β plasma. The infinite-n ballooning mode is the major obstacle to obtain the high β plasma. Here, β is the ratio of the volume averaged plasma pressure to the magnetic pressure. Troyon et al. [15] evaluated the maximum value of β in a tokamak plasma and showed the scaling of the beta limit, β_t, to be approximately given by $\beta_t(\%) = gI_p(MA)/a(m)B_t(T)$, where I_p, a and B_t are the total plasma current, the minor radius and the toroidal magnetic field strength at the plasma cross-section, respectively. The factor g takes the value 3 to 4 for an equilibrium with a moderately deformed cross-section.

One of the methods to enhance the value of β is seeking access to the second stable region of the ballooning modes[3,7,16-18]. Direct access to such stable equilibria without passing through an unstable region has been demonstrated for indented shape of the cross-section[19,20]. It has been also found for circular cross-sections with $q_0 > 1$ [9,21-25], using the stabilizing effects of a local shear near the plasma center [26]. Here, q_0 denotes the safety factor at the magnetic axis. On the other hand, access to the second stability in the whole plasma region has been demonstrated by using a high shear current profile with high $q_0(> 2)$ in a low aspect ratio plasma [27]. In these previous studies, the improvement of the beta limit, mainly in the plasma center, were carried out by the increase in the high safety factor on the magnetic axis ($q_0 > 1$) or the strong shaping

of the plasma. This section, however, discusses the ballooning stability near the plasma surface, which is related to the ELM instability, in term of the safety factor and the global shear.

5.4.2 Numerical procedure for the ballooning stability Analysis

The property of the second stability is numerically studied as follows. The ideal MHD beta limit due to the infinite-n ballooning modes is obtained by optimizing the plasma pressure for a given profile of the safety factor q ($= \Phi'/\Psi'$, defined in Eq.(2.30)). Here, Φ and Ψ are the toroidal flux and the poloidal flux, respectively. The infinite-n ballooning mode equation Eq. (5.1) and the Grad-Shafranov equation are solved iteratively to obtain the pressure of a marginally stable state (a zero growth rate) in a flux conserving manner holding the q profile fixed in the whole plasma region [28]. The profile of the safety factor is given by the following profile of the toroidal current density at an initial iteration stage:

$$J_\phi = -R\frac{dp}{d\psi} - \frac{1}{\mu_0 R}F\frac{dF}{d\psi}, \tag{5. 7}$$

$$\frac{dp}{d\psi} = \frac{1}{1+\sigma}\frac{J_0}{R_0}\beta_p\{(1-\tilde{\psi})^{j1})^{j2} + \sigma\}, \tag{5. 8}$$

$$F\frac{dF}{d\psi} = R_0^2\left(\frac{1}{\beta_p} - 1\right)\mu_o\frac{dp}{d\psi}, \tag{5. 9}$$

where $\tilde{\psi}$ is the normalized poloidal flux with $0 < \tilde{\psi} < 1$ ($\tilde{\psi} = 0$ at the magnetic axis and $\tilde{\psi} = 1$ at the plasma surface). σ is an amount of the pedestal component of J_ϕ. R_0, J_0 and β_p are the major radius of a plasma center, the toroidal current density at the magnetic axis and the initial poloidal beta value, respectively. Profile parameters $j1$, $j2$ and σ are used to determine the pressure profile and current profile in the initial stage.

During the iteration of optimization, $dp/d\psi$ is adjusted to the marginal value of ballooning modes and a toroidal field function F is calculated by the flux conserving

scheme such that the q-profile is held fixed. As the iteration proceeds, the pressure profile is optimized, i.e., the pressure gradient for each flux surface reaches the limit of the ballooning mode, and β increases. If the pressure gradients on all flux surface is limited by the first boundary of the ballooning mode, β reaches the saturated value, as shown in Fig. 5.9(a), which is the beta limit, while, if some flux surfaces exist in the connection or second stable region of the ballooning mode, β can increase indefinitely, as shown in Fig. 5.9(a). In the following calculation, we choose $\beta_p = 0.1$ in the initial stage. The safety factor at the magnetic axis is fixed to 1.05, so that the plasma is stable to the interchange instabilities.

5.4.3. Possibility of access to second stability

The effect of the global shear near the plasma surface, S_{95}, on the accessibility to the second stability is studied by varying the q-profiles, where $S = (2V/q)(dq/dV)$ and $V(\psi)$ is the volume within the magnetic surface and the subscript 95 denotes the value at 95% of the enclosed poloidal flux. We choose two types of current profile in a initial low β state, whose parameters are listed in Table 5.1. Figure 5.10 shows radial profiles of the toroidal current $< j_\phi/R >$, the safety factor q, and the global shear S for both cases in a initial state. For Case 1, both the safety factor and shear are high near the plasma surface (Fig. 5.10(a)). For Case 2 (Fig. 5.10(b)), even though the safety factor at 95% of the enclosed poloidal flux q_{95} is almost equal to that of Case 1, the shear near the plasma surface is smaller than that of Case 1 because of the effect of the pedestal current ($\sigma = 0.2$). From these initial states, the optimized beta value is obtained by the iteration in the equilibrium and the marginal stability calculations of the ballooning modes. The normalized pressure gradient α after the optimization is shown in Fig. 5.11(a) and (b) for Case 1 and Case 2, respectively, where

$$\alpha = -(\mu_0/2\pi^2)(V/2\pi^2 R_0)^{1/2}(dV/d\psi)(dp/d\psi). \tag{5.10}$$

The broken line shows the pressure gradient which is marginally stable to the ballooning modes. For Case 1, the beta saturates at the final iteration stage and α is almost marginal everywhere in a plasma (Fig. 5.11(a)). On the other hand, for Case 2, the marginal pressure gradient is larger than that of the equilibrium during the optimization process and the pressure gradient increases indefinitely near the plasma surface as the iteration proceeds. (Fig. 5.11(b)). It means that the plasma near the plasma surface ($\tilde{\psi} > 0.75$) enters the second stable region without passing through an unstable regime.

Table 5.1 Profile parameter of two type plasmas

	Case 1	Case 2
q_{95}	3.81	3.88
q_0	1.05	1.05
S_{95}	2.5	1.1
$j1$	1.0	1.0
$j2$	1.45	4.0
σ	0.0	0.2
A	3.0	3.0

In the previous papers [9,21-23,26], access to the second stable region in the circular plasma was obtained at low global shear around the magnetic axis. Near the plasma surface, however, the plasma can also access the second stability regime. This mechanism can be explained by the local shear S_ν. In a circular, low beta equilibrium, the local shear can be written by the global shear $r(dq/dr)$ and the safety factor q [27],

$$S_\nu(\chi = 0) \propto r\frac{dq}{d\psi}(\psi)\frac{1 - r/4R_0}{1 + r/R_0} - \frac{r}{R_0}q(\psi)\frac{1.25}{(1 + r/R_0)^2} \tag{5.11}$$

where R and r are the major radius and the minor radius on each flux surface, respectively. χ is a poloidal angle which is zero at the mid-plane on the outer side of torus. The low local shear region in low beta plasma would have a high accessibility on the corresponding flux surface because it produces a negative local shear in high beta plasma. From Eq.(5.11), the low local shear is made by the decrease of global

shear or the increase in the safety factor. In previous studies [9,21-23,26] the second stable region was obtained by the low global shear ($S \sim 0$) and the slightly high safety factor ($q_0 > 1.0$). Another approach, considered here, is to decrease the global shear near the plasma surface, though the global shear can not be reduced to the low value near the plasma axis. Figure 5.12 shows the contour map of the local shear for Case 1 (Fig. 5.12(a,c)) and for Case 2 (Fig. 5.12(b,d)), where the broken lines correspond to $S_\nu = const.$ and the bold broken lines indicate the zero of normal curvature ($\kappa_n = 0$). In low beta plasma, the local shear in Case 1 is monotonically increasing as a function of minor radius on the outer edge of torus (Fig. 5.12(a)). But in Case 2, the local shear decreases near the plasma surface due to the low global shear (Fig. 5.12(b)). As the beta increases for the plasma with the normal q-profile (Case 1) which has a high shear near the plasma surface, the local shear will reverse near the magnetic axis (the shaded region in Fig. 5.12(c)). For Case 2, the negative local shear appears near the plasma surface and, by the further increase in the beta value, the negative local shear covers the bad curvature region ($\kappa_n < 0$) due to an enough low global shear and high safety factor, as shown in Fig. 5.12(d).

The dependence of the aspect ratio A, the safety factor q_{95} and the global shear at the plasma surface S_{95} on the access to second stability is shown in Fig. 5.13, where the plasma can enter the second stability in the region below the each line. The accessibility is high in the lower aspect ratio, higher q_{95} and lower S_{95}, as is seen in Eq.(5.11). One method of making the low shear near the plasma surface is to produce the pedestal current profile. Figure 5.14 shows the dependence of the pedestal current profile on the accessibility to the second stable region. Although σ is the amount of pedestal in the initial stage ($\beta_p = 0.1$), the surface-averaged parallel current, $j_\parallel$ ($=< \mathbf{J}\cdot\mathbf{B} > / < B_T >$), has the almost same amount of pedestal after the iteration of the beta optimization. In low q_{95} case ($\lesssim 6$), the low shear near the plasma surface is necessary so that the large amount of pedestal is required, while, in high q_{95} case (~ 10), the pedestal structure is not necessary, because the plasma can access the second stability even in the high

global shear S_{95} (Fig. 5.13). The accessibility does not depend significantly on the elongation κ, but the triangularity δ enhances the accessibility, as shown in Fig. 5.15. The small triangularity plasma is acceptable for a future tokamak reactor.

In Fig. 5.16, an example is shown for the equilibrium in the second stable region with $A = 3$, $\kappa = 1.6$, $\delta = 0.2$, $q_{95} = 4.3$ and $S_{95} = 1.8$. In this case, the beta value is $\beta_t = 7.0\%$ ($g = 6.5$) and the flux surface in the second stability is $0.7 < \tilde{\psi} < 1.0$. Figure 5.16(a) to (c) show the profiles of the plasma pressure p the safety factor q and the toroidal current j_ϕ on the horizontal midplane, respectively. In Fig. 5.16(c), the surface-averaged parallel current $j_\parallel$ is plotted as a broken line. Although the toroidal current density j_ϕ shows a skin-like profile due to the Pfirsch-Schlüter current, the surface-averaged parallel current density profile remains almost the same form as in the low beta equilibrium.

Increasing the plasma pressure, the negative toroidal plasma current appears in the inner side of the torus due to the Pfirsch-Schlüter effect for $\beta_t \gtrsim 4.5\%$ ($g \gtrsim 4.5$). The appearance of this negative current can be suppressed by increasing the pedestal σ or the triangularity δ. For a large pedestal current ($\sigma = 0.3$) the negative current does not appear up to $\beta_t \sim 7.5\%$ ($g \sim 5.5$). Also, in a D-shaped plasma with a large triangularity δ of 0.5 and κ of 1.6, it does not appear up to $\beta_t \sim 5.4\%$ ($g \sim 5.3$) for the same pedestal current ($\sigma = 0.2$) as in Fig. 5.16. But the elongation is not effective for the suppression of the negative current.

5.4.4. Discussion

We have shown that it is possible for a tokamak plasma with a conventional shape to enter the second stable region of ballooning modes near the plasma surface without the effect of X-point. The essential point of this scheme is to decrease the global shear and to increase q near the plasma surface. A pedestal current profile is one of the

most effective methods to reduce the global shear near the plasma surface. In the H-mode plasma, a pedestal current is produced due to the increase in the edge electron temperature even in a limiter configuration [29,30]. Therefore, H-mode plasmas with high edge temperature and high q may enter the second stable region near the plasma surface. This effect is enhanced by shaping the plasma, especially, by increasing the triangularity.

To obtain the high β plasma, although this scenario is a partial access to the second stability, it has the advantage over scenarios using the high q_0 region or bean shaped cross-section because of simplifying the control of the safety factor and of reducing requirements on poloidal coil system.

Good accessibility is obtained at high q. From the engineering point of view, to make a high-q plasma, a high toroidal field is required for a future tokamak with high plasma current. However, a plasma with high current (or low q_J) can be made after the optimization of the beta value keeping q $(= \Phi'/\Psi')$ constant. Here, q_J is the current safety factor defined as follows,

$$q_J = 5a^2(m^2)B_T(T)(1+\kappa^2)/2R_0(m)I_P(MA). \tag{5.12}$$

q_J is the realistic safety factor used in the plasma operation, and a low q_J represents a high ratio of plasma current to toroidal field. Figure 5.17 shows the evolution of β_t, I_p and q_J during the iteration. The results are obtained for Case 2 of Fig. 5.10-5.12. q_{95} of 3.88 corresponds to q_J of 3.54 in low β_t. After optimization of the beta value, I_p increases and q_J decreases to 2.4 at $\beta_t = 4.2$, though the q_{95} is kept constant at 3.88. This value of q_J is acceptable for a future tokamak.

The pedestal current profile would enhance the current-driven instabilities, i.e., kink modes. The beta limit may be restricted by the stability of external kink modes. However, the external kink mode could be expected to be stabilized by a conducting shell placed closely to the plasma surface, so that further investigations for low n-mode stability are required to obtain the optimum safety factor profile for a high beta tokamak.

5.5 Summary

Stability against ideal infinite n ballooning modes near the separatrix has been analyzed in H-mode plasmas of DIII-D, and the stabilization of the ballooning modes has been demonstrated for suppressing giant ELMs.

No limit for ballooning stability near the separatrix is obtained by increasing the plasma elongation ($\kappa > 1.8$) and triangularity ($\delta > 0.4$) for the plasma with small values of ($\mu_B < 0.15$) in DIII-D divertor configuration. The plasma equilibrium near the separatrix surface with low μ_B can enter the connection region between the first and second stable region of the ballooning mode.

Experimentally, giant ELMs disappear in these shaped plasmas with low μ_B. Theoretical analysis of experimental data indicates the hypothesis that giant ELMs in DIII-D is triggered by the ideal ballooning mode and giant ELMs can be suppressed when the plasma is in the connection region between the first and the second stable region.

This chapter also systematically clarifies the accessibility condition to the second stability in terms of the safety factor, the global shear, the shaping and the aspect ratio. It is shown that the plasma with a high safety factor and a low shear near the plasma surface can access the second stable regime, even if the safety factor at the magnetic axis is low (< 1). A pedestal current profile reduces the global shear near the plasma surface, and improves the accessibility. A low aspect ratio and positive triangularity ($\delta > 0$) can also facilitate access to the second stable region.

References

[1] M. Keilhacker: Plasma Phys. and Contr. Fusion **29** 10A (1987) 1401.

[2] F. Wagner, et al.: J.Nucl.Mater. **121** (1984) 103.

[3] J.W. Greene, M.S. Chance: Nucl.Fusion **21** (1981) 453. Nucl.Fusion **25** (1985) 1611.

[4] P. Gohil, et al.: Phys. Rev. Lett. **61** (1988) 1603.

[5] C.M. Bishop: Nucl.Fusion **26** (1986) 1063.

[6] O.P.Pogutse and E.I.Yurchenko: Sov. J. Plasma Phys. **5** (1980) 441.

[7] B.Coppi, A.Ferreira and J.J.Ramos: Phys. Rev. Lett. **A44** (1980) 990.

[8] J.F. Clarke and D.J. Sigmar: Phys. Lett. **38** (1977) 70.

[9] L.Sugiyama and J.W.-K.Mark: Phys. Lett. **84** (1981) 123.

[10] L.L. Lao, H. St.John, R.D. Stambaugh, A.G. Kellman, W. Pfeiffer:

[11] R.W. Moore: MBC: A Ballooning Stability Code for Finite Toroidal Mode Number, Rep. GA-A16243, General Atomics, San Diego, CA (1981).

[12] M.S. Chance: in theory of Fusion Plasmas (Proc. workshop Varenna, 1987), Editrice compositori, Bologna (1987) 87.

[13] L.L. Lao, E.J. Strait, T.S. Taylor, et al., Plasma Phys. Controll. Fusion **31** (1989) 509.

[14] J.W. Connor, R.J. Hastie, J.B. Taylor: Phys. Rev. Lett. **40** (1978) 396.

[15] F.Troyon, R.Gruber, H.Saurenmann, S.Semenzato and S.Succi: Plasma Phys. **26** (1984) 209.

[16] D.Lotz and J.Nuhrenberg: Phys. Lett. **A68** (1978) 49.

[17] C.Mercier: in Plasma Physics and Controlled Nuclear Fusion Research 1978 (Proc. 7th Int. Conf. Innsbruck, 1978), Vol.1, IAEA, Vienna (1979) 701.

[18] H.R.Strauss, W.Park, D.A.Monticello, et al.: Nucl.Fusion **20** (1980) 638.

[19] M.S.Chance, S.C.Jardin and T.H.Stix: Phys. Rev. Lett. **51** (1983) 1963.

[20] K.Yamazaki, H.Naitou, T.Amano, et al.: in Plasma Physics and Controlled Nuclear Fusion Research 1986 (Proc. 11th Int. Conf. Kyoto, 1986), Vol.2, IAEA, Vienna (1987) 27.

[21] A.Sykes and M.F.Turner: in Controlled Fusion and Plasma Physics (Proc. 9th Europ. Conf. Oxford, 1979), Vol.1, (1979) 161.

[22] T.Antonsen, B.Basu, B.Coppi, et al.: in Plasma Physics and Controlled Nuclear Fusion Research 1980 (Proc. 8th Int. Conf. Brussels, 1980), Vol.1, IAEA, Vienna (1981) 83.

[23] B.Coppi, G.B.Crew and J.J.Ramos: Comments Plasma Phys. Controlled Fusion **6** (1981) 109.

[24] T.Takeda, T.Tsunematsu, T.Tuda, et al.: in Plasma Physics and Controlled Nuclear Fusion Research 1982 (Proc. 9th Int. Conf. Baltimore, 1982), Vol.3, IAEA, Vienna (1983) 23.

[25] A.M.M.Todd, M.Phillips, M.Chance, J.Manickam and N.Pomphrey: in Plasma Physics and Controlled Nuclear Fusion Research 1986 (Proc. 11th Int. Conf. Kyoto, 1986), Vol.2, IAEA, Vienna (1987) 37.

[26] S.Seki, T.Tsunematsu, M.Azumi and T.Nemoto: Nucl. Fusion **27** (1987) 330.

[27] M.J.Gerver, J.Kesner and J.J.Ramos: Phys. Fluids **31** (1988) 2674.

[28] M.Azumi, T.Takizuka, T.Tsunematsu, et al.: in Plasma Physics (Proc. 1984 Int.Conf.Lausanne), Vol.9f, Part I (1985) 375.

[29] K.Hoshino, T.Yamamoto, N.Suzuki, et al.: Nucl. Fusion **28** (1988) 301.

[30] K.Odajima, A.Funahashi, K.Hoshino, et al.: in Plasma Physics and Controlled Nuclear Fusion Research 1986 (Proc. 11th Int. Conf. Kyoto, 1986), Vol.1, IAEA, Vienna (1987) 151.

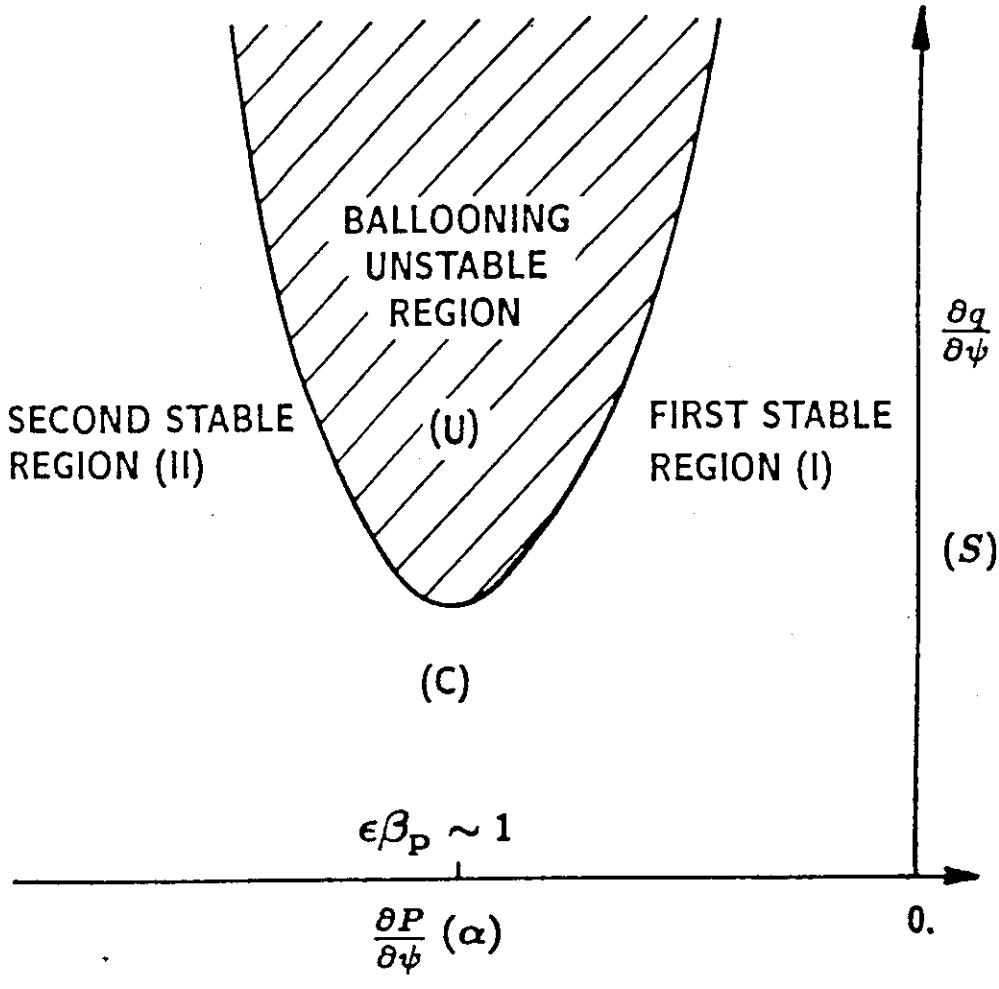

Fig. 5.1 Schematic diagram of the tokamak ballooning stability.

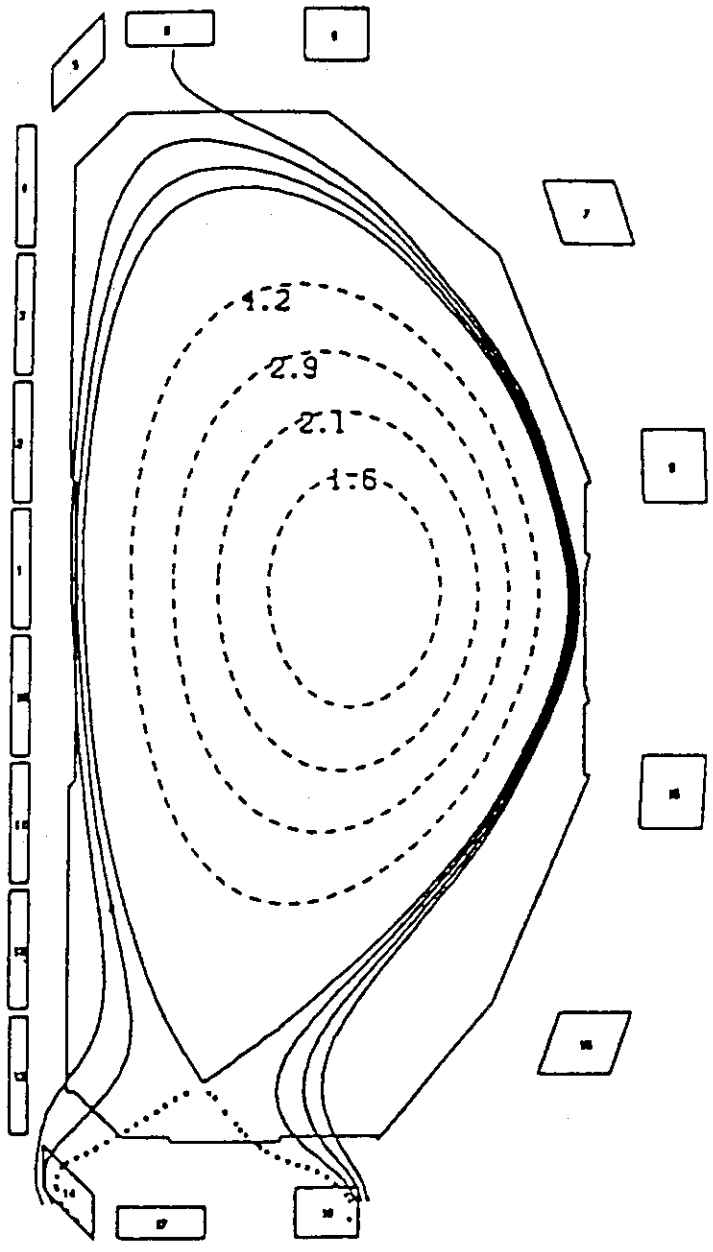

Fig. 5.2 Equilibrium flux surfaces for a single-null divertor configuration in DIII-D. Elongation κ=1.85, triangularity δ=0.5, major radius $R = 1.69m$, minor radius $a = 0.65m$, $q_{95} = 7.0$ and shear $S_{95} = 5.8$.

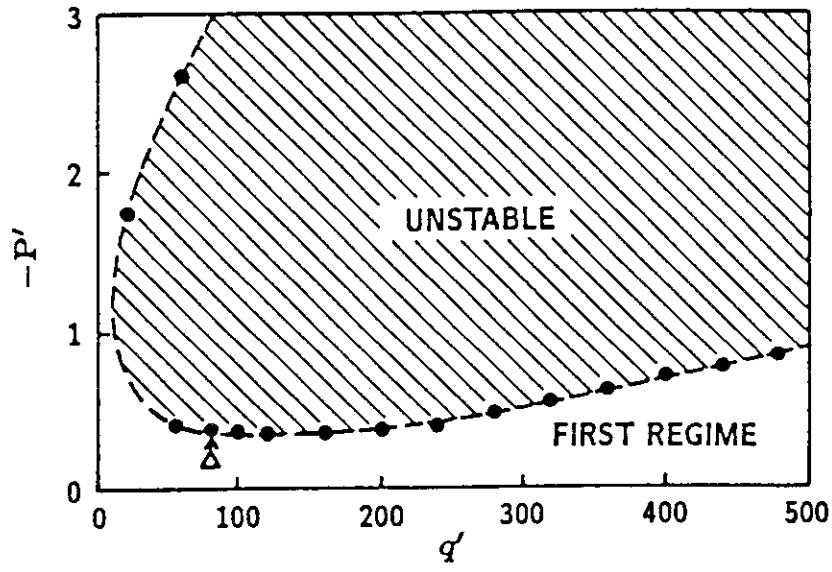

Fig. 5.3a The $q'-p'$ diagrams on the flux surface $\tilde{\psi}$=0.95; κ=1.75, δ=0.25 and μ_B=0.14. The equilibrium is in the first stability regime (triangle). The increase of p' (arrow) is limited by the unstable region.

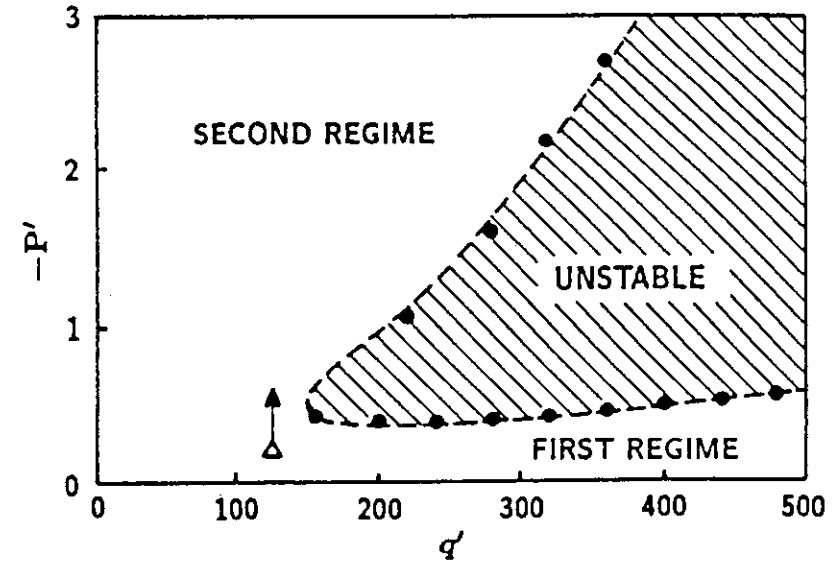

Fig. 5.3b The $q'-p'$ diagrams on the flux surface $\tilde{\psi}$=0.95; κ=1.86, δ=0.5 and μ_B=0.12. The equilibrium is in the connection regime between the first and the second stability areas (triangle). The increase of p' (arrow) is not limited by the unstable region.

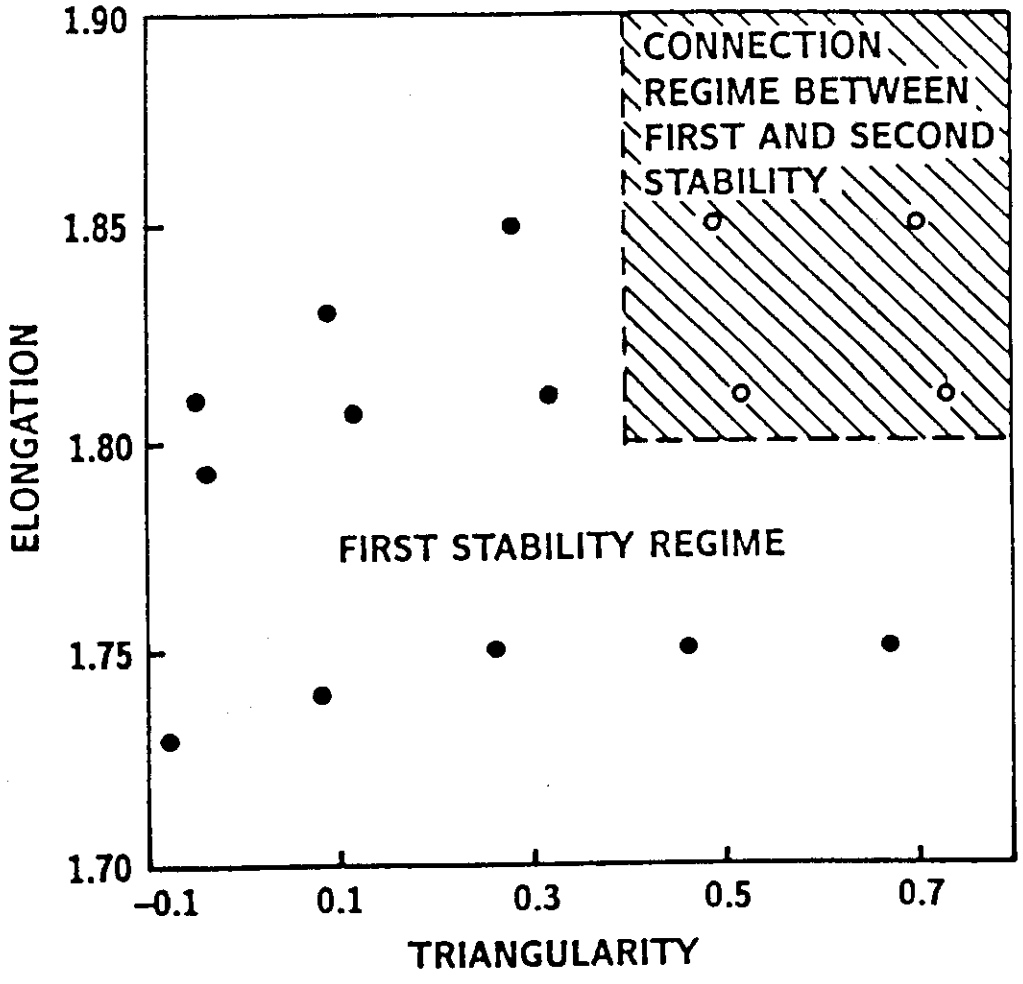

Fig. 5.4 Dependence of edge ballooning stability on elongation κ and triangularity δ at low μ_B ($0.11 < \mu_B < 0.16$). The edge enters the connection region at high elongation ($\kappa \geq 1.8$) and high triangularity ($\delta \geq 0.4$).

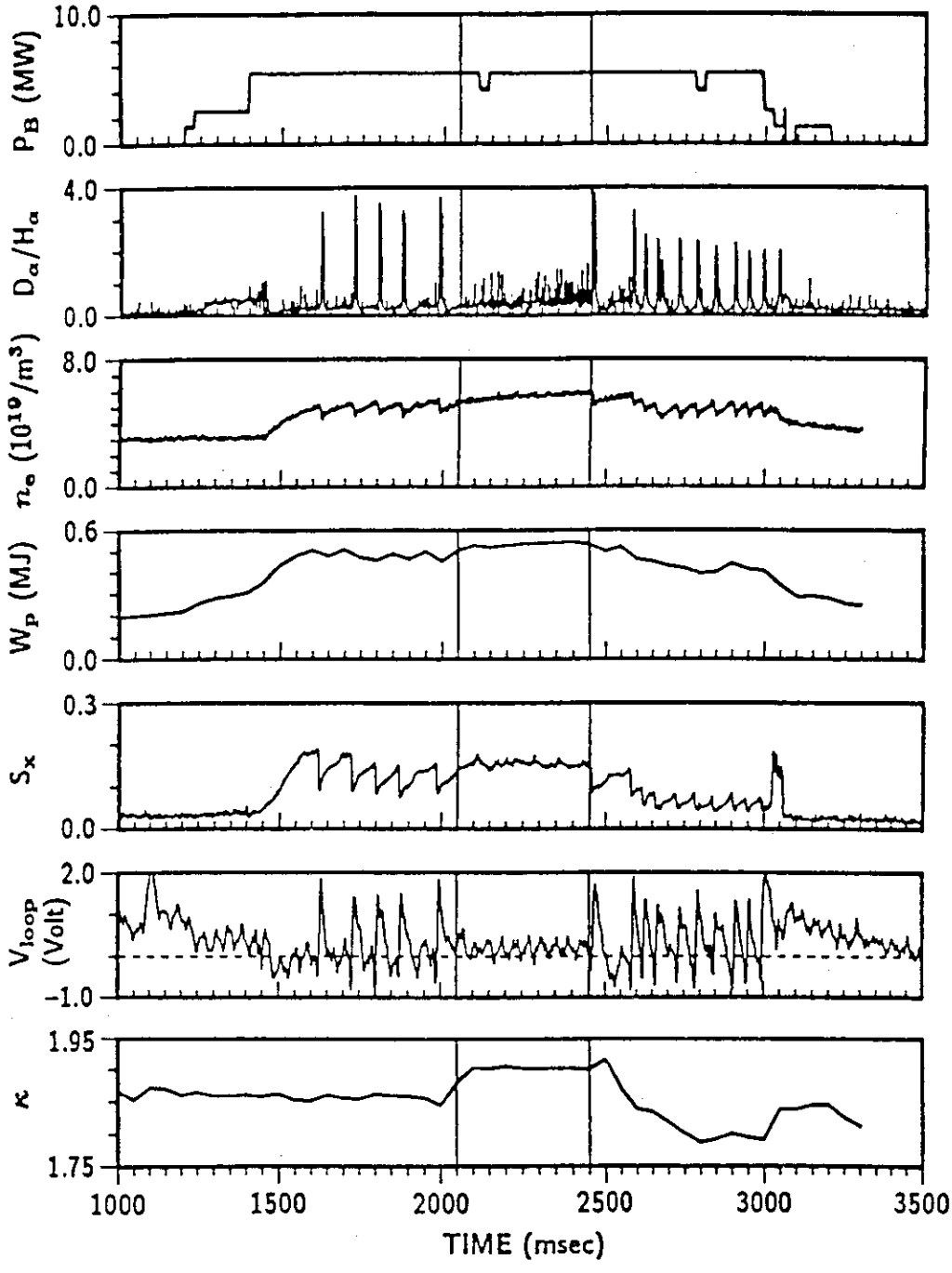

Fig. 5.5 Time traces of various plasma parameters for a elongation scan during an H-mode discharge 56421, $I_p = 1.0MA$, $B_T = 2.1T$; neutral beam injection power P_B, D_α/H_α radiation in the divertor region, line-averaged electron density n_e, plasma stored energy W_p, edge soft X-ray emission S_X, loop voltage V_{loop} and elongation κ.

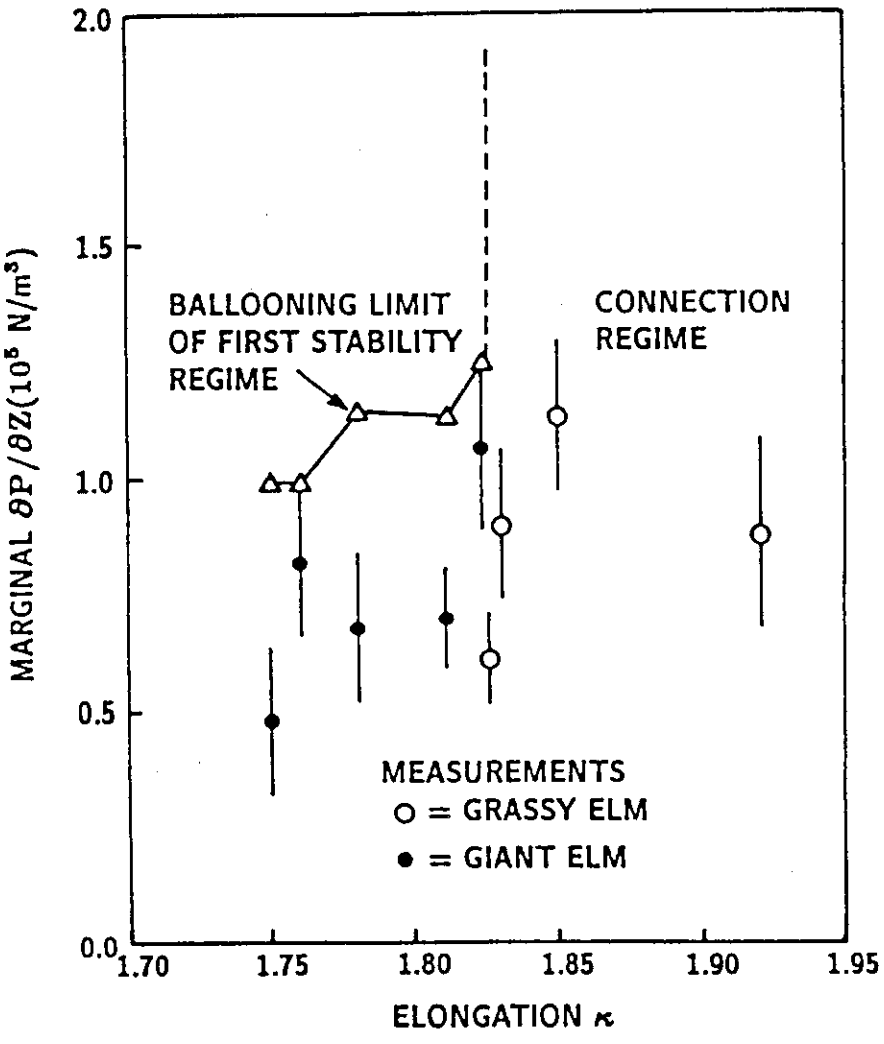

Fig. 5.6 Comparison of measured pressure gradients and computed marginally stable ballooning pressure gradients near the separatrix for various values of elongation, $I_p = 1.0MA$ and $B_T = 2.1T$. At the high elongation ($\kappa > 1.82$), giant ELMs disappear (open circle) and the flux surfaces near the separatrix enter the connection regime between the first and the second ballooning stability region.

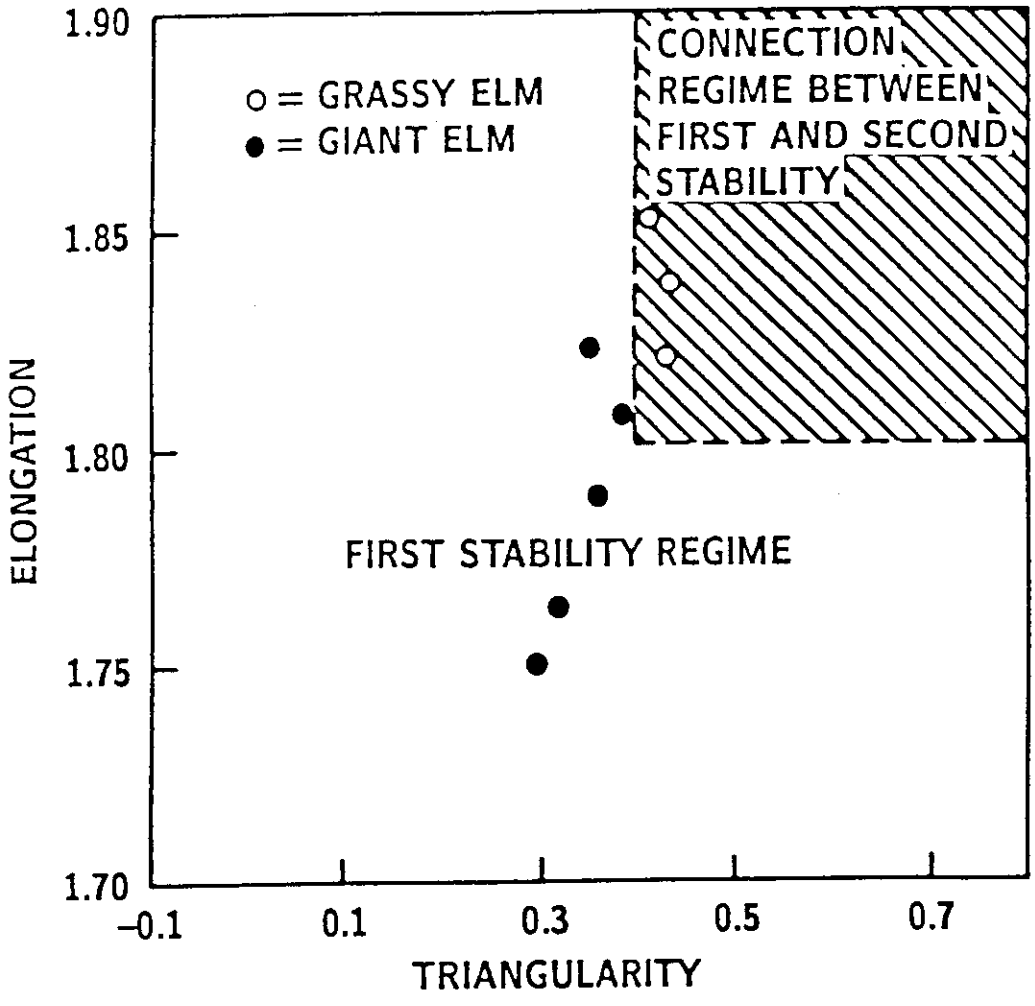

Fig. 5.7 Dependence of the observed edge MHD activity on elongation κ and triangularity δ at low μ_B. The computed ballooning mode stability behaviour corresponding to that given in Fig. 5.4 is also shown.

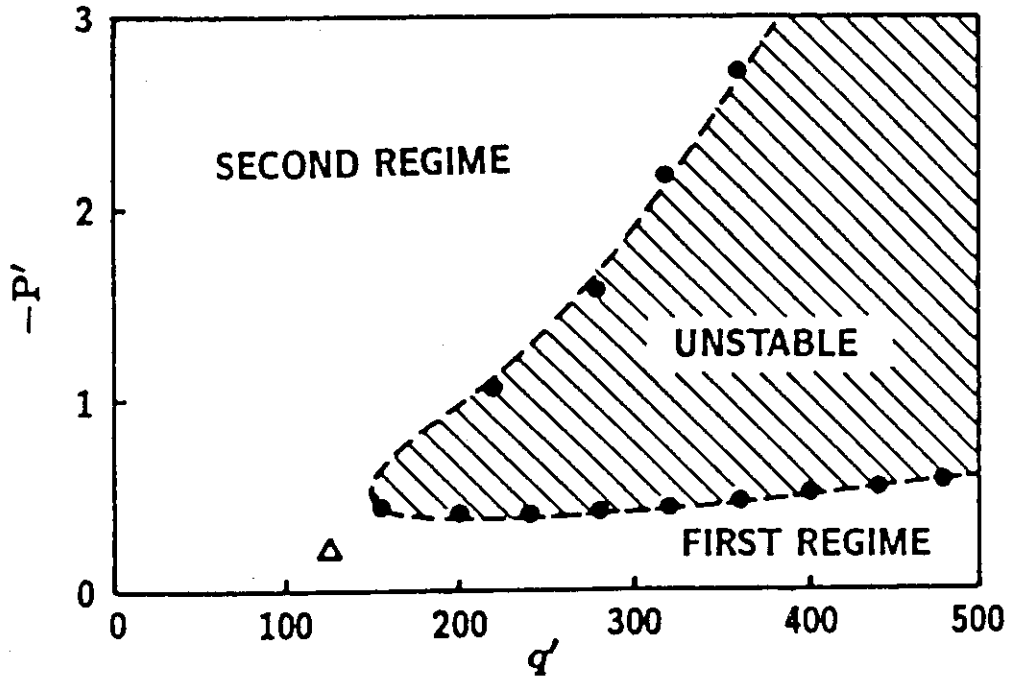

Fig. 5.8 The $q'-p'$ diagram at the flux surface $\tilde{\psi}$=0.95. The equilibrium is in the connection region between the first and the second ballooning stability region, κ=1.92, δ=0.45 and μ_B =0.11.

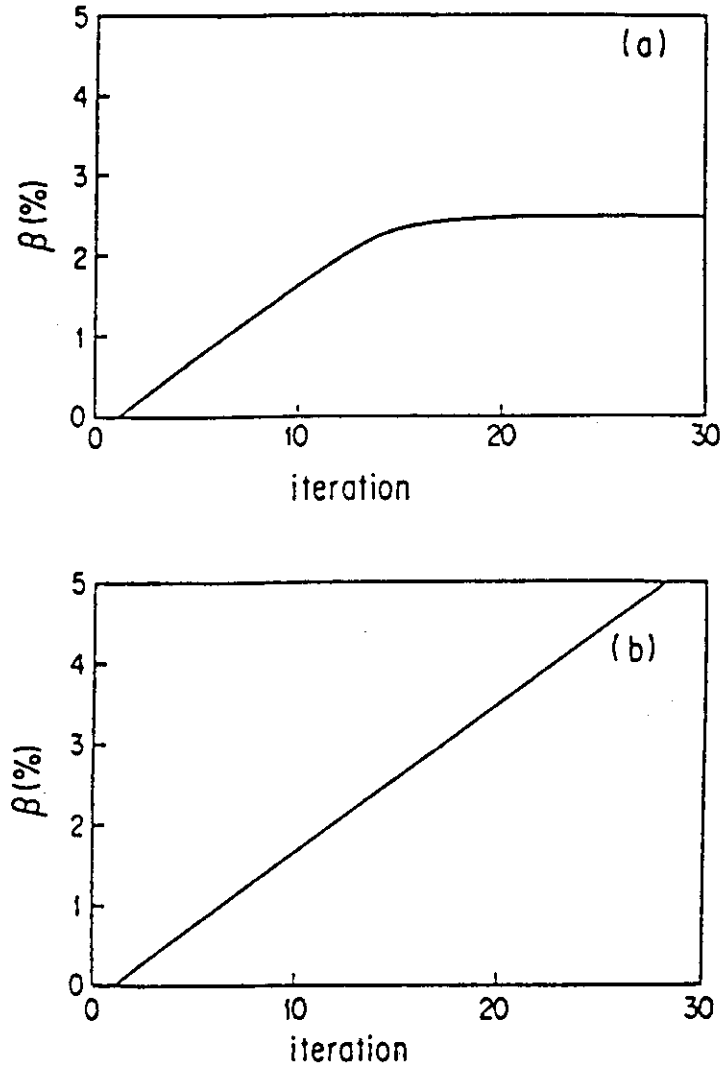

Fig. 5.9 β versus iteration number. For case (a), the beta value saturates at the first ballooning stability limit, $\beta = 2.5\%$, while it increases with iteration beyond this limit for case (b).

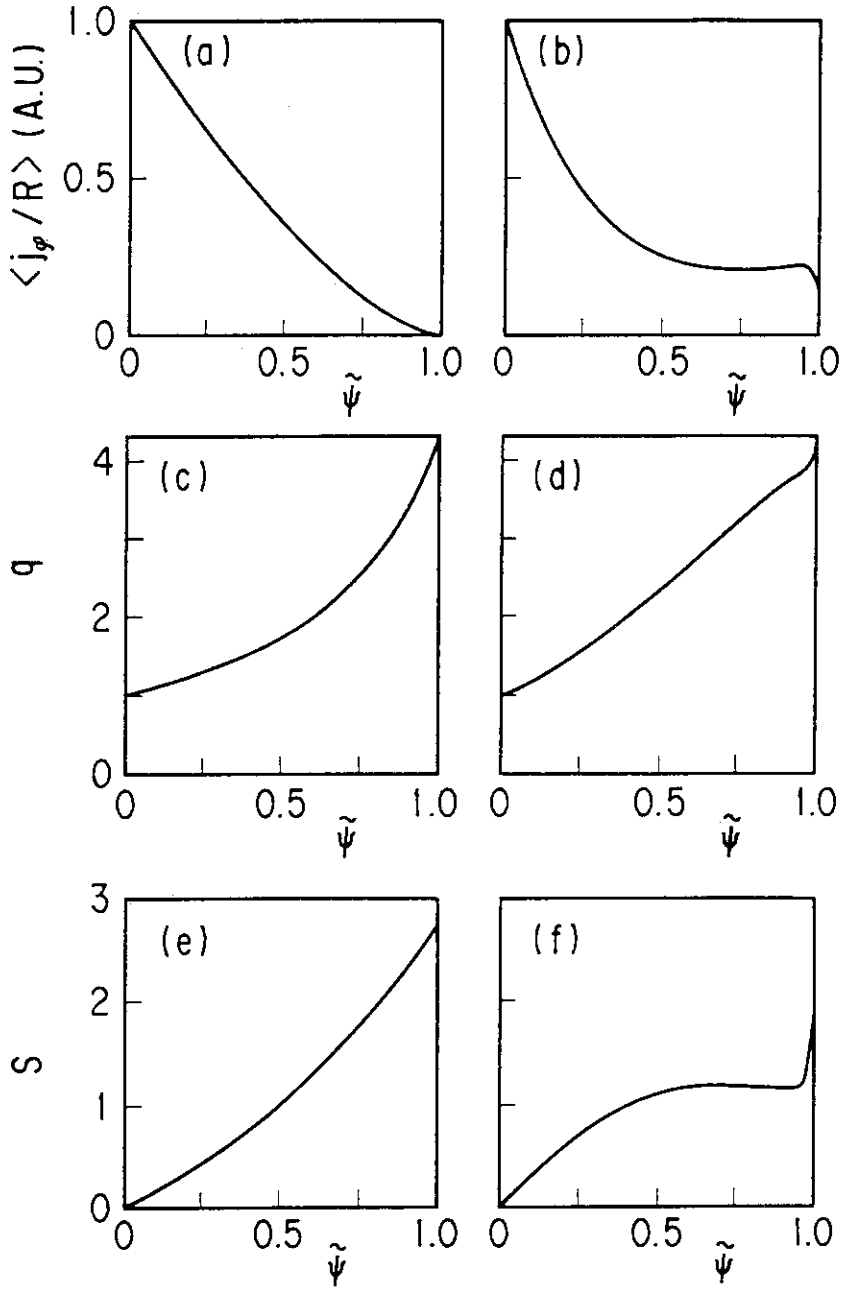

Fig. 5.10 Profile of toroidal current density $< j_\phi/R >$ at low beta plasma, safety factor q and global shear S as a function of $\tilde{\psi}$, for $A = 3.0$, κ=1 and δ=0. $< >$ denotes the average on the poloidal flux surface. Figures (a),(c),(e) are the results of Case 1 (S_{95} =2.5) and Figs. (b),(d),(f) correspond to Case 2 (S_{95}=1.1), respectively, where S_{95} is shear at 95% of the enclosed poloidal flux.

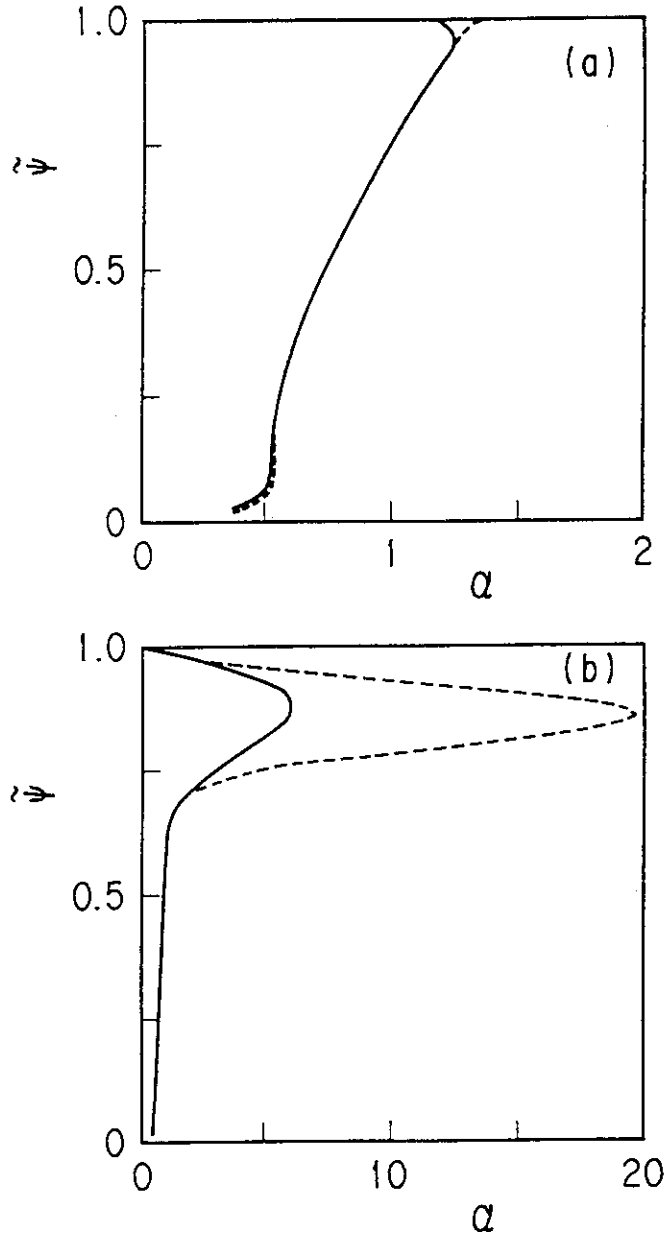

Fig. 5.11 Normalized pressure gradient α as a function of $\tilde{\psi}$ for (a) Case 1 and (b) for Case 2. Broken line denotes the marginal pressure gradient against the ballooning instability.

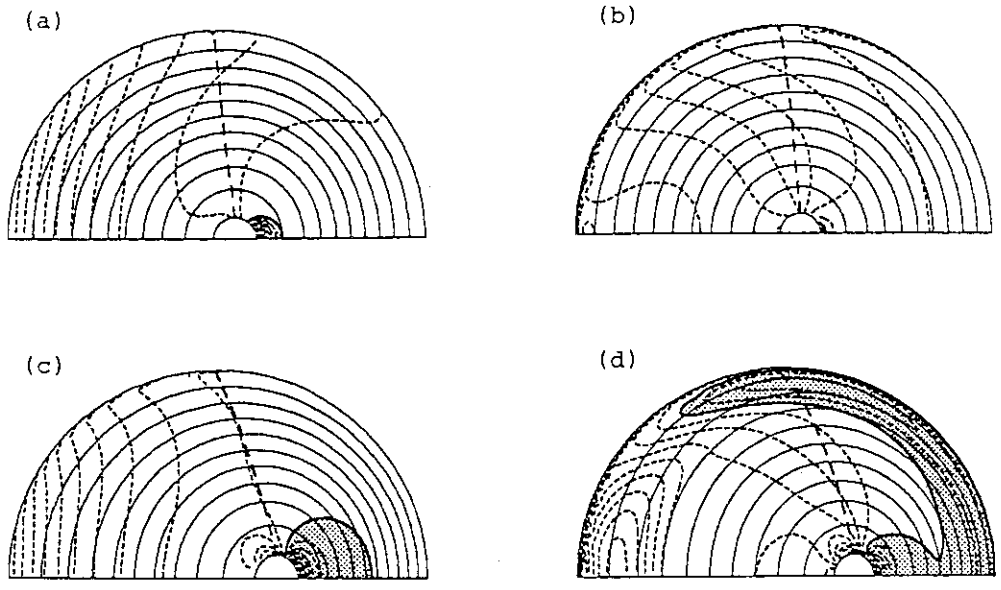

Fig. 5.12 Contours of local shear S_ν (broken lines) and κ_n=0 (bold broken line). Solid lines denote contours of $\tilde{\psi}$. Figures (a),(b) are the results in low beta state for Case 1 and Case 2, respectively. Figures (c),(d) correspond to the results in high beta state for Case 1 and Case 2, respectively. Shaded region denotes the negative local shear (S_ν <0), which extends to the good curvature region (κ_n >0) in Case 2.

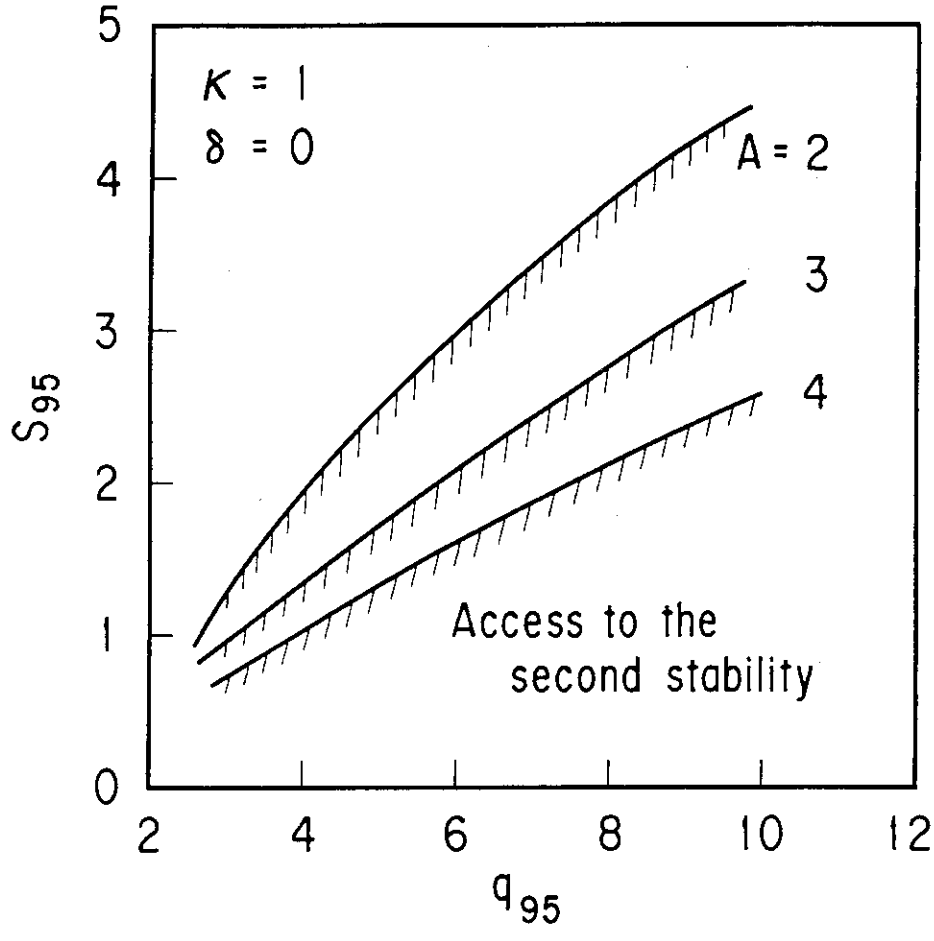

Fig. 5.13 Dependence of A, q_{95} and S_{95} on the access to second stability, where q_0=1.05. The plasma can access the second stability in the area below the each line.

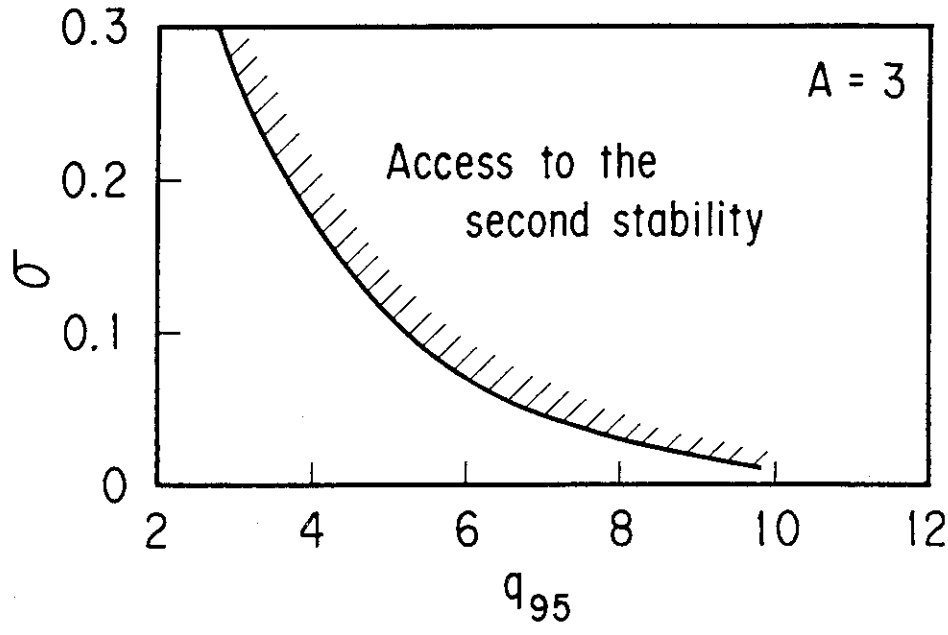

Fig. 5.14 Boundary of access to the second regime on $\sigma - q_{95}$ space, where σ is the amount of pedestal in low beta state (β_p=0.1).

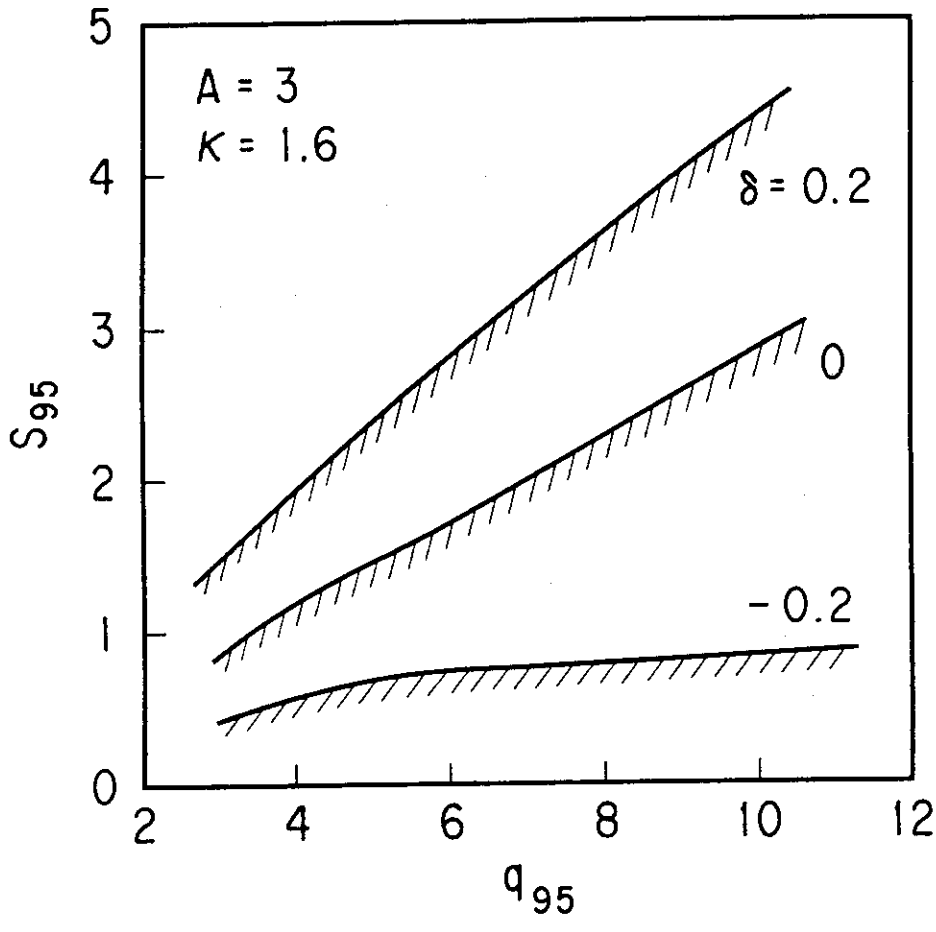

Fig. 5.15 Dependence of κ and δ on the access to second stability where q_0=1.05. The plasma can access the second stability in the area below the each line.

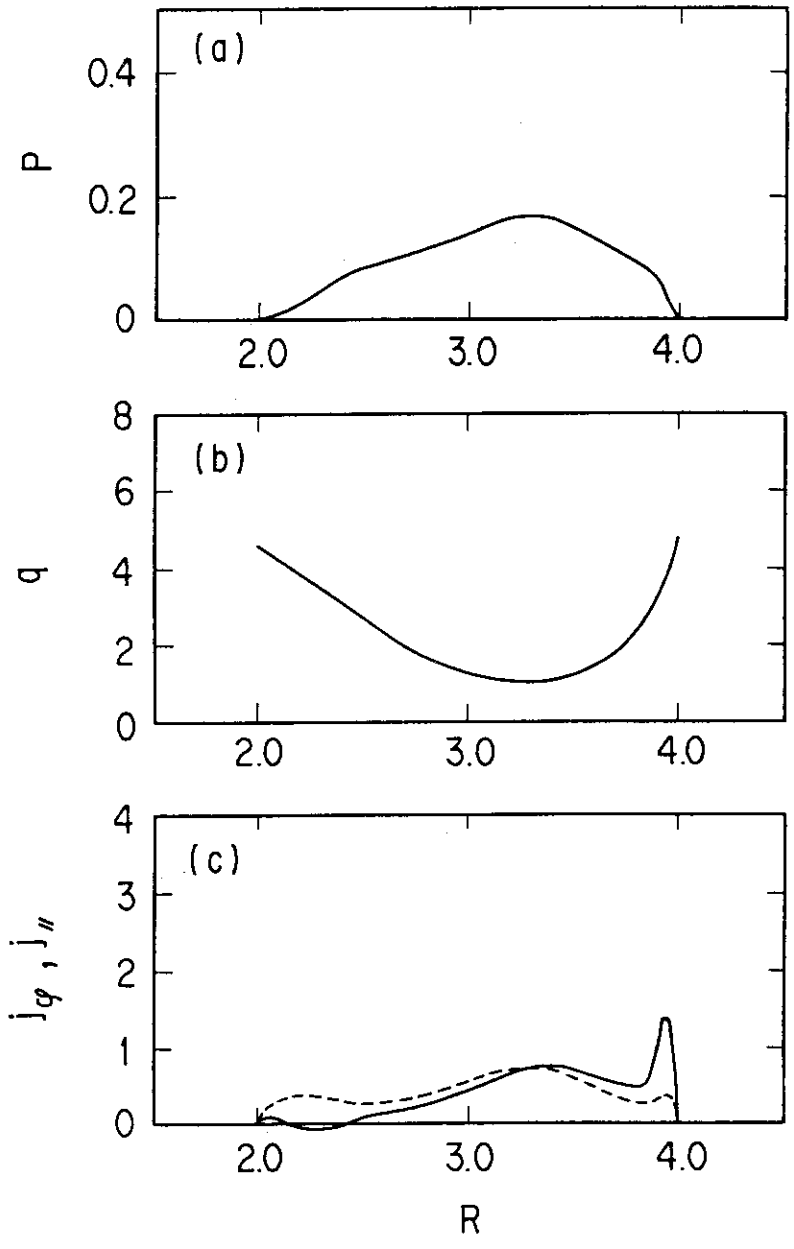

Fig. 5.16 Profiles of (a) plasma pressure, (b) safety factor and (c) toroidal current (bold line) in equilibrium with β_t=7.0% (g = 6.5), A = 3, κ=1.6, δ = 0.2, q_{95}=4.3, q_0=1.05 and S_{95}=1.8. The plasma is in a second stability regime near the plasma surface. Broken line in (c) shows surface averaged parallel current density, $j_{\parallel}$.

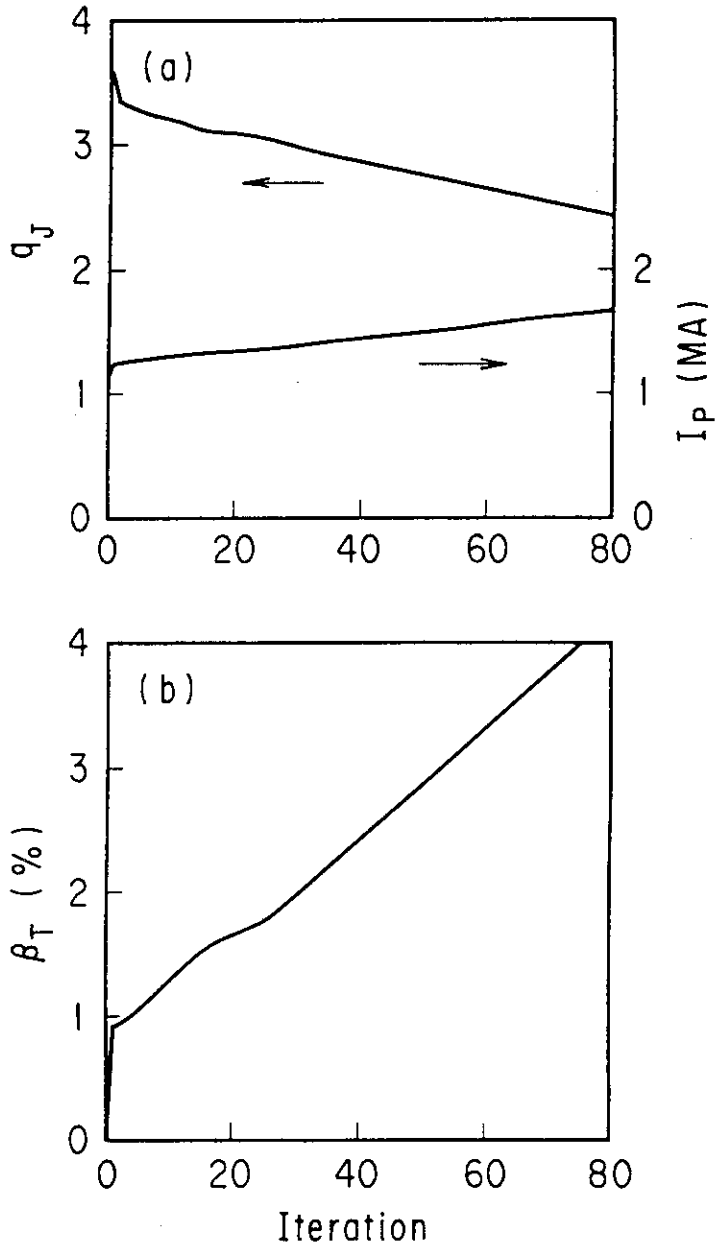

Fig. 5.17 q_J, I_p and β_T versus the iteration number of the optimization process for the plasma in Case 2. q_{95} and q_0 are fixed to 3.88 and 1.05 during the iteration process, respectively.

Chapter 6

Ideal MHD Stability of Plasmas with Peaked Pressure in JT-60

6.1 Introduction

Besides the H-mode, another method of enhancing energy confinement is to generate a plasma with a centrally peaked pressure profile. An injection of hydrogen pellets, which is called "pellet injection", is a useful method for obtaining a centrally peaked pressure profile and enhanced particle and energy confinement in the central region. The nature of pellet-fuelled plasmas has been investigated at several facilities; a summary of this work is given in Ref. [1]. The enhanced central values of the density, the temperature and the energy confinement time provide us with a high possibility to reach the breakeven condition in the central plasma region. However, as the peakedness of plasma pressure profile increases, the limitation of the plasma pressure near the plasma center becomes an important problem.

In pellet fuelled experiments of JT-60, a strongly peaked pressure profile was produced, but the limitation of the plasma pressure near the plasma center was observed with internal MHD activities [2]. First, we investigate the experimentally observed limitation and reveal the mechanism of this limitation by computational analyses. Next, we numerically clarify the characteristics of the MHD stability, which restrict the central plasma pressure, in terms of pressure profiles and plasma shaping. We also discuss ways for further improvement based on the results of the above analysis.

In Section 6.2, ideal MHD stabilities of the pellet fuelled plasma in JT-60 are examined and compared with experimental results. In Section 6.3, the nature of the ideal internal kink mode stability for plasmas with a strongly peaked profile is described. Finally, our conclusions are summarized in Section 6.4.

6.2 Ideal MHD Stability of Pellet Fuelled Plasmas in JT-60

6.2.1 Introduction

Pellet fuelled experiments in JT-60 were carried out in both the limiter configuration with a circular poloidal shape and the divertor configuration with a lower X-point ($1.3 < \kappa < 1.4$, where κ is the plasma elongation). Plasma heating was mainly by neutral beam (NB) injection. Although the H-mode was not obtained even in the divertor configuration, the energy confinement time was enhanced up to 40% relative to usual gas fuelled discharges with NB heating, as described in detail in Ref. [2]. A strongly peaked pressure profile was produced in the area inside the inversion radius of sawteeth activity (relaxation oscillations near the plasma center), when the pellets penetrated into the region close to the plasma center. Here, the inversion radius is the radius of an inversion of soft X-rays signals of the sawteeth, and it is considered to be the radius of the flux surface with the safety factor q =1.0. However, the stored energy inside the q=1 surface (the inversion radius) did not increase to more than a certain value, even though the NB input power increased. High pressure gradients ($dp/dr \approx 5 \times 10^5 Pa/m$) formed in a low shear region near the q=1 surface, so that the confinement within the q=1 surface may be restricted by the ideal infinite n ballooning mode or by low n kink mode (where n is the toroidal mode number). In this section, we investigate the characteristics of these modes for peaked profile plasmas in the JT-60 operation regime ($1.0MA \leq I_p \leq 3.1MA$, $3.5T \leq B_T \leq 4.8T$) and discuss the restriction of the peakedness within the q=1 surface.

The stability of infinite n ballooning and low n kink modes in high beta plasmas have been investigated in a number of experiments. In high beta experiments of ASDEX tokamak, after a maximum beta was transiently attained, the beta was reduced and reached a new stationary state [3]. When this "hard beta saturation" occurred, the observed pressure gradients were found to be close to the stability limit of the ideal ballooning mode, although no clear correlation of MHD fluctuations was found.

A subsequent study explained this "hard beta saturation" by the enhancement of χ_e (electron heat conduction coefficient) due to the resistive ballooning mode [4]. In high beta experiments of Doublet III tokamak, near the experimental beta limit, a plasma with a high q value at the plasma edge (> 3.5) reached a stationary value of the toroidal beta. This correlated well with the fact that a large portion of the plasma pressure gradient reached the ballooning mode limit [5]. In DIII-D high beta experiments, it was found that the beta limit imposed by the ideal low n kink mode without a conducting wall is in good agreement with the experimentally attained beta value [6]. These experiments show that the violation of the infinite n ballooning mode limit in a wide region enhances the transport and leads to destabilization of the low n kink mode. However, the pellet fuelled plasmas have different characteristics; they have locally high pressure gradients and they are usually low beta plasmas. In JET tokamak, pellet fuelled plasmas were analysed for the ideal ballooning stability [7,8]. The electron density profiles were strongly peaked and the pressure gradient locally reached high values, $(3-4) \times 10^5 Pa/m$. These pellet fuelled plasmas had high values of $q_0 (> 1.2)$, and the pressure gradients near the plasma center apparently reached the ideal ballooning limit. However, details of the MHD stability in a centrally peaked plasma with low q_0 (< 1.0) were not investigated.

6.2.2 Pellet fuelled plasma in JT-60 and reconstruction of equilibrium

In JT-60, strongly peaked pressure profiles were obtained in a wide range of operation regime when the pellets penetrated to the plasma center. However, the poloidal beta inside the q=1 surface, β_{p1}, which is related to the pressure peakedness, was saturated even though the NB input power increased. Figure 6.1 shows the saturation of β_{p1} with the absorbed power P_{abs} for a fixed plasma current ($I_p = 1.5MA$), a fixed toroidal field ($B_T = 4.5T$) and a divertor configuration ($\kappa \approx 1.38$, $q_{eff} \approx 3.55$) with

NB heating only. P_{abs} is the total heating power, i.e. the sum of joule heating and NB absorbed power. Here, β_{p1} is defined [9] as

$$\beta_{p1} = \frac{2\mu_0}{B_p^2(r_1)} \int_0^{r_1} \left(\frac{r}{r_1}\right)^2 \left(-\frac{dp}{dr}\right) dr, \qquad (6.\ 1)$$

where r_1 is the minor radius of the q=1 surface. β_{p1} is determined by dp/dr within the q=1 surface, so that this parameter does not give the total pressure. However, for centrally peaked plasma with low β_p studied here, β_{p1} is a good figure of merit for discussing the stability of the n=1 internal kink mode (in Section 6.2.4).

To analyse the saturation phenomena of β_{p1}, we first describe the characteristics of pellet fuelled plasmas in JT-60. Sawteeth were suppressed during the peaking of pressure profile and they reappeared after the peaked profile was established, but the inversion radius was not changed before and after sawtooth suppression. The q=1 surface estimated from the pellet ablation profile coincides with the inversion radius [10]. The central q value q_0 is estimated by solving a magnetic diffusion equation including the bootstrap current, using experimentally obtained data such as the plasma current and the electron temperature and density profiles, and adjusting the $Z_{\rm eff}$-profile so that the calculated loop voltage and the internal inductance agree well with the measured ones [10]. In this simulation, q_0 is estimated to be 0.9-0.98 at the time when the strongly peaked profile is obtained. Therefore, we consider that the radius of the q=1 surface does not change even during the sawteeth suppression phase after the pellet injection [2]. Inside this q=1 surface, the plasma pressure increases owing to the significant increase in the plasma density by the pellet injection. The characteristics of pressure and current profiles in JT-60 pellet fuelled plasmas are summarized as follows: (1) A high pressure gradient exists inside the inversion radius of sawteeth, which is the q=1 surface; (2) the electron temperature profile is broad, so that the q-profile seems to be flat; and (3) the center q value is probably below one. The experiments in the limiter configuration were carried out for plasmas with $1.0MA \leq I_p \leq 3.1MA$, with a circular poloidal shape, and the experiments in the divertor configuration were carried out for

plasmas with $1.0MA \leq I_p \leq 1.8MA$, with a lower X-point ($1.3 < \kappa < 1.4$). In this study, we mainly analyse plasmas in the limiter configuration because data are available for a wide operation regime and because the stability code for low n modes is restricted to an up-down symmetry equilibrium.

The MHD equilibria used in the following stability calculations are reconstructed by solving the following Grad-Shafranov equation iteratively, using the above characteristics:

$$\Delta^* \psi = \mu_0 R J_\varphi, \tag{6. 2}$$

$$J_\varphi = -R\frac{dp}{d\psi} - \frac{1}{\mu_0 R} F \frac{dF}{d\psi}, \tag{6. 3}$$

where ψ is the poloidal flux function, J_φ is the toroidal current density and μ_0 is the permeability of vacuum. To ensure numerical accuracy of this study as far as possible, the MHD equilibria are reconstructed self-consistently from the measured external magnetic data, as well as from the measured kinetic profile data, which include the profiles of the electron density n_e and of the temperature T_e. The sawteeth inversion radius from soft X-rays (SX) is used to constrain the location of the $q = 1$ surface. The two free functions, the plasma pressure $dp/d\psi$ and the toroidal field function $F(\psi)$, are obtained from the kinetic data and from the surface averaged parallel current $< J_\parallel >$ $(=< J_\parallel \cdot B > / < B >)$, respectively.

The pressure profiles are mainly determined by the n_e, T_e data from Thomson scattering measurements. The electron density from Thomson scattering is calibrated using the line averaged density from a far infrared (FIR) spectrometer. The electron temperature is also measured by electron cyclotron emission (ECE), and these data agree well with the Thomson scattering data within the error bar (~20%). The ion temperature at the plasma center is measured from Doppler broadening of Ti XXI in a few shots; these data are the same as those of T_e from Thomson scattering within the error bar (~20%). In this calculation, the shape of the ion pressure profile is

assumed to be equal to that of the electron pressure profile because of the high density due to the pellet injection. The total stored energy obtained from the kinetic data (Thomson scattering, $Z_{\rm eff}$, etc.) agrees well with that obtained from the diamagnetic data, within an error of 10%. We adjust the total pressure to the stored energy from a diamagnetic measurement. In addition to kinetic data, we employed SX profile data to compensate for the lack of data from Thomson scattering. The profile of the electron pressure is well represented by the SX data, as shown in Fig. 6.2. The SX emission rate is roughly proportional to $n_e^2 T_e^m$. In JT-60 pellet fuelled plasma, the value of m is from 1.3 to 2.5 because $Z_{\rm eff}$=1.1-2.0 and T_e=0.5-2.0 KeV. Therefore, the square root of the SX intensity is proportional to $n_e T_e^{0.65-1.25}$, which can be considered to give the electron pressure. The error bar due to the uncertainty in the exponent of T_e is less than 20%, as shown in Fig. 6.2. Two data of $Z_{\rm eff}$, from Bremsstrahlung at the plasma center and $0.6r_p$, where r_p is a minor radius, indicate that the profile of $Z_{\rm eff}$ is flat and not peaked. Therefore, the error bar for the pressure profile from the SX data is not much influenced by the profile of $Z_{\rm eff}$.

The surface averaged parallel current is assumed in this study to be given by a following function:

$$< J_{\parallel} \cdot B > \propto \frac{1}{1+\sigma}\{(1-\tilde{\psi}^{\alpha 1})^{\alpha 2} + \sigma\}, \qquad (6.\ 4)$$

The parameters, $\alpha 1$, $\alpha 2$ and σ are determined by the $q = 1$ surface, the internal inductance ℓ_i and the central q value; $\tilde{\psi}$ is the normalized poloidal flux, defined as $\tilde{\psi} = (\psi - \psi_{axi})/(\psi_{bun} - \psi_{axi})$, where ψ_{axi} and ψ_{bun} are the poloidal fluxes at the plasma axis and the boundary, respectively. ℓ_i is determined from $\beta_p + \ell_i/2$ measured by magnetic pick-up coils, with β_p obtained by diamagnetic measurements. Although q_0 has not been measured, its value can be assumed to be below one. Therefore, we have investigated profiles with q_0 from 0.9 to 0.98. Figure 6.3 shows three types of q-profiles, where the q=1 surface is defined by the observed inversion radius and the surface q is constant (=3.4). In this model, the equilibrium with the relatively higher value of q_0

(=0.98) has a lower shear near the plasma center, and the equilibrium with the lower value of q_0 (=0.9) has a relatively higher shear.

6.2.3 Ballooning stability analysis

Ballooning stability analysis was carried out by solving the infinite n ballooning equation of Eq. (5.1). The shape of the flux function and the pressure and current profiles, which have been reconstructed by the equilibrium code, are used for stability analysis. In this ballooning code [11], the marginal pressure gradient P'_m associated with a particular equilibrium, is obtained with the boundary condition that the radial displacement (at $\ell = \pm\infty$) is zero, fixing the growth rate at zero. Figure 6.4 shows the measured pressure gradient and the marginal value of the pressure gradient with regard to the ideal ballooning mode for the cases with low and high plasma currents in the limiter configuration, when the pressure profile becomes mostly peaked (about $0.5 - 1.0s$ after pellet injection). In the discharge of Fig. 6.4(a), two pellets with an NB absorption power of 3.4MW were injected into a plasma with $I_p = 2.1MA$. In the discharge of Fig. 6.4(b), four pellets with an NB absorption power of 13.4MW and a small ICRF power of 1MW were injected into a plasma with $I_p = 3.1MA$. The experimental pressure gradient in Fig. 6.4(a) is determined by the data from Thomson scattering measurements and from the SX-intensity profile, while that in Fig. 6.4(b) is determined by the data from the Thomson system and from ECE. The measured pressure gradient just inside the $q = 1$ surface violates the ideal ballooning stability limit for $q_0 = 0.95$ and 0.98. For $q_0 = 0.90$, the measured pressure gradient is very close to the marginal value. We note that the pressure gradient from the Thomson scattering measurements (Fig. 6.2) has a error of ≈20%-30%. Therefore, the region of the highest pressure gradient is considered to have a marginal value for the ideal ballooning stability. The difference in the marginal ballooning pressure gradient limits by scanning of q_0 (from 0.9 to 0.98) is small, especially in the region around the highest pressure gradients, so that the marginal value does not strongly depend on q_0.

As the plasma current increases, i.e. as q_{eff} decreases, the sawteeth inversion radius r_s increases and is proportional to the inverse of the safety factor q_{eff} ($r_s \approx r_p/q_{eff}$) [12]. The observed pressure gradients for different values of q_{eff} reached the marginal

ballooning pressure gradients in a similar way, although the shear was reduced owing to an increase of r_s for fixed q_0. Here, the q_{eff} is defined as

$$q_{eff} = \frac{2\pi r_p^2 B_T}{\mu_0 I_p R_p}\left(\frac{1+\kappa^2}{2}\right)\left\{1+\left(\frac{r_p}{R_p}\right)^2\left(1+\frac{(\beta_p+\ell_i/2)^2}{2}\right)\right\}$$
$$\times\left(1.24-0.54\kappa+0.3(\kappa^2+\delta^2)+0.13\delta\right). \qquad (6.5)$$

where R_p is the major radius, r_p is the minor radius, κ is the elongation and δ is the triangularity of the poloidal shape. This expression was originally derived as an empirical fit to Doublet III data [13] and was also employed in JT-60 experiments. In the limiter configuration, the q_{eff} agrees well with the plasma surface value of q within ± 0.05, so that we use the q_{eff} in this paper.

It is of interest to examine the temporal evolution of various plasma parameters for a strongly peaked plasma. Figure 6.5, which is for the same shot as presented in Fig. 6.4(a), shows the time evolution of the NB input power, the line averaged electron density at $\approx 0.6r_p$, the electron temperature at the plasma center from ECE, the SX intensity near the center and at $0.4r_p$, the central poloidal beta and the maximum pressure gradients. After injection of two pellets at $6.0s$, the density rose rapidly and decayed slowly. The temperature decreased transiently and recovered relatively fast. The SX intensity, which is nearly proportional to p^2, significantly increased near the plasma center, while the value at the peripheral point ($0.4r_p$) remained unchanged. Consequently, the pressure profile became peaked. In this case, the measured pressure gradients were estimated from the SX intensity profile and the diamagnetic data. At $t = 6.5s$, the pressure gradient was also estimated by the Thomson system (error bar in Fig. 6.5).

As the discharge proceeded, the maximum pressure gradient increased and reached the marginal value for ballooning mode stability (shaded region in Fig. 6.5). We note that the radial position of the maximum pressure gradient moves with time toward the plasma center, and the marginal pressure gradient is evaluated at the same radius as

the experimentally observed maximum value. The upper limit of the shaded region corresponds to $q_0 = 0.9$ and the lower limit corresponds to $q_0 = 0.98$. However, as the pressure gradient increases, the marginal values also increase because of the effect of magnetic well stabilization, and the influence of the q_0 variation becomes small. At $t = 6.3s$, the observed pressure gradient became close to the marginal pressure gradient, and at $\approx 6.4s$ the observed pressure gradient was the same as the marginal value and the increase of the pressure gradients was suppressed. The behaviour of the pressure gradient with respect to the marginal pressure gradient is shown in Fig. 6.6 for the shot presented in Fig. 6.5. Figure 6.6 shows the time evolution of the contours of P'/P'_m=constant as a function of the minor radius, where, P'/P'_m is the fraction of the measured pressure gradients versus the marginal pressure gradients. It is shown that the region of P'/P'_m=1.0 tends to increase with time and the marginal region becomes wider. The maximum value of P'/P'_m is less than 1.1, so that the pressure gradient in the unstable region is almost the marginal value against ballooning mode. Outside the q=1 surface, the measured pressure gradient is lower than the marginal one, to a sufficient degree.

Experiments for a scan of B_T have been carried out in a limiter plasma with a circular cross section, keeping q_{eff} fixed. The observed pressure gradient for the minor radius, dp/dr, is almost proportional to the square of the toroidal field ${B_T}^2$, as shown in Fig. 6.7. In the infinite n ballooning analysis, the normalized pressure gradient α is usually used:

$$\alpha = -2\mu_0 \frac{R q^2}{{B_T}^2} \frac{dp}{dr}. \qquad (6.6)$$

From this definition, dp/dr is proportional to ${B_T}^2$ for the same value of α because $q \approx 1.0$ and R is constant. The limits of the marginal ballooning pressure gradient for the given q profile, with $q_0 = 0.9 - 0.98$, which are obtained from all of the experimental equilibria, lie within the hatched region in Fig. 6.7. Therefore, the maximum pressure gradients are close to the ideal ballooning limit for various toroidal fields. The high

toroidal field is preferable in order to obtain a high pressure gradient for a fixed q profile.

The Mercier mode[14] becomes unstable as the q_0 becomes close to the unity and the shear is reduced in the area inside the q=1 surface. However, the critical pressure gradient due to the ideal ballooning mode is lower than that due to the Mercier mode, so that the ballooning mode is more restrictive in limiting the increase of the pressure gradients.

6.2.4 Kink stability analysis

The MHD stability against the low n ideal kink modes has been computed with the ERATO-J code described in Section 3.4.2, which solves the linearized ideal MHD equations in variational form using a finite hybrid element approach. As in the analysis of the ballooning mode, the current profile is chosen to obey the Eq. (6.4) and the value of q_0 was scanned from 0.9 to 0.98. The q=1 surface was set at r_p/q_{eff} [12]. In the analysis of ERATO-J code, a sufficiently smoothing pressure profile is required because of numerical accuracy; therefore, instead of using experimental data, the pressure profile is given in the form

$$p(\tilde{\psi}) \propto exp\left\{-\left(\frac{\tilde{\psi}}{\lambda_1}\right)^{\nu}\right\} + \lambda_2\left(1-\tilde{\psi}\right), \qquad (6.7)$$

which gives a fair description of the pressure profile in the pellet fuelled plasma of JT-60, as shown in Fig. 6.8. Here, ν, λ_1 and λ_2 are profile parameters, and a large value of ν means a steep pressure gradient at a flux surface $\tilde{\psi}$ of λ_1. The value ν=4.0 almost reflects the experimentally observed pressure gradient, and λ_1 is adjusted just inside the $q = 1$ surface. The plasmas in the limiter configuration, which have a circular shape and up-down symmetry, are used for low-n stability analysis because of restrictions on

the ERATO-J code. A fixed boundary is used in the stability calculations because our present problem is the internal kink mode.

A careful convergence study is important because the internal kink mode has a small growth rate and needs a very fine mesh. The ERATO-J code employs the flux co-ordinate ρ, χ, where $\rho = \sqrt{\tilde{\psi}}$ and the poloidal angle χ is selected so that the magnetic field lines are straight. Figure 6.9 illustrates a convergence check of the squared growth rate $\hat{\gamma}^2$ versus the squared radial grid mesh, where the mesh number in the ρ direction, N_ρ, is surveyed from 90 to 270 with a uniform mesh. The convergence check in ρ direction is important because of the large pressure gradient. The mesh number in the χ direction, N_χ, is fixed at 90. This poloidal mesh number is accurate enough to calculate the low n mode stability. For the n=1 internal mode, a good offset linear dependence of the squared growth rate $\hat{\gamma}^2$ is obtained; $\hat{\gamma}^2$ is normalized by the Alfvén velocity v_A and the major radius R_0 ($\hat{\gamma}^2 = \gamma^2/(v_A/R_0)^2$). For the n≥2 modes, a linear dependence is also obtained, although the dependency of $1/{N_\rho}^2$ is stronger for these modes than that for the n=1 mode.

The stability of the n=1 internal kink mode is studied first because this mode is considered to be most restrictive for a strongly peaked plasma with low q_0 (< 1.0) in JT-60 pellet fuelled discharges. Figure 6.10 shows the critical limit of β_{p1} as a function of q_0 for fixed q_{eff}=3.55, using several pressure profiles. For a q_0 value of $0.9 - 0.95$, the change of the stability boundary against q_0 is small. As was pointed out by Nave and Wesson [15], the boundary of critical beta decreases by approximately 20% as q_0 increases to 0.98, because of the decrease of the global shear. The boundary of the critical β_{p1} with a locally high pressure gradient just inside the q=1 surface is higher than that with a squared parabolic pressure profile. This means that a plasma with a strongly peaked pressure profile is more stable against the n=1 internal kink mode than a plasma with a broad pressure profile. Here, the unstable condition is defined by $\hat{\gamma}^2 \geq 5 \times 10^{-5}$, which is more restrictive than the beta limit calculation by Troyon et al.[16], because the internal kink mode has a smaller growth rate.

The dependence of the critical beta limit on q_{eff} is examined for a fixed q_0 value of 0.95 and a pressure profile parameter ν of 4.0. Figure 6.11 shows the theoretically predicted beta limit as a function of q_{eff} for fixed q_0 and for several experimentally obtained values of q_{eff}. The boundary of the critical β_{p1} for ν=4.0, indicated by the bold solid line, decreases with q_{eff} because of the decreasing shear. Also the boundary of the critical β_{p1} decreases by about 20% because of the flattening of the pressure profile (dashed line). In the present study the kink stability analyses have been carried out with a fixed boundary. However, the stability calculation with the free boundary model for the shot marked A in Fig. 6.11 shows the same mode structure (m/n=1/1 mode) as that for the case of a fixed boundary, which indicates the stability boundary for the internal kink mode is less sensitive to the boundary condition for the cases studied here. Fast crashes due to the m=1 mode, which behaves as a rigid body (crash time $\approx 300\mu s$), were observed after the peaked profile was obtained in JT-60 [17]. The experimental values of the critical beta in the discharge with a fast crash (open circles in Fig. 6.11) lie in the range of the critical β_{p1} limit for different pressure profiles. The results of this experimental observation together with the numerical analysis suggest that the strongly peaked profile is limited by the ideal n=1 internal kink mode.

On the other hand, the maximum pressure gradients of the experimental data locally reach the stability boundary of the ideal ballooning mode for several various of q_{eff}, as explained in the previous section. In a plasma with a pressure profile parameter ν=4.0, the ideal ballooning mode becomes locally unstable at a value of β_{p1} which is lower than that imposed by the n=1 internal mode (broken line in Fig. 6.12). However, by optimizing the pressure profile, the critical β_{p1} against the ballooning mode could be increased to a value above the boundary imposed by the n=1 internal kink mode. To obtain an optimized pressure of a marginally stable plasma, the ideal ballooning mode equation and the Grad-Shafranov equation have been solved iteratively in a flux conserving manner, holding the q profile fixed until the pressure gradient converges to the marginal value, where the growth rate is fixed at zero [11]. This result is illustrated

in Fig. 6.12, where the critical β_{p1} imposed by the ideal ballooning mode stability rises from the pressure profile ν of 4.0 (broken line) to the optimized critical β_{p1} (thin solid line), which is above the value of the critical β_{p1} imposed by the n=1 internal kink mode. These results suggest that the locally unstable ballooning mode suppresses the increase of pressure gradients and makes it possible to reach the optimum (marginally stable) pressure gradient; consequently, β_{p1} is finally restricted by the n=1 internal mode and not by the infinite n ballooning mode.

Next, the $n \geq 2$ kink modes are investigated for a fixed boundary plasma in order to evaluate the kink-ballooning effects due to the high β_{p1}. Figure 6.13 shows the square growth rate, normalized by the Alfvén time, as a function of the β_{p1} for the n=1 and n=2 modes. The critical beta of the n=2 mode is higher than that of the n=1 mode. For the n=2 mode, the dominant poloidal mode number is two, and the perturbation is localized at the q=1 surface. The observed value of $\beta_{p1}$for the plasma with Ip=3.1MA, Bt=4.8T and $\nu \approx$4.0, corresponding to the parameters in this figure, are below the n=1 critical beta (shaded region) and, therefore, the experimentally obtained plasma can be regarded as being stable against the n=2 mode. In the analysis of the higher toroidal modes (3, 5, 10 and 20), the eikonal transform is used to maintain the numerical accuracy of the calculation. As shown in Fig. 6.9, the square growth rate converges to zero in the infinite mesh number for n>3 modes.

6.2.5 Discussion and conclusion

The ideal MHD stability for a plasma with a strongly peaked pressure profile within the q=1 surface has been investigated. The results of the study show that the plasma locally reaches the limit of the ideal ballooning mode just inside the q=1 surface. After reaching the marginal value on the magnetic flux surface, the increase of the pressure gradient is suppressed and the marginally stable region extends toward the plasma center. The achieved values of β_{p1} are lower than the optimized β_{p1} limit imposed by

the ballooning mode. However, they are close to the β_{p1} limit due to the ideal n=1 internal kink mode and they are limited by the occurrence of fast crashes caused by the m=1 mode.

The process of the growth of the poloidal beta to its limit near the plasma center has been studied by analyses of the ideal ballooning and kink modes. Enhanced transport caused by ballooning instability prevents the pressure gradient inside the q=1 surface from increasing beyond the marginally stable value. Thus, a further increase of the beta value requires an increase of the marginally stable region, and the marginally stable region spreads inside the q=1 surface. Therefore, β_{p1} can increase up to the kink mode limit although the pressure gradient is locally limited by the ballooning mode.

It is important to increase the critical β_{p1} in order to obtain a centrally peaked pressure profile. A plasma with a steeper pressure gradient just inside the q=1 surface has a higher value of the critical β_{p1} against the n=1 internal kink mode, as shown in Fig. 6.10. This pressure gradient is, however, limited by the infinite n ballooning mode (Fig. 6.12). The ballooning mode limit increases with the toroidal field (see Fig. 6.7). Therefore, to increase β_{p1}, a higher toroidal field can lead to an increase of β_{p1}, i.e. a higher toroidal field can increase the limit of the pressure gradient just inside the q=1 surface so that the value of the critical β_{p1} against the n=1 internal kink increases.

6.3 Stability of the n=1 Internal Kink Mode in Plasmas with Centrally Peaked Pressure

6.3.1 Introduction

In the previous section, it has been obtained that the increase of the centrally peaked pressure profile by means of the pellet injection is limited by the n=1 internal kink mode. To obtain the further increase of the confinement near the central region of the plasma cross section, it is important to clarify the property of the n=1 internal kink stability for the plasma with the peaked pressure profile. Of particular interest are the effects of the pressure profile and the shape of plasma cross section, i.e., the elongation and the triangularity, on a stability limit of the n=1 internal kink mode.

The n=1 internal kink stability has been extensively studied by numerous authors. The stability condition of the internal kink mode in a low beta plasma with a finite shear and a circular cross section was first derived analytically by Bussac et al.[9] and this result was numerically confirmed by means of ERATO code [18]. The reduction of the stability boundary for the low shear plasma and the onset of interchange-like instability was discovered by Nave and Wesson [15]. At a high beta plasma, the existence of the second stable region was numerically demonstrated by Tokuda et al. [19] and also analytically studied by Crew and Ramos [20]. The extensive numerical study of the internal kink stability was carried out by Manickam in the wide range of parameters, such as the aspect ratio, shaping of the cross section, the current profile and the pressure profile [21].

In these previous works [9,18-21], plasmas with a rather smooth pressure profile were exploited, and the $\sigma-$scaling technique (Eq. (3.6)) was used for scanning of q_0, in which the radius of the $q = 1$ surface is changed with q_0. The plasma, considered here, is different from the plasmas investigated in the previous works [9,18-21]. The pressure profile is peaked only within the q=1 surface, and the radius of the q=1 surface scales

with the inverse of q_s. The stability of the n=1 internal kink about these plasmas has been left unsolved.

In this section, we numerically investigate the stability of the n=1 internal kink mode for the centrally peaked pressure profile in the wide range of parameters and reveal effects of the pressure and the current profiles and the plasma shape.

6.3.2. Calculation procedure

Key parameters to study the n=1 internal kink stability are the pressure and current profiles. Since the purpose of this section is to clarify the effect of pressure profile, we choose two types of plasma with the different pressure profile and the same current profile. One is the peaked pressure profile; that is, the pressure peaks inside the q=1 surface. This type of pressure profile can be well expressed by Eq. (6.7). In this equation, the first term corresponds to the peaked part of the pressure profile and λ_2 denotes the ratio of the broad part to the peaked part. The parameter ν denotes the steepness of the pressure gradient at the location of λ_1. In the following, we use $\nu = 4.0$ and $\lambda_2 = 0.6$ as the standard case, and the parameter λ_1 is adjusted from the position of the q=1 surface. For the comparison with this centrally peaked pressure profile, the rather smooth functional form, i.e., the squared parabolic pressure profile,

$$p(\tilde{\psi}) \propto (1 - \tilde{\psi})^2 \tag{6. 8}$$

is also employed in the following calculations.

The surface averaged parallel current density is assumed to have the Eq. (6.4). In many tokamak experiments [12,22,23], it was found that the minor radius of the q=1 surface, r_1, scales as $r_1 = a/q_s$, where a is the plasma minor radius and q_s is the safety factor at the plasma surface. On the other hand, the q value at the plasma center, q_0, is not well measured. Thus, the scanning of q_0 is carried out keeping the value of q_s

and the radius of the q=1 surface fixed. The current profile parameters, i.e., α_1, α_2 and σ, are adjusted from the position of the q=1 surface ($r_1 = a/q_s$) for given total plasma current and q_0. Figure 6.14 shows the typical q-profiles with various q_s and the corresponding pressure profiles.

The MHD equilibria with toroidal symmetry and up-down symmetry against the $Z = 0$ plane are obtained by solving the following Grad-Shafranov equation of Eq. (6.2)-(6.3) iteratively in the cylindrical co-ordinates (R, Z, φ) for prescribed current and pressure profiles, as described in Section 3.4.1. Since the internal kink mode is a weak instability, the accuracy requirements of the equilibrium and stability analysis are quite stringent. To ensure that these requirements are adequately met, we solve the equilibrium equation in the fine rectangular grid with N_R=512 in the R-direction and N_Z=256 in the Z-direction so that the ratio of the grid size to the average minor radius of the plasma is about 5×10^{-3}. The convergence criterion for the iteration of equilibrium calculation has been $\epsilon < 10^{-6}$, where ϵ is the maximum amplitude of the relative change between iterations. The two free functions, the $dp/d\psi$ and the toroidal field function $F(\psi)$, are specified by the pressure profile and the surface averaged parallel current $< J_{\parallel} >$ (=$< J_{\parallel} \cdot B > / < B >$), respectively.

The stability of the n=1 internal kink mode is studied with the ideal MHD linear stability code ERATO-J described in Section 3.4.2. Convergence study is carried out for mesh number of 90 to 270 in the ρ direction. The good offset linear dependence of the squared growth rate, $\hat{\gamma}^2$, against the squared radial grid mesh, N_ρ^2, is confirmed for every case by using the radial mesh number of 90 to 270 with equal spacing. Here the $\hat{\gamma}$ is the growth rate normalized by the Alfvén velocity v_A. The N_χ is fixed 90 because this poloidal mesh number is accurate enough to calculate low n mode. We take the value of $\hat{\gamma}^2$ (on $N_\rho \to \infty$) of 5×10^{-5} as the stability limit.

6.3.3 Pressure profile and plasma shaping effects

We study effects of the peaked pressure profile and of the shaping on the n=1 internal kink mode in comparison with that of the squared parabolic profile. Since the purpose of this section is to investigate the nature of the n=1 internal kink mode, we use the fixed boundary plasma.

First, we investigate the stability boundary for the peaked pressure profile plasmas against q_0. The circular cross section is used to isolate the influence of geometry. Here, the scanning of q_0 is carried out keeping the radius of the q=1 surface fixed, as shown in Fig. 6.15. Figure 6.16 shows the limited value of β_{p1} as a function of q_0 for both plasmas with the centrally peaked pressure profile and the squared parabolic pressure profile. Here, β_{p1} is the poloidal beta defined within the q=1 surface, introduced in Eq. (6.1). The stability boundary of the centrally peaked pressure profile is higher than that of the squared parabolic profile. The limit of β_{p1} does not change so much as q_0 decreases. The finding is in contrast with the previous work[19], in which the scanning of q_0 changes the radius of the q=1 surface. We also observe that, when q_0 approaches to unity, the stability boundary of β_{p1} largely decreases because the eigenfunction becomes interchange-like as was pointed out by Nave and Wesson [15].

In the internal kink mode, the destabilizing terms consist of the pressure driven and current driven components. Figure 6.17 shows contributions of the pressure driven component W_{ball} and the current driven component W_{kink} for both profiles of the centrally peaked pressure and the squared parabolic pressure with the same q-profile ($q_0 = 0.9$ and $q_s = 3.5$) and the same value of β_{p1} (≈ 0.63). Here, W_{ball} and W_{kink} are the surface integral of the pressure driven term and the current driven term of Eq. (2.89) on the each flux surface, respectively. W_{kink} on both the plasmas with different pressure profiles exhibits the similar radial distribution because of the same q-profile (Fig. 6.17(e),(f)). In the plasma with the centrally peaked pressure profile, W_{ball} is concentrated within the q=1 surface (Fig. 6.17(c)) and the sharp step-function like

behaviour of ξ_r is evident (Fig. 6.17(a)). In the parabolic pressure profile, W_{ball} is distributed inside and outside the q=1 surface (Fig. 6.17(d)) and the amplitude of the eigenfunction outside the q=1 surface is larger than that of peaked profile (Fig. 6.17(b)). Table 6.1 shows the values of q and β_{p1}, the contribution of the current driven component and the pressure driven component of the plasmas in Fig. 6.17. The two plasmas with the different pressure profile are adjusted to have the same amount of β_{p1} and q-profile, so that the squared parabolic pressure profile has the same amount of the pressure driven contribution within the q=1 surface ($\sum_{IN} W_{ball}/\sum_{IN} T$) as the peaked one has. However, the parabolic profile plasma has larger amount of the pressure driven contribution from the outside of the q=1 surface by the mode coupling ($\sum_{OUT} W_{ball}/\sum_{OUT} T$). Thus, the total pressure driven component is larger than that of the peaked pressure profile, and the stability boundary of β_{p1} is lower than that of the peaked pressure profile.

Table 6.1 Plasma parameters, the current driven contribution and the pressure driven contribution for each plasma in Fig. 6.17. W_{kink}, W_{ball} and T are the potential energy of the current driven and the pressure driven, and the kinetic energy, respectively. $\sum$, $\sum_{IN}$ and $\sum_{OUT}$ are the summation in the whole plasma region, the summation inside the q=1 surface and the summation outside the q=1 surface, respectively.

	Parabolic		Peaked
q_0/q_s	0.9/3.5	$\approx$	0.9/3.5
β_{p1}	0.64	$\approx$	0.63
$\sum W_{kink}/\sum T$	-9.4×10^{-4}	$\approx$	-9.8×10^{-4}
$\sum_{IN} W_{ball}/\sum_{IN} T$	-2.8×10^{-4}	$\approx$	-2.4×10^{-4}
$\sum_{OUT} W_{ball}/\sum_{OUT} T$	-4.1×10^{-4}	$>$	-0.7×10^{-4}

Next, we extend the study to the non-circular plasma in order to investigate the effect of the shaping. In the future tokamak, the shape of the poloidal cross-section will be elongated and be made to have a week triangularity. Hence, it is important to

examine the effect of the elongation and triangularity on the peaked pressure profile plasmas. A sequence of equilibria is examined with the elongation varying from $\kappa = 1.0$ to $\kappa = 1.8$ while keeping the total current and the q_0 fixed. Triangularity is kept fixed to $\delta = 0$ or $\delta = 0.25$. Generally, the internal kink mode is destabilized by the elongation and is stabilized by the triangularity [21]. Figure 6.18(a) shows the limited value of β_{p1} against the elongation with and without triangularity for the squared parabolic pressure profile plasma. The increase of the elongation reduces the β_{p1} limit, while the stability is slightly improved by the triangularity. These results confirm the previous results [21]. For the centrally peaked pressure profile, the β_{p1} limit also decreases with the increase of the elongation. However, when the triangularity is added, a larger improvement of the stability boundary is obtained as shown in Fig. 6.18(b). Figure 6.19 shows contributions of the pressure driven component W_{ball} and the current driven component W_{kink} for the corresponding pressure profiles in Fig. 6.18 ($\kappa = 1.6$ and $\delta = 0.25$). Plasmas with each pressure profile have the same values of q_0 (0.95), r_1/a (0.33) and β_{p1} (≈ 0.45). In both types of plasmas, the distribution of W_{ball} becomes broad as the elongation increases (Fig. 6.19(c),(d)), compared with the circular one shown in Fig. 6.17. Especially in the parabolic pressure profile, the distribution of W_{ball} largely spreads both inside and outside the q=1 surface (Fig. 6.19(d)) and the displacement $r\xi_r$ is mixed by the higher modes (Fig. 6.19(b)). The corresponding two dimensional plot of the displacement vector is shown for the squared parabolic pressure case (Fig. 6.20(b)), where the vortex rotates around the magnetic axis with a convective feature. These figure show that the W_{ball} in the squared parabolic pressure profile is larger than the W_{ball} in the peaked pressure profile due to the larger mode coupling. Therefore, the plasma with the peaked pressure profile has the higher boundary of critical β_{p1} against the n=1 internal kink mode, especially in the elongated shape with the triangularity.

6.3.4. Access to second stability

The second stable region of the n=1 internal kink mode was theoretically demonstrated by the decrease of q_0 using the σ scaling analysis (Eq. (3.6)). In the scanning of q_0 by the $\sigma-$scaling, the minor radius of the q=1 surface, r_1, increases with the decrease of q_0. In the usual tokamak operation regime ($q_s > 2.0$), r_1/a is below 0.5 because $r_1 = a/q_s$ [12]. The plasma with the small value of r_1/a (< 0.5) remains in the first stable regime of the n=1 internal kink mode, as shown in Fig. 6.16. Thus, we try to increase the radius of the q=1 surface over the experimentally observed value. Figure 6.21 shows the stability boundary for the plasma with the larger values of r_1/a ($= 0.67, 0.78$). When $r_1/a = 0.78$, the stability region in the $\beta_{p1} - q_0$ space drastically spreads from the restricted stable region for the plasma with $r_1/a = 0.67$. According to the analysis of Crew and Ramos [20], the access to second stability is caused by deepening the magnetic well due to the shift of the magnetic axis in the high β equilibrium. Figure 6.22 shows the value of the shift of the axis on the $\beta_p - r_1/a$ plane. The plasma with the larger r_1/a has the larger shift of the magnetic axis for the same value of β_p. Therefore, the large value of r_1/a facilitates access to the second stable region.

Figure 6.23 shows the possible range to access the second stable region in the $\beta_{p1}/\beta_p - r_1/a$ plane. In the this study, we focus on the plasma with the centrally peaked pressure profile, i.e., a large value of β_{p1}/β_p. However, from the viewpoint of the accessibility to the second stable region, plasmas with a small value of β_{p1}/β_p can easily access the second stable region, as shown in Fig. 6.23. This is because, in the plasma with the large value of β_{p1}/β_p, the increase of the magnetic well stabilization due to the high β equilibrium is less than the increase of the destabilization of the pressure driven contribution within the q=1 surface. Therefore, the low β_{p1}/β_p and the large r_1/a can easily access the second stable region, so that the strongly peaked one is not effective for the access to second stability.

6.3.5. Conclusion

The n=1 internal kink stability for the plasma with strongly peaked pressure profile within the q=1 surface has been numerically investigated using ERATO-J code. On comparing the two plasmas with different pressure profiles (peaked and squared parabolic pressure profile) and with the same value of β_{p1}, the plasma with the peaked pressure profile has higher value of the critical β_{p1} against the n=1 internal kink mode than that of the squared parabolic profile, because the plasma with the peaked pressure profile has smaller pressure driven component from the outside of the q=1 surface.

Effect of shaping the cross-section has been also obtained. Though the increase of the elongation reduces the stability boundary in both plasmas with the peaked and parabolic pressure profiles, the triangularity can improve the stability boundary. In the plasma with a peaked pressure profile, the stabilization due to the triangularity is pronounced. In the future tokamak with the elongated shape, therefore, a strongly peaked plasma can reduce the degradation of the β_{p1} limit by adding the triangularity.

When rearranging the calculation results, the plasma with the peaked pressure profile, i.e., the high value of β_{p1}/β_p, is preferable to increase the first stability boundary due to the week mode coupling, while the plasma with the low value of β_{p1}/β_p and the large value of r_1/a is preferable to access the second stable region due to the large magnetic well. However, in the standard tokamak operation ($q_s > 2.0$), the minor radius of r_1/a can not be increased beyond 0.5. Thus, the access to the second stability regime requires the current profile control.

6.4 Summary

Stability against ideal infinite n ballooning and low n internal kink modes has been analyzed for pellet fuelled plasmas in JT-60, which have strongly peaked pressure profiles within the q=1 resonance surface. The observed pressure gradient in pellet fuelled plasmas locally reaches the marginal value for the infinite n ballooning mode just inside the q=1 surface. After reaching the marginal value at the magnetic flux surface, the marginally stable region spreads inside the q=1 surface. However, the poloidal beta within the q=1 surface, β_{p1}, has not reached the limit imposed by the ideal ballooning mode. A comparison of the results of the analysis of the low n kink mode with the experimental observation shows that the attained maximum β_{p1} is consistent with the beta limit imposed by the n=1 internal kink mode.

The nature of the n=1 internal kink mode stability has been numerically clarified for plasmas with a centrally peaked pressure profile. The effect of the pressure profile is studied by comparing a profile strongly peaked inside the q=1 surface with a parabolic pressure profile. The plasma with the strongly peaked pressure profile has a higher limiting value of the poloidal beta defined within the q=1 surface than that of the parabolic pressure profile. The effects of shaping, i.e., elongation and triangularity, are also studied for both pressure profiles. Though the beta limit reduces with an increase in elongation, the plasma with the peaked pressure profile has a larger improvement with triangularity than that with the parabolic pressure profile. However, to enter the second stable region of the n=1 internal kink mode, a flat pressure profile and large minor radius of the q=1 surface are effective.

References

[1] M. Kaufmann: Plasma Phys. Controll. Fusion **28** (1986) 1341.

[2] Y. Kamada, R. Yoshino, M. Nagami, et al.: Nucl. Fusion **29** (1989) 1785.

[3] O. Gruber, G. Becker, G.von Gierke, et al., in Plasma Physics and Controlled Nuclear Fusion Research 1986 (Proc. 11th Int. Conf. Kyoto, 1986), Vol.1, IAEA, Vienna (1987) 357.

[4] K. Grassie, H.-P Zehrfeld: Nucl. Fusion **28** (1988) 899.

[5] M.S. Chu, L.L. Lao, R.W. Moore, et al.: Nucl. Fusion **27** (1987) 735.

[6] L.L. Lao, E.J. Strait, T.S. Taylor, et al.: Plasma Phys. Controll. Fusion **31** (1989) 509.

[7] The JET team: G.L. Schmidt: in Plasma Physics and Controlled Nuclear Fusion Research 1988 (Proc. 12th Int. Conf. Nice, 1988), IAEA, Vienna (1988) A-IV-1.

[8] R.M.O. Galvão, J.P. Goedbloed, G. Huysmans, et al.: in Controlled Fusion and Plasma Physics (Proc. 16th Eur. Conf. Venice, 1989), Vol.2, European Physical Society (1989) 501.

[9] M.N. Bussac, R. Pellat, D. Edery, J.L. Soule: Phys. Rev. Lett. **35** (1975) 1638.

[10] R. Yoshino: Nucl. Fusion **29** (1989) 2231.

[11] M. Azumi, T. Takizuka, T. Tsunematsu, et al.: in Inter. Conf. on Plasma Phys. (Proc. Int. Conf. Plasma Phys. Lausanne, 1984), Vol.9f, Part I, (1985) 375.

[12] Y. Kamada, R. Yoshino, M. Nagami, T. Ozeki: Nucl. Fusion **31** (1991) 23.

[13] R.D. Stambaugh, R.W. Moore, L.C. Bernard, et al., in Plasma Physics and Controlled Nuclear Fusion Research 1984 (Proc. 10th Int. Conf. London, 1984), Vol.1, IAEA, Vienna (1985) 217.

[14] C. Mercier: Nucl. Fusion **1** (1960) 47.

[15] M.F.F. Nave, J. Wesson: Nucl. Fusion **28** (1988) 297.

[16] F. Troyon, R. Gruber, H. Saurenmann, et al., Plasma Phys. and Controlled Fusion **26** No. 1A (1984) 209.

[17] Y. Kamada, T. Ozeki, M.Azumi: Phys. Fluids B4 (1992) 124.

[18] W. Kerner, R. Gruber, F. Troyon: Phys. Rev. Lett. **25** (1980) 536.

[19] S. Tokuda, T. Tsunematsu, M. Azumi, T. Takizuka, T. Takeda: Nucl. Fusion **22** (1982) 661.

[20] G.B. Crew, J.J. Ramos: Phys. Rev. **A26** (1982) 1149.

[21] J. Manickam: Nucl. Fusion **24** (1984) 595.

[22] R.J. Goldston: Plasma Phys. Controll Fusion **26** (1984) 87.

[23] JT-60 Team: in Plasma Physics and Controlled Nuclear Fusion Research 1986 (Proc. 11th Int. Conf. Kyoto, 1986) Nucl. Fusion, Vol. 1, (1987) Suppl. 217.

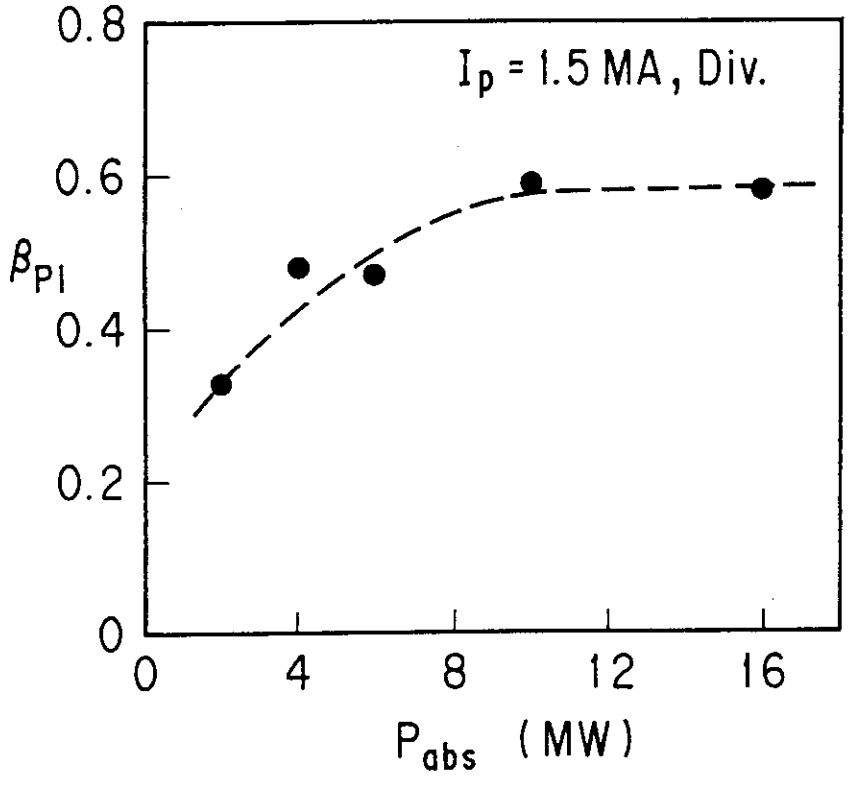

Fig. 6.1 Experimentally observed β_{p1} as a function of the absorbed power for discharges with $I_p = 1.5MA$ and $B_T = 4.5T$ in the divertor configuration.

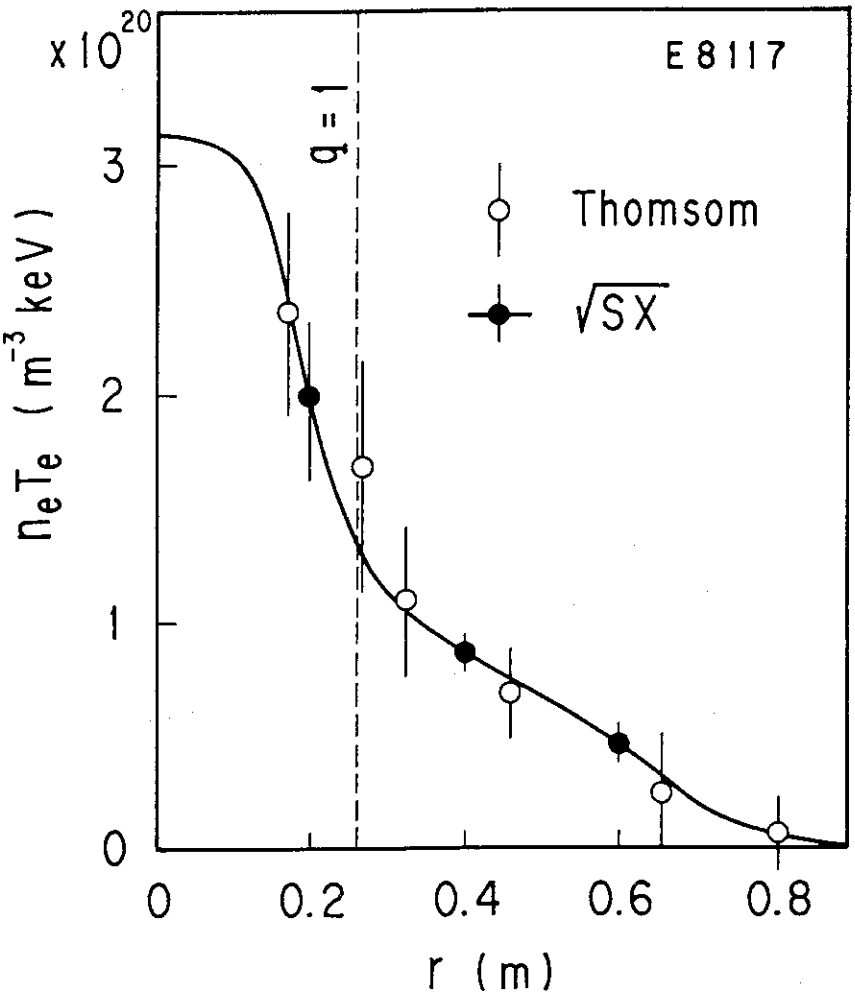

Fig. 6.2 Comparison of the electron pressure profile n_eT_e from Thomson scattering measurement with that from SX intensity, at the time when the strongly peaked profile is obtained.

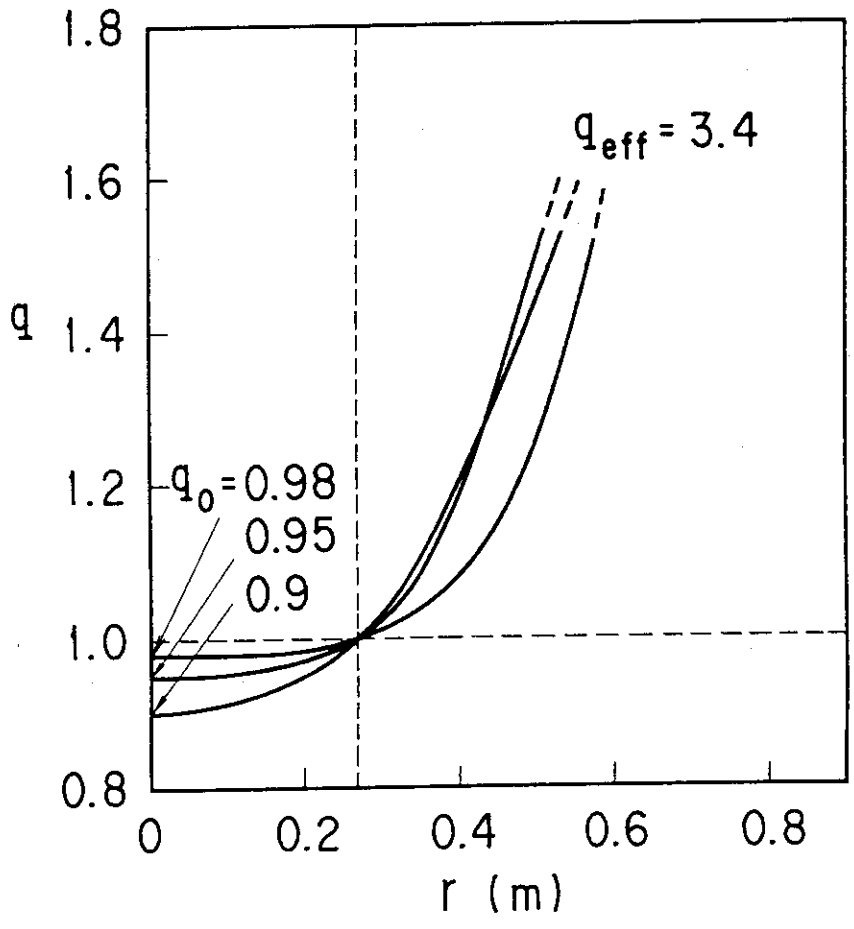

Fig. 6.3 Profiles for three values of the central q, i.e. q_0 =0.9, 0.95, and 0.98, with a fixed value of the surface q, i.e. q_{eff} =3.4; these values are used in the stability calculations.

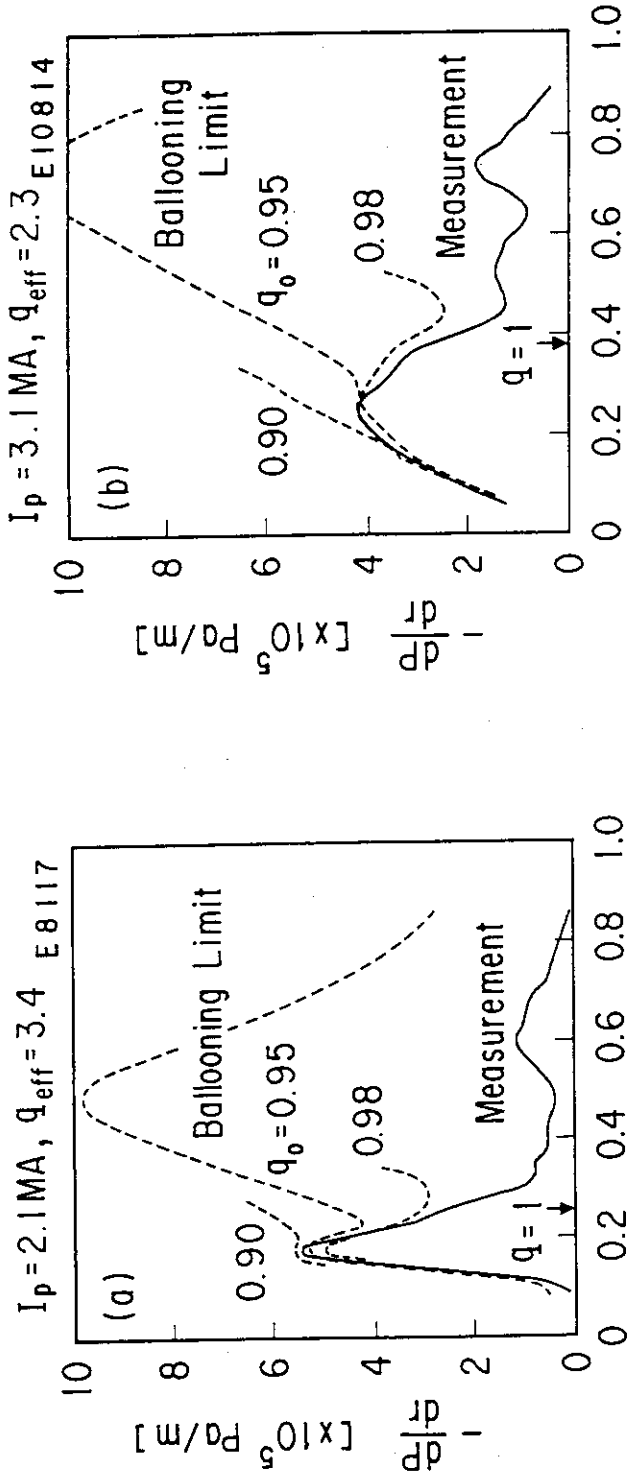

Fig. 6.4 Comparison of the marginal ballooning pressure gradient (broken line) with the experimental pressure gradient (solid line) as a function of the minor radius r(m) in plasmas with (a) a relatively low current and (b) a high current.

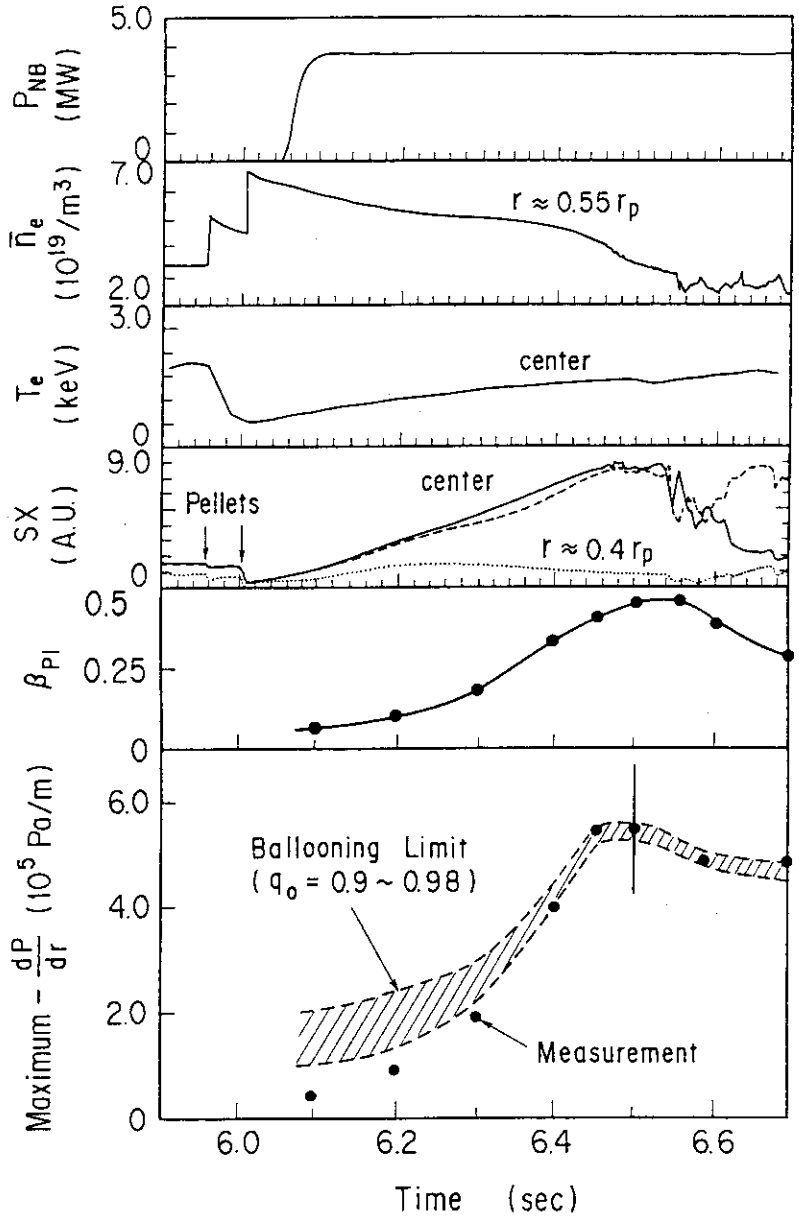

Fig. 6.5 Temporal evolution of various plasma parameters for a strongly peaked plasma, with $I_p = 2.1MA$ and $B_T = 4.8T$. Shown are the beam injection power P_{NB}, the line averaged electron density $\bar{n}_e$ at $r \approx 0.55r_p$, the electron temperature at the plasma center, the SX intensity of several chords near the plasma center (solid and broken lines) and in the peripheral region (dotted line), the central poloidal beta β_{p1} and a comparison of the marginal pressure gradients with the maximum observed pressure gradients.

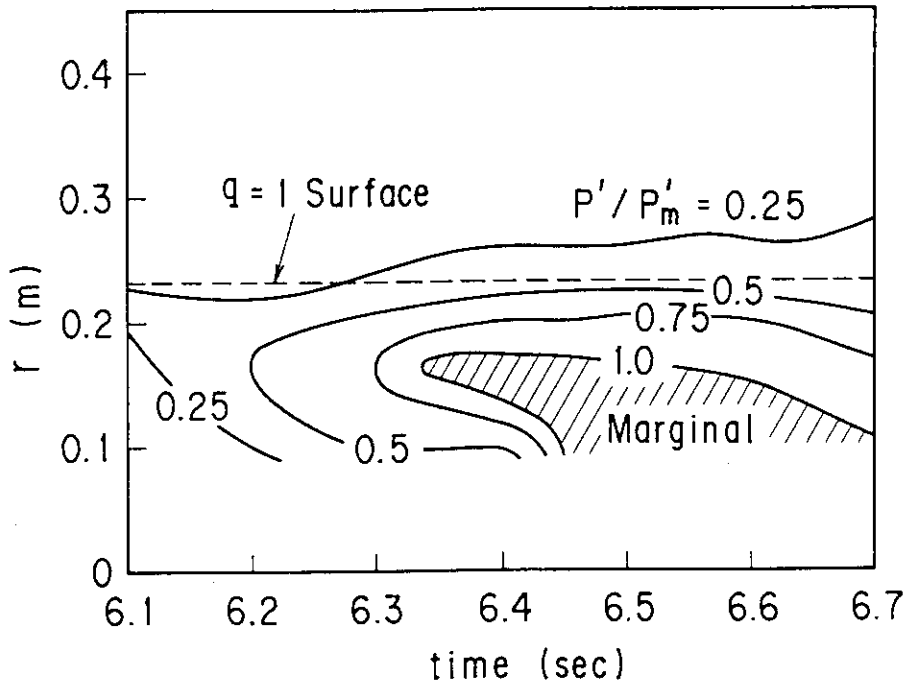

Fig. 6.6 Contours of the constant pressure gradient P' normalized to the marginal pressure gradient P'_m for infinite n ballooning mode stability as a function of time and minor radius r, for the plasma with q_0 =0.95 illustrated in Fig. 6.5.

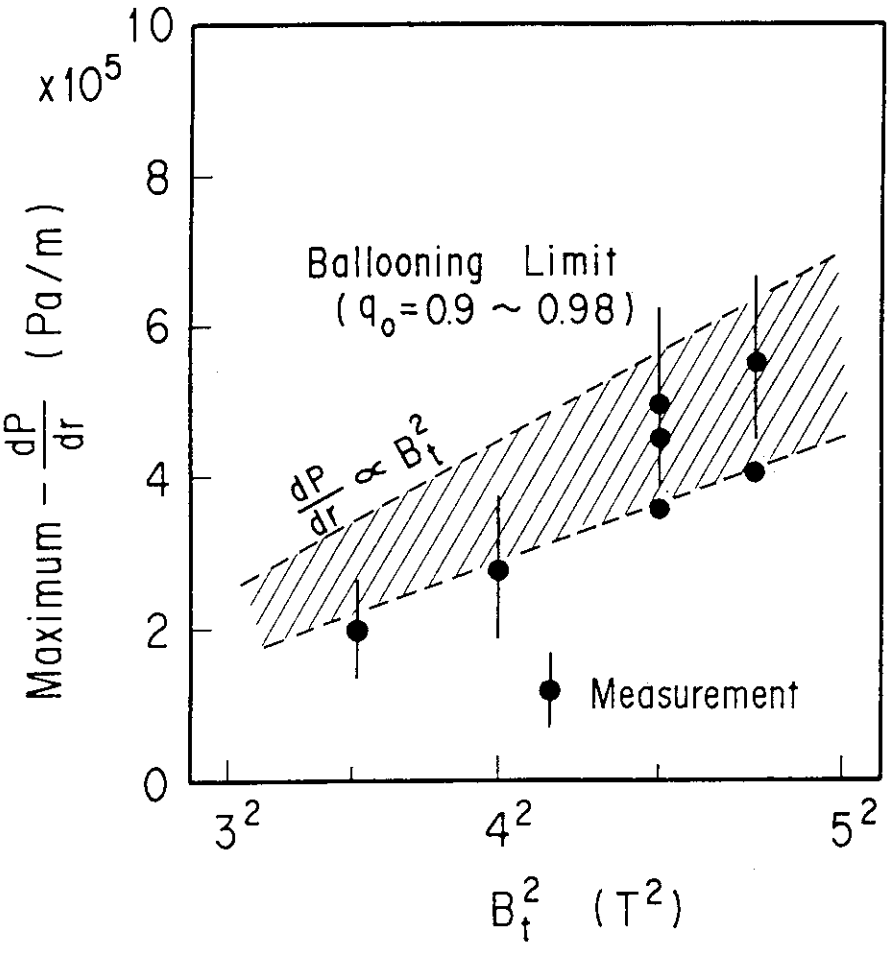

Fig. 6.7 Marginal (hatched region) and measured (closed circles) pressure gradients as a function of the squared toroidal field ($B_T{}^2$).

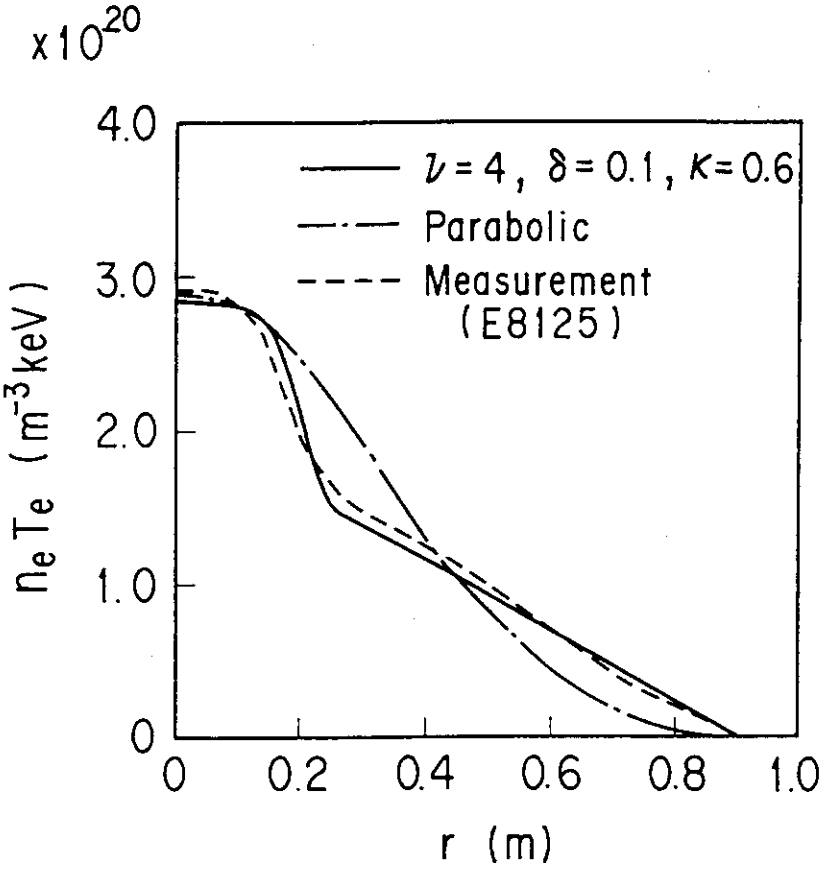

Fig. 6.8 Electron pressure profile n_eT_e defined by the Eq. (6.7) with ν=4.0, λ_1=0.1 and λ_2=0.6 (solid line); parabolic profile defined as $dP/d\tilde{\psi} \propto (1-\tilde{\psi})$ (dotted line); and the measured pressure profile from SX intensity (broken line).

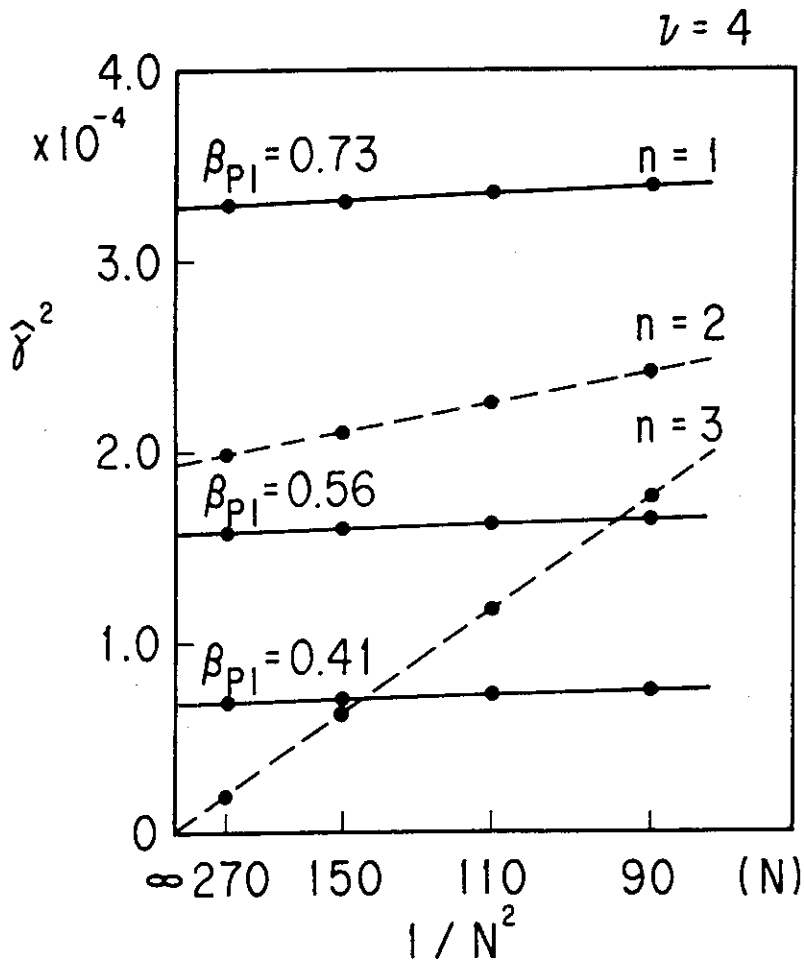

Fig. 6.9 Convergence check for several values of β_{p1} and the toroidal mode number n. The solid lines represent the $n = 1$ mode. $\hat{\gamma}^2$ is the squared growth rate and N is the mesh number of the ρ direction.

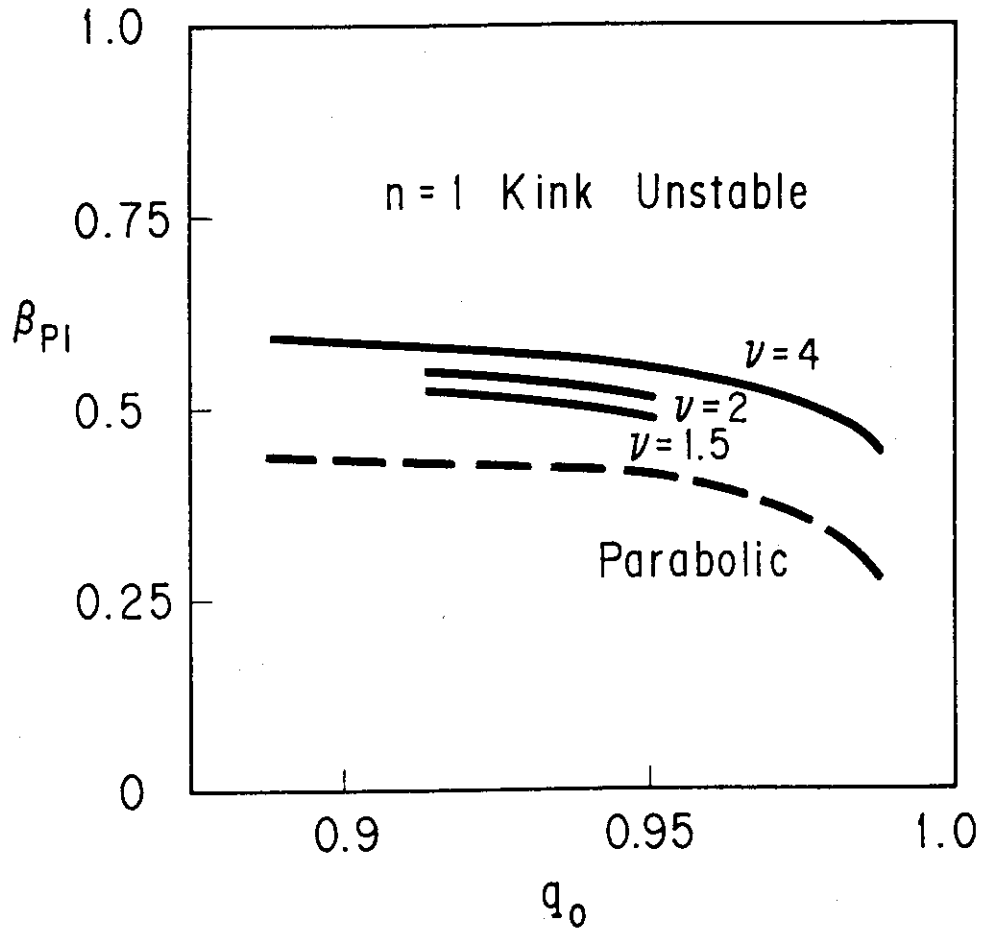

Fig. 6.10 Dependence of the critical β_{p1} on the central pressure profile with steep pressure gradients (ν =1.5, 2 and 4) and on the parabolic pressure profile as a function of q_0 with fixed q_{eff} =3.55.

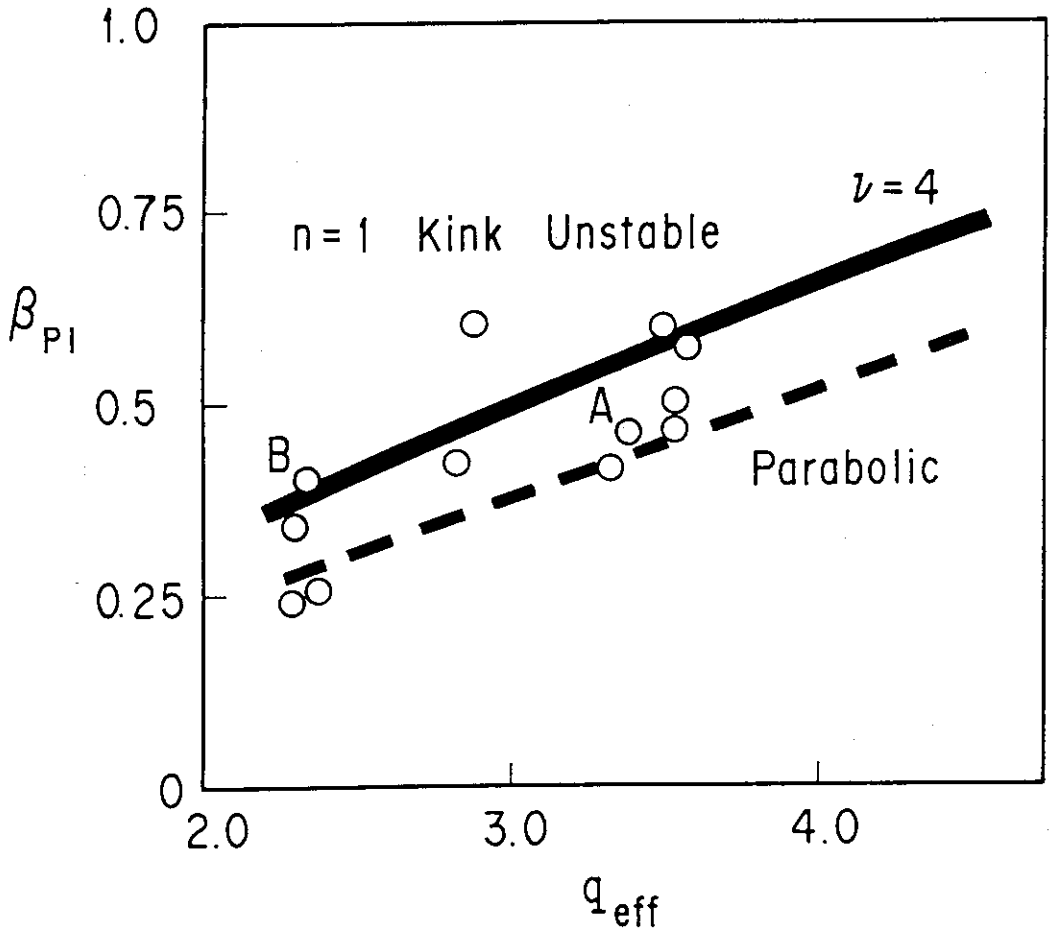

Fig. 6.11 Comparison of the theoretically predicted critical β_{p1} with the experimentally obtained values for a discharge with a fast crash (open circles), as a function of q_{eff} with a fixed value of $q_0 = 0.95$. The solid line is the limit for a plasma with $\nu = 4.0$, $\lambda_1 = 0.1$ and $\lambda_2 = 0.6$. The broken line is that for a parabolic pressure profile. The open circles marked A and B correspond to the discharges in Figs. 6.4(a) and 6.4(b) in the ballooning stability analysis.

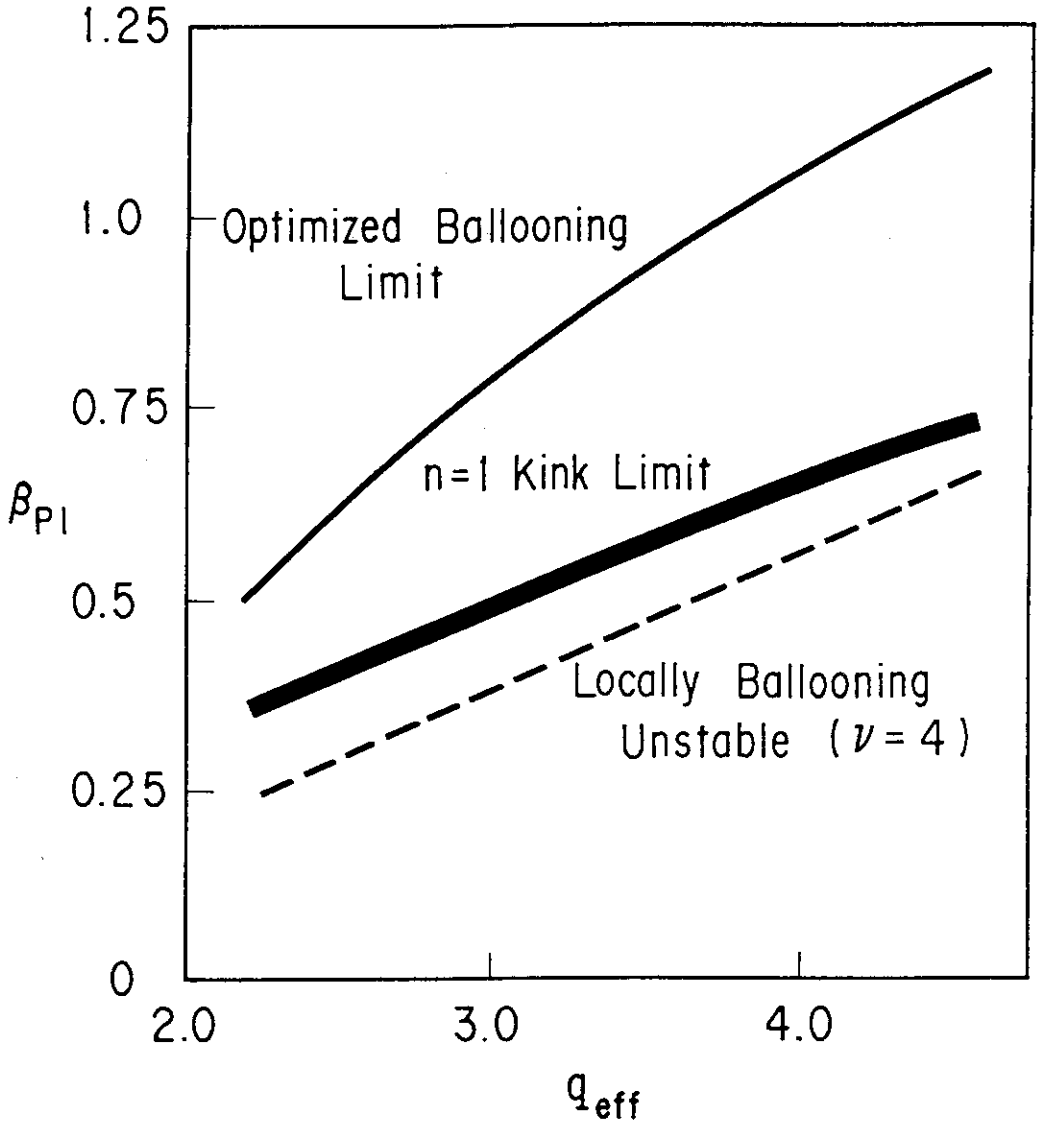

Fig. 6.12 Comparison of the critical β_{p1} for the n=1 internal kink mode (thick solid line) with the critical β_{p1} for the ideal ballooning mode with pressure profile optimization (thin solid line). In a plasma with a pressure profile parameter ν =4.0, the ideal ballooning mode becomes locally unstable (broken line) below the n=1 internal kink limit.

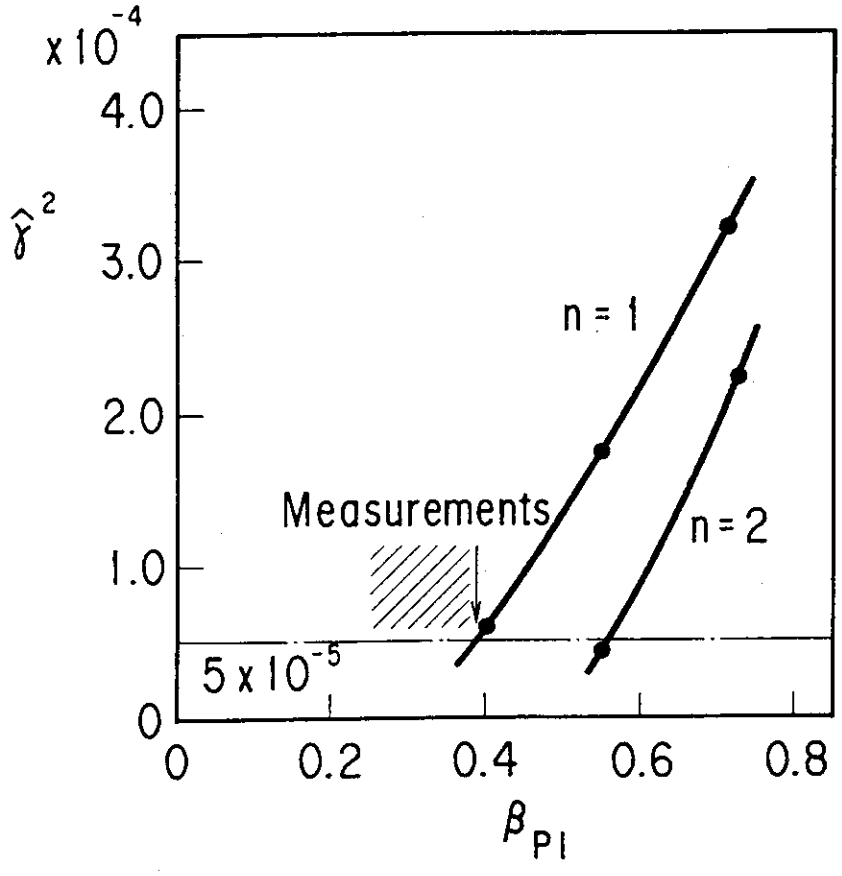

Fig. 6.13 Squared growth rate of the n=1 and n=2 kink modes as a function of β_{p1} for a plasma with q_{eff}=2.3 and q_0=0.95.

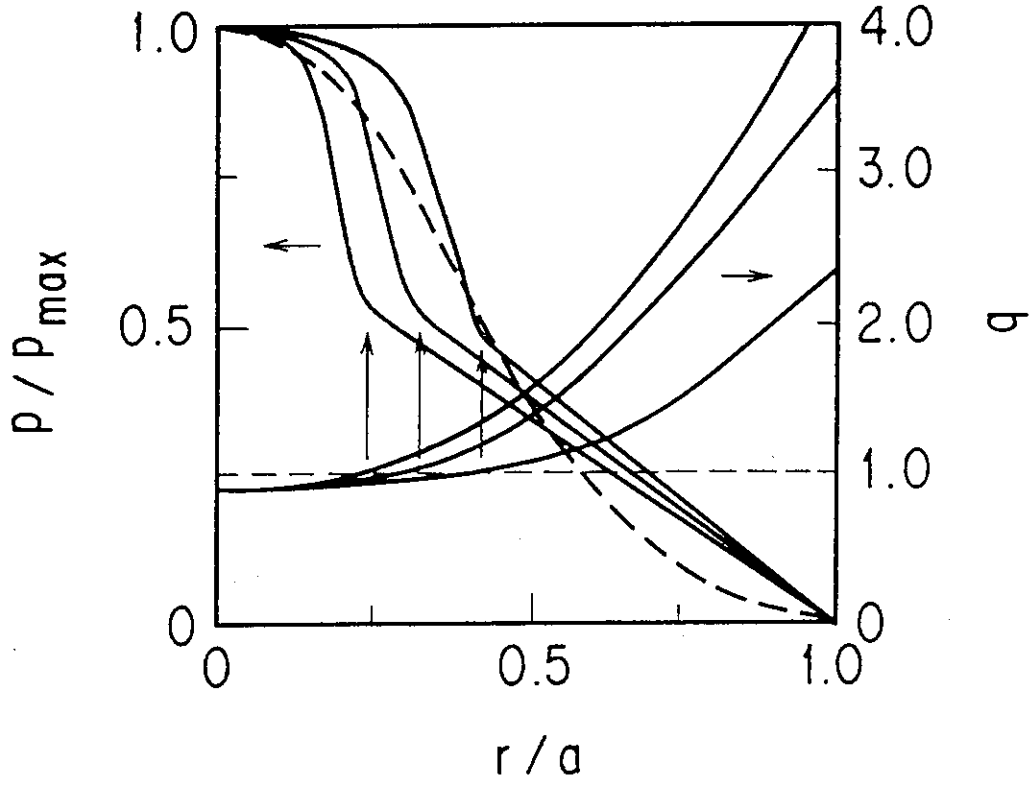

Fig. 6.14 q-profiles for various q_s and corresponding peaked pressure profiles, which are used in the calculation. Broken line shows a squared parabolic pressure profile.

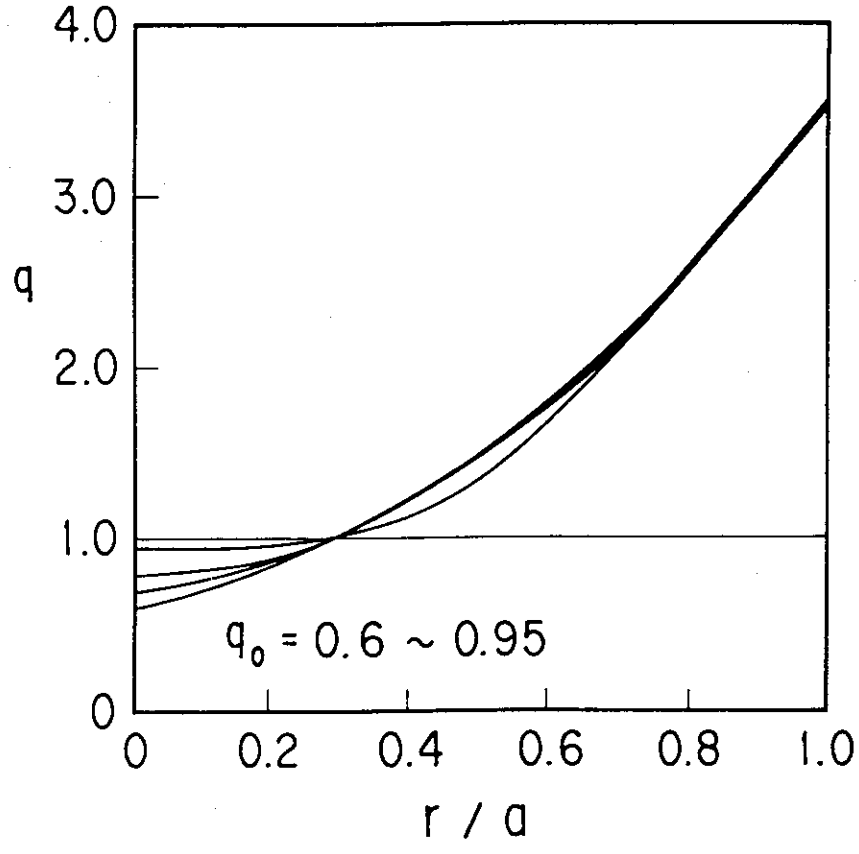

Fig. 6.15 q-profiles used for the q_0-scanning in the stability calculation.

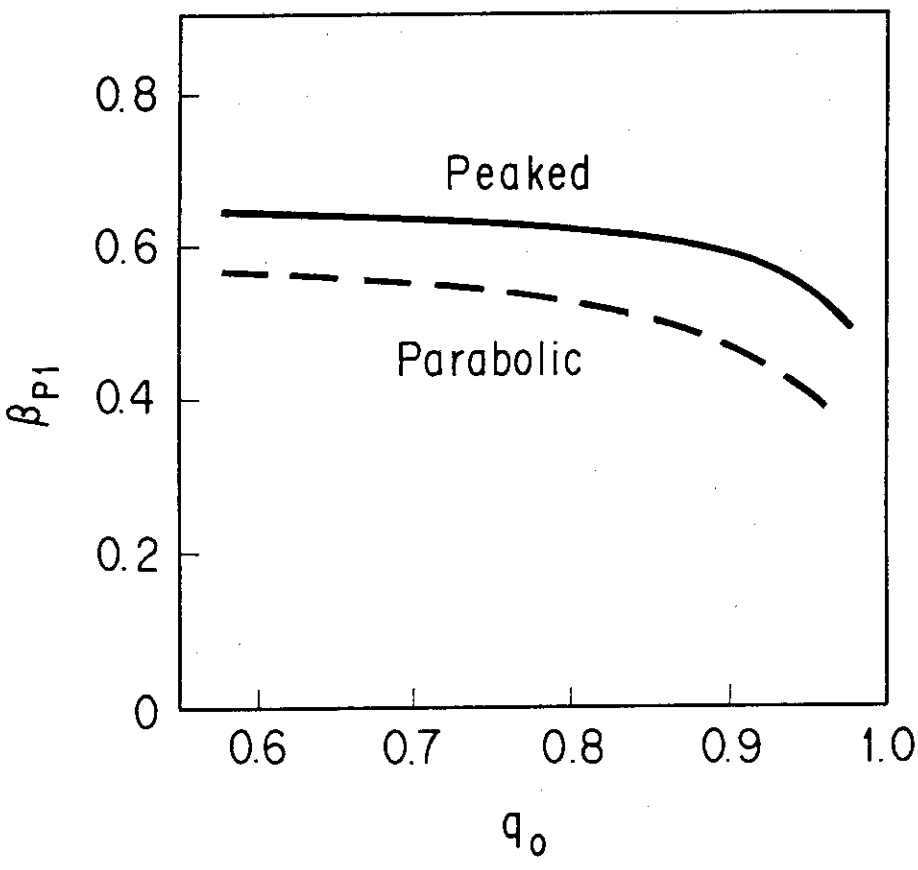

Fig. 6.16 Comparison of the critical β_{p1} of the peaked pressure profile; $\nu = 4.0$, $\lambda_1 = 0.1$ and $\lambda_2 = 0.6$ (Solid line), with that of the squared parabolic pressure profile (Broken line). Above the each line, the n=1 internal kink is unstable.

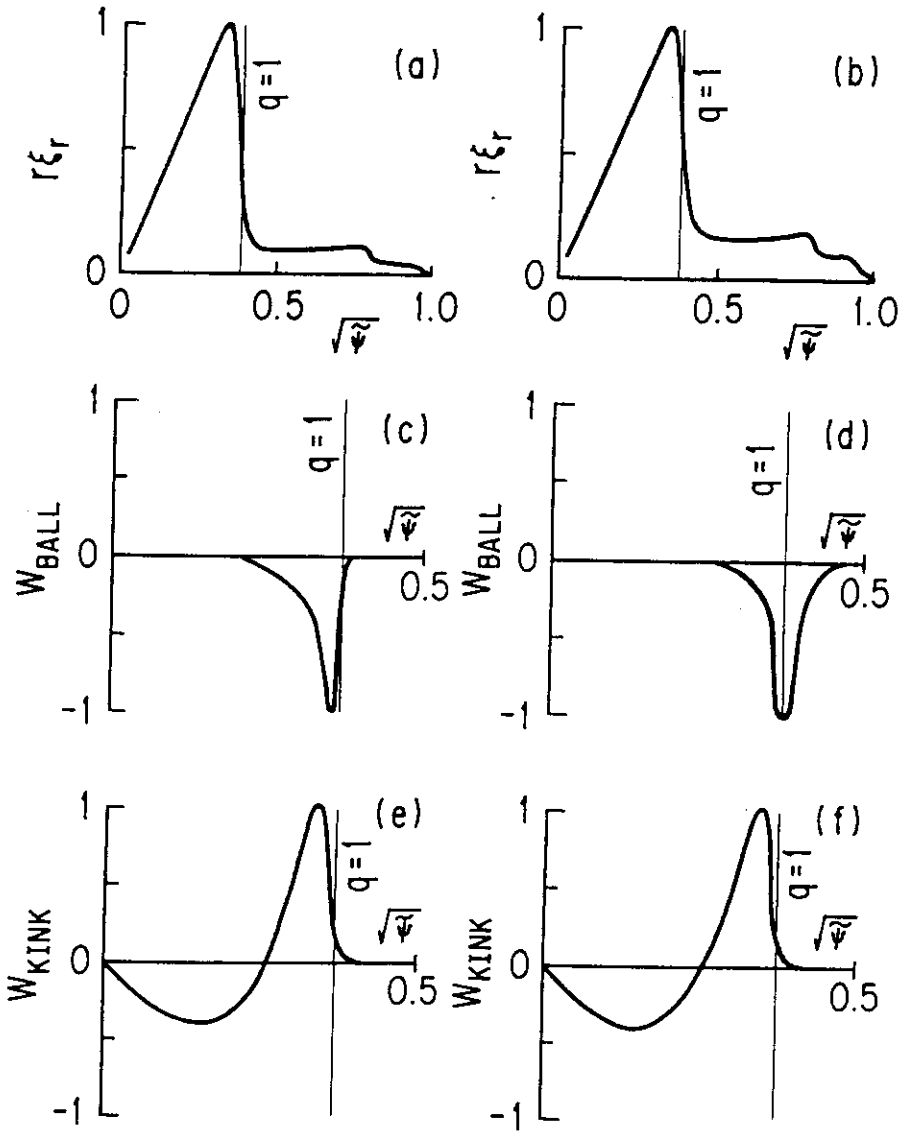

Fig. 6.17 Radial dependence of the normal displacement $r\xi_r$, the normalized pressure driven contribution W_{ball} and the normalized current driven contribution W_{kink} for the peaked pressure profile ((a),(c),(e)) and for the squared parabolic pressure profile ((b),(d),(f)). These plasmas correspond to those with $q_0 = 0.9$, $q_s = 3.5$ and $\beta_{p1} \approx 0.63$ in Fig. 6.16.

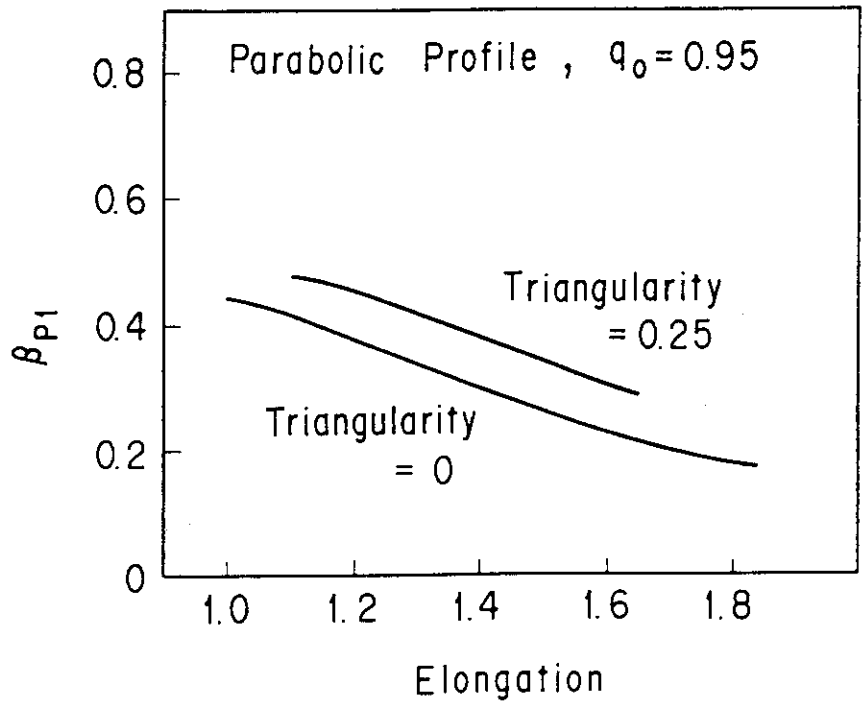

Fig. 6.18(a) Dependence of the critical β_{p1} of the squared parabolic pressure profile on the elongation and the triangularity.

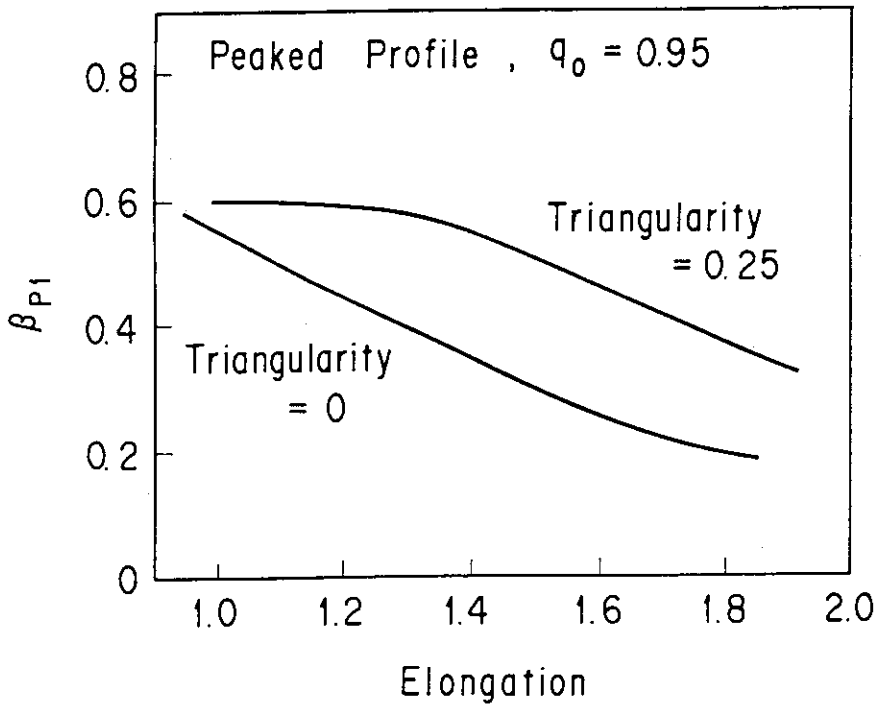

Fig. 6.18(b) Dependence of the critical β_{p1} of the peaked pressure profile with $\nu = 4.0$, $\lambda_1 = 0.1$ and $\lambda_2 = 0.6$ on the elongation and the triangularity.

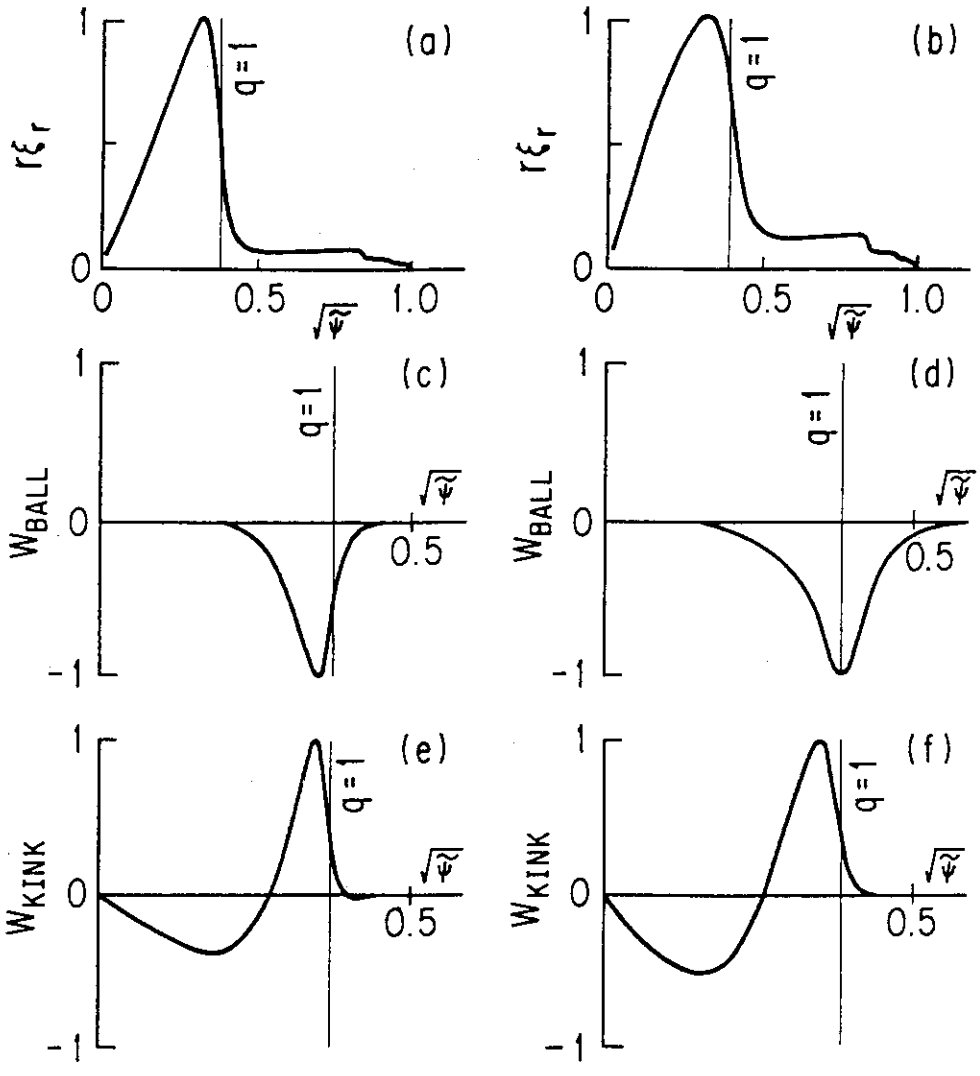

Fig. 6.19 Radial dependence of the normal displacement $r\xi_r$, the normalized pressure driven contribution W_{ball} and the normalized current driven contribution W_{kink} for the peaked pressure profile ((a),(c),(e)) and for the squared parabolic pressure profile ((b),(d),(f)) in non-circular plasmas with $\kappa = 1.6$, $\delta = 0.25$, $q_0 = 0.95$ and $\beta_{p1} \approx 0.45$.

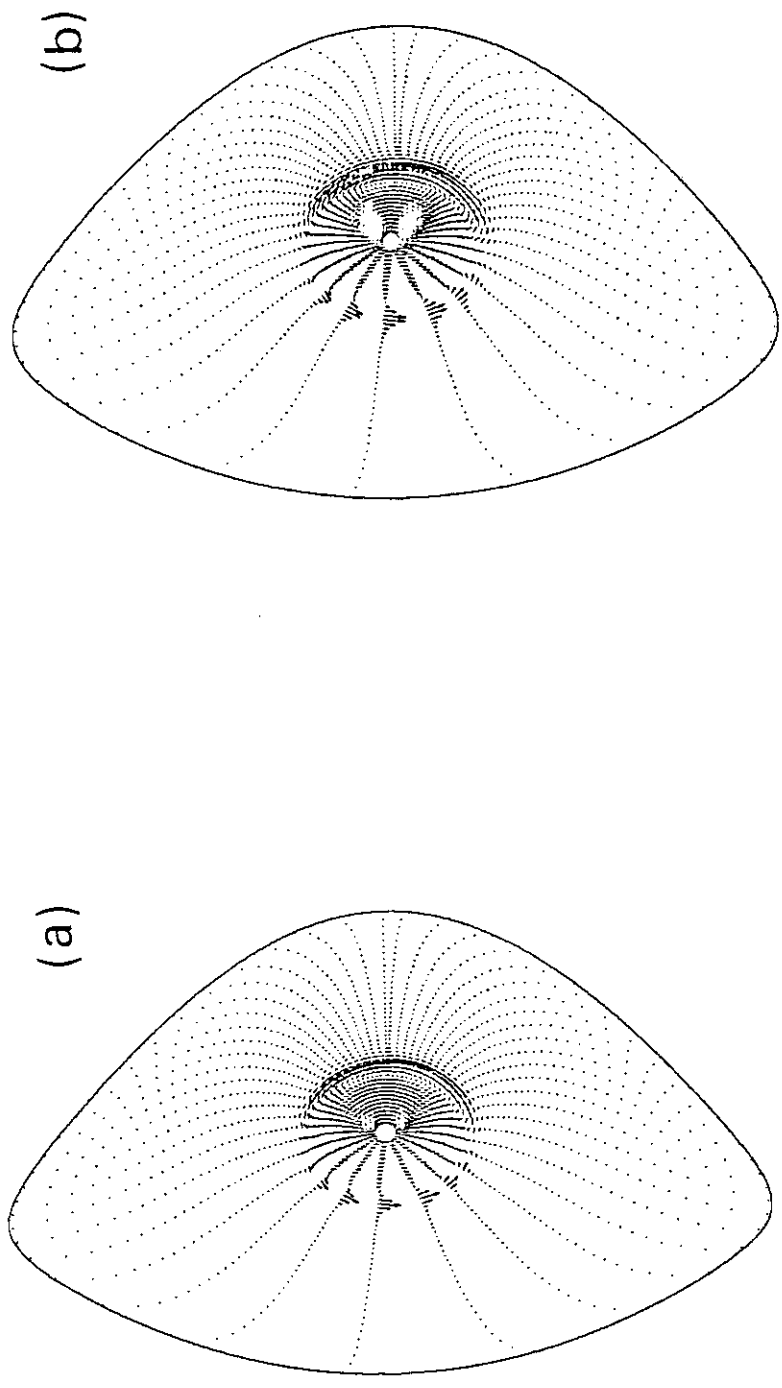

Fig. 6.20 Displacement vector of the poloidal component for (a) the peaked pressure plasma and (b) the squared parabolic pressure profile in Fig. 6.19.

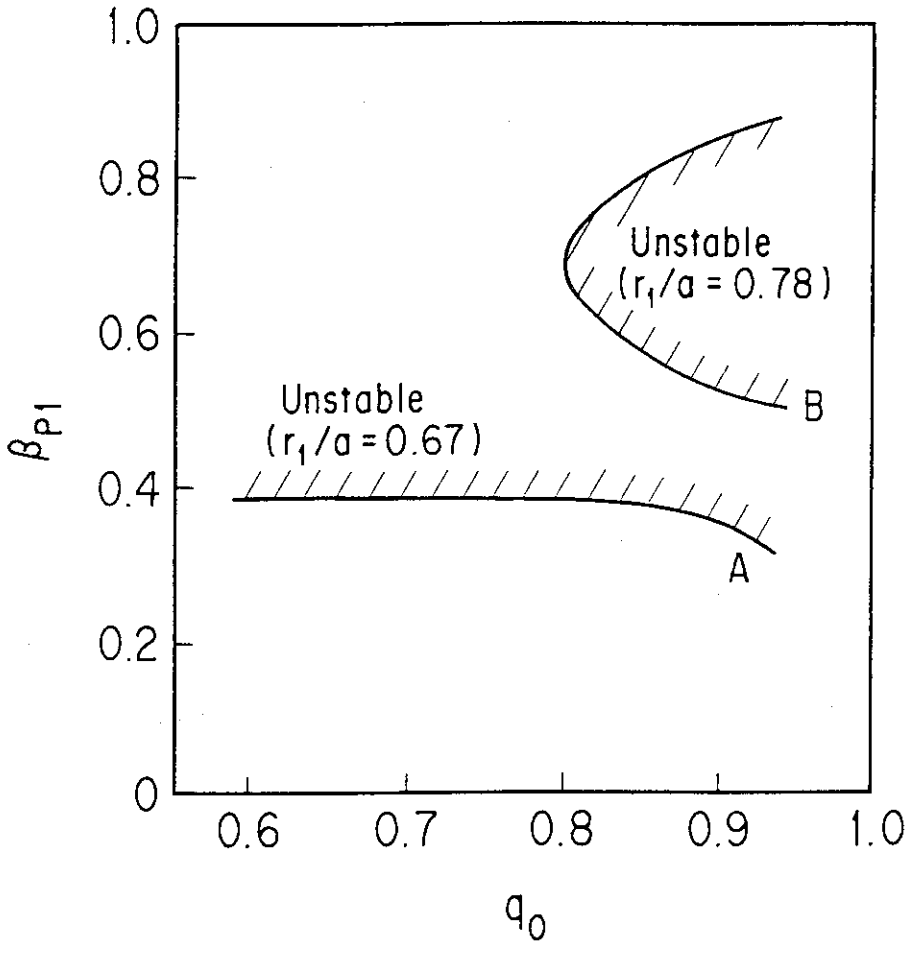

Fig. 6.21 Stability boundary on the $\beta_{p1} - q_0$ plane for the different values of the minor radius of the q=1 surface r_1/a. The shaded region is unstable for the n=1 internal kink. By the increase of r_1/a from $r_1/a = 0.67$ ($\beta_{p1}/\beta_p = 0.75$) to $r_1/a = 0.78$ ($\beta_{p1}/\beta_p = 0.45$), the stability boundary changes from the line A to the line B.

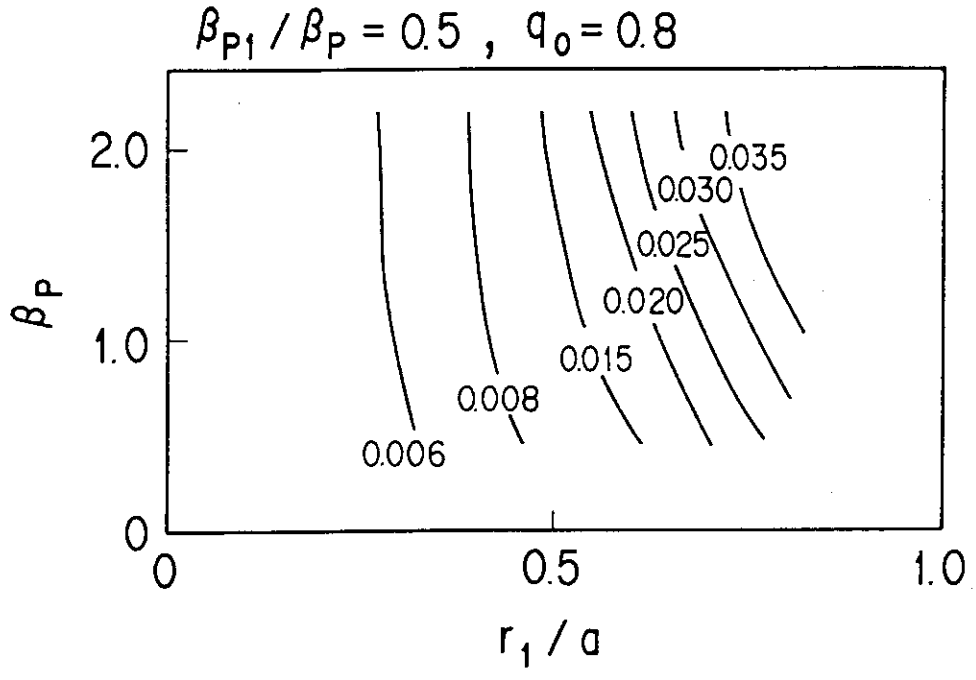

Fig. 6.22 Contour of the axis shift for the q=1 surface when $q_0 = 0.8$, $q_s = 2.2$ *and* $\beta_{p1}/\beta_p = 0.5$. *The shift is given by* $R_{axis} - R_c$, *where* R_c *is the geometric center of the q=1 surface.*

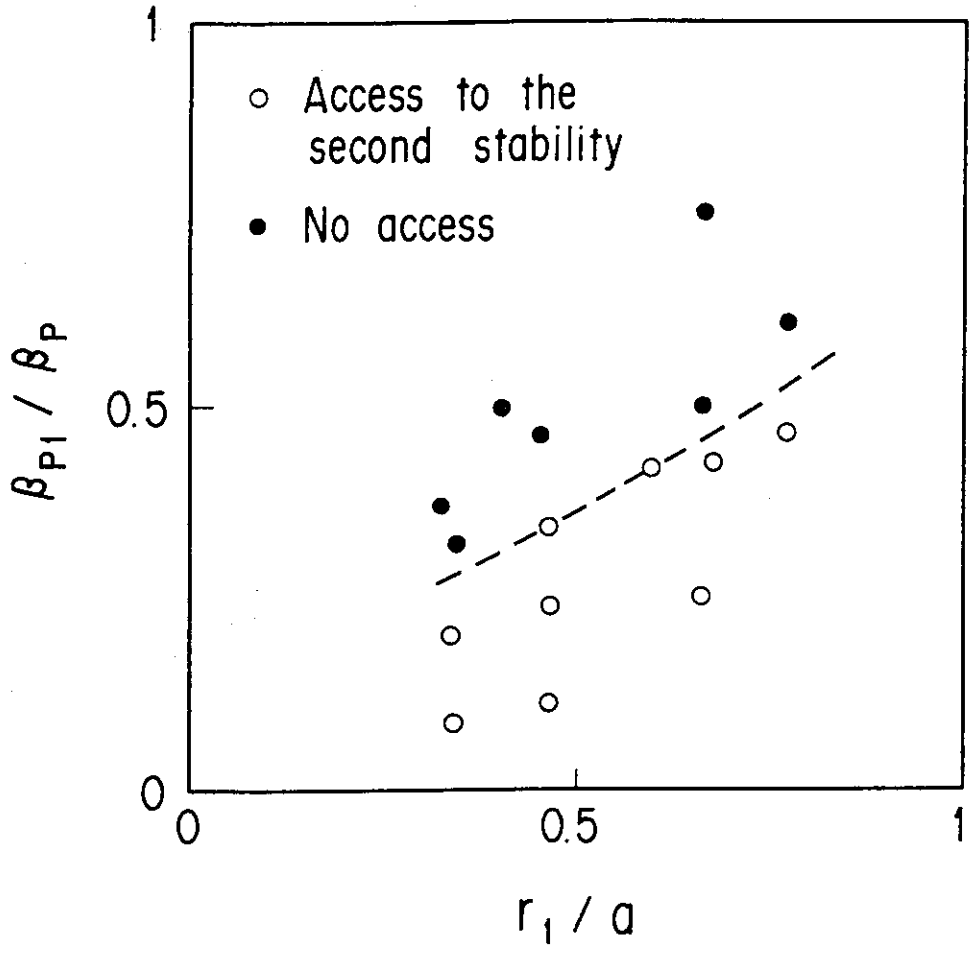

Fig. 6.23 Dependence of β_{p1}/β_p and r_1/a on the access to the second stability regime.

Chapter 7

Summary and Conclusion

Analyses of ideal MHD stabilities have been presented for plasmas in the divertor configuration, for H-mode plasmas in the DIII-D tokamak, and for pellet fuelled plasmas in the JT-60 tokamak. Chapter 1 reviewed the status of nuclear fusion research and MHD instability in tokamaks. The tokamak is presently the most advanced device. To obtain high-performance plasmas reaching the breakeven condition for nuclear fusion, enhanced confinement is necessary by means of, for example, the divertor configuration or pellet injection. Several kinds of MHD activity, however, limit improvement of the confinement. This thesis has investigated the MHD stability of the improved confinement plasmas in JT-60 and DIII-D, and discussed further improvement by the suppression of MHD stability.

The ideal MHD model and MHD stabilities in a tokamak were described in Chapter 2. Ideal MHD is the most fundamental single-fluid model for determining the macroscopic equilibrium and stability properties of a magnetically confined fusion plasma. For real plasmas encountered in tokamak experiments, the ideal MHD model provides a very reliable description of equilibrium and stability. The typical and important instabilities in the tokamak are positional stabilities, the kink stability and the ballooning stability.

In Chapter 3, the JT-60 and DIII-D tokamaks were introduced, and the problems of MHD stability in these tokamaks were presented. Numerical codes used for determining

ideal MHD stability were also described. JT-60 has a poloidal divertor on the outboard side of the torus. The poloidal divertor coil is expected to destabilize the horizontal mode of the positional stability because the divertor coil tends to make the plasma ring expand. On the other hand, it is expected to stabilize the kink mode because the divertor configuration produces strong shear near the plasma surface. It is important to clarify these features when considering improved confinement. DIII-D tokamak has a non-circular cross section plasma with a poloidal divertor at the bottom of torus. Enhanced confinement is observed in the H-mode plasma, but MHD activity near the plasma surface, called edge-localized modes (ELMs), occurs. The ELMs degrade the particle and energy confinement at the plasma edge and inhibit the increase in the plasma density. It is important to investigate the cause of the instability and to find a method for suppression of ELMs. In JT-60, enhanced confinement was obtained with a centrally peaked pressure profile obtained by pellet injection. The peaked pressure and associated improved central β are constrained by MHD activities. Therefore, it is necessary to investigate the cause of the limitation and the improvement of the peaked pressure profile. To analyze these problems of MHD stability, numerical codes are usually required to deal with realistic plasma models with enough accuracy. In this thesis, a 2-dimensional equilibrium code was used to prepare for the stability analysis. Low n modes, i.e., the positional stability and the kink stability, were analyzed by the ERATO-J code. High n ballooning stability was analyzed by the BETA, MBC and CAMINO codes.

The problems of MHD instabilities encountered in the JT-60 and DIII-D tokamaks provided us with the following three subjects:

(1) Effects of the divertor configuration on ideal MHD stability (Chapter 4).

(2) Correlation of the ideal MHD stability near the plasma surface with the ELM activity of the H-mode plasma and the suppression of the ELM (Chapter 5).

(3) Correlation of the ideal MHD stability near the plasma center with the internal MHD activities of the pellet fuelled plasma, and the improvement of the limitation of the peaked plasma pressure (Chapter 6).

Chapter 4 presented the effects of the divertor configuration on axisymmetric modes and kink modes in a tokamak. (a) Regarding positional stability, a divertor configuration results in a large variation of the decay index n_z over the plasma region. However, a wide stability window is obtained for axisymmetric modes because of the stabilizing effect of sub divertor coils. The threshold value of the averaged decay index $< n_z >$ for the horizontal instability in the divertor configuration with an outside X-point is higher than the value in the limiter. For the unstable mode with displacement vectors moving toward the X-point, the perturbation is localized near the plasma surface and the growth rate is lower than that in the limiter configuration. (b) For the kink mode, the large shear near the X-point strongly stabilizes the external kink mode. The reduction of growth rate, the wider stability window and the localization of displacement are obtained in the divertor configuration. The stabilizing effect is reduced with the increase in the plasma pressure. The critical beta value is sightly improved in the divertor configuration ($\sim 0.1\%$) and depends on the internal inductance.

Chapter 5 theoretically demonstrated no limit for ballooning stability near the separatrix by increasing the plasma elongation ($\kappa > 1.8$) and triangularity ($\delta > 0.4$) in a plasma with small values of $\mu_B (< 0.15)$ in the DIII-D divertor configuration. Experimentally, giant ELMs disappear in these shaped plasmas with low μ_B. Theoretical analysis of experimental data supports the hypothesis that giant ELMs in DIII-D are triggered by the ideal ballooning mode and can be suppressed when the plasma is in the connection region between the first and second stable regions. To determine the mechanism of ELM suppression, the conditions for accessibility to the region of second stability were investigated in terms of the safety factor, the global shear, the shaping and the aspect ratio. It was shown that plasmas with high safety factor and low global

shear near the plasma surface can access the second stable region through the connection region. Low aspect ratio and positive triangularity ($\delta > 0$) can also facilitate access to the second stable region.

Chapter 6 presented the analysis of ideal MHD stability in pellet fuelled plasmas in JT-60. A comparison of the results of the analysis of the low n kink mode with the experimental observations showed that the attained maximum β_{p1} is consistent with the β_{p1} limit imposed by the n=1 internal kink mode. To obtain a larger value of β_{p1}, the effect of the peaked pressure profile on the n=1 internal kink mode stability was numerically investigated. A plasma with a strongly peaked pressure profile has a higher critical value of β_{p1} than that with a parabolic pressure profile. Thus, a higher toroidal field can produce a more peaked pressure profile and increase the critical β_{p1}, because the pressure gradient just inside the q=1 surface is limited by the ideal ballooning mode. Though the beta limit reduces with increased elongation, triangularity can largely improve the critical β_{p1} in a plasma with a peaked pressure profile rather than that with a parabolic pressure profile.

Finally, this study revealed the role of ideal MHD stabilities in enhanced confinement plasmas approaching nuclear fusion conditions. Consideration of the mechanisms of the MHD stabilities can help to guide future experiments in H-mode plasmas and pellet fuelled plasmas in tokamaks. Further analyses of MHD stability in reactor-relevant plasmas are necessary to deduce some information about the production of the nuclear fusion reactor.

Acknowledgements

I would like to express sincere gratitude to Professor M. Ogasawara of Keio University for his valuable instruction to a successful conclusion and his affectionate encouragement. I also wish to express my gratitude to Professor T. Tanahashi, Professor T. Makabe, Professor K. Niu and Associate Professor M. Kindaichi for their valuable suggestion and instruction.

I wishes to express my appreciation to Dr. M. Azumi for his useful discussion and collaboration. I also wish to thank Drs. S. Tokuda, T. Tsunematsu and T. Takeda for their useful theoretical discussions and the use of ERATO-J code.

I wishes to acknowledge Drs. M.S. Chu, L.L. Lao, T.S. Taylor, K.H. Burrell, and R.D. Stambaugh of General Atomics and Dr. S. Kinoshita of Hitachi Ltd. for fruitful discussions about the analysis of ELMs in DIII-D and the use of EFIT code and MBC code. I wish to thank Dr. M.S. Chance of Princeton Plasma Physics Laboratory for the use of the CAMINO code. I also would like to acknowledge Drs. M. Shimada, S. Konoshima and T.C. Simonen for their fruitful discussions and continuous support.

I wishes to acknowledge Drs. Y. Kamada, R. Yoshino, K. Nagashima, H. Yoshida and M. Nagami for fruitful discussions about the analysis of the pellet fuelled plasma in JT-60. I also acknowledges all members of JT-60 and Drs. Y. Shimomura, H. Kishimoto and S. Tamura for their collaboration and continuous encouragement.

I also appreciate Dr. S.W. Wolfe for his improvement of the English text. Finally, the thesis would not have been completed without the understanding and the constant support from Keiko of my wife during these years. Thank you.